Polymer microring resonators for optofluidic evanescent field sensors

Camille Delezoide

ENSC-xxxx

THESE DE DOCTORAT
DE L ECOLE NORMALE SUPERIEURE DE CACHAN

Présentée par

Monsieur Camille Delezoide

pour obtenir le grade de

DOCTEUR DE L ECOLE NORMALE SUPERIEURE DE CACHAN

Domaine :

SCIENCES PHYSIQUES

Sujet de la thèse :

MICRORESONATEURS EN ANNEAUX POLYMERES POUR CAPTEURS OPTOFLUIDIQUES A CHAMP EVANESCENT

Thèse présentée et soutenue à Cachan le 18/12/2012 devant le jury composé de :

Pierre VIKTOROVITCH	DR CNRS - Ecole Centrale de Lyon	Président
Henri BENISTY	Professeur - Institut d'Optique	Rapporteur
Olivier PARRIAUX	Professeur - Université St-Etienne	Rapporteur
Joseph ZYSS	Professeur - Institut d'Alembert	Examinateur
Frank VOLLMER	Ass. Professeur - Max Planck Institute	Examinateur
Malcolm BUCKLE	DR CNRS - ENS Cachan	Examinateur
Chi Thanh NGUYEN	IR CNRS - ENS Cachan	Encadrant de thèse
Isabelle LEDOUX-RAK	Professeur - ENS Cachan	Directrice de thèse

Laboratoire de Photonique Quantique et Moléculaire
ENS CACHAN/CNRS/UMR 8537
61, avenue du Président Wilson, 94235 CACHAN CEDEX (France)

Contents

LIST OF TABLES 7

LIST OF FIGURES 9

1 Optofluidic and label-free sensors 23
1 Elements of sensor theory . . . 24
1.1 Introduction . . . 24
1.2 Sensor characteristics . . . 27
2 Optical evanescent-wave sensing . . . 38
2.1 Introduction . . . 38
2.2 Basic applications . . . 42
2.3 Application to label-free biosensing . . . 45
3 Microring resonators in measuring instruments . . . 57
3.1 Introduction . . . 57
3.2 Optical characteristics . . . 59
3.3 Detection schemes . . . 61
3.4 State-of-the-art . . . 78
3.5 Microfluidic integration . . . 81

2 Models and simulations of passive microring resonators 85
1 Effects occurring in microring resonators . . . 85
1.1 Optical material-related effects . . . 86
1.2 Effects related to the guiding of light . . . 88
1.3 Influence of environmental physical quantities . . . 92
2 Analytical model: starting point . . . 92
2.1 Elements of the model . . . 92
2.2 Intensity transmittance . . . 93
2.3 Optical characteristics . . . 96
3 Analytical formulation of internal parameters . . . 105
3.1 Challenges . . . 105
3.2 Effective index . . . 106
3.3 Loss mechanisms . . . 107
3.4 Coupling mechanisms . . . 112
4 Additions to the analytical model . . . 117
4.1 Modal Dispersion . . . 117
4.2 Modal Birefringence . . . 120

4.3 Multimodal behavior . . . 123
5 Numerical simulations of microring resonators . . . 126
5.1 Challenges . . . 126
5.2 Application of FDTD method to ring resonators . . . 127
5.3 Numerical simulation of internal parameters . . . 134
5.4 Estimation of coupling coefficients . . . 136

3 Fabrication of microring resonators 139
1 Fabrication Procedures . . . 140
1.1 Introduction . . . 140
1.2 Spin coating . . . 141
1.3 UV lithography patterning . . . 147
1.4 Reactive Ion Etching (RIE) . . . 154
1.5 Wafer slicing . . . 157
2 Control tools . . . 158
2.1 Optical microscopy . . . 159
2.2 Contact profilometer . . . 159
3 Fabrication of vertically-coupled microresonators . . . 160
3.1 Materials . . . 160
3.2 Description of the fabrication steps . . . 160
3.3 Technical defects . . . 174
3.4 Fabrication challenges . . . 178

4 Optical characteristics of microring resonators 183
1 Characterization Methods . . . 183
1.1 Cavity Ring Down (CRD) Techniques . . . 183
1.2 Optical Low-Coherence Interferometry (OLCI) . . . 186
1.3 Wavelength-Scanning Method . . . 191
2 Measurement setup . . . 207
2.1 Basic Setup . . . 207
2.2 Acquisition method . . . 213
3 Optical characteristics . . . 217
3.1 Experimental characterization of a microring resonator . . . 217

5 Sensing properties of microring resonators 237
1 Sensitivity, resolution and LOD . . . 238
1.1 First expression for the limit of detection (LOD) . . . 238
1.2 Microresonator sensivitity and LOD . . . 239
1.3 Optimization of the LOD . . . 239
1.4 Analysis of the microresonator sensitivity . . . 241
2 Evaluation of the waveguide sensitivities . . . 243
2.1 Use of numerical tools: application to glucose sensing . . . 244
2.2 Use of analytical models . . . 246
2.3 Sensitivities of rectangular waveguides . . . 250
3 Microresonator sensitivities in homogeneous sensing . . . 262
3.1 Microresonator sensitivity . . . 262
3.2 Sensitivity to the measurand . . . 264

3.3 Optimization of the cladding sensitivity . . . 266
4 Optimization for surface sensors . . . 269
4.1 Introduction to surface sensing . . . 269
4.2 Sensitivity in surface sensing experiments . . . 270
4.3 Sensitivity of the RI distribution to the analyte . . . 271
4.4 Waveguide sensitivity to the RI distribution . . . 276
4.5 Application to the optimization of microresonators for surface sensing . . . 278

6 Instrumentation of evanescent field sensors 293
1 Microfluidics integration . . . 294
1.1 Introduction . . . 294
1.2 Materials for microfluidic circuits . . . 294
1.3 Fabrication of PDMS microfluidic caps . . . 295
1.4 Chip integration . . . 299
1.5 Microfluidic circuit . . . 303
2 Optoelectronic instrumentation . . . 309
2.1 Introduction . . . 309
2.2 Optoelectronic architecture . . . 309
2.3 Control program . . . 311
3 Temperature control . . . 312
3.1 Introduction . . . 312
3.2 Thermal control from the substrate . . . 313
3.3 Thermal control of buffer and analyte solutions . . . 316
3.4 Thermal control of the microfluidic circuit . . . 316

7 Sensing experiments 319
1 Homogeneous sensing experiments . . . 319
1.1 Refractive index of glucose as function of the concentration . . . 319
1.2 Evolution of the resonance linewidth in homogeneous sensing . . . 323
1.3 Optofluidic detection of glucose in aqueous solution . . . 327
2 Surface sensing experiments . . . 335
2.1 Static detection of TAMRA-cadaverine . . . 335
2.2 Optofluidic detection of adsorption/desorption kinetics of TAMRA on anti-TAMRA . . . 342
1 General thoughts . . . 345
2 Developed skills . . . 346
2.1 Theoretical skills . . . 346
2.2 Experimental skills . . . 346
2.3 Computer skills . . . 347
2.4 Presentation skills . . . 347
2.5 Language skills . . . 347
3 Main achievements . . . 347
3.1 Analytical models for microring resonators . . . 347
3.2 Numerical simulation of microring resonators . . . 347
3.3 Fabrication of polymeric, vertically-coupled microring resonators 347

3.4 Understanding of key parameter for the LOD 347
3.5 Optimization of waveguide for homogeneous and surface sensing 348
3.6 Demonstration of highly-sensitive surface sensing 348
3.7 Demonstration of optofluidic sensing 348
3.8 Demonstration of label-free sensing 348
4 Perspectives 348

Bibliography **349**

List of Tables

1.1 Typical grades and expressions for the limit of detection (LOD) 37
1.2 Uncertainty budget related to the fixed-wavelength method (FWM). . . . 65
1.3 Uncertainty budget related to the wavelength-scanning method (WSM). . 70
1.4 Specific uncertainty budget for the measurement of $\delta\lambda$ in the WSM. . . . 73
1.5 Comprehensive uncertainty budget for the wavelength-scanning method. . 74

3.1 Comparison between two typical negative and positive photoresists. . . . 148
3.2 General properties of fabrication materials. 160

4.1 Estimated values of the accuracy for the determination of the resonant wavelength 233

7.1 Tabulated values of refractive index for an aqueous solution of D-glucose as function of the relative mass and the molar concentration. 320
7.2 Evolution of resonance characteristics as function of the sucrose concentration 325

List of Figures

1.1 Local linearisation of a nonlinear transfer function. 28
1.2 Effect of an hysteresis on the transfer function. 32
1.3 Saturation and dead band on a transfer function. 33
1.4 Statistical comparison between grades of LOD. 38
1.5 Total internal reflection (TIR) of an incident wave at an interface 39
1.6 Principle of evanescent-wave homogeneous detection. 43
1.7 Principle of evanescent-wave surface detection. 44
1.8 LOD versus the response time. 49
1.9 Schematic view of a typical SPR sensor setup. 51
1.10 Typical view recorded by the CCD camera in a SPRi setup. Different shades of measurement spots represent the amount of analyte adsorbed on the surface. 52
1.11 Schematic view of a MZI label-free biosensor. Information of the analyte is carried in the transmitted optical intensity of the device. 53
1.12 Trajectory of light (green line) associated to a guided mode in a WGM resonator (black line). 55
1.13 Trajectory of light (green line) associated to a guided mode in a ring resonator (black lines). 55
1.14 Schematic view of a ring resonator in a typical configuration. 57
1.15 Schematic view of a racetrack resonator in a typical configuration. 58
1.16 Idealized intensity transmittance of a microring resonator as function of wavelength 59
1.17 Illustration of the detection principle in microring-based biosensors. . . . 63
1.18 Illustration of the application of the fixed-wavelength method (FWM) to biosensing. 64
1.19 Illustration of the use of the wavelength-scanning method (WSM) for biosensing. 69
1.20 Illustration of a method based on an intensity threshold to measure the variations of the resonant wavelength λ. Relation between measurement uncertainties are displayed in the zoom window. 72
1.21 Vertical and lateral configurations for evanescent coupling. 78
1.22 Optofluidic cell combining a microring resonator to a microfluidic channel. 82

2.1 Schematic drawing of an asymmetrical slab waveguide. Directions of the major directions of electric fields corresponding to TE and TM modes are indicated. 90

2.2 Schematic drawing of a rectangular waveguide. Directions of the major directions of electric fields corresponding to quasi-TE and quasi-TM modes are indicated. 91
2.3 Schematic drawing of a single-bus microring resonator 93
2.4 Schematic view of amplitude cross-coupling, transmission and loss coefficients 94
2.5 Intensity transmittance vs the single trip phase delay Φ for γ = 0, a = 0.8 and τ = 0.7 corresponding to $A_0 = 0.948$ and F = 11.6 approximately . . 96
2.6 Intensity transmittances vs the single trip phase delay Φ for different sets of parameters a and τ. For each set of plots, $a\tau$ varies between 0 (dashed blue) and a (dotted red) where (a) $a = 0.2$, (b) $a = 0.4$, (c) $a = 0.6$, (d) $a = 0.8$ and (e) $a = 0.95$. Curves with larger values of $a\tau$ have larger values at $\Phi = \pm\pi$ 97
2.7 Contrast vs the cross-coupling coefficient τ and the total loss factor a with $\gamma = 0$ 98
2.8 Maximum of transmission T_{max} vs the cross-coupling coefficient τ and the total loss factor a with $\gamma = 0$ 98
2.9 Q factor and contrast of a ring resonator for a linear attenuation of 1dB/cm with a cavity length L = 1mm vs the internal transmission coefficient τ. Critical coupling is obtained when $a = \tau = 0.89$ but does not correspond to the highest achievable Q factor. 101
2.10 Q factor (a) and contrast (b) (in percents) of a ring resonator for a linear attenuation of 1dB/cm vs internal transmission coefficient τ and cavity length L. Critical coupling is obtained when $a = \tau$, represented by the solid black line. 102
2.11 Intensity transmissions and its first and second order derivatives; F=10. . . 103
2.12 Angular position Φ_C of the maximum of intensity slope vs the coefficient of finesse F. 103
2.13 Contours for the Q factor and maximal slope as functions of loss coefficient a and transmission coefficient τ. Actual values are normalized by the highest Q factor and maximal slope, respectively. The dashed line represent the critical coupling condition. For a = 0.9, the red, green and grey spots correspond to maximal contrast, slope and Q factor, respectively. 104
2.14 Transmitted (solid blue line) and coupled (green dashed line) optical powers with λ = 1.55 μm and $N_{eff,1}$ = 1.56. (a) ρ = 0.05 μm^{-1} and $N_{eff,2}$ = $N_{eff,1}$ resulting in η = 1 and L_c = 31.4 μm; (b) ρ = 0.05 μm^{-1} and $N_{eff,2}$ = 1.57 resulting in η = 0.86 and L_c = 29.1 μm; (c) ρ = 0.01 μm^{-1} and $N_{eff,2}$ = 1.57 resulting in η = 0.196 and L_c = 69.5 μm 115
2.15 3D representation of the power-coupling efficiency η as a function of ρ and δ and associated level curves from η = 0.1 (dark blue) to η = 0.9 (dark red). 115
2.16 Intensity transmittances as functions of wavelength and frequency on corresponding ranges for a cavity length L = 100 μm and N_{eff} = 1.55 118

2.17 Effective index, single trip phase delay and intensity transmittances with (green dots) and without (blue line) first-order dispersion as function of the wavelength for a cavity length L = 200 μm, $N_{eff,0}$ = 1.55 and $\frac{\partial N_{eff}}{\partial \lambda}(\lambda_0)$ = -0.05 UIR/μm corresponding to $N_G(\lambda_0)$ = 1.628 119
2.18 Effective index, single trip phase delay and intensity transmittances with (green dots) and without (blue line) first-order dispersion as function of the wavelength for a cavity length L = 200 μm, $N_{eff,0}$ = 1.55 and $\frac{\partial N_{eff}}{\partial \lambda}(\lambda_0)$ = -1.2 UIR/μm corresponding to $N_G(\lambda_0)$ = 3.41 119
2.19 On top, arbitrary variations of parameters a and τ due to dispersion are presented. Q factors, contrasts and transmittances as functions of the wavelength are computed in presence (green dashed line) or without (blue solid line) these specific dispersion effects (variations in the positions of the resonances are not displayed). Taking into accounts variations of a and τ due to dispersion, the shape of the resonance strongly varies from one extremity to the wavelength range to the other. 121
2.20 TE and TM transmittances as well as the total transmittance for $\alpha^\star$ = 0.3 and $\beta^\star$ = 0.7 122
2.21 Transmittances of the fundamental and first-order propagation modes, and resulting total transmittance. 125

3.1 Examples of thin film defects produced by impurities. 144
3.2 Fabrication steps for a SU-8 vertically-coupled ring resonator 144
3.3 Direct patterning of a photoresist material. 148
3.4 Undirect patterning of a etchable material via negative photoresist. 149
3.5 SEM image of an edge of a rectangular waveguide produced by direct photolithography patterning 150
3.6 Schematics of two superposed photomasks for the fabrication of vertically-coupled microresonator. 152
3.7 Successful slicing of the wafer resulting in a clean break of SU8 waveguides all along the cut. 158
3.8 Fabrication steps for a SU-8 vertically-coupled ring resonator 161
3.9 Thickness measurements for the control of the vertical gap separation. . . 169
3.10 Alignment between patterns from first and second lithographies. 172
3.11 Single defect localized in the coupling region of a microring resonator. . . 174
3.12 Dust or bubble-related (left) and elongation breaks (right) on fabricated waveguides. 175
3.13 Vertical steps of the microresonator due to planarity defect of the Cytop upper surface. 176
3.14 Visible surface roughness and waveguide corrugation on a fabricated device. 177
3.15 Lateral distortion of the bus waveguide near the coupling region. 177
3.16 "Circularly curved" waveguide with clear discretization of the bend. . . . 178

4.1 OLCI setup in reflection mode 187
4.2 OLCI setup in transmission mode 188
4.3 Diagram of characteristic intensity levels and wavelengths of a resonance 193
4.4 Comparison between Lorentzian, quadratic and 4th-order polynomial equivalents of the intensity transmittance for a coefficient of finesse $F = 5$. . . 198

4.5 Evaluation of the accuracy of the Lorentzian approximation as a function of the coefficient of finesse F. In the transmittance plots, solid black lines are the Lorentzian equivalents, and red dashed lines are the theoretical transmittances for F values ranging from $F = 5$ (largest resonance) to $F = 100$ (narrowest resonance). 199
4.6 Spectrum of the transmitted intensity when dispersion is neglected. $a = \tau = 0.6$ and $\gamma = 0$. 206
4.7 Schematic diagram of the basic setup for intensity transmittance measurements. 208
4.8 Schematic diagram of the self-aligned external laser cavity in a Tunics-Plus tunable laser source. 209
4.9 Photodetection voltage measured at the output of the DUT for an input optical power of 10 mW and a TE polarization state. 217
4.10 Photodetection voltage around a maximum of transmitted intensity and smoothed signal from a moving average filter with various spans. 218
4.11 Influence of the span of the moving average filter on the measured signal near resonance. 219
4.12 Smooth signal and resonant wavelengths found from a peak finding algorithm. 220
4.13 Positions of the resonances, anti-resonance and maximum of intensity determined from the smoothed signal. 221
4.14 Comparison between partially normalized (dashed red line) and fully normalized (solid blue curve) signals C_1 and C_2. 223
4.15 Upper (red dot-dash line) and lower (blue dash line) envelope of the transmitted intensity interpolated from the positions of the maxima and minima, respectively. 224
4.16 Comparison between the results of the second (dotted blue line) and the third (red solid line) normalizations C_2 and C_3, respectively. 225
4.17 Wavelength-dependent Free Spectral Ranges for the DUT. 226
4.18 Effective group index dispersion in the DUT. 226
4.19 Wavelength-dependent Q-factor for the DUT. 227
4.20 Wavelength-dependent Finesse for the DUT. 228
4.21 Wavelength-dependent resonance contrast for the DUT. 230
4.22 Signal C_0 and its first and second-order derivatives D_1 and D_2. 231
4.23 Wavelength-dependence of the maximal intensity slope for the DUT. . . . 232
4.24 Photodetection noise for different spans of the moving average filter. . . . 232
4.25 Wavelength-dependent values of $a\tau$, α and β for the DUT. 233
4.26 Comparison between the wavelength-dependences of the (absolute) relative difference between a and τ, the contrast, the product $a\tau$ and the Q-factor. 234

5.1 Schematic drawing of an asymmetrical slab waveguide. Directions of the dominant electric field components corresponding to TE and TM modes are represented 248

5.2 Schematic drawing of a rectangular waveguide. Directions of the major electric field components corresponding to quasi-TE and quasi-TM modes are represented. Corner regions appear as dashed zones 251
5.3 Comparison of effective indices of fundamental TE and TM modes of a typical polymeric rectangular waveguide with a varying height. Legend of the plot is: MM = solid, EIM = dash and ADI = cross 259
5.4 Comparison of waveguide cladding sensitivities for the fundamental TE and TM modes of a typical polymeric rectangular waveguide with a varying height. Legend of the plot is: MM = solid, EIM = dash and ADI = cross 259
5.5 Comparison of waveguide core sensitivities for the fundamental TE and TM modes of a typical polymeric rectangular waveguide with a varying height. Legend of the plot is: MM = solid, EIM = dash and ADI = cross . 260
5.6 Full waveguide sensitivity analysis for the fundamental TM mode of a polymeric rectangular waveguide using the effective index method. $N_{core} = 1.56$ (SU-8), $N_{sub} = 1.444$ (silica) and $N_{clad} = 1.323$ (water). 262
5.7 Sensitivities of the effective indices of fundamental TE and TM modes to the refractive index of the cladding of a rectangular waveguide vs normalized height and width. (a) asymmetric waveguide with $N_{core} = 1.56$, $N_{sub} = 1.444$ and $N_{clad} = 1.323$, (b) symmetric waveguide with $N_{core} = 1.56$ and $N_{clad} = N_{sub} = 1.323$ 267
5.8 Evanescent field for various rectangular waveguide configurations. In (a), the cladding RI is higher than the substrate RI; the opposite situation is presented in (b). 269
5.9 Separation of the section of the cladding into two complementary regions (H) and (S). A general case, where analyte molecules are not necessarily in contact with the core, is presented. 282
5.10 Separation of the section of the cladding into two complementary regions (H) and (S). A general case, where analyte molecules are not necessarily in contact with the core, is presented. 288
5.11 Ratio of power flows η_{Pow} as function of the normalized molecular position $x^\star = x_0/L_D$ and the normalized molecular dimension $L^\star = L_M/L_D$ 289
5.12 As functions of the parameters x_0 and L_M are plotted (a) the optimal decay length of the evanescent field $L_D^{(Opt)}$ and (b) the optimal value of the power ratio $\eta_{Pow}^{(Opt)}$ in dBs. All lengths are in nm. 291

6.1 Fabrication steps for PDMS microfluidic caps 294
6.2 Fabrication steps for PDMS microfluidic caps 296
6.3 Use of an optical adhesive for microfluidic integration. 301
6.4 Optofluidic cell obtained after microfluidic integration of the optical chip. 301
6.5 Typical configuration of the flow for analyte detection in homogeneous and surface sensing. 304
6.6 Ideal and real flow configurations obtained in optofluidic detection when the analyte reaches the microresonator. Plots correspond to the local values of concentration in analyte molecules. 305
6.7 Positions of a six-port injection valve. 307

6.8 Architecture of the microfluidic circuit and flow pattern for both *loading* and *injection* positions of the valve. 308
6.9 Diagram for the optoelectronic instrumentation. 310
6.10 Snapshot of the user interface of the control program during an experiment of homogeneous glucose sensing. 312
6.11 Temperature-controlled mount for thermal control of the microresonator. . 313
6.12 Transverse view of the microring waveguide with substrate thermal control. Substrate is composed of Cytop, silica, silicon and copper, from top to bottom. The core material is typically SU-8 314
6.13 Schematic view of the microfluidic circuit with unilateral temperature control 317

7.1 Refractive index of an aqueous solution of glucose as function of the glucose concentration (mol/L) and the relative glucose mass (%) 320
7.2 Chemical structures of glucose and sucrose molecules. 323
7.3 Evolution of the resonance shape and position as function of the relative sucrose mass in solution. 324
7.4 Transfer function of the microresonator: resonance spectral position (as wavelength) as function of the relative sucrose mass. 326
7.5 Experimental transmissions for TE and TM polarizations of a typical microresonator. 328
7.6 Presence of higher-order modes in the TE and TM intensity transmittances. 328
7.7 Repeatability of the detection of glucose solution with relative mass of 10% for TE and TM polarizations. 329
7.8 Transfer function of the microring resonator, measured for glucose masses of 0, 0.5, 2.5, 5 and 10% and both polarizations. 330
7.9 Biased response due to variation of the temperature of the buffer solution during the experiment. 331
7.10 Measurements over a long period of time and for various glucose concentrations. Thermal controls of the substrate and the microfluidic circuit are active. 334
7.11 Measurements over a long period of time and for various glucose concentrations. As compared to Fig. 7.10, the thermal drift is corrected. 335
7.12 5-TAMRA cadaverine molecule. 336
7.13 Effect of the UV/ozone treatment on SU-8 measured by FTIR spectrometry. 338
7.14 Calibration curve for quantification: fluorescence signal as function of 5-TAMRA cadaverine quantity in moles. 339
7.15 Intensity transmittances corresponding to a selected resonance measured after each 5-TC binding cycle. 340
7.16 Resonant wavelength shift as a function of the surface density of grafted 5-TC molecules in molecules per mm^2. 341
7.17 TE and TM responses of the microring resonator to the adsorption of anti-TAMRA molecules on its surface. The concentration of anti-TAMRA in the injected solution is 0.1 μM. Thermal drifts of TE and TM responses are corrected from simultaneous measurements of the substrate temperature. 342

7.18 TE and TM responses of the microring resonator to the modification of the buffer during the experiment. Heratic responses is measured right after the buffer switch, due to the arrival and stabilization of a large air bubble over the microresonator under study. Thermal drifts of TE and TM responses are corrected from simultaneous measurements of the substrate temperature. 343
7.19 TE and TM responses of the microring resonator to the adsorption/desorption of TAMRA molecules with anti-TAMRA molecules grafted on the surface. The concentration of TAMRA in the injected solution is 10 μM. Thermal drifts of TE and TM responses are corrected from simultaneous measurements of the substrate temperature. 344

Introduction

Microring resonators as photonic devices are formerly passive, ring-shaped optical cavities where a waveguide in closed-loop configuration is coupled to one or two bus waveguides. Buses constitute interfaces between optical inputs and outputs, and the cavity.

Origins

Such resonant photonic devices were first proposed approximately fifty years ago as optical filters: when optical waves are coupled to the buses inputs, multiple-wave interferences occur at the buses outputs producing a strong dependency of the transmitted intensity, or transmittance, on the optical frequencies of the input waves. In the simplest single-bus configuration, particularity of the transmittance is in the presence of resonant optical frequencies, or wavelengths. Near these resonant wavelengths, a minute variation of the input wavelength can result in a variation of the transmitted intensity from 100 to 0%.

Resonances sensitivities

Because of the strong variations of transmittance near the resonant wavelengths of the optical cavity, their positions can be measured very accurately. For a given microresonator, position of each resonant wavelength is strongly dependent on the phase velocity of the wave propagating in the closed-loop. Due to evanescent-waves, located near the core of the waveguide, and accompanying the propagation of light in the cavity, the phase velocity not only depends on the core material, but also on the refractive index distribution in the vicinity of the core, specifically in the cladding region.

Detection applications

Values of the resonant wavelengths of a microring resonator strongly depend on the refractive index distribution in the cladding, and can be measured very accurately with simple techniques. As consequence, such devices are very well suited for the detection of very small variations of the refractive index distribution, which can be related to many physicochemical quantities. This is the basic principle of multi-sensors instruments integrating ring resonators.

Presentation of Label-Free Sensing (LFS)

The main applications of these instruments are in label-free biochemical sensing. In label-free sensing, the surface of the microresonator is functionalized so that specific molecules, or targets, brought by a solution dropped or flown over the closed-loop waveguide, bind to functional groups on the surface. These functional groups, or receptors, can either be present on the surface of the optical core material, or on a recognition molecular layer previously deposited on the optical surface during its functionalization. When binding event occurs, because of the increasing concentration of binded molecules near the surface of the waveguide, the refractive index distribution is progressively modified, and resonant wavelengths of the resonator are shifted. The real-time measurement of the resonant wavelengths thus provide a signal which is an image of binding events on the surface.

LFS as a powerful biochemistry tool

Depending on the experiment, expected results of the analysis of the detection signal can be values of the binding selectivity and affinity of a molecular interaction, between target and receptor, or more importantly its stoichiometry, kinetics, and more generally thermodynamics. However, the determination of these parameters is made difficult by numerous parasitic effects biasing the detection signal. As consequence, the main challenge of label-free detection is to extract the relevant information, task that as to do with both nature of the sensing scheme and the detection signal analysis.

Specificity and microfluidics for LFS

In the dominant configuration where the receptor is a specific biological or chemical entity bound on the waveguide surface, the relevant information is related to the only binding events between the receptor entity and the target. Consequently, a first bias of the detection signal are detected unspecific binding events, occurring between targets and third-party molecules or binding sites, those of the core material for instance. Unspecific binding events also integrate events that are not related to a chemical bound, but simply due to contact between targets and third-party molecules. The binding specificity, rate between specific and unspecific binding events, has a dominant role in the reliability of the measurements, and its optimization is one of the keys for achieving a proper label-free biosensor. First, combination of the waveguide surface state and the nature of the interaction under study naturally affects the binding specificity. Thus, control and adjustment of the surface state is an important factor. Secondly, when the solution is not just put in contact, but flown over the waveguide, the binding specificity is improved as targets are less likely to just deposit on the surface by mechanical effect. This function is efficiently performed when integrating the resonator with microfluidics, resulting in optofluidic sensors with low biochemical material consumption. In the dominant configuration of optofluidic sensors, target is brought to the surface of the optical cavity via a micro-channel fed by an intricate system of pumps and valves. The addition of microfluidics not only reduces detection bias, but makes it also possible to perform repeated, automated experiments. This functionality is particularly important in label-free biosensing to guarantee reliable and reproducible results.

Diffusion in Optofluidic LFS (OLFS)

However, the use of microfluidics comes at a price. Since the solution containing the targets is directly preceded and followed by a buffer solution in the microfluidics circuitry, targets are free to diffuse to the buffer, making the concentration of targets inhomogeneous. Because of these concentration gradients near the interfaces of the sandwiched solution, the relevant detection signal is temporarily displaying a transient behavior, more difficult to analyze than the stationary binding curve obtained when the

concentration of the solution flown over the resonator becomes homogeneous. As consequence, the microfluidics should be designed to reduce diffusion effects.

A main issue of OLFS: homogeneous effects

Besides biases related to binding events, another class of biases applying to the detection signal is formed by homogeneous effects. Homogeneous effects stand for all variations of the refractive index distribution near the waveguide that are not related to binding events. Since homogeneous effects modulate the refractive index distribution, they are responsible for parasitic variations of the resonant wavelengths.

Origins of homogeneous effects

A first homogeneous effect is due to the variation of bulk refractive index between the solution and the buffer. This difference in index is, in most instances, solely from the presence of the targets in the solution - base of the solution being the buffer. A second effect is related to temperature variations. To some extent, refractive indexes of all materials depend on their temperature. As consequence, variations of temperature tend to modify the refractive index distribution. Furthermore, because of thermal expansion, geometry of the waveguide - width and height - is also temperature-dependent. These two temperature-related effects combined, resonant wavelengths can be strongly shifted due to temperature variations. In the same fashion, geometry and refractive index distribution are pressure-dependent, hence a potential bias due to pressure variations.

Pressure-related homogeneous effects

Amongst these three homogeneous effects, the one due to pressure is the most difficult to analyze. Variations of pressure near the waveguides could result from vibrations, discontinuity of the flow rate in the microfluidic channel, or variations of viscosity between buffer and solution.

Temperature-related homogeneous effects

In comparison, effects of temperature variations are easier to observe. They are essentially of two natures. The first is related to variations of the room temperature, affecting the optical device, the solution and the buffer. It generally results in a slow, linear variation of the signal referred to as thermal drift, and can be easily corrected. A second effect occurs when temperature of the solution does not match the temperature of the buffer, and/or that of the waveguide. This results in fast variations of the detection signals that are, compared to the thermal drift, very difficult to correct. Although these temperature variations can be largely reduced by adequate measurement procedures, the main issue occurs when target molecules need to be introduced at colder temperatures in order to preserve their functionalities.

Concentration-related homogeneous effects

Concentration-related homogeneous effects are also easily observable, and specifically occur at buffer-solution transitions. The particularity of this effect is that it is intrinsically related to the measure.

Reducing the influence of homogeneous effects

As homogeneous effects can have larger contributions to the detection signal than specific binding events, it is necessary to reduce them as much as possible. To do so, two philosophies can be applied: one related to the waveguide, the second, more general, to the structure of the instrument.

Waveguide optimization scheme

The geometry of the closed-loop waveguide forming the optical cavity, and the materials it is made from, as a lot to do with sensitivities of the detection to homogeneous effects. As consequence, reduction of the contribution of homogeneous effects to the detection signal can be achieved by proper design of the optical waveguide.

Multi-sensor scheme

The second approach is quite different. The core principle is to replace the single optical cavity by two or more cavities, each one having a specific sensing task. For instance, in a three-cavity scheme, one cavity can be designed to be specifically sensitive to temperature variations, another to concentration-related homogeneous effects, and the final cavity to binding events at its surface. In such configuration, detection signals from the first two cavities provides specific information on the variations of temperature and of bulk refractive index of the solution. Combination of these sensing capabilities result in a multi-sensor instrument for label-free detection. With proper calibration of this multi-sensor instrument, most homogeneous effects can be deduced from the detection signal of the third cavity. This corrected detection signal, obtained thanks to the multi-sensor scheme, is highly correlated to specific binding events.

Chapter 1

Generalities on optofluidic and label-free sensors

Introduction

Over the last two decades, integrated optofluidic sensors have been intensively researched and developed. This mainly comes from the fact that such sensors are used in several fields related to health: fundamental interactions and macromolecular systems in biology [1], medical diagnostics, drug discovery [2], environment monitoring, food and water safety [3], *etc* .... In this general context, they can be referred to as biosensors. For such applications, the most appealing characteristics of integrated optofluidic sensors are their accuracy, rapidity, robustness, versatility, multiplexing capacity and cost efficiency. More importantly, the great promise of such devices comes from their unrivalled ability to detect and quantify specific, targeted biomolecules in very low concentrations, down to the single molecule resolution.

Because of their tremendous potential, the research on optofluidic devices as biosensors is extremely rich and diversified. A proof is the remarkable amount of optical phenomena, materials, configurations, fabrication techniques, surface chemistries, detection formats, sensor interrogations and data analysis techniques that were proposed over the years to improve specific or overall performances of biosensors [4]. Biosensors can also rely on non optical transducers [5]: mechanical, piezoelectrical, electrochemical, *etc* ... Overall, many combinations of physical phenomena and technical solutions can be applied to biosensing, and hundreds have been proposed.

In this context, establishing a hierarchy between systems can prove extremely difficult, not only due to the wide variety of existing systems and applications, but also from the lack of consensus and clarity in the evaluation of key performances. It is also noticeable that despite the multiplicity of devices that were proposed, very few of systems have been commercialized [1]. This constitutes a major motivation to design a biosensor instrument achieving a good trade-off between performances and practical considerations. In consequence, the paradigm for the design of our integrated optofluidic biosensor instrument was focused on the development of a device combining excellent sensing performances with simplicity, versatility, reliability and cost efficiency.

In order to understand most aspects related to sensing, a first section of the chapter is dedicated to elements of sensor theory. A second section introduces measuring instruments referred to as label-free biochemical sensors, and more specifically optofluidic label-free biosensors. The third and final section focuses on the choice of polymer microring resonators as transducers for such instruments, and other potential applications.

1 Elements of sensor theory

1.1 Introduction

1.1.1 What is a sensor ?

A *sensor* can be defined in a very general manner as a device that receives and responds to a signal, or *stimulus*. A *stimulus* can be understood as any quantity, property or condition.

In their vast majority, modern sensors are not standalone devices. They are part of larger systems that may incorporate other detectors, signal conditioners and processors, memory devices, data recorders and transducers. In consequence, sensors need to provide a signal which is readable by all other elements of the system they are incorporated in. This is why in the overwhelming majority of artificial systems, information on the stimulus, first carried by the sensor's response, is processed and transmitted as an electrical signal: a voltage, a current or a charge. This electrical signal

can be further described typically in terms of amplitude, frequency, and/or phase. Therefore, the most common definition of a (man-made) sensor is [6, 7]:

> "A sensor is a device that receives a stimulus and responds with an electrical signal."

1.1.2 Measuring instruments

Many devices only uses sensors internally: information from the sensors is used to monitor operation of the device, and is never made available to the user. In opposition, devices whose purpose is to record and/or display information provided by the sensor on the stimulus are *measuring instruments*, or *measurement systems*. In the context of measuring instruments, the term *stimulus* is often replaced by the more quantitative notion of *measurand*.

1.1.3 Sensors, transducers and actuators

A sensor can be interpreted as a device that converts any form of energy to electrical energy. Consequently, sensors are a subclass of *transducers*, which are simply defined as energy converters, from one kind into another. Devices referred to as *actuators* also constitute a subclass of transducers, and are the dual objects of sensors: they convert electrical energy into another kind.

1.1.4 Direct and complex sensors

When one or more transducers are necessary to convert the initial stimulus into an electrical signal, the system formed is a *complex* sensor. In opposition, a *direct* sensor uses physical effects for straightforward conversion of the stimulus into an electrical signal generation or modification.

1.1.5 Passive and active sensors

According to sensor theory [6, 7], all sensors can be classified into two large categories: *passive* sensors and *active* sensors. An *active* sensor

requires an external source of energy, referred to as an excitation signal, whereas active sensors directly generate an electrical signal in response to a stimulus, without the need for an external excitation.

Since their own properties, described by internal parameters, are modified in response to an external effect, active sensors can be referred to as *parametric* sensors. In these sensors, the variations of one or more internal parameters modulate the excitation signal. Such modulation carries information on the stimulus, or measurand. Examples of active or parametric sensors are capacitive contact sensors, based on capacitors. A capacitor is an electronic component characterized by a capacitance C, which can be designed so that the value of C is sensitive to a finger's touch, for instance. The capacitance of the sensor, carrying information on skin contact, can be deduced from the response of the capacitor to an electronic excitation signal.

In opposition, photodiodes are typical examples of passive sensors, or more generally passive transducers: energy carried by optical waves is directly converted into a voltage (solar cells), or a current (photodetectors) depending on the operation mode, also called polarization of the photodiode.

1.1.6 Absolute and relative sensors

Sensors can also be separated into absolute and relative sensors. An *absolute* sensor detects a stimulus in reference to an absolute physical scale that is independent on the measurement conditions. Comparatively, a *relative* sensor produces a signal that relates to the difference between the measured stimulus and a reference stimulus.

1.1.7 Further classification

A further classification of sensors can be achieved by considering all of their properties [8]: stimulus, targeted applications, specifications, physical effect(s) for transduction, type of energy conversion, materials, *etc*...

1.1.8 Sensor and instrumentation

For ultra-sensitive scientific instruments, performances are a resultant of the quality of the sensing instrumentation and the properties of the sensor(s). In an optimal instrument, both need to be related, and matched at some level. In this respect, it is important to evaluate the overall quality of an instrument from quantitative criteria that integrate both sensor and instrumentation. Otherwise, it could result in mislead design priorities. A related matter is to know if the limitations of the performances of the instrument come from the sensor, or the application, or both. This is challenging, mainly because of the interactions between instrumentation and sensors (cf.§3.3.3). As a result, a deep understanding of the independent and combined limitations from the sensor and its instrumentation is necessary.

This chapters focuses on sensors properties and specifications, only to analyse the performances of both common systems, and on newly reported optofluidic sensors and label-free sensors. In further chapters, specifications of sensors integrating microring resonators will be considered, from theoretical analysis to experimental studies.

1.2 Sensor characteristics

1.2.1 Introduction

Sensor characteristics or specifications take many forms. Some, such as the *span* or the *sensitivity* apply to all sensors, when others only apply to very specific devices. In this part, we present very general specifications of sensors and measuring instruments [1]. Other terms, only relevant to optofluidic and label-free sensors, will be introduced in subsequent sections.

1.2.2 Transfer function

An ideal sensor would be a sensor that always provide the *true value*, or simply *value* [9], of the stimulus. The ideal input (stimulus e) versus output (electrical signal S) relationship of an ideal sensor is described by the

[1] It is important to point out that on some occasions, terms used as sensor specifications, are also used as specifications of a measuring instrument that integrates the sensor, therefore creating ambiguity.

transfer function $S = \mathcal{T}(e)$. Depending on the sensor, the transfer function $\mathcal{T}$ can take many forms. However, it can be written in most cases to one linear or nonlinear scalar function.

In the simple case of a linear and scalar transfer function $\mathcal{T}$, the signal S can be written as $S = \alpha + \beta e$ where α is the *linear intercept* and β is the *slope*, also referred to as the *sensitivity*. Depending on the sensor, e may be any physical quantity, and S may be an amplitude, an intensity, a frequency, a phase, *etc* ...

Nonlinear transfer functions are generally more difficult to handle for the characterization of the input/output relationship of a sensor. For many devices, the nonlinear transfer function is linearized on a neighborhood of a specific input value e_0. For values of e near e_0, a linear relation $S(e) = S(e_0) + \beta(e_0) \cdot (e - e_0)$ can be written, where $\beta(e_0)$ is defined as a *local sensitivity* around e_0, and calculated from:

$$\beta(e_0) = \frac{dS}{de}(e_0) \tag{1.1}$$

The validity of the linear approximation of a nonlinear transfer function $\mathcal{T}$ naturally depends on the function itself, but also on the *span*, corresponding to the extent of values that the input e can take around e_0.

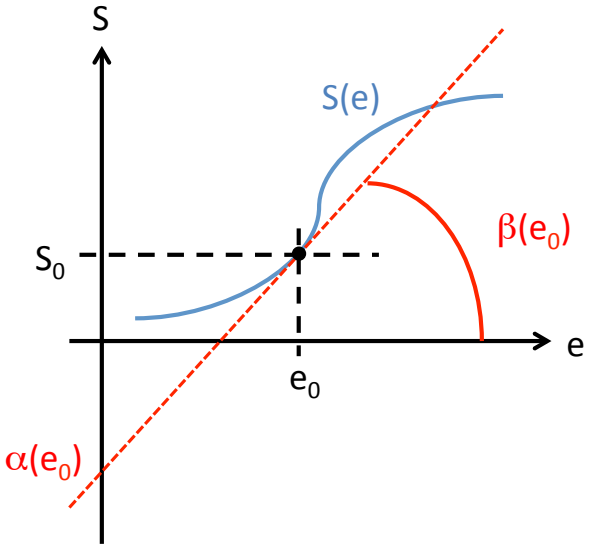

Figure 1.1: Local linearisation of a nonlinear transfer function.

1.2.3 Span

The *span* of a device, also called *input full-scale*, can be defined as the dynamic range of stimuli or measurand that can be converted by the sensor. It relates to the highest input value that can be applied to the sensor without causing *inaccuracy* over requirements.

The same definition applies for measuring instruments. The only difference is that the span of a measuring instrument depends on both sensor and instrumentation. In many instruments such as optical spectrum analyzers, sensor and instrumentation can be configured at each spectrum acquisition to perform an analysis on a specific frequency span, within the span of the sensor.

1.2.4 Accuracy

Depending on the reference, *accuracy* can be a qualitative [6] or quantitative [7] view of the *inaccuracy*, or *error*, accompanying any measurement. *Inaccuracy* or *measurement error* can be defined for one measurement point as the largest difference expected between the measured value and the "real" value.

The measurement error results from two classes of contributions that are very different in nature. The first class of contributions are *systematic errors*, which can always be related to another measurable quantity. Therefore, systematic errors may always be corrected, to some extent, by calibration of the sensor and/or that of the measuring instrument, or by the control of environmental conditions.

The second class regroups *random errors*. Assuming that all systematic errors are corrected, and all measurable physical quantities are perfectly stable, random variations of the measured value around an average point occur. These random variations are due to *noises*, which can be of different natures depending on the sensor: thermal noise, shot noise, flicker noise, burst noise, *etc*... In particular, thermal noise affects all electronic circuits, hence all artificial sensors and all measuring instruments.

The accuracy can be specified as standard deviation of the *error signal*, $i.e.$ the difference between real and measured values. However, in an attempt to build an universal system for the specification of sensing performances, the general recommendations [9] are to use *accuracy* as a quantitative term, and *uncertainty* to quantify accuracy.

1.2.5 Noise

All sensors produce some output noise in addition to the output signal $S(e)$. In some cases, the noise of the sensor is less than the noise of the next element in the instrumentation, or less than the fluctuations in the physical signal. In such case, the noise produced by the sensor is not important. Many other cases exist where the noise produced by the sensor limits the performances of the system integrating the sensor.

Noise is generally distributed across the frequency spectrum. For instance, thermal noise shows a *white distribution*, characterized by a frequency-independent spectral noise density in $V_{RMS}/\sqrt{Hz}$. A white distribution adds noise to a measurement with amplitude proportional to the square root of the measurement bandwidth Δf. Noise in the output signal can be reduced by signal integration, or averaging. Averaging or integration act on the signal as a low-pass filter, limiting the bandwidth of the measurement, hence proportionally reducing the total amount of noise in V_{RMS} over the bandwidth. A related thumb rule is that the noise decreases with the square root of the measurement time.

1.2.6 Calibration

Calibration of a sensor can be defined as the determination of the parameters of the sensor's transfer function $\mathcal{T}$. Referring to the example of a scalar and linear transfer function, the role of calibration would be to measure precisely what are the values of the sensitivity β and the intercept α, instead of applying values found in the sensors specifications. Indeed, values of these coefficients can slightly vary from one sensor to another because of deviations in the fabrication process. If the accuracy required is high, an individual calibration of each sensor is necessary to limit systematic errors related to the misevaluation of the sensitivity and the linear intercept.

Systematic errors due to environmental factors can also be corrected via calibration. These specific errors come from the dependence of parameters of the transfer function on environmental physical quantities, such as room temperature, pressure, and humidity. A first approach for correcting these effects is to directly measure the transfer function, from a calibration routine. In the case of a linear transfer function for instance, α and β are determined at each calibration, thus zeroing systematic errors. However, this correction is temporary, since after calibration, environmental factors can vary and modify once again values of the parameters of the transfer function, re-creating systematic errors. As calibration routines require relatively long durations, during which the sensor is not available, this simple approach is far from being optimal.

A second approach, much more powerful, is available for instruments incorporating multiple sensors, referred to as multi-sensor instruments. A multi-sensor instrument is based on a primary sensor, the sensor that converts the stimulus the instrument is designed to measure, and secondary or auxiliary sensors whose purpose is to measure environmental factors in a broad sense, ie any measurable quantity that may cause systematic errors on the output signal of the primary sensor.

An initial calibration of a multi-sensor instrument will provide a model describing how each value measured by auxiliary sensors relates to values of the parameters of the primary sensors. Then, during operation of the instrument, the transfer function of the primary sensor is constantly re-evaluated from measurements of the environmental factors, thus performing a continuous calibration, or real-time correction of systematic errors.

1.2.7 Hysteresis

Hysteresis is a common nonlinear property of physical systems, related to memory effects. In sensors, because of an hysteresis phenomenon, the output S_0 corresponding to an input e_0 is different depending on whether the previous value of the input was higher or lower than e_0.

Hysteresis can be considered as a dynamic effect since it depends on

the time growth or decay of the input e. In consequence, systematic errors due to this effect are can be difficult to correct.

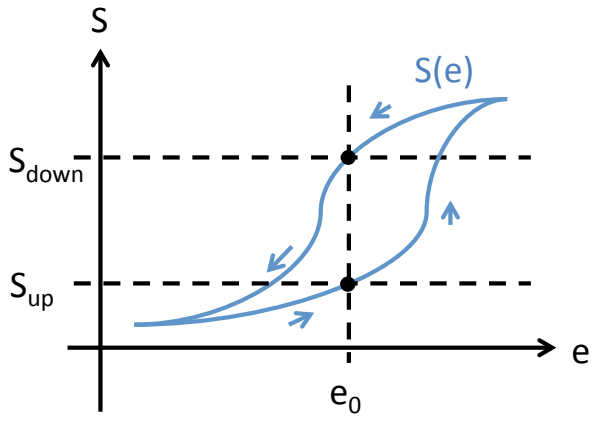

Figure 1.2: Effect of an hysteresis on the transfer function.

1.2.8 Nonlinearity

In sensors, the term *nonlinearity* refers to the systematic errors caused on large measurement spans by the linear approximation of the transfer function on a neighbourhood of an input value e_0.

Nonlinearity depends on the form of the actual transfer function and on the measurement span. It is important to point out that, despite the fact that the sensor is responsible for the nonlinearity of its response, an inadequate instrumentation is responsible for nonlinearity errors. In order to obtain large measurement spans, the instrumentation needs to take into account the nonlinear transfer function of the sensor to retrieve values of the input signals without nonlinearity errors. This is easily done when the transfer function is monotonous, but much more challenging when $\mathcal{T}$ has local extrema in the measurement span. Indeed, these extrema mathematically correspond to zeros of the sensitivity. The same issue is met when the transfer function presents *saturation*.

1.2.9 Saturation and dead band

Regarding the transfer function of a sensor, a *saturation* is defined as a region where the sensitivity, ie the slope of the transfer function, monotonously tends to zero. Wherein saturated, the output signal of the sensor will, in any case, remain approximately constant while the input may strongly vary.

Consequently, the sensor is mostly inoperative for input ranges where the transfer function is saturated. In comparison, a *dead band* is a range of inputs where the sensitivity locally tends to zero. Both saturation and dead band effects have common consequences, but they should not be treated in the same manner for systematic error correction.

Despite a saturation, provided that the transfer function is known, the input can be theoretically deduced from the output. The actual issue of saturation is the limitation of the accuracy. Indeed, in saturated regions, variations of the output due to variations of the signal are lower and lower as compared to the noise level. When the signal-to-noise ratio (SNR), *ie* the ratio between output variation and noise level, tends to unity and below, input variations are no longer detectable by the instrument.

The effect of a dead band is different in the sense that a zero sensitivity for a specific input does not necessarily mean that the sensitivity cannot be large at the vicinity of the zero. If the transfer function is a Gaussian for instance, the sensitivity tends to zero at the peak of the Gaussian, but can be very high not far from the peak. Following on this example, the peak of the Gaussian can be assimilated to a "blind spot" for the sensor: small variations of the input near the peak position cannot be detected because of the low SNR. However, if the variations of the input around this blind spot are sufficiently large, missing information related to the presence of the input in the blind spot can be extrapolated from the rest of the response.

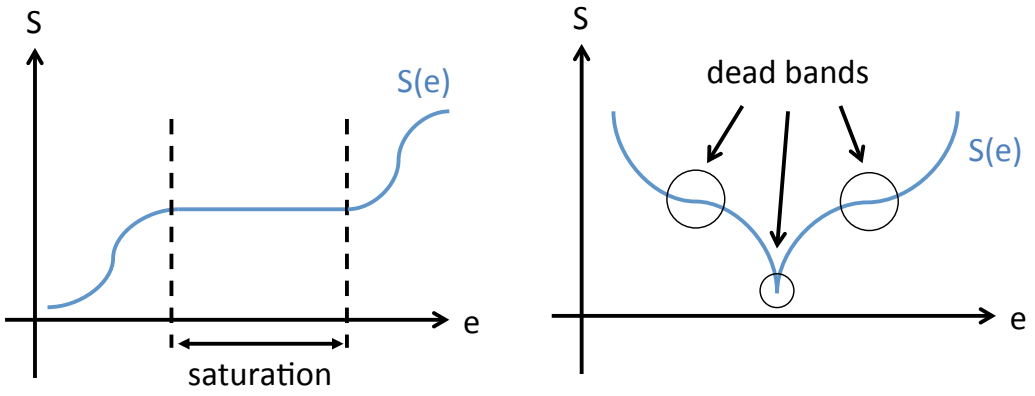

Figure 1.3: Saturation and dead band on a transfer function.

1.2.10 Repeatability and reproducibility

Repeatability is a statistical evaluation, usually via a standard deviation, of the inability of a sensor or measuring instrument to provide the same output for repeated and identical excitations. As such, it can be used to track the evolution of systematic errors in between two calibrations or adjustments. It can also be used to evaluate the deviation of the output measured, for identical excitations, right after repeated calibrations.

Reproducibility is quite similar to repeatability, used to evaluate the inability of a sensor or measuring instrument to provide the same output for identical excitations under different conditions, only after calibration.

As precise definitions of these terms may vary from one scientific community to another, a general discussion on repeatability and reproducibility is not trivial. In relation to how these terms are defined in this dissertation, it can be said that repeatability can be used to evaluate the efficiency of the calibration procedure under similar environmental conditions, whereas reproducibility evaluates the efficiency of the calibration procedure when environmental conditions are modified. More comprehensive definitions of both terms can be found in [9].

1.2.11 Resolution

Resolution of a sensor or measuring instrument is generally defined as the smallest variation of stimulus or measurand that can be detected. Because the definition of a "detectable variation" is not clear, many interpretations of what the resolution of a measuring instrument is exist, depending on the nature of the stimulus.

As variations are inherently dynamic, the definition of the resolution must relate to the time scale of the input variations, and also to the noise level. For instance, in a experiment with a given white noise distribution, from signal averaging, slow variations of the stimulus are much easier to detect than fast, ie high-frequency, ones. As a direct consequence, the resolution of any measurement can be extremely high[2] if the variation occurs

[2] An unavoidable ambiguity comes from the fact that high-resolution (qualitatively) is achieved when the value of the resolution is low, and inversely.

on large time-scales, and a specified resolution would be meaningless if not associated to a time scale.

Due to its close relation with the time scale, resolution can be quantified, similarly to the noise, in units of signal per square root of the bandwidth Δf in frequency units (signal unit per $\sqrt{\text{Hz}}$). In a device where the bandwidth can be adjusted, the resolution can also be defined as a function of the *response time* of the instrument.

In some situations, all temporal considerations have no effect on the resolution of a measuring instrument. This is generally due to a quantification of the measured output voltage S performed during an analog-to-digital conversion. For instance, a 12-bit converter can only provide $2^{12} = 4096$ distinct values on a given voltage span. If the voltage span is 10 V, the minimal increment δS between two values is about 2.5 mV. Because all analog output values are rounded to the nearest coded digital value, the resolution is inherently limited to the ratio between δS and the sensitivity β.

1.2.12 Dynamic characteristics

Up to now, the transfer function has been treated solely has a static, ie frequency-independent, characteristic of the sensor. Accordingly, variations of the parameters of the transfer function could only be caused by internal or external perturbations. However, in all systems, the response of the sensor depends on the frequency components of the stimulus. When this dependence its critical to describe the behavior of the sensor, the actual relationship between the time-dependent stimulus $e(t)$ and the corresponding time-dependent electrical output $S(t)$ must be expressed as a differential equation.

The applicable differential equation can be identified by measuring the response to a step variation of the input. Depending on the differential equation, linear or nonlinear, and its order, the step response can take many forms: delayed, overdamped, damped, ... resulting in dynamic errors. Dynamic errors specifically occur during the transient response of the sensor, the extent of which being the *response time*. For further reference, the response time will be formally defined as the typical time the sensor takes to return to a stationary output after a step variation of the stimulus.

The *bandwidth* of the sensor can be defined as the maximal frequency of the stimulus for which the sensor can provide an accurate output.

1.2.13 Uncertainty

As explained before, it is generally recommended that accuracy should be used only as a qualitative term, while *uncertainty* quantifies the dispersion of measurement results. As defined before, the measurement error is the difference between the measured value and the real value of the measurand. Thus, the measurement error can only be quantified if the real value of the measurand is simultaneously measured by an ideal instrument. Comparatively, the measurement uncertainty quantifies how large the measurement error might be. In that respect, the measurement error can eventually be much smaller than the uncertainty. For instance, the measurement uncertainty in time for a broken watch is 12 hours, whereas the measurement error tends to zero twice a day.

In a complex measuring instrument, contributions to the overall uncertainty u_c can be listed in an *uncertainty budget*, where each independent source i of uncertainty is associated to a *standard uncertainty* u_i, defined as the standard deviation of the measured value attributed to the source i. The total uncertainty of the measurement, referred to as the *combined standard uncertainty* u_c, is usually evaluated using the *law of propagation of uncertainty* [9], stating that u_c can be expressed as:

$$u_c = \left[\sum_{i=1}^{N} u_i^2 \right]^{1/2} \tag{1.2}$$

where N is number of independent sources of uncertainty.

Estimation of some standard uncertainties[3] may be very difficult, and rely on a scientific judgement that integrates many sources of information: general knowledge, manufacturer's specifications, calibration data, data from previous measurements, ... In comparison, estimation of other uncertainties[4], is performed via a straightforward statistical analysis of mea-

[3] *Type B* uncertainties[9]
[4] *Type A* uncertainties

surement data.

According to [9], in many practical measurement situations, the probability distribution characterized by the measurement result M and its combined standard uncertainty $u_c(M)$ is approximately normal. When this is the case, the empirical *68-95-99.7 rule* can be applied to quantify the probability that a (real) value of the measurand M_{real} belongs to an interval specified by a measured value M_0 and a measurement uncertainty $u_c(M)$. This is expressed mathematically as:

$$\begin{cases} \mathcal{P}(M_{\text{real}} \in [M_0 - u_c(M),\ M_0 + u_c(M)]) & \approx 0.6827 \\ \mathcal{P}(M_{\text{real}} \in [M_0 - 2u_c(M),\ M_0 + 2u_c(M)]) & \approx 0.9545 \\ \mathcal{P}(M_{\text{real}} \in [M_0 - 3u_c(M),\ M_0 + 3u_c(M)]) & \approx 0.9973 \end{cases} \tag{1.3}$$

1.2.14 Limit of detection (LOD)

The term *limit of detection (LOD)* is often used as a synonym for resolution in biosensors. It can thus be defined as the smallest variation of biological stimulus or measurand that can be detected. It is naturally related to the uncertainty, and should be associated to a response time (cf. §1.2.11). It is important to point out that when measuring variations of the measurand, in opposition to the measurement of the absolute value of the measurand, most systematic errors are corrected[5]. In consequence, when relative variations of the measurand are measured, the relevant uncertainties are related to the variations of the systematic errors. The uncertainty $u_c(M)$ then combines standard uncertainties from measurement noises to those of the systematic errors.

When measuring variations of the measurand, since systematic errors are (to some extent) corrected, it can be reasonably assumed that the *68-95-99.7 rule* can be applied. Accordingly, various grades of LOD can be defined, according to the probability that a real value of the measurand is within the LOD:

Grade	$\text{LOD}_{68.3}$	$\text{LOD}_{95.5}$	$\text{LOD}_{99.7}$
Expression	$2u_c$	$4u_c$	$6u_c$

Table 1.1: Typical grades and expressions for the limit of detection (LOD)

[5] provided that they affect all measured values in the same manner

In Fig. 1.4, the different grades of LOD are compared, for a given combined uncertainty, in the statistical separation of a reference measured value M_0 and subsequent measured values M_a, M_b and M_c. Surface of shaded areas represent, for each grade, the probability that a real value M_{real} can either be measured as M_0 or M_i with $i \in \{\text{a, b, c}\}$, hence the probability that the measured variation between M_0 or M_i is not related to a variation of the measurand.

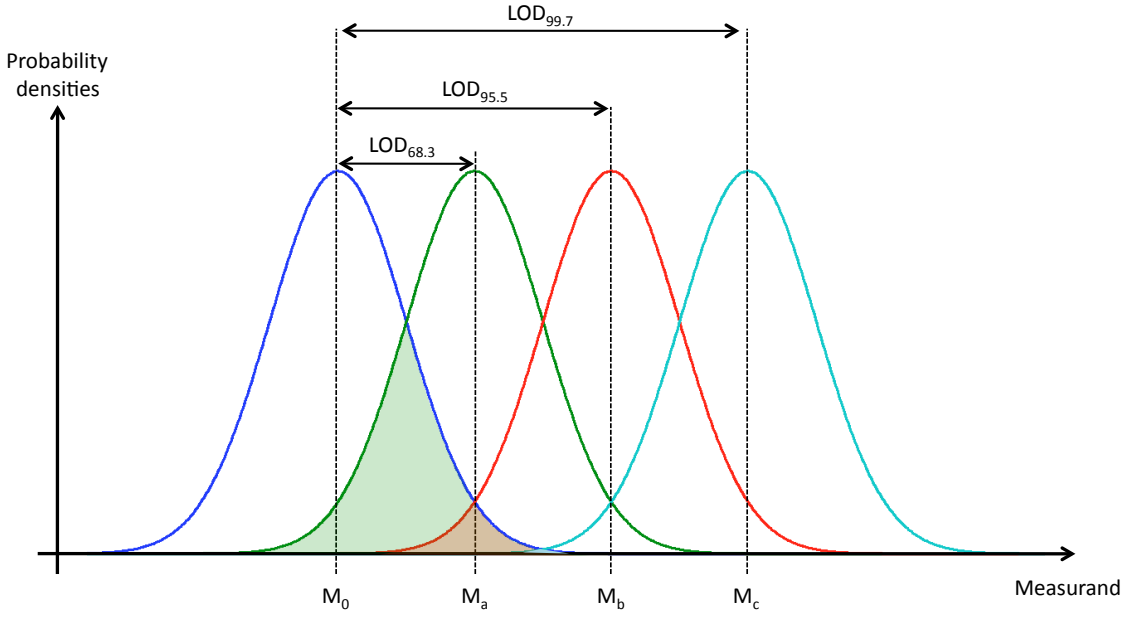

Figure 1.4: Statistical comparison between grades of LOD.

2 Optical evanescent-wave sensing

2.1 Introduction

2.1.1 Origins of evanescent waves

An evanescent wave is a near-field stationary[6] wave whose intensity decays exponentially from the boundary at which it was formed. Evanescent waves can occur in any physical situation where wave equations apply, and are formed at the interface between two media with different wave motion properties.

[6] in a transverse direction

More specifically, in optics and acoustics, an evanescent wave is formed when an incident wave propagating in a primary medium undergo total internal reflection (TIR) at its interface with a secondary medium. For the TIR to occur, hence for the evanescent wave to be created, the phase velocity of the wave in the primary medium $v_{\phi,1}$ should be lower than that in the secondary medium $v_{\phi,2}$. Also, the incidence angle, ie the angle between the wave-vector of the incident wave and the normal to the interface, should be larger than a critical angle θ_C, whose sinus is equal to the ratio of the phase velocities of the secondary and primary media:

$$\sin(\theta_C) = \frac{v_{\phi,2}}{v_{\phi,1}} \tag{1.4}$$

The physical reason of the existence of evanescent waves lies in the necessary continuity of specific scalar or vector fields associated to the waves at interfaces when TIR occurs. For instance, evanescent acoustic waves ensure the continuity of the gradient of the pressure field, representing the pressure force field.

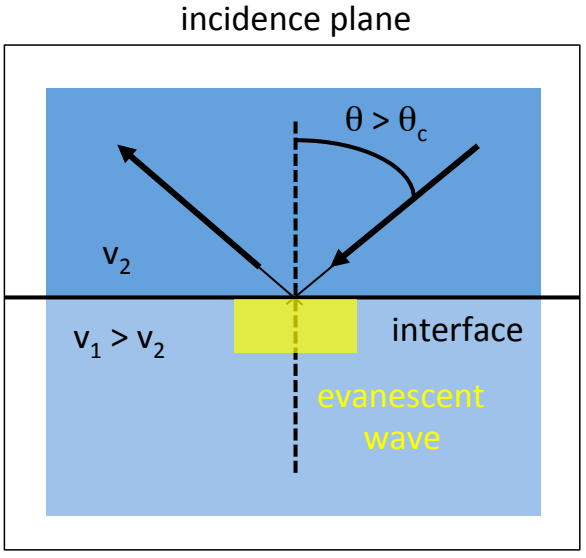

Figure 1.5: Total internal reflection (TIR) of an incident wave at an interface .

In optics, and more generally for electromagnetic waves, the mathematical origin of the evanescent waves lies in the continuity equations at interfaces of the electromagnetic fields **E**, **D**, **B** and **H**. Sometimes, the term *evanescent wave* is replaced by *evanescent field* in electromagnetism, probably to reflect the fact that waves are more naturally associated to scalar

fields in acoustics than the vector fields constituting electromagnetic waves in optics. In the dissertation however, both terms may be employed with a similar meaning.

2.1.2 TIR induced phase-shifts

A non trivial effect of the TIR, or more generally any reflection of an electromagnetic wave at the interface between two media, is the phase shift between reflected and incident waves that occur at reflection. The expression of this phase shift can be determined for both linearly polarized TE and TM waves via Fresnel equations and show that the values of the phase shift depend on the polarization of the wave, the angle of incidence and the complex refractive indices of both media. This means that the reflected wave, which does not exist in the secondary medium in Fresnel's model, carries information on the refractive index of this medium anyway, in its phase.

Let us take the example of the reflection of a plane electromagnetic wave at the plane interface between two dielectric media characterized by their refractive indices n_1 and n_2, for the primary and secondary media, respectively. Incident wave is linearly polarized perpendicular to the incident plane (TE wave). The wave-vector of the incident wave makes an angle $\theta > \theta_C$ (cf. Eq.(1.4)) with the plane interface so that it undergoes total internal reflection (TIR). In such situation, the amplitude reflection coefficient r can be written as [10]:

$$r = \frac{n_1 \sin\theta + j\sqrt{n_1^2 \cos^2\theta - n_2^2}}{n_1 \sin\theta - j\sqrt{n_1^2 \cos^2\theta - n_2^2}} \tag{1.5}$$

Because of total internal reflection, the absolute value of r is identically equal to 1. This also means that the average power of the transmitted wave, i.e. the evanescent wave, is identically zero. Incidentally, the complex reflection coefficient r can be written as $r = \exp(-j\Phi)$. The phase-shift Φ induced by the reflection of the wave can then be written as [10]:

$$\Phi = -2\arctan\left[\frac{\sqrt{n_1^2 \cos^2\theta - n_2^2}}{n_1 \sin\theta}\right] \tag{1.6}$$

A similar, but not identical, expression can of the phase-shift Φ can be derived for a TM wave.

In an optical waveguide, optical waves coupled in the core, with a refractive index (RI) n_1 higher than the RI of surrounding cladding n_2 and substrate n_3 materials, undergo total internal reflections at core/cladding and core-substrate interfaces. Because of TIR-induced phase-shifts, the phase velocity v_ϕ of the wave propagating in the waveguide depends, amongst other parameters, on n_2.

2.1.3 Evanescent-wave sensors

According to the definitions in Sec.1, an evanescent-wave sensor is an *active*, or *parametric* sensor. In most optical evanescent-wave sensors, the *excitation signal*, a linearly polarized electromagnetic wave, is coupled to the core of an optical waveguide in contact with a medium, usually the cladding of the waveguide, whose refractive index n_2 carries information on the stimulus, or measurand. Because of TIR-induced phase shifts, information on the stimulus is converted into the phase velocity of the guided wave. In order to read this phase-velocity, the carrier wave is, directly or combined with other waves, converted into an electrical signal, in the end a voltage, via a photodetector.

In consequence, an evanescent-wave sensor is a complex sensor, where the stimulus is first converted by a transducer, the optical waveguide, the optical energy (or intensity) being then converted into electric energy by a direct sensor, a photodetector.

The variety of evanescent-wave sensors comes from the many transducers that can be build. In addition, each transducer can be used in various configurations, and associated to different excitation signals and photodetection schemes. The main advantage of these sensors, compared to others, is the high accuracy achieved in RI measurements. The resolution of evanescent-wave sensors in refractive index, down to 10^{-7} RIU (Refractive Index Unit) in recent systems [4], allows for measurements of very small variations of the measurands.

Theoretically, all physical quantities that have an effect on a refractive index can be the measurand in an evanescent-wave sensor. The common quality and main interest of evanescent wave sensors in all their applica-

tions is the high resolution they are able to provide. They also share a limited span, which means that they will not, in most cases, be able to measure large variations of the measurand.

2.2 Basic applications

2.2.1 Refractometers

The most obvious application of an evanescent-wave sensor is simply to measure refractive indices. Principle of such measurement is to compare the signal obtained with the medium to measure to a reference medium with a known refractive index. This can be used, for example, to measure small variations of the refractive of aqueous solutions with varying concentrations of a given chemical compound.

2.2.2 Homogeneous concentration sensors

An evanescent field sensor can be used as a highly-accurate concentration sensor, liable to detect and to measure low concentrations of a chemical compound in a buffer solution. For this application, calibration is necessary to plot the signal response to a range of known concentrations of the compound in solution. Generally speaking, this method for measuring concentrations, where the molecules to sense are uniformly distributed in the solution is referred to as *homogeneous detection* (cf. Fig. 1.6).

Although homogeneous detection is an interesting application of evanescent field sensors, the limited resolution in concentration they are able to provide does not entirely justify the use of this class of sensors. It is mainly because they can be much more expensive than already commercialized sensors with similar resolutions. This limitation comes from the fact that the effective indices of optical guided modes are only slightly dependent on the bulk refractive index of the cladding, which is usually where the analyte solution is present. Another way to account for this limitation is to think about the limited spatial extent of the evanescent field, which does not exceed the optical wavelength. In that view, the probability for the evanescent field of a guided mode to sense the presence of a molecule in a semi-infinite space is very low.

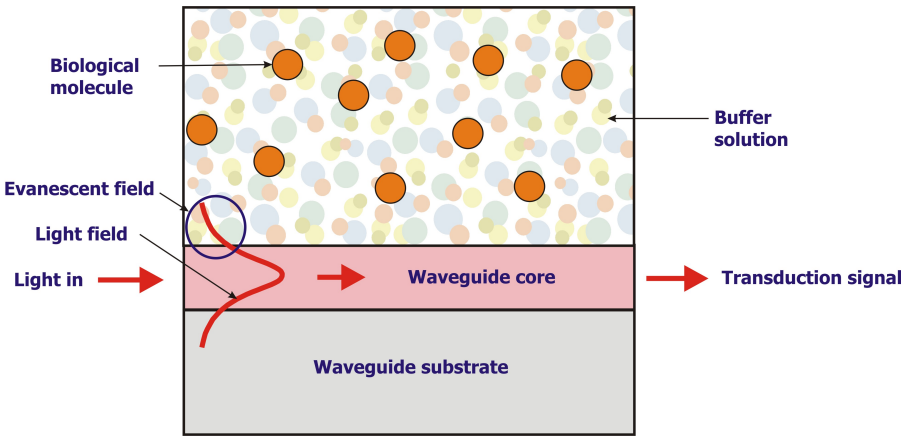

Figure 1.6: Principle of evanescent-wave homogeneous detection.

2.2.3 Surface concentration sensors

Considering the intrinsic limitation of homogeneous detection, surface detection, where analyte molecules to sense are adsorbed at the core/cladding interfaces of the waveguide[7], is a way to achieve much more resolved detection and measurement of a chemical compound in solution. In addition, if only the analyte molecules are adsorbed at the surface, the detection is specific. In other words, the analyte can be detected and quantified in a complex solution, where other chemical species are present. Because of both sensitivity and specificity, this scheme represents the most interesting application of evanescent field sensors (cf. Fig. 1.7).

The necessity to bind molecules on the waveguide in order to detect them requires chemical engineering of its surface. The ability to treat the surface of a material[8] in order to immobilize a specific molecule[9], almost solely determines the range of applications an evanescent field sensor can have in chemical sensing. Resolutions in refractive index (RI) of evanescent field sensors are very likely to reach a practical limit in a few years time, if not already. This means that even though research efforts will lead to lower and lower RI resolutions, commercial sensors will eventually have to settle for intermediary RI resolutions achieved by equipments with reasonable practicality: user-friendliness, robustness and cost. These are

[7] where the evanescent field of the guided mode is at its most intense
[8] mainly selected for its optical properties
[9] this is usually referred to as functionalization of the surface [11]

decisive characteristics for a research product to meet a market, which is always an important aspect to take into account in applied physics. These are the reasons why research on optical surface functionalization will become an increasingly important branch in the development of these sensors, probably the most important.

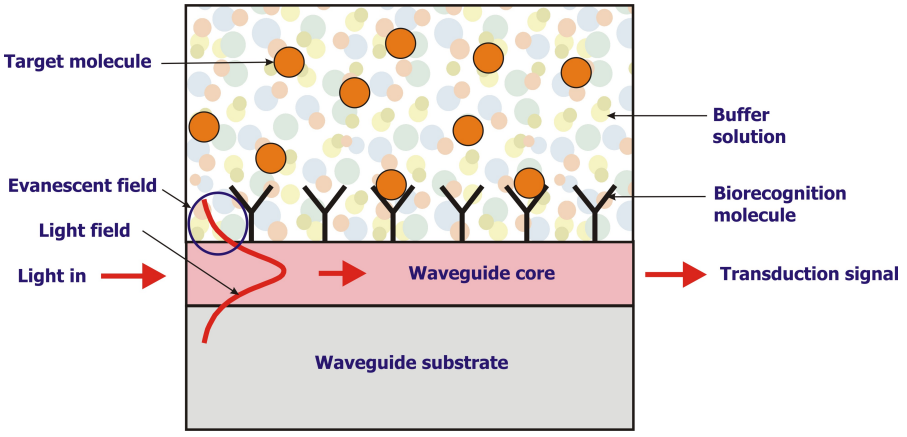

Figure 1.7: Principle of evanescent-wave surface detection.

2.2.4 Temperature and pressure sensors

In evanescent-wave sensors, temperature has been primarily seen as a perturbation. Indeed, typical optical materials used for evanescent wave sensors have thermooptic coefficients (TOC) ranging from 10^{-5} to 10^{-4} in $RIU/°C$, and can also have large values of thermal expansion coefficients (TEC). Accordingly, for waveguide-based sensors, temperature not only modifies the RI of the sensing medium but the RIs of all materials constituting the waveguide, in addition to the geometry of the core. As the effective index of the guided mode in those sensors usually depends prominently on the RI of the core material, the sensitivity of the signal to temperature can be very important comparatively to its sensitivity to the measurand. For sensors functioning with RI resolutions down to $10^{-7}RIU$, effects of small variations of the temperature can be extremely detrimental to the accuracy of the measuring instrument. For this reason, different schemes can be used to reduce the error signal induced by temperature variations, and will be discussed in a subsequent chapter.

As evanescent field sensors can be very sensitive to temperature vari-

ations, a quite obvious idea is to use them as temperature sensors. Of course, simpler systems to measure the room temperature exist, and this application would not have much interest. However, as sensitive elements of evanescent fields sensors can be made very small, from hundreds to a few microns large, they can be used to measure a temperature locally, in a fluid for example, with very high resolution. Such a scheme can be used to study exo or endothermic chemical reactions In addition, if coupled to chemical sensor or label-free biosensor scheme, it can be used to remove the bias due to temperature variations of the analyte solution.

RIs and geometry of waveguides can also be strongly dependent on pressure. Consequently, ultrasound detectors on the base of an evanescent field sensor were proposed [12].

It has to be noted that, since major contributions of the sensitivity to temperature, or pressure, does not come from the evanescent optical field - in most cases - but from the part of the field that propagates in the core material, temperature and pressure sensors thus build are not an evanescent-field sensor *per se*.

2.3 Application to label-free biosensing

2.3.1 Label-free biosensors

Applications of evanescent field sensors as label-free biosensors directly derive from chemical sensing in the surface detection scheme. A biosensor can be defined in a formal way as an analytical device for the detection of an analyte that combines a biological component with a physicochemical detector component. Label-based biosensors use fluorescent or radioactive markers that specifically bind to the target analyte, i.e. a biomolecule of interest, for its detection, its quantification, and/or to study its evolution in a biological system. For that reason, most label-based biosensors are related to microscopy techniques. In comparison, label-free biosensors rely on a specific binding of the analyte on the surface of the sensor, where it can also be detected and quantified. Therefore, they can be viewed as complex sensors where a specific transducer, a biochemical entity, converts chemical energy into an electrical energy, directly or through two or more transducers.

We can distinguish two classes of applications of label-free biosensors. First class of applications is closely related to surface concentration sensing as discussed above. The main objective is the detection and quantification of biomolecules. With proper surface functionalization, an evanescent field sensor with multiplexing capabilities can be designed to recognize many analytes in a given solution. This can be used as a tool for medical diagnosis by specific recognition of one or several biomolecules that are known to be linked to diseases. Chemical equivalent of this setup is the artificial nose with potential to identify, for example, complex aromas from the quantified analysis of its chemical components. Main interest of evanescent wave sensors in these applications, referred to as *end point* and/or *labelled detection*, is their ability to detect very low quantities of the analyte and their compatibility with multiplexing, allowing to perform complex diagnosis from a very small amount of biological solution.

Second class of applications of label-free biosensors is more relevant to fundamental biology, aimed at the study of fundamental biological interactions. It is often referred as *label-free real-time detection*. In these experimental schemes, the aim is to study the binding kinetics between a recognition molecule present on the surface and an analyte brought to the surface by a fluidic system. The knowledge brought by these experiments actively contribute to the development of biomolecular chemistry and other modern branches of biology. Furthermore, we can expect that related discoveries will result in the engineering of new generations of drugs with targeted actions that may efficiently treat diseases with minimal side effects for the patients.

2.3.2 Performances and limitations

For label-free biosensors, the limit of detection (LOD), also called detection limit (DL), can be defined as the lowest concentration at which target detection is possible. In systems where the primary goal of the detection is the quantification of the analyte, the LOD (or DL) matches the definition of the instrument's resolution. This is the case for instance in end-point detection.

In other cases, such as in real-time detection, the LOD can be con-

sidered as an additional specification of the label-free sensing instrument, defining indirectly the amount of biomaterial needed to perform the measurement, related to the thermodynamics of the targeted interaction.

In order to compare label-free biodetection schemes, the first task is to define what is an ideal instrument. An answer to this tricky question is attempted in [5]:

> "the ideal biosensor would offer low limits of detection and short analysis time"

The *analysis time*, though not clearly defined in the reference, can be viewed as the amount of time necessary from the injection of the analyte to obtain one or several pieces of information on the specific interaction. Therefore, it integrates all time constants associated to the detection scheme: transport, incubation, time response of the sensor. The latter is the most difficult parameter to evaluate. Indeed, the time response of the sensor will undoubtedly depend on the physico-chemical quantity measured. For instance, in order to measure the association/dissociation constant of an interaction, the time response can very well be limited by the interaction itself. However, if the response time is larger than the characteristic binding time of the interaction, the measure of such thermodynamic quantities would be impossible. Such limitations might not occur in the same way for the measurement of other quantities. As a consequence, the term *analysis time* may only be used as an accurate tool only to compare performances of instruments for the measurements of similar properties for a given class of interactions.

The definition of the *ideal biosensor* such as defined in [5] does not really take into accounts those considerations. However, it can be interpreted as resulting from the fact that, as expensive scientific instruments, most label-free biosensing (LFB) instruments are expected to be versatile, ie to be able to adapt to various experiments. From the engineer's point-of-view, two design lines can be drawn from these considerations:

1. LFB instruments can be designed to perform only one task, or a specific set of tasks. A perfect example of such systems are blood glucose monitoring devices, where performances can be easily and clearly identified: time of analysis as time from blood extraction to quantita-

tive instrument's response, resolution, and LOD as minimal amount of blood necessary to perform the analysis.

2. As laboratory instruments, LFB are mainly designed to perform multiple tasks which are, in many cases, tasks the instruments were not initially designed to perform. For such random utilization, what comes to mind is that a good LFB instrument for scientific research should be first and foremost versatile. This means that the quality of such an instrument is more adequately defined by its limitations rather than by its performances, the latter being mainly application-dependent, whereas the former defines the range of potential applications. Optimization of such instruments should then rely on reducing their limitations. This can be achieved by reducing identified and independent sources of limitations, and/or in the development of a adaptable instrument, where limitations can be modified from one experiment to another, according to specific requirements of each.

In the scope of this dissertation, the primary objective of the research was to develop a scientific instrument for LFB, with versatility and adaptability as a key issue. To that regard, two limitations were clearly identified: the limit of detection (LOD) described earlier, and the response time of the instrument, established independently from any consideration related to what is measured, and for which interaction. As it was clearly established that the resolution was bound to a time scale for the stimulus for all sensors (cf. §1.2.11), it is also clear that as a general property of LFB instruments is that the LOD increases when the response times decreases and *vice versa*. This can be clearly identified from [5], where for most systems, the time of analysis is most probably limited by the response time of the instrument.

On a plane with LOD and response time as x and y coordinates, respectively, the global performance of a specific LFB instrument is well characterized by the region corresponding to all points M(x,y) where the instrument is able to perform measurements:

- The centre of the region M_0 defines the typical operation of the instrument
- The area $\mathcal{A}$ defines the range of operation, and characterizes the versatility of the instrument

- The x-coordinate extent of the region ΔRT characterizes the range of achievable response times
- The y-coordinate extent of the region ΔLOD characterizes the range of achievable LOD
- The furthest point on the left M_1 defines the minimal achievable response time
- The furthest point on the left M_2 defines the minimal achievable LOD

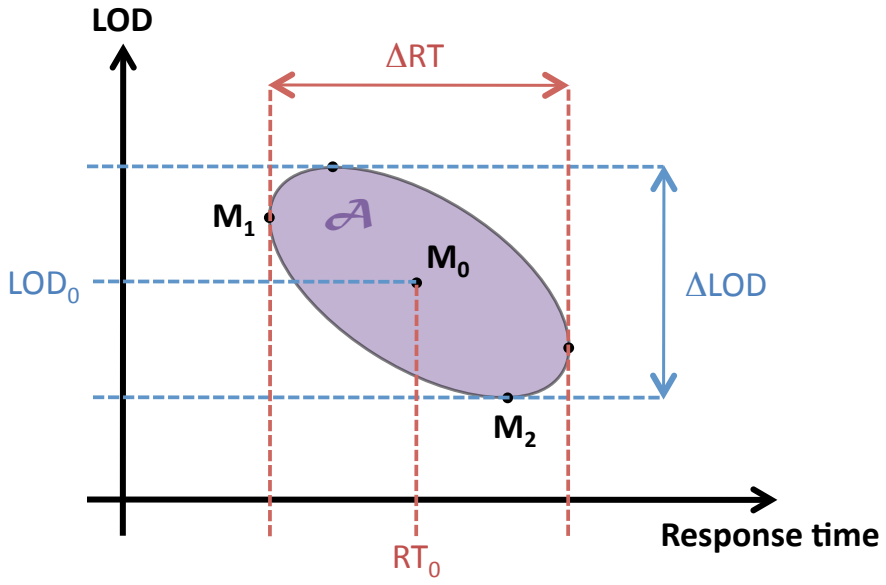

Figure 1.8: LOD versus the response time.

2.3.3 Non-optical techniques

There are two families of non-optical techniques, or detection schemes, in label-free sensing: mechanical and electrical. Electrical detection essentially relies on nanowires (NW) [13]. Mechanical detection schemes are typically based on microcantilevers (MC), suspended microchannel resonator (SMR) and quartz crystal monitors (QCM). A very thorough review of such techniques, with performances compared to other detection schemes can also be found in [5].

2.3.4 Surface Plasmon Resonance (SPR) sensors

All optical detection schemes for label-free biosensing (LFB) are based on evanescent-wave sensing (EWS). Surface plasmon resonance sensors - commonly referred to as SPR sensors- are evanescent field sensors that have found their main application in label-free biosensing. SPR sensors have been under constant development in the last twenty years, and are beginning to be a standard equipment in biology labs across the world. It is all natural to treat these sensors as models for inspiration since numerous aspects of SPR sensors investigated over the years can be transposed, with some effort, to other evanescent field sensors. An elaborate study of SPR sensors is also important to understand their intrinsic advantages and limitations, in order to develop systems that effectively creates new perspectives, for both fundamental and applied research, in opposition to developing systems that are only able to reproduce what an already existing and well established technology can do.

Working principle

As its name indicate, optical phenomenon at the most basic level of a SPR sensor is the surface plasmon, also called surface plasmon polariton. A surface plasmon can be considered as a limit case of a guided mode in a slab waveguide with a width that tends to zero. From electromagnetic theory, such an optical mode can only propagate at the interface between a dielectric material and a metal. The particularity of surface plasmons is that their evanescent fields are mainly present on the dielectric side[10] and represent a major part of the mode's energy. In evanescent field sensing terms, this means that the effective index of the plasmon is very sensitive to the refractive index of the dielectric near the gold/dielectric interface, hence to biological interactions occurring in this region.

SPR and SPR imagery (SPRi) sensors

Compared to other evanescent field sensors, the main difficulty of SPR sensors lies in the retrieving of the effective index of the plasmon, quantity that contains the information on the measurand. This is due to the fact that,

[10] where the biological is introduced and adsorbed

because of optical absorption in the metallic medium, plasmons cannot effectively propagate on long distances. It is then most difficult to retrieve the measurand from interferometry techniques. However, effect of the modification of the effective index can be detected indirectly via optical coupling.

In order to excite the surface plasmon properly, the effective index of the excitation beam must match that of the surface plasmon. The incident beam is then said to be in resonance with the plasmon, hence the name of surface plasmon resonance. The effective index of the plasmon can the ratio of the incident intensity that was coupled to the plasmon, then absorbed in the metallic layer. Different coupling mechanisms can be used to excite surface plasmons on a thin metallic layer sandwiched in between two dielectric media: waveguide couplers, grating couplers and prism couplers. In most situations though, prism couplers, where the plasmon resonance can be sought by modifying the angle between the light source and the metallic surface and measuring the reflected intensity with a photodetector, are preferred (cf. Fig. 1.9).

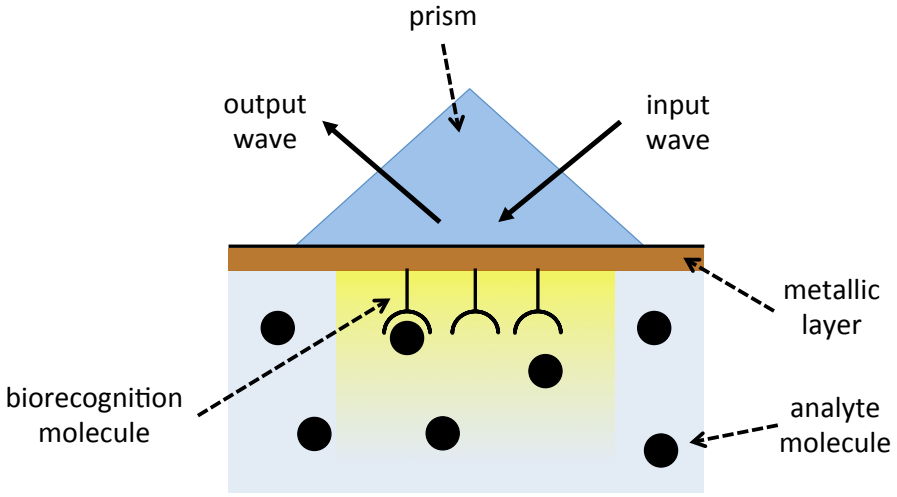

Figure 1.9: Schematic view of a typical SPR sensor setup.

In SPRi - or SPR imagery - part of the surface of a prism coated with a metal, usually gold, is imaged with a CCD camera. The angle of the incident beam to the coated surface is chosen near the inflexion point of the resonance curve, where the overall sensitivity is at maximum. The corresponding image formed on the CCD camera is recorded and used as reference. During the experiment, the real-time difference signal from each

pixel of the camera can be used to map refractive index variations on the imaged metallic surface (cf. Fig. 1.10). This makes SPRi particularly interesting for label-free biosensing. Indeed, the imaged metallic surface can be treated and spotted with different solutions. *In fine*, in commercial systems, results from several hundreds of spots, each representing a surface binding experiment, can be read simultaneously and in real time. This multiplexing capacity is a very important aspect in label-free biosensors to achieve high specificity in the measurements, and is the main reason of the commercial success of these systems.

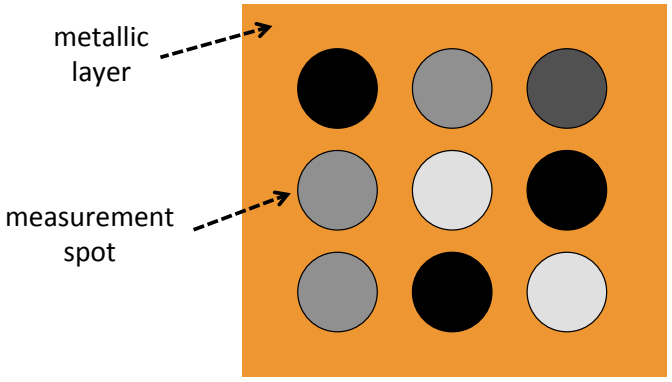

Figure 1.10: Typical view recorded by the CCD camera in a SPRi setup. Different shades of measurement spots represent the amount of analyte adsorbed on the surface.

For further information on SPR technology, three reviews, from 1999 [14], 2007 [15] and 2012 [16] provide a very comprehensive view of the evolution of this technology, and its future in LFB instruments.

2.3.5 Integrated optofluidic sensors

As described in the last paragraph, one of the main advantage of SPR is probably its important multiplexing capacity. This capacity is related to the relatively short interaction length between surface plasmons and analytes, allowing to perform independent measures from two spots that are close-by. However, because of this short interaction length, the LOD achieved with SPR are quite large compared to other optical or non-optical techniques [5].

Instead of using surface plasmons to produce evanescent waves, solely responsible for the sensitivity of evanescent-wave sensors (EWS), a first

idea was to use regular, two-dimensional optical guided modes propagating in straight waveguides, which can be referred to as IO-LFB, for integrated optics label-free biosensors. In this subclass of optical LFB, the weakest density of light/analyte interaction, due to a reduced typical length of the modal evanescent field compared to that of a surface plasmon, is vastly compensated by a much longer light/analyte interaction length. This is mainly due to the fact that light can propagate in optical fibres or planar waveguides on very large distances with very little optical loss. A classical sensing scheme associated to such sensors is the Mach-Zehnder interferometer (MZI) (cf. Fig. 1.11). Information on the analyte is obtained from the output optical intensity, resulting from the interference between waves from the reference arm and waves from the sensing arm, where the core of the waveguide is in contact with the analyte [17]. In addition, two independent orientation-related reading can be obtained from orthogonal propagation modes TE and TM in IO-LFBs, compared to the single TM polarization operation of SPR sensors. This makes IO-LFBs potentially much more sensitive to conformational changes during interaction, which is a very topical subject in biology.

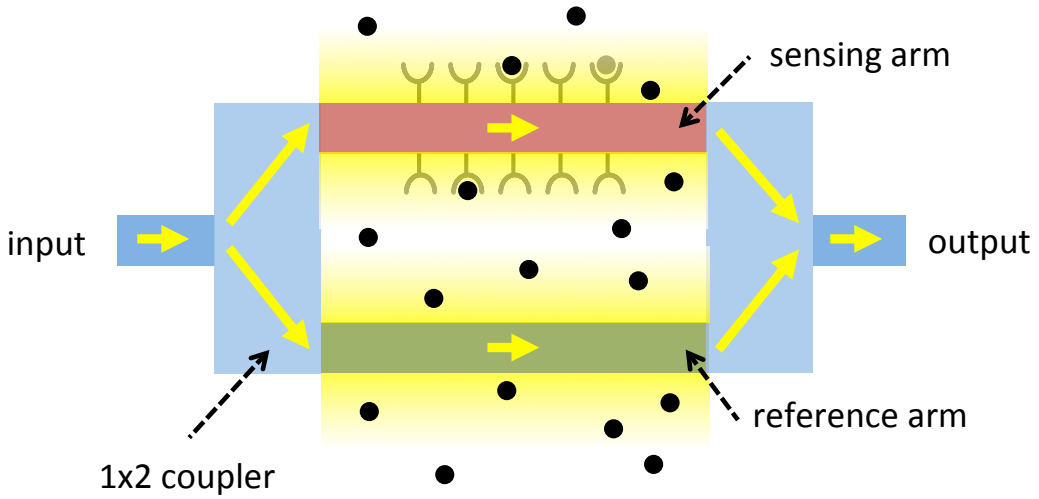

Figure 1.11: Schematic view of a MZI label-free biosensor. Information of the analyte is carried in the transmitted optical intensity of the device.

As compared to SPR-based instruments, this technology had very little commercial success. Despite a better theoretical LOD than for SPR, the main issue of IO-LFB instruments is the large surface on which light/analyte interaction occurs. Indeed, in order to achieve higher resolutions or LODs

than SPR instruments, IO-LFB instruments use relatively very long waveguides, in the *cm* range, with several consequences on the limitations of the instrument. Specifically, because of the extent of the sensing area, the response time of the optofluidic device is longer, and multiplexing capacity is limited. Also, because surface functionalization is hardly homogeneous over the millimetre scale, such detection scheme is not really compatible with biosensing.

The main limitation of IO-LFB is the long interaction length they require to achieve resolutions, or LODs, that are comparable with that of SPRi instruments. One solution to overcome this issue is to optimize the light/analyte interaction strength in the transverse directions, in order to work with reasonable interaction lengths, *ie* longer than those typical of SPR, but not so long as to create incompatibility with biosensing. This is the basic idea behind hybrid sensors, integrating plasmonics on regular waveguides. Thus, they use both short and long interaction length schemes to find an optimal configuration.

To summarize, in order to achieve better LODs than that is currently achievable by typical SPR instruments, the issue at stake for any optical LFB is to optimize the interaction strength[11]. Since the interaction length should be small[12] for biosensing applications, one of the key parameter to optimize is the interaction strength in the transverse plane. Independently from the nature of the evanescent field, this quantity can be effectively increased, simply by multiplying the occurrences where a single guided wave interacts with the analyte in a given region. This is achieved in optical microresonators.

2.3.6 Microresonator-based sensors

In optical microresonators, the light propagates in a closed-loop photonic structure, with typical sizes from few μm to 1 mm. Several microresonator geometries exist, and are usually classified according to the type of propagation.

[11] The interaction strength can be defined as the product of a density of interaction strength, characteristic of the evanescent field, and the interaction length, which is the length of the waveguide in contact with the analyte

[12] 1 mm and under

Whispering gallery modes (WGM) resonators are high index closed geometrical structures, typically spheres, toroids, disks or polygons (triangles, squares, ...). In such resonators, light undergoes multiple TIRs along the interface between the resonator and the cladding, usually air or water. These resonators are characterized by very low optical loss.

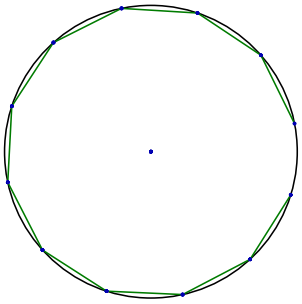

Figure 1.12: Trajectory of light (green line) associated to a guided mode in a WGM resonator (black line).

Waveguide modes (WM) resonators are based on regular waveguides, *ie* optical fibres or channel waveguides. The first possible configuration are Fabry-Pérot cavities formed by Bragg gratings imprinted on straight waveguides. The second one is a physical closed-loop configuration of the waveguide, typically a ring or racetrack. In such resonators, light waves are typically reflected on both sidewalls of the waveguide. These reflections, depending on the curvature of the waveguide, are not necessarily TIRs, explaining in part (cf. Chap. 2) the higher degree of optical loss in such resonators, compared to WGM resonators. In WM resonators, whispering gallery modes can also be supported if the waveguide cross section is large enough compared to the curvature.

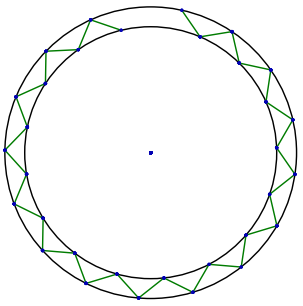

Figure 1.13: Trajectory of light (green line) associated to a guided mode in a ring resonator (black lines).

An important parameter describing the optical loss inside a microresonator is the Q factor, defined as:

$$Q = 2\pi \frac{E_{st}}{\Delta E_{cycle}} \tag{1.7}$$

where E_{st} is the energy stored in the resonator and ΔE_{cycle} is the energy dissipated per cycle, which corresponds for a ring resonator to the field oscillation period $T_f = 1/f$.

In comparison to sensors based on non-resonant photonic structures, the effective light/analyte interaction length in microresonator-based sensors is not determined by the geometrical length of the structure, but by the amount of optical loss inside the optical resonator. Therefore, the effective interaction length L_{eff} can be expressed as a function of the Q factor [4]:

$$L_{eff} = \frac{\lambda Q}{2\pi N_{eff}} \tag{1.8}$$

where λ is the resonant wavelength and N_{eff} the effective index of the guide mode in the resonator.

This expression shows the potential of microresonator-based devices: with a Q factor of 10^6, N_{eff} = 1.45 and λ = 1550 nm, the resulting effective length is L_{eff}= 17 cm, whatever the geometrical size of the resonator. Consequently, a large improvement can be obtained on the density of interaction strength in microresonator-based devices.

Numerous configurations of IO-LFBs integrating microresonators have been proposed over the years. Performances of such devices as compared to other IO-LFBs are reviewed in [4]. In [5], they are compared with all other systems proposed for label-free biosensing.

It is important here to point out that some sensing techniques, although they show great promises in sensing experiments, cannot easily be applied to measuring instruments. This is mainly due to important issues related to device fabrication, device and instrumentation cost, and the compatibility with microfluidics. In addition, the commercial success of SPRi instruments outlined the importance to build multiplexed systems, allowing to overcome specific issues in biosensing related to the specificity of the

measurements. With state-of-the-art sensing performances, excellent microfluidics integration and multiplexing capacities, microring resonators appear as very good candidates for label-free biosensing instruments.

3 Microring resonators in optofluidic multi-sensor instruments

3.1 Introduction

Microring resonators are essentially planar waveguides bent in order to form a closed loop in which the light can propagate in circles. With adequate materials, such devices can be active[13]. However, for sensing purposes, passive devices are dominantly used. Since they are not optical sources, passive microring resonators are not standalone devices. In all configurations, such resonators operate as parametric devices, characterized by a transfer function between the optical input, *ie* the source of the excitation of the microresonator, and an output from which the response to the excitation can be measured. Transport of light from the input to the microring, and from the microring to the output is, in a typical configuration, performed by a straight *bus* waveguide (cf. Fig. 1.14) in close contact with a portion of the bent waveguide constituting the microcavity.

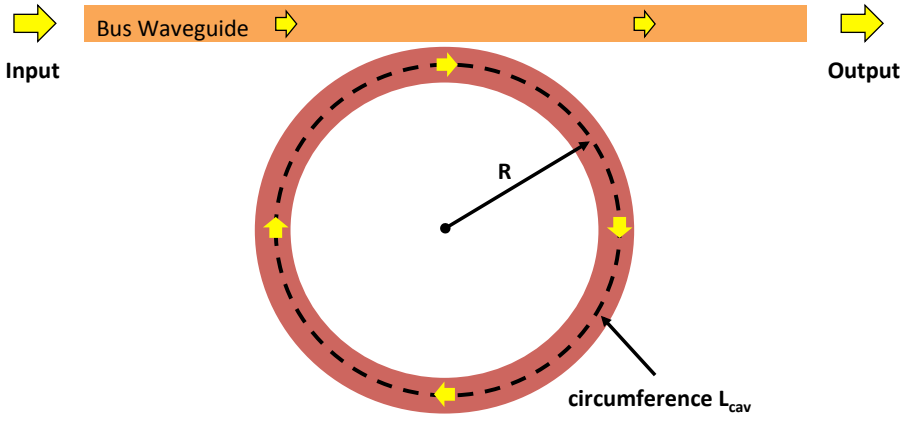

Figure 1.14: Schematic view of a ring resonator in a typical configuration.

From this close contact, light can be coupled from the bus waveguide into the ring, and reciprocally from the ring into the waveguide. These

[13] as photonic devices

exchanges typically occur in an approximate zone referred to as the *coupling region*. Since the passive ring-shaped optical cavity needs the bus waveguide to operate, the term *microring resonator* usually refers to the standalone photonic device, resulting in the combination of the bus waveguide and the ring. For further reference, the following definition will be used:

$$\text{Microring resonator} = \{\text{bus waveguide} + \text{microring}\}$$

A microring resonator can be characterized either from a designer's point of view, either from a user's point of view:

- From the designer's point of view, the microring resonator is defined by how it is build: materials of the core, the substrate, the cladding; section of the bus and bent waveguide, coupling configuration, radius of the ring, ... All these design parameters play an important role on the relation between optical input and output.

- From the user's point of view, the device is simply described by the input/output relation. This relation defines the expected behaviour of the microring resonator in all of its applications, optical filter or sensor in most cases.

A variant of the microring is the microracetrack resonator (cf. Fig. 1.15). It is essentially constituted of two half-circles linked to one another by straight waveguide portions of length L_{str}.

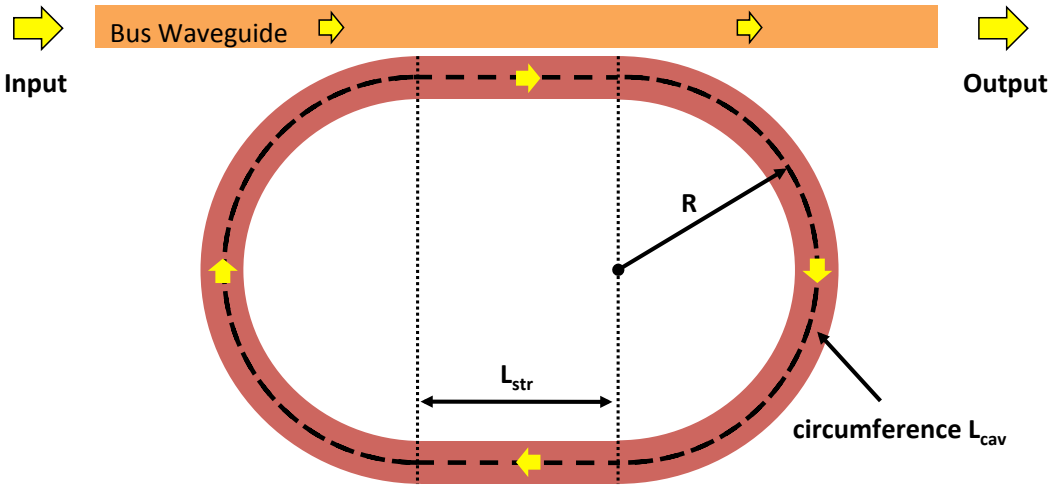

Figure 1.15: Schematic view of a racetrack resonator in a typical configuration.

The main advantage of this geometry compared to the ring is the additional independent parameter L_{str} it offers, which is sometimes useful to achieve an optimal design. From the only slight difference between microrings and microracetracks, the term *microring* is often employed for both geometries in further reference.

3.2 Optical characteristics

3.2.1 Intensity transmittance

The intensity transmittance T is most commonly used to describe the input/output relationship of the microring resonator. It is defined as the ratio between the optical intensity at output I_{OUT} and that at the input I_{IN}:

$$T = \frac{I_{\mathrm{OUT}}}{I_{\mathrm{IN}}} \tag{1.9}$$

The intensity transmittance is most simply expressed as a function of the single-trip phase delay inside the resonator Φ, which is itself a function of the frequency (or wavelength) of the light propagating in the device. In most experiments, T is measured as a function of wavelength, as presented in Fig. 1.16.

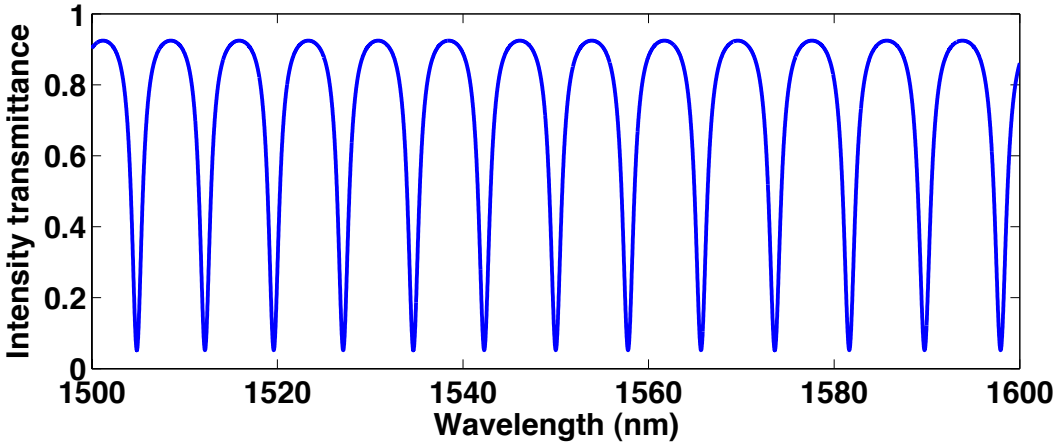

Figure 1.16: Idealized intensity transmittance of a microring resonator as function of wavelength

In sensing applications, the general purpose of the detection scheme is to track the variations of one or more resonant wavelengths, corresponding

to the minima peaks in the intensity transmittance. This provides variations of the phase velocity of light in the resonator, carrying information on the stimulus or measurand. Therefore, performances of the measuring instrument are strongly influenced by the characteristics of the intensity transmittance. These characteristics are defined hereafter. A more thorough analysis of their dependencies is presented in Chap.2.

3.2.2 Resonance contrast

The resonance contrast, describing the depth of a resonance, is defined as:

$$C = \frac{T_{max} - T_{min}}{T_{max} + T_{min}} \tag{1.10}$$

In sensing, a high contrast facilitates the analysis of the resonances, and results in lower measurement uncertainties.

3.2.3 Free Spectral Range

The *free spectral range* (FSR) refers to the period of the intensity transmittance. It is defined as the typical distance between two resonance peaks. Depending on the variable used to describe T, it can be expressed in phase units (rad), frequency units (Hz) and wavelength units (nm).

Depending on the detection scheme, the FSR can be an important factor of the span of the measuring instrument integrating a microresonator.

3.2.4 FWHM and Finesse

The *full width at half maximum* (FWHM) describes how narrow a resonance peak of the intensity transmittance is. Similarly to the FSR, it can be expressed in phase, frequency or wavelength units. In contrast, the *Finesse* $\mathcal{F}$, defined as the ratio between the FSR and the FWHM, is independent from the variable chosen to describe the intensity transmittance.

$$\mathcal{F} = \frac{FSR}{FWHM} \tag{1.11}$$

The Finesse is mainly used for the characterization of microresonators for filtering applications. The reason to define the FWHM is mainly to introduce a simplified expression of the Q factor, already introduced in §2.3.6.

3.2.5 Q factor

For values of Q factors that are large compared to unity, which is the case for all microring resonators that are worth characterizing, this parameter can be expressed using wavelength as:

$$Q = \frac{\lambda_{res}}{\text{FWHM}_\lambda} \tag{1.12}$$

where λ_{res} is a resonant wavelength and FWHM_λ the FWHM expressed in wavelength units.

As outlined in §2.3.6, a high Q factor is important to provide a large effective interaction length in sensing applications, particularly for label-free biosensing. It can also play an important role in the resolution of the sensor, also affecting the combined uncertainty of the measuring instrument.

3.2.6 Maximal intensity slope

The *maximal intensity slope* (MIS) is defined as the maximal value of the derivative of the intensity transmittance. The MIS is attained for each resonance peak at its two inflection points. Using wavelength as a variable, it can be expressed as:

$$\text{MIS} = \frac{dT}{d\lambda}(\lambda_{inf}) \tag{1.13}$$

where λ_{inf} is the position of an inflection point.

As it it will be demonstrated in the following, the MIS is a ultimate parameter to describe the measurement resolution in determining the positions of the resonances.

3.3 Detection schemes

In the following are presented the main detection schemes that are used to collect information on the stimulus from the microresonator response. For illustration purposes, the case of label-free biosensing is treated. However, principles and expressions remain applicable to all other sensing applications.

3.3.1 Detection principle

As explained before, information on the stimulus is carried in the phase velocity of the propagation mode inside the resonator, which is also described by the modal effective index N_{eff}. The single-trip phase delay Φ accumulated by an optical wave of wavelength λ is expressed as:

$$\Phi = \frac{2\pi}{\lambda} N_{eff} L_{cav} \tag{1.14}$$

where L_{cav} is the mean circumference of the resonator.

A minimum of transmission corresponds to the situation where Φ is an odd multiple of π. Therefore, if λ_0 is the resonant wavelength corresponding to an odd number p, the corresponding effective index$N_{eff,0}$ can be expressed as:

$$N_{eff,0} = \frac{p}{2L_{cav}} \lambda_0 \tag{1.15}$$

A direct consequence of this expression is that the variation of the position of the resonance $\delta\lambda$ around λ_0 is proportional to the variation of effective index δN_{eff} around $N_{eff,0}$. This is summarized in the equation:

$$\delta N_{eff} = \frac{N_{eff,0}}{\lambda_0} \delta\lambda \tag{1.16}$$

Consequently, an increasing effective index, for instance due to the binding of molecules on the surface of the microresonator, results in a shift of all resonant wavelengths to the right, such as presented in Fig. 1.17.

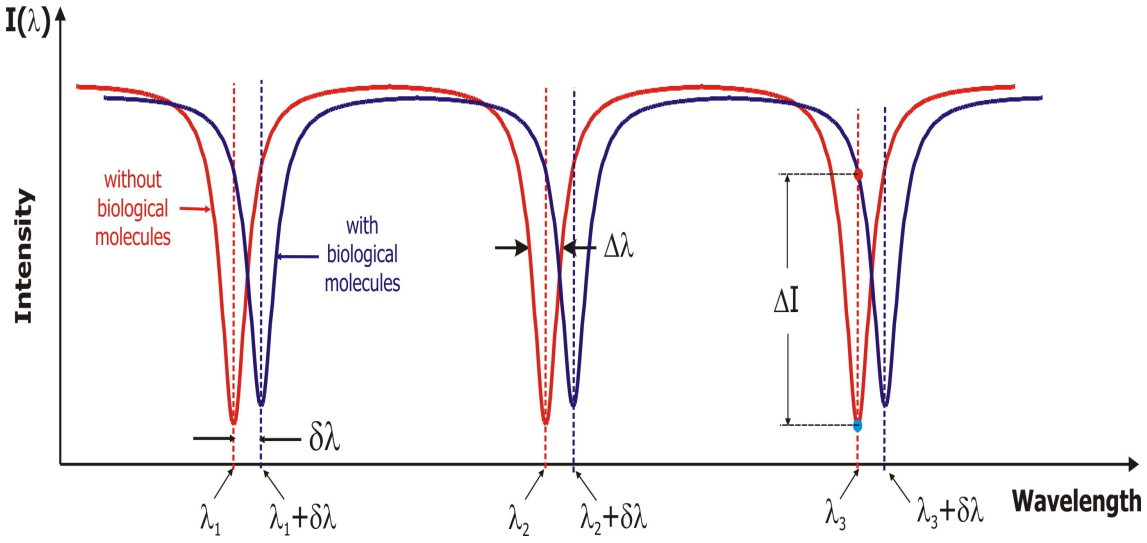

Figure 1.17: Illustration of the detection principle in microring-based biosensors.

The detection principle associated to microring resonators for sensing applications is to measure the shift of the resonant wavelengths $\delta\lambda$, proportional to the variation of the effective index δN_{eff}, which is an image of the stimulus or measurand. The main detection schemes used to achieve this are the fixed-wavelength method, and the wavelength scanning method.

3.3.2 Fixed-wavelength method

In the fixed-wavelength method, light from a laser emitting with a narrow linewidth around a wavelength λ_0 is coupled to the input of the microring resonator, and the intensity at the output is measured with a fast photodetector. In such configuration, a shift of resonant wavelength $\delta\lambda$ is measured indirectly, since what is actually measured is the variation of transmitted intensity δI, induced by the shift $\delta\lambda$ (cf. Fig. 1.18) on a neighbourhood of a wavelength λ_0. In this scheme, the wavelength λ_0 can be chosen anywhere on the initial resonance peak, although it is better to choose λ_0 matching one position of inflection point on the resonance peak. Reasons for this are detailed in the following.

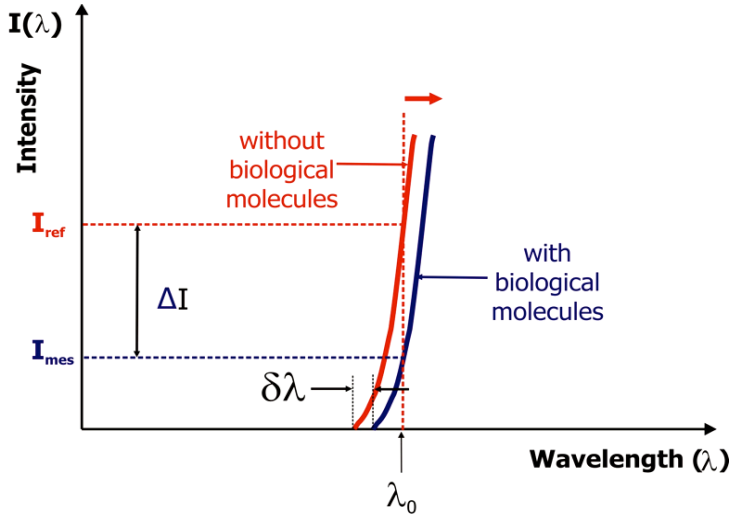

Figure 1.18: Illustration of the application of the fixed-wavelength method (FWM) to biosensing.

The transmitted intensity $I_0 = I(\lambda_0)$ can be written as:

$$I_0 = T(\lambda_0) \cdot I_S \tag{1.17}$$

where I_S is the intensity of the source, assumed to be constant. According to the previous equation, on a neighbourhood of λ_0, the variation of intensity δI induced by the shift $\delta\lambda$ can be expressed as:

$$\delta I = I_S \cdot \frac{dT}{d\lambda}(\lambda_0) \cdot \delta\lambda \tag{1.18}$$

Hereafter, we assume that the transfer function between the measurand $M(t)$ and the time-dependent effective index $N_{eff}(t)$ can be written as:

$$M(t) = K \cdot N_{eff}(t) + M_0 \tag{1.19}$$

where K and M_0 are assumed to be constants.

Accordingly, the variation of the measurand $\delta M(t)$ related to the variation of the effective index δN_{eff} can be written as:

$$\delta M(t) = K \cdot \delta N_{eff}(t) \tag{1.20}$$

In consequence, the relation between $\delta M(t)$ and the variation $\delta I(t)$, deduced from (1.20), (1.18), and (1.16), is expressed as:

$$\delta M(t) = \frac{K N_{eff,0}}{p_0 \lambda_0 I_S} \cdot \delta I(t) \tag{1.21}$$

where $p_0 = (dT/d\lambda)(\lambda_0)$.

Measurement uncertainty

Equation (1.21) provides, from measurements of all parameters during a calibration step, and from the measurement of δI, a central value of $\delta M_{\text{real}}(t)$, the real variation of the measurand. The difference between $\delta M_{\text{real}}(t)$ and $\delta M(t)$ is quantified by the combined uncertainty $\sigma(\delta M)$ of the measuring instrument. This can be expressed as:

$$\delta M_{\text{real}}(t) = \delta M(t) + \sigma(\delta M) \tag{1.22}$$

According to §1.2.13, the combined uncertainty $\sigma(\delta M)$ can be deduced from an uncertainty budget, listing all sources of errors and fluctuations of the measure. For the fixed-wavelength method, a typical uncertainty budget is established in Tab. 1.2.

Source of uncertainty	**Parameter**	**Deviation**	**Uncertainty**
Fluctuations of the source intensity	I_S	$\sigma(I_S)$	$\sigma[M](I_S)$
Fluctuations of the emission wavelength	λ_0	$\sigma(\lambda_0)$	$\sigma[M](\lambda_0)$
Photodetection noise	δI	$\sigma(\delta I)$	$\sigma[M](\delta I)$
Variations of linear slope K	K	$\sigma(K)$	$\sigma[M](K)$
Variations of linear intercept M_0	M_0	$\sigma(M_0)$	$\sigma[M](M_0)$
Variations of the effective index unrelated to the measurand	$N_{eff,0}$	$\sigma(N_{eff,0})$	$\sigma[M](N_{eff,0})$
Variations of the slope	p_0	$\sigma(p_0)$	$\sigma[M](p_0)$
Variations of the input intensity	I_{IN}	$\sigma(I_{\text{IN}})$	$\sigma[\delta\lambda](I_{\text{IN}})$
Variations of the typical resonance width	FWHM	σ(FWHM)	$\sigma[\delta\lambda]$(FWHM)
Variations of the resonance contrast	C	$\sigma(C)$	$\sigma[\delta\lambda](C)$

Table 1.2: Uncertainty budget related to the fixed-wavelength method (FWM).

The relation between the uncertainty $\sigma[M](A)$ and the deviation $\sigma(A)$ of a parameter A can be expressed as:

$$\sigma[M](A) = \frac{\partial(\delta M)}{\partial A}\sigma(A) \tag{1.23}$$

According to the law of propagation of uncertainty, the combined uncertainty $\sigma(\delta M)$ can be expressed as the square root of the sum of the independent uncertainties squared (cf. §1.2.13). The challenge is thus to evaluate all uncertainties listed in Tab. 1.2, primarily to establish which sources are dominant in the combined uncertainty, and secondly to quantify the uncertainty of the measurement.

It is important to point out that, amongst the uncertainty sources listed in the budget, the first two are solely dependent on the laser source used for emission of the input signal. The third uncertainty source is related to the photodetector place at the output of the microresonators, and all other sources are related to the behaviour of the microresonator.

As explained before, performances of a label-free biosensor (LFB) instruments are primarily defined as the operating range in terms of response time (RT) and limit of detection (LOD), also called detection limit (DL). The combined uncertainty on the raw output $\delta M(t)$ defines the LOD achieved when RT is at minimum, intrinsically limited by the instrumentation. When the signal is averaged on N acquisitions, uncertainties related to fluctuations are divided by a factor $\sqrt{N}$, whereas the response time of the instrument is multiplied by N. Therefore, the LOD can be reduced by averaging, at the cost of a longer time response.

In the situation where the LOD is to be optimized, it can be considered that with sufficient averaging, all uncertainties related to fluctuations will tend to zero. Consequently, the combined uncertainty will then be entirely defined by systematic errors, related to deterministic variations of all parameters listed in the uncertainty budget. It is is important to point out here that δI, as measured signal, is not a parameter. The deterministic variations of the parameters can be attributed either to environmental variations (temperature, pressure, humidity, ...), potentially affecting all parameters, or sensing related variations, only affecting parameters related to the microresonator (K, M_0, $N_{eff,0}$, p_0, ...). These variations inherently limit the lowest achievable LOD in LFB instruments.

Because of the deterministic origin of systematic errors, further improvement of the LOD can be achieved independently from the response

time by calibration, where a renewed measurement of all parameters listed in the budget limits the uncertainties due to parameter drifts. However, such calibration cannot be performed during measurement, thus limiting the reach of this scheme.

In comparison, an ideal solution would be to measure all parameters in real-time. This can be easily achieved for the source intensity I_S, with an additional photodetector, and for the emission wavelength, with a lambdameter, of course with additional complexity and cost of the system. In the fixed-wavelength detection scheme, other parameters, related to the microresonator, cannot be directly determined during operation. However, some parameters that are known to modify their values can be measured, such as environmental parameters (temperature, pressure, ...). Provided that an accurate model for the transfer functions between environmental parameters and microring parameters can be established, real-time corrections of environmentally-induced systematic errors can be performed.

Amongst all systematic errors, the most difficult to deal with are related to the sensing. In LFB instruments, these errors play a dominant role in the limitation of the LOD, and more generally in the uncertainty of the measurements. What is particularly problematic about sensing-related errors are the local variations of the relevant physical quantities at the vicinity of the microring. These physical quantities are typically the temperature and pressure distributions in and near the microring, and the homogeneous refractive index of the cladding. In addition, in to label-free sensing, non-specific interactions occurring near or at the surface of the microresonator can induce very strong systematic errors.

In SPRi systems, thanks to the important multiplexing capacity, systematic errors can be removed in real-time by using one or multiple references. Measurement signals are compared to reference signals to provide a combined signal where, ideally, all systematic errors are removed. Such a scheme can be reproduced, using not one but several microrings, thus providing several measurement signals and references to combine.

At this stage, the fixed-wavelength method reaches an important limitation. Indeed, real microresonators, even built on the same substrate,

with the same design, will not have, except by pure luck, exactly similar intensity transmittances. The issue is mainly that microresonators cannot be repeatedly build with aligned resonances. As a consequence, a multiplexed configuration would have to offer one source and one photodetector for each microresonator, or two of each per microresonator if responses from both TE and TM polarizations are studied. Compared to SPRi, where multiplexing capacity is only a matter of resolution of the optical system and of the density of measurement spots on the metallic surface, a microring based LFB instrument using the fixed-wavelength scheme would have to demonstrate exceptional sensing performances to justify the additional cost and complexity, mainly due to the necessary multiplication of the laser sources. On the other hand, using the wavelength-scanning method, signals from any number of microresonators can be measured simultaneously with a single tunable laser source.

3.3.3 Wavelength-scanning method

In the wavelength-scanning method, the instrumentation of the sensor is quite similar to that presented for the fixed-wavelength scheme. The major difference is to replace the laser source operating at a fixed wavelength λ_0 by a tunable laser (cf. Chap.2). The tunable laser source emits light with a time-dependent emission wavelength $\lambda_S(t)$, varying continuously or step-by-step between two wavelengths λ_{min} and λ_{max}. Thus, a photodetector placed at the output of the microresonator measures a time-dependent intensity signal $I(t)$. Ideally, the evolution of the emission wavelength $\lambda_S(t)$ can be expressed, for a scan starting at $t = 0$, as:

$$\lambda_S(t) = \lambda_{\text{min}} + V_\lambda \cdot t \tag{1.24}$$

where V_λ is the scanning speed, in wavelength unit per time unit (typically nm/s). From this, the duration τ_{scan} of a wavelength scan between λ_{min} and λ_{max} is expressed as:

$$\tau_{\text{scan}} = \frac{\lambda_{\text{max}} - \lambda_{\text{min}}}{V_\lambda} \tag{1.25}$$

During this period of time, since the emission wavelength varies with time, the recorded intensity $I(t)$ is an image of the intensity transmittance, measured on a wavelength range defined by λ_{min} and λ_{max}. Thus, from $I(t)$, a method is necessary to convert the time-scale into a wavelength scale, in order to plot the measured intensity transmittance as function of the

wavelength. As described in Chap.4, this can be achieved either by extrapolation, or by direct measurement of the wavelength.

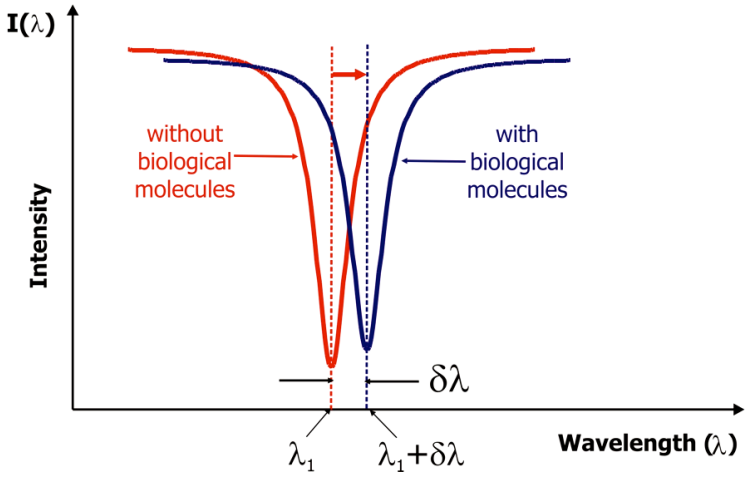

Figure 1.19: Illustration of the use of the wavelength-scanning method (WSM) for biosensing.

In sensing, the purpose of measuring the intensity transmittance as function of the wavelength $T(\lambda_S)$ is to determine the positions of one or several resonant wavelengths in the scanned wavelength range. Consequently, another method is necessary to determine the resonant wavelengths at each period T_{scan} from the measured intensity transmittance.

For this detection scheme, assuming for simplicity that only one resonant wavelength is measured at each period τ_{scan}, the output signal can be defined as the time-dependent variation of the resonant wavelength $\delta\lambda(t)$ around a reference value $\lambda(t_0) = \lambda_0$ measured at $t = t_0$:

$$\delta\lambda(t) = \lambda(t) - \lambda_0 \tag{1.26}$$

Even though the measurement method is different, the signal $\delta\lambda(t)$ is identical to the wavelength shift deduced from $\delta I(t)$ in the fixed-wavelength method. Therefore, the relation between the variation of the measurand $\delta M(t)$ and that of the wavelength can be expressed as:

$$\delta M(t) = \frac{K N_{eff,0}}{\lambda_0} \cdot \delta\lambda(t) \tag{1.27}$$

where parameters K and $N_{eff,0}$ have the same significations as parameters defined in the fixed-wavelength scheme.

Uncertainty budget

From Eq.(1.27), the uncertainty budget presented in Tab.1.3 is established.

Source of uncertainty	**Parameter**	**Deviation**	**Uncertainty**
Detection noise	$\delta\lambda$	$\sigma(\delta\lambda)$	$\sigma[M](\delta\lambda)$
Variations of linear slope K	K	$\sigma(K)$	$\sigma[M](K)$
Variations of linear intercept M_0	M_0	$\sigma(M_0)$	$\sigma[M](M_0)$
Variations of the effective index unrelated to the measurand	$N_{eff,0}$	$\sigma(N_{eff,0})$	$\sigma[M](N_{eff,0})$

Table 1.3: Uncertainty budget related to the wavelength-scanning method (WSM).

From a first analysis, the uncertainty budget seems lighter than the one established for the fixed-wavelength scheme. More specifically, fluctuations due to the source do not appear directly. The main reason is the fact that the measurement signal is directly the wavelength shift $\delta\lambda(t)$. However, this signal is not directly determined. It is a result of the analysis of the recorded intensity $I(t)$, using one method to determine the time-dependent value of the wavelength during a scan $\lambda_S(t)$, and a second method to retrieve the resonant wavelength $\lambda_(t)$, sampled once every period τ_{scan}.

Uncertainty on the signal $\delta\lambda(t)$

With several independent uncertainties related to the measurement of $\delta\lambda(t)$, a specific uncertainty budget can be established. To simplify the calculations, similarly to the measurand δM, the measured signal can be treated as a central value for the real variation of the resonant wavelength $\delta\lambda_{\text{real}}(t)$, solely due to the variations of the measurand. The combined uncertainty $\sigma(\delta\lambda)$ is defined in the relation:

$$\delta\lambda_{\text{real}}(t) = \delta\lambda(t) + \sigma(\delta\lambda) \tag{1.28}$$

In the evaluation of $\sigma(\delta\lambda)$, the first source of uncertainty is related to the determination of the time dependent wavelength of the source $\lambda_S(t)$, as

quantified by the deviation $\sigma(\lambda_S)$. The resulting uncertainty $\sigma[\delta\lambda](\lambda_S)$ is thus directly related to the uncertainty in the measurement of the quantity λ_S. The second source of uncertainty, as explained before, is in the determination of the resonant wavelength $\delta\lambda(t)$ from the measured intensity transmittance $T(\lambda_S)$.

The variation of the position of the resonance $\lambda(t)$ can be deduced from each scan by measuring the shift $\delta\lambda_{Tr}(t)$ of the position of the intersection between a fixed intensity threshold I_{Thr} and the recorded intensity transmittance $T(\lambda_S)$. In an ideal situation, the relation $\delta\lambda(t) = \delta\lambda_{Thr}(t)$ is verified. The specific uncertainty on the measurement of $\delta\lambda(t)$ introduced by this method is written $\sigma[\delta\lambda](\delta\lambda_{Thr})$. Whereas $\sigma[\delta\lambda](\lambda_S)$ is only dependent on the method used to measure the emission wavelength of the source, the analysis of $\sigma[\delta\lambda](\delta\lambda_{Thr})$ shows its dependence on the photodetection noise, quantified by $\sigma(I)$, and by the parameters of the microring. From Fig. 1.20, considering the ideal situation where the intensity slope $p_0 = (dI/d\lambda)(\lambda_{Thr})$ is constant, and where the resonance lateral shift is not accompanied by variations of the intensity levels, the uncertainty $\sigma[\delta\lambda](\delta\lambda_{Thr})$ can be evaluated from:

$$\sigma[\delta\lambda](\delta\lambda_{Thr}) = \sigma(\delta\lambda_{Thr}) = \frac{\sigma(I)}{p_0} \tag{1.29}$$

It is important to point out that $\sigma[\delta\lambda](\delta\lambda_{Thr})$ is not necessarily equal to $\sigma(\delta\lambda_{Thr})$. For instance, a variant of the method is to measure the positions of both intersections between the threshold and the resonance. In such case, the following relation applies: $\sigma[\delta\lambda](\delta\lambda_{Thr}) = \sqrt{2} \cdot \sigma(\delta\lambda_{Thr})$.

From this analysis, a comprehensive uncertainty budget can be established for the measurement of $\delta\lambda(t)$. Such a budget is presented in Tab. 1.4.

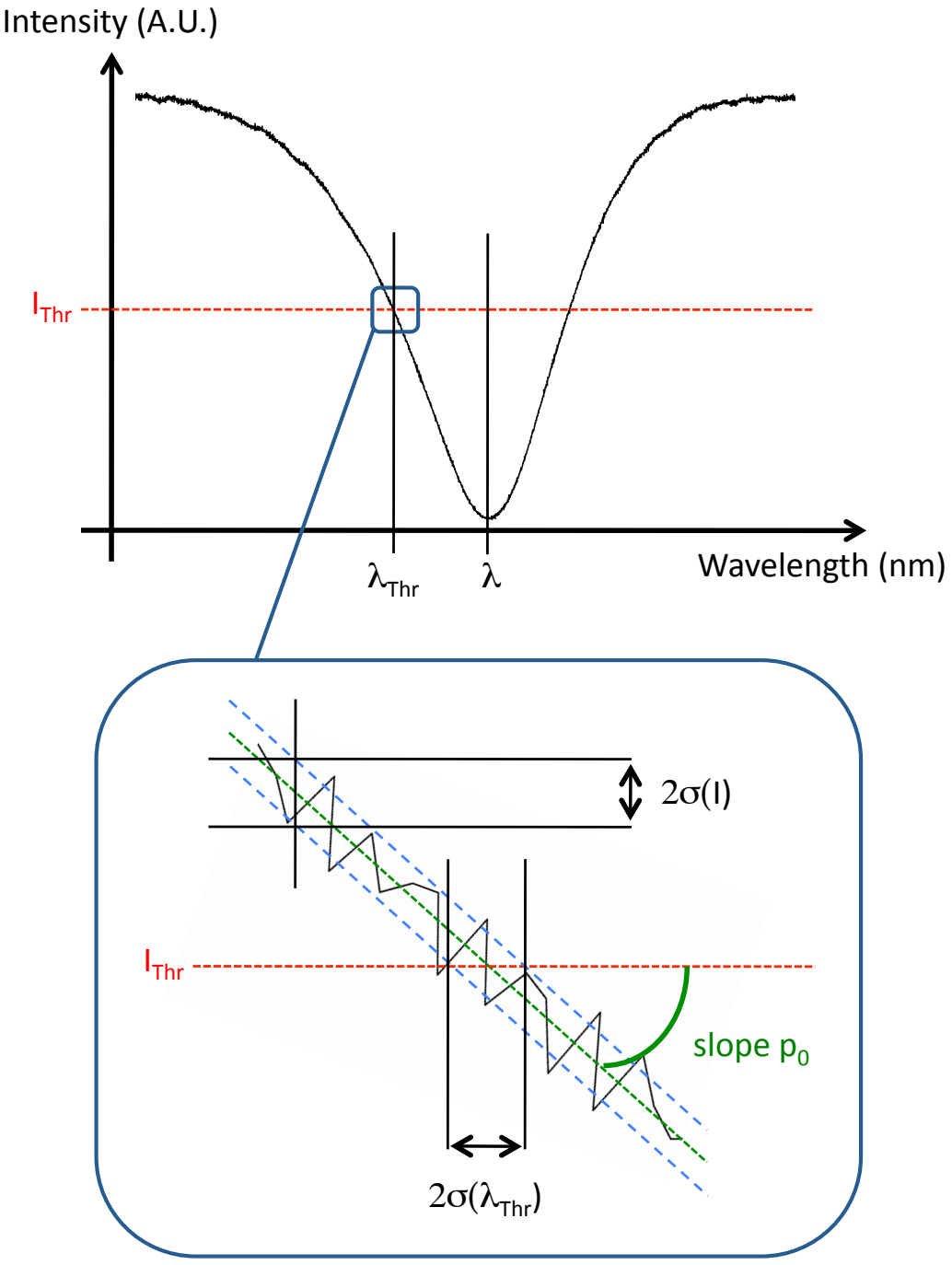

Figure 1.20: Illustration of a method based on an intensity threshold to measure the variations of the resonant wavelength λ. Relation between measurement uncertainties are displayed in the zoom window.

Source of uncertainty	**Parameter**	**Deviation**	**Uncertainty**
Method for the determination of the time-dependent emission wavelength	λ_S	$\sigma(\lambda_S)$	$\sigma[\delta\lambda](\lambda_S)$
Method for the determination of $\delta\lambda$	$\delta\lambda_{Thr}$	$\sigma(\delta\lambda_{Thr})$	$\sigma[\delta\lambda](\delta\lambda_{Thr})$
Variations of the input intensity	I_{IN}	$\sigma(I_{\text{IN}})$	$\sigma[\delta\lambda](I_{\text{IN}})$
Variations of the typical resonance width	FWHM	σ(FWHM)	$\sigma[\delta\lambda]$(FWHM)
Variations of the resonance contrast	C	$\sigma(C)$	$\sigma[\delta\lambda](C)$
Variations of the intensity slope	p_0	$\sigma(p_0)$	$\sigma[\delta\lambda](p_0)$

Table 1.4: Specific uncertainty budget for the measurement of $\delta\lambda$ in the WSM.

During measurement, the input intensity I_{IN} entering the microring can vary, either from variations of the intensity of the source I_S, or from variations of the coupling coefficient between the source and the microring, due to modifications of the alignment of optical elements, for instance. For this reason, I_{IN} cannot be measured. In consequence, shifts of the intersection between the intensity threshold and the resonance peak can be induced by variations of I_{IN}, thus biasing the measurement of $\delta\lambda(t)$. Another important bias introduced in this measurement technique is due to the variations of the typical width of the resonance, which can be quantified from an uncertainty on the FWHM. However, additional treatments of the signals produced by the previously described measurement techniques can greatly reduce these biases.

The first additional treatment is the normalization of the recorded output intensity $I(t)$. Indeed, the maximum I_{max} and minimum I_{min} of transmitted intensity, defining the contrast of the resonance, are both proportional to I_{IN}. Therefore, if a resonance peak is normalized, by simply dividing all intensities by I_{max} for instance, the data is no longer dependent (ideally) on I_{IN}. In such a case, the uncertainty on the input intensity I_{IN} is cancelled. Further uncertainty related to variations of intensity levels are related to the uncertainty on the contrast.

The second additional treatment was shortly discussed before, and consist in using both intersections between the threshold and the resonance. This treatment is primarily meant to reduce the uncertainty due to the variations of the typical width of the resonance. When associated to the normalization described in the paragraph above, it also reduces the uncertainty

related to contrast variations. With this second treatment, the uncertainty on the FWHM can be replaced by a lower uncertainty, this time on the asymmetry A_λ of the resonance peak, defined as:

$$A_\lambda = \text{abs}\left(|\lambda_{Thr}^{(L)} - \lambda| - |\lambda_{Thr}^{(R)} - \lambda|\right) \tag{1.30}$$

where $\lambda_{Thr}^{(L)}$ and $\lambda_{Thr}^{(R)}$ are the lower and higher wavelength values of the intersections between the threshold and the resonance, respectively.

A final treatment consist in using all data available in a recorded intensity, at each period τ_{scan}, to measure key parameters of the resonance, *ie* parameters that are listed in the uncertainty budget: the resonance contrast C, the intensity slope p_0 and the FWHM. From these measurements, uncertainties due to variations of the values of these parameters in between calibrations are replaced by uncertainties of the measurement methods of these parameters, which can be significantly lower.

Taking into account those additional treatments, a comprehensive uncertainty budget for the wavelength-scanning method (WSM) can be established (cf. Tab. 1.5).

Source of uncertainty	**Parameter**	**Deviation**	**Uncertainty**
Method for the determination of the time-dependent emission wavelength	λ_S	$\sigma(\lambda_S)$	$\sigma[M](\lambda_S)$
Method for the determination of $\delta\lambda$	$\delta\lambda_{Thr}$	$\sigma(\delta\lambda_{Thr})$	$\sigma[M](\delta\lambda_{Thr})$
Measurement of the contrast	C	$\sigma^\star(C)$	$\sigma^\star[M](C)$
Measurement of the typical resonance width	FWHM	$\sigma^\star$(FWHM)	$\sigma^\star[M]$(FWHM)
Measurement of the intensity slope	p_0	$\sigma^\star(p_0)$	$\sigma^\star[M](p_0)$
Asymmetry of the resonance	A_λ	$\sigma(A_\lambda)$	$\sigma[M](A_\lambda)$
Detection noise	$\delta\lambda$	$\sigma(\delta\lambda)$	$\sigma[M](\delta\lambda)$
Variations of linear slope K	K	$\sigma(K)$	$\sigma[M](K)$
Variations of linear intercept M_0	M_0	$\sigma(M_0)$	$\sigma[M](M_0)$
Variations of the effective index unrelated to the measurand	$N_{eff,0}$	$\sigma(N_{eff,0})$	$\sigma[M](N_{eff,0})$

Table 1.5: Comprehensive uncertainty budget for the wavelength-scanning method.

3.3.4 Comparison of the detection schemes

Comparison in resolution or LOD

The measurement uncertainty $\sigma(M)$ is directly related to the resolution, or LOD, of the measuring instrument before signal averaging. A brief comparison of the uncertainty budgets shows that both detection schemes share most of their independent sources of uncertainties. Consequently, knowing which detection scheme is the best suited to optimize the LOD is difficult. In addition, since some uncertainties are related to the performances of the optical laser sources and and that of additional devices (sensors) used in the detection scheme, a realistic comparison is all the more difficult. Nevertheless, it is important to point out that the role of the intensity slope p_0 of the microring on the uncertainty, hence the LOD, is similar for both detection schemes. Specifically, for a constant uncertainty due to photodection noise $\sigma(I)$, a higher value of the slope p_0 results in a lower effect of the photodection noise on the combined uncertainty provided by the measuring instrument (cf. Fig. 1.20). Consequently, a very large value of p_0 would cancel the effect of $\sigma(I)$. Then, the uncertainty of the instrument would be limited by all other uncertainty sources, that are not related to the value of p_0.

A partial conclusion on the importance of the slope p_0 is that it only matters if the uncertainty is dominantly limited by the photodetection noise $\sigma(I)$. However, considering a situation where all uncertainties have similar orders of magnitudes, a higher value of p_0 will reduce the uncertainty, but not very significantly.

In conclusion, it is only possible to state that working with the highest possible slope p_0 will improve, to some extent, the resolution or LOD of the measuring instrument, whatever the detection scheme. The relative gain due to a higher slope can only be quantified if all sources of uncertainties of the instrument are taken into account.

However, it is quite obvious that, for a given noise $\sigma(I)$, very low values of the slope p_0 will result in dramatic measurement uncertainty. The actual value of the p_0 depends on two factors: the intrinsic performance of the res-

onator, and the choice of the wavelength λ_0 where the slope is defined[14]. Consequently, for a given resonator, with a given intensity transmittance, the highest value of p_0 is achieved by selecting the wavelength λ_0 so that it corresponds to the inflection point of a resonance. In such a case, p_0 matches the maximal intensity slope (MIS) defined before. The value of the MIS can then be perceived as an intrinsic performance of a microresonator, susceptible to play an important role in the combined uncertainty of the measuring instrument. Therefore, the MIS should be used to compare microring resonators used for sensing applications, even though the relation between the effective index and the measurand is probably more important in the resulting LOD.

A safe conclusion on the use of fixed-wavelength method or wavelength-scanning method to optimize the LOD would be to state that both methods should lead to similar performances. However, their costs might be significantly different.

Comparison in span

The measurement span can be roughly defined for microresonator-based sensors as the range of measurand that can be measured from the instrument.

Using the fixed-wavelength method, the span is typically limited by the FWHM of the resonance peak used for measurement. This is due to the presence of a *dead band*, corresponding to a laser emission wavelength in between two resonances. In addition, on such a range, the nonlinearity of the transfer function cannot be neglected. This increases the influence of parameter variations on the combined uncertainty. The transfer function can only be linearised if the measurement span is limited to a fraction of the FWHM, where the intensity slope can be assumed to be constant.

On the other hand, the wavelength-scanning method offers a virtually infinite measurement span. This is due in part to the fact that the position of a resonance can be tracked whatever the shift, provided that the evolution of the resonant wavelength in time is continuous, or more generally with

[14] in the scheme to measure the resonant wavelength

discontinuities[15] inferior in amplitude to the FSR. In a real microresonator, however, the span is limited because the value of the MIS of a resonance peak can tend to zero when modifications of the effective index induced by the measurand become too great. Specifically, when the effective index is too low, additional propagation modes can be supported in the microring, thus modifying the intensity transmittance to a point where tracking one resonance becomes impossible. When the effective index is too high, close to that of the core of the waveguide constituting the microring, the optical loss in the ring is so great that modulation from the resonator cannot be detected at the output, corresponding to a identically zero resonance contrast.

Comparison in bandwidth or response time

For a measuring instrument integrating a microring resonator, the bandwidth can be defined as the range of frequencies, characterizing the time-dependence of the measurand, in which the instrument can accurately operate. The response time is closely related to the bandwidth, defined as the time necessary to the sensor to stabilize to a new output after a step excitation. The inverse of the response time (RT) is roughly the high cut-off frequency of the bandwidth of the instrument.

In IO-LFB instruments, the bandwidth or (RT) is dominantly limited by the detection scheme, and not by the dynamic properties of the transducers. In that regard, the wavelength-scan method (WSM) is more limited than the fixed-wavelength method (FWM). The reason for this is that a value of δI, in the FWM, can be acquired at very high sampling rates, only limited by the signal acquisition board. Coupled to a fast photodetector, the minimal response time can be down to 1 μs and below corresponding to bandwidths over 1 MHz.

In comparison, with the WSM, the response time RT is limited by the period τ_{scan}, itself limited by the scanning speed V_λ and the availability of the tunable source to perform a wavelength scan. The lowest achievable response time is, in consequence, very dependent on the tunable laser source.

[15] variations occurring on time scales shorter than the response time

3.4 State-of-the-art

Microring resonators have been under intensive study from the 1970s to date, first and foremost as integrated optical filters for telecommunications. Over the last decade, microring resonators raised much interest as sensors for measuring instruments, specifically for label-free biosensing (cf. §2.3.6). Because of this continuous interest, many devices have been proposed over the years. In sensing applications, the design of such devices can be adjusted to work with a specific detection scheme. This results in configurations integrating all aspects of the instrument, from the design of the microresonator to the instrumentation. In the following, these configurations are classified by coupling configuration, materials, and fabrication technique.

3.4.1 Coupling configuration

In a microring resonator, the close contact between bus waveguide and ring waveguide is responsible for the evanescent coupling of light between the two waveguides (cf. Chap 2). This close contact, or proximity, can be achieved either laterally, or by vertical superposition. These configurations are lateral and vertical coupling, respectively (cf. Fig. 1.21).

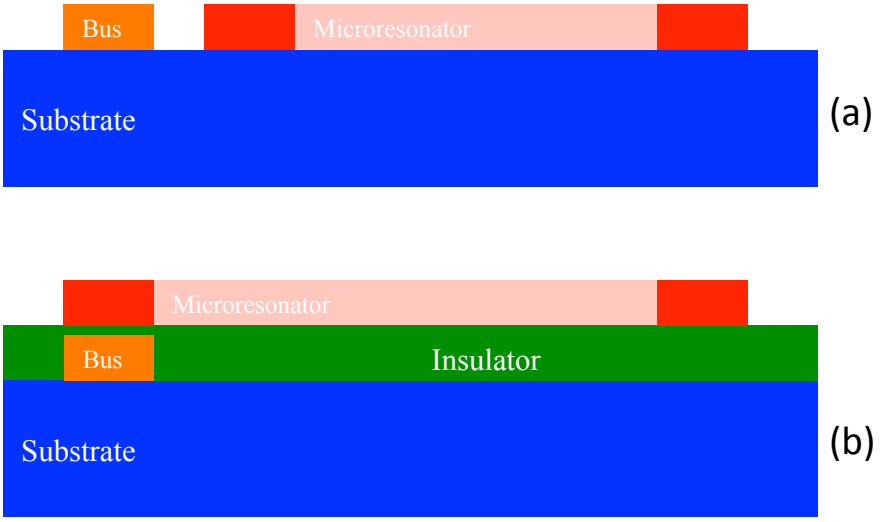

Figure 1.21: Vertical and lateral configurations for evanescent coupling.

In a lateral coupling configuration, both bus and bent waveguides are

on the same plane, *ie* built on the same substrate. The minimal distance between the two waveguides is the gap separation, and is usually in the hundreds of *nm*. In the vertical configuration, the straight waveguide is build on a substrate, whereas the bent waveguide, hence the resonator, is build on a different plane, on a material referred to as *insulator* because its low refractive index prevents light propagating in the resonator to travel to the substrate. In this configuration, the gap separation is the minimal vertical distance between straight and bent waveguides.

The coupling configuration, although it is not obvious, is one of the key aspect in the design of microring resonators since it often determines the class of materials to use, and the fabrication method. More importantly, the coupling configuration has large repercussions on the performances of label-free biosensing instrument integrating microring resonators [18]. In that regard, the lateral coupling configuration has two principal issues:

1. Achieving a sub-wavelength gap separation between the waveguides through fabrication is a lot more challenging in lateral than in vertical configuration (cf. Chap3). Consequently, the fabrication of laterally-coupled microresonators requires more expensive equipments, sometimes using techniques that are not compatible with parallel fabrication of the devices.

2. The second issue is related to homogeneous and surface sensing. When the analyte is introduced in the cladding of the laterally-coupled waveguides, it is free to diffuse and/or bind in the coupling region, thus modifying the cross-coupling coefficients (cf. Chap.2), describing the amount of light that is cross-coupled from one waveguide to another. The problem is that the lineshape of the resonances of the resonator are strongly dependent on these coefficients. Hence, during sensing, the measurement signal can be severely biased by the modification of the index distribution in the coupling region. In a vertical coupling configuration, since it is constituted of insulator, the coupling region has a well defined refractive index, which cannot be modified by the analyte. In consequence, measurement uncertainties related to the resonator parameters are expected to be much lower with a vertical coupling configuration.

3.4.2 Materials

Lately, Silicon-On-Insulator (SOI) technology has been dominantly used for the fabrication of microring resonators. In such devices, bus and bent waveguides have typically rectangular sections, with silicon as core material and silica as substrate material.

The main advantage of SOI technology for building microring resonators is in the large refractive index contrast it offers. This results in the possibility to build very compact[16] devices while maintaining good optical characteristics. However, the high refractive index of the silicon waveguide core is at the origin of large reflection coefficients at the input and output interfaces of the straight waveguide. This results in a relatively large modulation of the intensity transmittance from parasitic interferences, and can constitute an important source of uncertainty.

SOI technology is also limited in the sense that the vertical coupling configuration, presenting numerous advantages in evanescent-wave sensing applications, has, to the best of our knowledge, yet to be achieved with SOI technology. Consequently, it seems that the only coupling configuration compatible with SOI technology is lateral coupling. Therefore, in order to achieve gap separations in the hundreds of nm, the lateral resolution of the lithography technique employed to pattern the microresonators has to be in the tens of nm. This is to achieve an accurate control of the gap separation, and requires the use of expensive lithography techniques, not necessarily compatible with mass production of microring resonators.

In comparison, polymer materials, recently proposed for the fabrication of laterally-coupled microring resonators [19], are well compatible with the fabrication of vertically-coupled devices. As an important property, polymer-based vertically-coupled microring resonators can be fabricated using only near UV lithographies and plasma etching (cf. Chap.3). This makes the use of polymer materials particularly advantageous in terms of large-scale fabrication costs, particularly if the polymers are photoresins, which can be directly patterned.

[16] with radii inferior to 10 μm

Because polymer materials have much lower refractive indexes than silicon, the refractive index contrast is much more limited with polymer technology than with SOI. A direct consequence is a necessary larger scale of microring resonators with polymer technology, limiting the density of microresonators on a single chip. A good compensation of this drawback is the fact that the index of the polymer material constituting the core of the waveguide can be very close to that of silica, thus making polymer microring resonators very well-suited for integration with optical fibers. This is not only because insertion loss between fibre optics and straight waveguide is potentially very small, but also because of the very small reflection coefficients obtained at the input and output interfaces of the waveguide, greatly reducing effects of parasitic interferences.

3.5 Microfluidic integration

One of the key aspects of all label-free biosensing instruments (cite arlett) is the microfluidic integration, responsible for the fast introduction of the analyte above the surface of the sensor. The liquid flow in microfluidic channels is characterized by a very high Reynolds number, resulting in a laminar flow. This achieves a good homogeneity of the flow rate near the surface of the microresonator. In addition, the very small flow rates, also characteristic of microfluidic channels, reduces the total amount of analyte required to perform a measurement.

Some geometries of microresonators, microspheres or microtoroids for instance, are not particularly well suited for optical integration. As a result, in proposed sensors based on such optical cavities, the bus waveguide of the microring resonator is replaced by a tapered optical fibre, free-standing near the microresonator in order to achieve evanescent coupling. This configuration makes microfluidics integration very difficult, mainly because of the potential variations of the gap separation under microfluidic flow, also because such structure can easily trap tiny air bubbles potentially present in the microfluidic channel. In comparison, the integration with microfluidics of planar microresonators, and specifically microring resonators, as integrated photonic devices, is relatively easy and robust, particularly in a vertical coupling configuration.

In IO-LFB instruments based on microring resonators, an elementary

cell, or *optofluidic* cell is formed by the combination of a microring resonator with a microfluidic channel, as presented in Fig. 6.4.

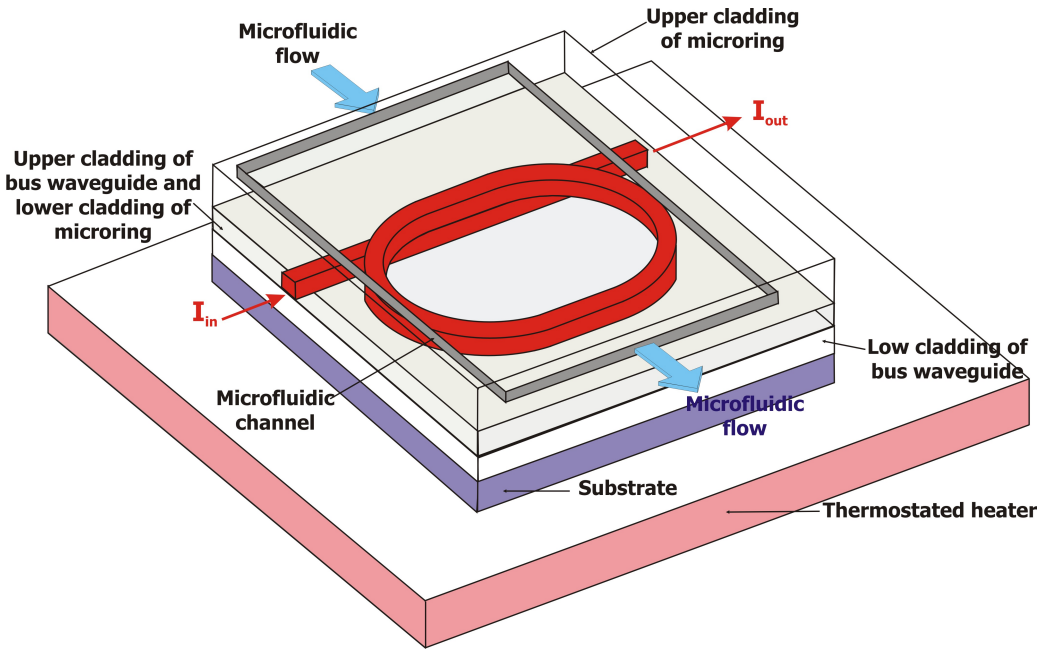

Figure 1.22: Optofluidic cell combining a microring resonator to a microfluidic channel.

In the rest of the dissertation, chapters are dedicated to specific elements of the optofludic cell: models, fabrication techniques and characterization of the microring resonators; then, the instrumentation of the sensor including, amongst other aspects, microfluidics integration and the temperature regulation schemes. In final chapters, the focus is in the performances of the sensor based on the presented optofluidic cell.

Conclusion

In this chapter, elements of sensor theory that apply to optofluidic and label-free sensors are first introduced. The aim of such an introduction was primarily to define clearly the terms relating to sensing, used in the rest of the dissertation. To that regard, key concepts such as the measurement uncertainty and the limit of detection (LOD) were presented. It was also outlined that since the performances of a measuring instrument depend on the sensor and its instrumentation, the optimization of optofluidic label-free sensors requires a study of both aspects.

Then, optical evanescent-wave sensors were reviewed, and compared to non-optical devices that are also used in label-free biosensing. From an analysis of what seems to be the main limitations of such sensors nowadays, a scheme to compare performances was proposed based on the limits of detection and the response times of the instruments. This led to the introduction of microring resonators as transducers for a new generation of high-performance label-free biosensing instruments.

The final section of the chapter was dedicated to the technological aspects related to microring resonators: configurations, materials, fabrication techniques, detection schemes, and their influences on their performances as transducers. In that respect, a thorough study of what limit the LOD for such sensors was undertaken. More importantly, the fundamental design directions adopted for the rest of the dissertation were presented and justified, specifically the use of polymer materials combined to vertical coupling configuration for the microresonator.

Chapter 2

Models and simulations of passive microring resonators

Introduction

One of the keys to achieve an optimal design for a device is a good understanding of the targeted applications, but more prominently, a very good understanding on how the device operates. In the scope of the dissertation, for all the applications described in Chap.1, the most important element is the microring resonator. A large amount of time has been devoted to find efficient ways to accurately describe its behavior.

In this chapter, models of passive microring resonators and simulation methods are presented. First, a review of all effects liable to occur in those optical cavities is presented. Then, the starting point of an analytical model, providing expressions for the intensity transmittance and its characteristics as functions of internal parameters, is described. Formulations for internal parameters are, later, the *a posteriori* result of a specific study, and justify important additions to the analytical model. Finally, the input of numerical simulations to the study of microring resonator is thoroughly discussed.

1 Effects occurring in microring resonators

Before the construction of analytical or numerical models of microresonators, the initial task was to gather information on all effects liable to occur in such photonic devices. Because microring resonators are guided optics elements, two categories of effects need to be taken into account:

effects strictly related to the selected optical materials, and those strictly related to the guiding of light. In addition, environmental physical quantities, namely pressure and temperature, have relatively large effects on both optical material properties and waveguide geometry, and thus require special handling.

1.1 Optical material-related effects

1.1.1 Short review of proposed materials for microresonators

Many materials, displaying various optical properties, have been proposed for the fabrication of microring resonators. From these materials, a large amount of core/substrate configurations where successfully demonstrated: silicon/silicon nitride [20], InP/InGaAsP [21], silica/pentatantalum dioxyde (Ta_2O_5)[22].

Recently, the more prominent configuration has been silicon/silica, a technology usually referred to as Silicon On Insulator (SOI). This enthusiasm [23] can be explained by the large index contrast offered by this technique, resulting in the achievement of large Q factors. However, this technology has numerous flaws in terms of fabrication cost, patterning limitations, and also in its compatibility to fiber optics.

Such limitations motivated research on polymer microring resonators [19]. Since then, numerous experiments have demonstrated that, despite a lower refractive index contrast compared to SOI microresonators, performances of polymer-based devices could be superior to silicon-based device [24]. In addition, polymer materials offer numerous advantages in terms of ease of fabrication, cost and versatility. For further information, [25] is a thorough review of polymer materials and their optical properties.

1.1.2 Material Dispersion

At an elementary level, the dispersion of an optical medium characterizes the wavelength-dependence of phase and group velocities of an optical wave propagating through the bulk material. The origin of material dispersion lies in the medium susceptibility, and is caused by the fact that the response of the medium to optical excitation does not decay instantaneously [26]. This directly results in a wavelength-dependence of the bulk

refractive indices of optical materials, usually quantified by Abbe number [27]. In many optical media, material dispersion is further described by coefficients applying to Cauchy or Sellmeier empirical equations.

1.1.3 Material anisotropy

Material anisotropy describes the dependence of the optical properties of a medium on the polarization state of the propagating electromagnetic wave. In amorphous or quasi-amorphous optical media, material anisotropy can be neglected as compared to the anisotropy induced by material strain or deformation [28]. It has also been widely reported that polymer materials display specific anisotropic properties when deposited as thin films [29].

1.1.4 Material absorption or attenuation

Another important effect to consider is material absorption, or attenuation, of electromagnetic waves in an optical medium. Absorption describes the loss of electromagnetic energy of the wave accompanying the propagation. This effect is in part related to the imaginary part of the medium susceptibility, whereas dispersion comes from the real part. This contribution to absorption is strongly dependent on the frequency (or wavelength) of optical wave propagating in the medium [26]. Further information on optical attenuation in polymer materials can be found in [30].

In many situations, specifically in passive photonic devices, material absorption has to be minimized. As consequence, if a specific material has to be used, the range of optical wavelengths is usually chosen in order to minimize absorption. Alternatively, a material can be selected because of its low absorption in a specific wavelength range required for operation.

1.1.5 Local defects

The presence of local physico-chemical defects in the bulk of a material is usually the source of additional absorption. For instance, the purity of optical materials is generally a basic limitation for ultra high-Q microresonators [31]. In silicon and other materials, absorption can be increased and controlled by ion implantation [32]. As compared to material absorption which is mostly intrensic to the material, defects-induced optical attenuation is mainly related to material processing. The limitation of this

specific attenuation motivates the selection of materials minimizing the appearance of new defects after patterning, and also motivates the optimization of fabrication processes.

1.1.6 Non-linear effects

Various optical non-linear effects have been reported in optical microresonators. In most cases, a strong non-linear behavior is obtained by proper selection of the materials. For instance, some polymers matrices incorporating selected molecules can, after a polling step, exhibit strong electro-optic coefficients. Such materials are used to achieve compact electro-optic modulators [33]. However, materials used to build microring resonators for sensing applications have, in their natural form, low non-linear coefficients, making most non-linear manifestations negligible. However, thermal non-linear effects [34] may have interesting properties when it comes to microresonator characterization [35] and label-free biosensing [36].

1.2 Effects related to the guiding of light

1.2.1 Evanescent wave

The propagation of optical waves in waveguides can be seen as a result of the total internal reflection (TIR) at core/cladding interfaces in optical fibers, and at both core/cladding and core/substrate interfaces in planar waveguides. During propagation, as seen in Chapt.1, each TIR is accompanied by the creation of an evanescent wave in the cladding or substrate, with an amplitude exponentially decaying from the interface [27, p. 125].

1.2.2 Effective index

In waveguides, optical waves can effectively propagate if they are interfering constructively in the waveguide core, which only occurs when they are reflected at specific angles corresponding to distinct transverse propagation modes [10, p. 5]. Further study, partly described in Chap.1, show that in planar waveguides, phase and group velocities of the guided modes depend on the refractive indices of the core, of the cladding and of the substrate materials, on the geometry of the waveguide and on wavelength. Thus, the notion of phase effective index N_{eff}, *i.e.* the ratio between the

speed of light in vacuum and the phase velocity of a mode propagating in the waveguide, integrates all waveguide parameters.

1.2.3 Waveguide dispersion

The propagation time τ_G of a given optical wave through a waveguide of length L is given by $\tau_G = L/v_G$ where v_G is the group velocity expressed as:

$$v_G = \frac{c}{N_G} = \frac{c}{\left[N_{eff} - \lambda \frac{dN_{eff}}{d\lambda}\right]} \tag{2.1}$$

In reference to pulse broadening in fiber optics, waveguide dispersion describes the variability of the propagation time τ_G amongst waves susceptible to propagate in the waveguide, and four dispersion mechanisms are clearly identified [10, p. 89]:

- **Multimode dispersion** is due to the difference of effective indices between the various transverse modes supported by the waveguide. This dispersion mechanism result in the fact that the response of a microresonator strongly varies from one transverse mode to another (cf. Chap.3), thus complicating the analysis of intensity transmittance in optical cavities supporting several transverse modes. This usually motivates single transverse mode operation of microring resonators for sensing applications [19].

- **Polarization mode dispersion**, contrary to multimode dispersion, also occurs (in a general sense) in single transverse mode operation. It is due to the difference of effective indices between orthogonally polarized propagation modes. The corresponding waveguide birefringence, *i.e.* the difference between the phase effect indices of orthogonal modes, is a direct result of the dependence of continuity equations at waveguide interfaces on the orientations of the major electromagnetic field components associated to each mode. It also integrates the material anisotropies of the waveguide materials. Waveguide birefringence may be modulated and/or cancelled by modification of the waveguide geometry [37].

- **Material dispersion** was already discussed in material-related effects. For a planar waveguide, material dispersions of the core, the cladding and the substrate contribute to a global effect of material

dispersion, with specific weights depending on the guided mode. It must be pointed out that material dispersion, similarly to waveguide dispersion and unlike multimode and polarization mode dispersion, still occur when the waveguide only support one guided mode.

- **Waveguide dispersion** comes from the explicit wavelength dependency of the dispersion equations the guided modes are solutions of (cf. [10, p. 16, 29]), hence applying to all modes, and is unrelated to the material dispersion. However, the variations of the effective index of a guided mode as function of the wavelength combine effects of both material and wavelength dispersions.

1.2.4 Hybrid modes

Amongst planar optical waveguides, only slab waveguides support independent electromagnetic modes denoted as TE and TM. TE modes have a single non-zero electric field component in a direction defined as the intersection between the interface and transverse plane, whereas TM modes have a single non-zero magnetic field component along the same direction. TE and TM modes are independent in the sense that they do not share common electric or magnetic field components.

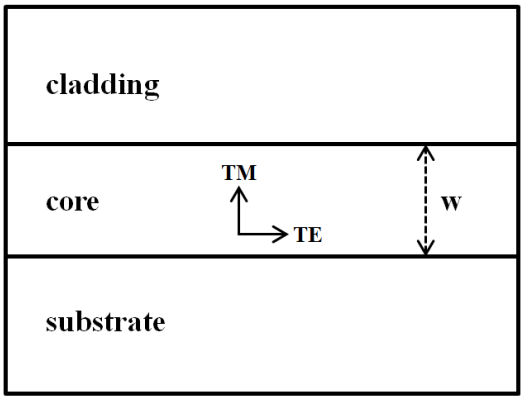

Figure 2.1: Schematic drawing of an asymmetrical slab waveguide. Directions of the major directions of electric fields corresponding to TE and TM modes are indicated.

In comparison, TE and TM guided modes in two-dimensional transverse guiding structure - rectangular waveguides for instance - are not strictly independent. As consequence, resulting hybrid modes are usually

referred to as quasi-TE and quasi-TM modes, or E^u modes where u is the direction of the dominant component of the electric field associated to the mode [10, p. 29].

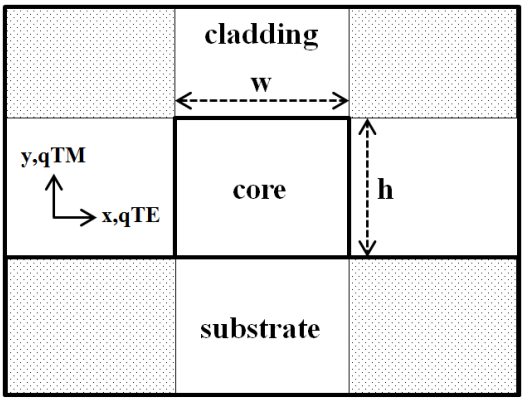

Figure 2.2: Schematic drawing of a rectangular waveguide. Directions of the major directions of electric fields corresponding to quasi-TE and quasi-TM modes are indicated.

A consequence of this mode hybridization is a non-zero polarization conversion accompanying the propagation in the waveguide. This effect is significantly enhanced in bent waveguides [38], and thus may have an important role in the behavior of microring resonators. In addition, non-ideal planar waveguide fabrication always result in slanted vertical sidewalls, which also contributes to further polarization conversion in the fabricated waveguide [39].

1.2.5 Bending losses

Guided modes in bent waveguides are more accurately referred to as weak loss modes. Indeed, the total internal reflection at work in a straight waveguides does not strictly apply anymore on the internal sidewall of the bent waveguide because of the smaller incidence. Such modes can be described by complex effective indices, where the real part relates to the propagation constant, and the imaginary part to bending losses. In microring resonators, as it will be further described later in the chapter, bending losses have important consequences on optical performances, and reduction of such losses is one of the keys of an efficient design. For such purpose, numerous schemes to understand, model, calculate and reduce bending losses can be used [40, 41, 42, 43, 44, 45, 46].

1.3 Influence of environmental physical quantities

1.3.1 Pressure effects

Effects of pressure applied to a polymer waveguide on a guided mode effective index are described in [47]. The two major contributions are due to the waveguide deformation and materials elasto-optic properties, respectively. Waveguide deformation due to applied pressure or stress solely depends on the mechanical properties of the materials, specifically the Young's modulus and Poisson's ratio. Elasto-optic properties of optical materials are quantified by photoelastic constants describing the deformation of the materials' index ellipsoid induced by stress. Photoelastic coefficients thus depend on the mechanical properties, the refractive index and Pockels coefficients [10, p. 311].

1.3.2 Temperature effects

Similarly to pressure, variations of temperature modify the effective index through the waveguide geometry, and through the temperature-dependence of the refractive indices of optical materials. The former effect is quantified by thermal expansion coefficients of the materials, and the latter is described by thermo-optic coefficients[48]. Further study of temperature effects in waveguides and microring resonators will be presented in Chap.y.

2 Analytical model: starting point

2.1 Elements of the model

2.1.1 Description

A microring closely coupled to a single straight waveguide is considered. This configuration will be referred to as a single-bus microresonator. We can describe the microring resonator as a directional coupler where an output is optically connected to an input. Such a photonic structure can be analyzed and modeled using coupled-mode theory (CMT) and basic electromagnetic theory to relate the transmitted optical amplitude E_4 to the incident amplitude E_1 via E_3 and E_2, the amplitudes inside the ring after and before the coupling region (Fig. 2.3). Manipulation of the fundamental relations coupling these scalar fields will provide expressions of the intensity transmittance and its characteristics as functions of internal parameters.

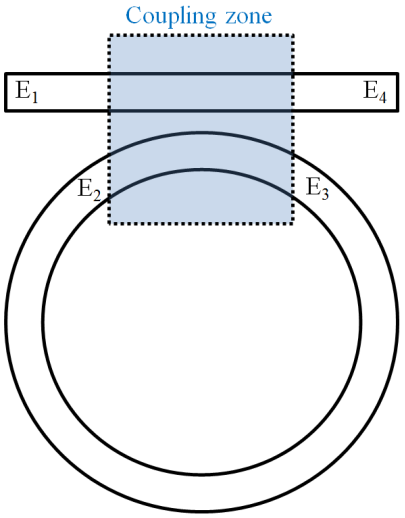

Figure 2.3: Schematic drawing of a single-bus microring resonator

2.1.2 Assumptions and hypotheses

- The waveguides only support the fundamental mode.

- The guided modes, propagating in the bus waveguide and the ring resonator, are described by a single component of their corresponding electromagnetic field. As consequence, all polarization-related effects are neglected. Furthermore, both modes are assumed to propagate with the same propagation constant β.

- The directional coupler is assumed to be symmetrical which means that cross-coupling coefficients κ between ports (1) and (3), and between (2) and (4) are assumed to be identical. So are the internal transmission coefficients τ between (1) and (4), and between (2) and (3). Also, it is assumed that all optical paths in the coupling region, cross paths and direct paths, are equal.

2.2 Intensity transmittance

2.2.1 Coupled field equations

The directional coupler is treated as a lossless device (Fig. 2.4) to which is added a lumped loss factor γ referred to as the intensity-insertion-loss

coefficient [49]. This is described by:

$$\begin{cases} \gamma = 1 - \dfrac{|E_3|^2 + |E_4|^2}{|E_1|^2 + |E_2|^2} \\ 1 = \kappa^2 + \tau^2 \end{cases} \tag{2.2}$$

where κ and τ are the amplitude cross-coupling coefficient and the internal amplitude transmission coefficient, respectively. The second equation denotes a virtual conservation of the electromagnetic energy in the coupler. In fact, as can be seen in Eq.(2.3), only $\kappa^\star = (1-\gamma)^{1/2}\kappa$ and $\tau^\star = (1-\gamma)^{1/2}\tau$ have actual physical meaning.

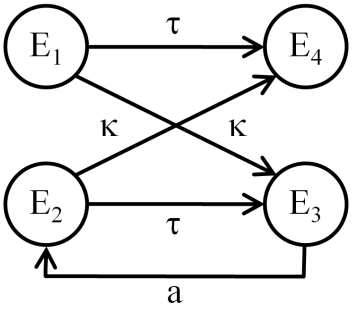

Figure 2.4: Schematic view of amplitude cross-coupling, transmission and loss coefficients

The stationary input-output relations of the optical ring resonator are expressed by:

$$\begin{cases} E_3 = (1-\gamma)^{1/2} \left[j\kappa E_1 + \tau E_2 \right] e^{j\Phi_c} \\ E_4 = (1-\gamma)^{1/2} \left[\tau E_1 + j\kappa E_2 \right] e^{j\Phi_c} \end{cases} \tag{2.3}$$

where Φ_c is the phase accumulated in the coupling region. Cross-coupling is accompanied by a $\pi/2$ phase-shift of the optical wave, hence the factor j ($j^2 = -1$) in Eq.(2.3). These relations are coupled by a supplementary equation related to the feedback loop:

$$E_2 = E_3 \exp\left[(-\rho + j\beta)\, L_{mc} \right] \tag{2.4}$$

where ρ is the in-loop amplitude attenuation coefficient, β the propagation constant of the guided mode and L_{mc} is mean circumference of the ring excluding the coupling region. In the following, we will use parameters $a = \sqrt{1-\gamma}e^{-\rho L_{mc}}$, referred to as the total amplitude loss factor, and $\Phi_{mc} = \beta L_{mc}$ the phase accumulated over L_{mc}.

2.2.2 Transmittance

From (2.3) and (2.4) we deduce the amplitude transmittance of the optical ring resonator:

$$t = \frac{E_4}{E_1} = (1-\gamma)^{1/2} \frac{\tau - a e^{j\Phi}}{1 - a\tau e^{j\Phi}} e^{j\Phi_c} \tag{2.5}$$

where $\Phi = \Phi_c + \Phi_{mc} = \beta L$ is the single-trip phase delay inside the resonator. The intensity transmittance T of the ring resonator can then be written as

$$T(\Phi) = |\frac{E_4}{E_1}|^2 = (1-\gamma)\left[1 - \frac{\left(1-a^2\right)\left(1-\tau^2\right)}{\left(1-a\tau\right)^2 + 4a\tau\sin^2\left(\Phi/2\right)}\right] \tag{2.6}$$

This transmittance can be rewritten in analogy to that of a Fabry-Pérot (FP) etalon:

$$\begin{cases} T(\Phi) = (1-\gamma)\left[1 - T_{\text{FP}}(\Phi)\right] = (1-\gamma)\left[1 - \dfrac{A_0}{1 + F\sin^2\left(\Phi/2\right)}\right] \\ A_0 = \dfrac{\left(1-a^2\right)\left(1-\tau^2\right)}{\left(1-a\tau\right)^2} \\ F = \dfrac{4a\tau}{\left(1-a\tau\right)^2} \end{cases} \tag{2.7}$$

where F appears, in analogy to the FP etalon, as the coefficient of finesse of the resonator. In addition, the factor $a\tau$ is analogous to the intensity reflection coefficient R of a FP etalon. As shown in Fig. 2.5, the intensity transmittance is 2π-periodical and presents resonance peaks, i.e. minima of transmittance, when the single-trip phase delay is a multiple of 2π. The resonances get narrower when the coefficient of finesse F increases.

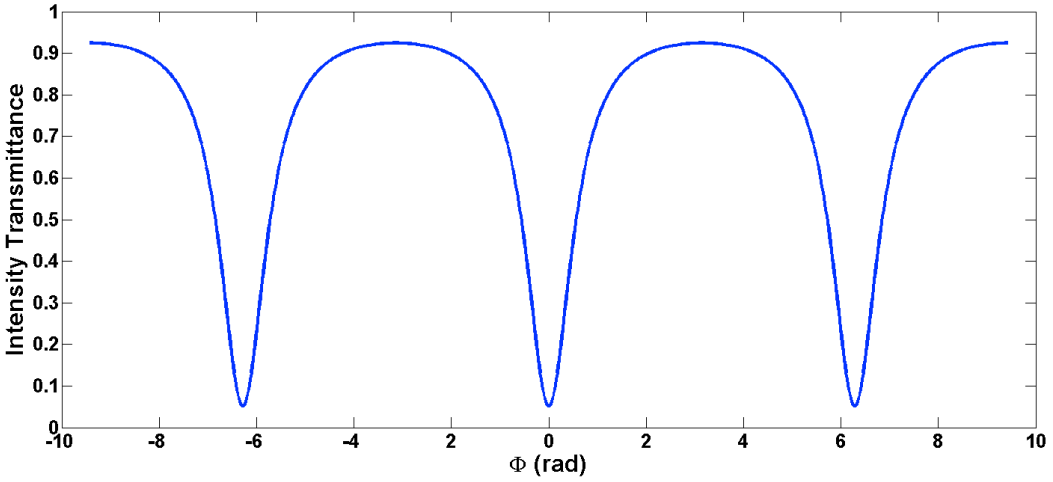

Figure 2.5: Intensity transmittance vs the single trip phase delay Φ for γ = 0, a = 0.8 and τ = 0.7 corresponding to $A_0 = 0.948$ and F = 11.6 approximately

It is also clear from Eq.(2.7) that the lineshape of the resonances is mainly determined by a and τ. This is illustrated in Fig. 2.6. Finally, it is noticeable from Eq.(2.7) that $T(a,\tau) = T(\tau,a)$. This reveals the impossibility to determine specific values of a and τ from a fit of the intensity transmittance. This point will be further discussed in Chap.3.

2.3 Optical characteristics

2.3.1 Resonance contrast and critical coupling

Maximal and minimal transmittances are given, with m as a random integer, by:

$$\begin{cases} T_{max} = T(\Phi = 2m\pi) = (1-\gamma)\dfrac{(a+\tau)^2}{(1+a\tau)^2} \\ T_{min} = T(\Phi = 2m\pi + \pi) = (1-\gamma)\dfrac{(a-\tau)^2}{(1-a\tau)^2} \end{cases} \tag{2.8}$$

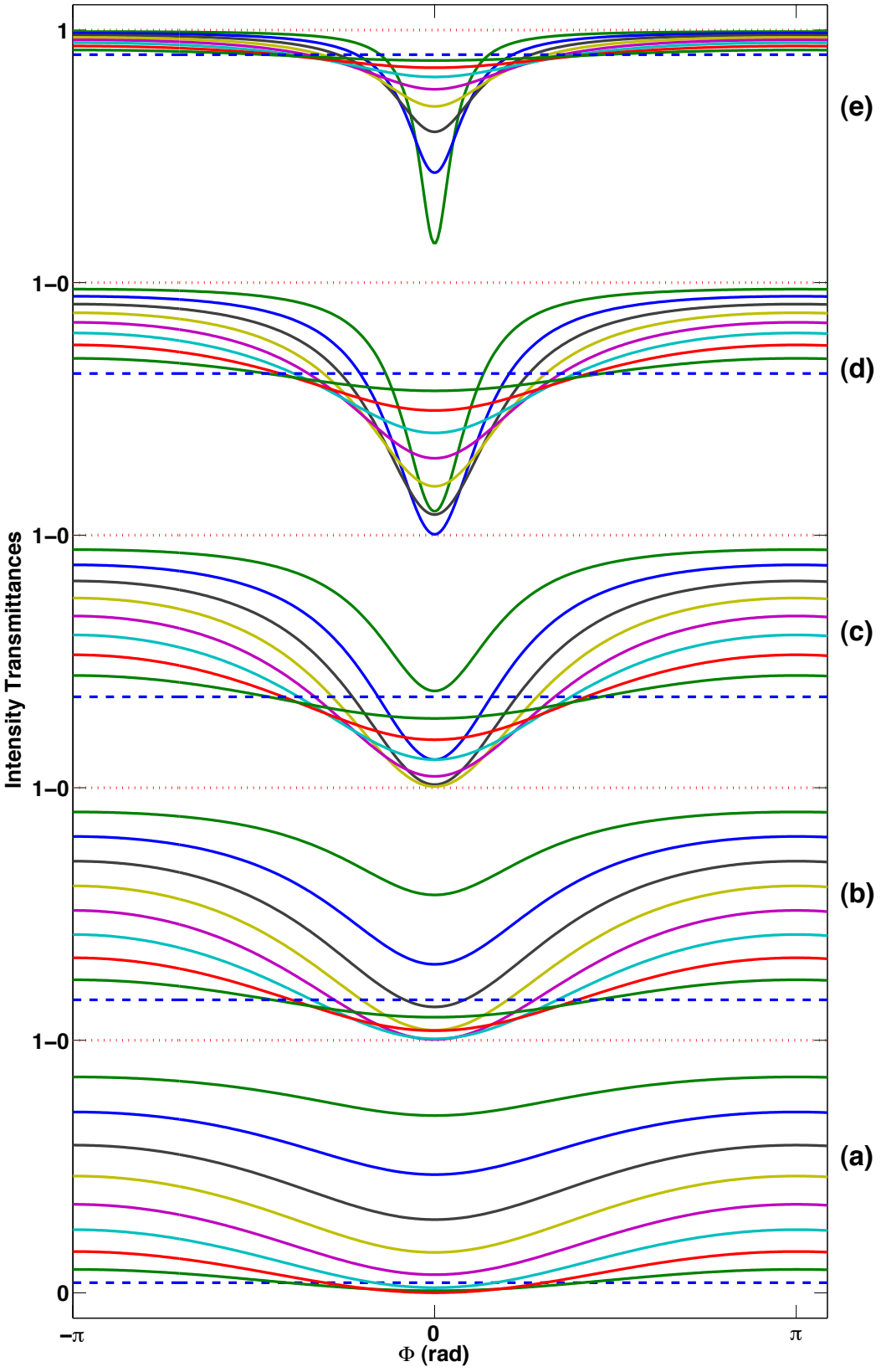

Figure 2.6: Intensity transmittances vs the single trip phase delay Φ for different sets of parameters a and τ. For each set of plots, $a\tau$ varies between 0 (dashed blue) and a (dotted red) where (a) $a = 0.2$, (b) $a = 0.4$, (c) $a = 0.6$, (d) $a = 0.8$ and (e) $a = 0.95$. Curves with larger values of $a\tau$ have larger values at $\Phi = \pm\pi$

Maximal transmission is achieved when all waves in port (4), the output port, are in-phase and thus interfere constructively, whereas the minimal transmission is achieved when waves are in phase opposition, *i.e.* with phase-shifts of π *modulo* 2π, and thus interfere destructively. The resonance contrast, describing the depth of a resonance, is defined as:

$$C = \frac{T_{max} - T_{min}}{T_{max} + T_{min}} \tag{2.9}$$

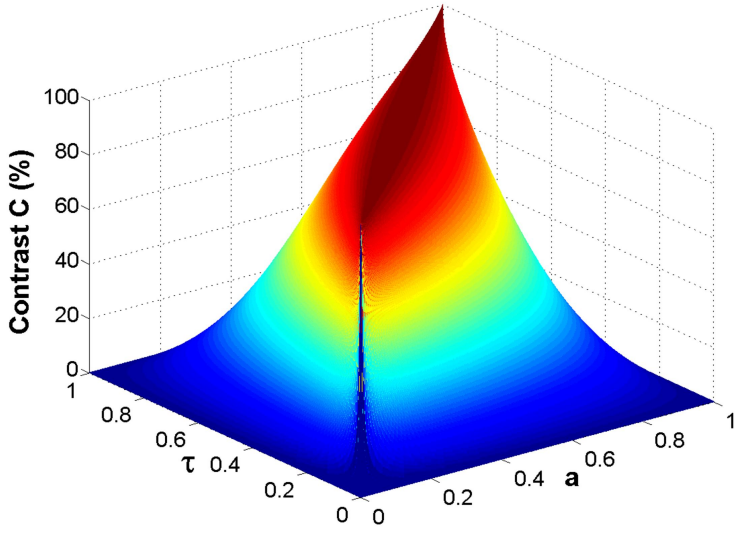

Figure 2.7: Contrast vs the cross-coupling coefficient τ and the total loss factor a with $\gamma = 0$

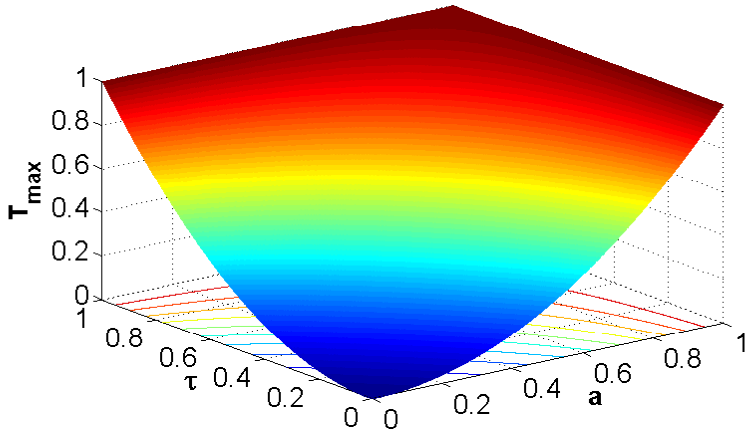

Figure 2.8: Maximum of transmission T_{max} vs the cross-coupling coefficient τ and the total loss factor a with $\gamma = 0$

It is clear from Eq.(2.9) and Fig. 4.7 that the condition $a = \tau$ needs to be satisfied in order to maximize the contrast, which corresponds to $T_{min} = 0$. This condition is known as the critical coupling condition. It is achieved when the total intensity loss inside the resonator is balanced by the cross-coupled intensity. As a consequence, all interfering waves in the output port have the same amplitude, hence the maximal contrast. When $a = \tau = 1$, $T_{min} = 0$ and $T_{max} = 1$ which gives the best configuration for the observation of the resonances.

2.3.2 Free Spectral Range

A resonance peak of the ring resonator corresponds to $T = T_{min}$ and is thus obtained when

$$\Phi = \beta L = \frac{2\pi}{\lambda} N_{eff} L = 2m\pi \tag{2.10}$$

We now focus on the spacing between two resonance peaks of the ring resonator. We write the wavenumber corresponding to $\Phi = 2m\pi$ as k and that corresponding to $\Phi = 2(m+1)\pi$ as $(k + \Delta k)$. Since m is very large (the optical path is at the very least hundred times bigger than the wavelength), the deviation Δk of the wavenumber is small compared to k. As a consequence, the deviation in β caused by the slight variation of the wavenumber is obtained from Eq.(2.10) as

$$\beta(k + \Delta k) - \beta(k) = \frac{2\pi}{L} \tag{2.11}$$

This relation can be rewritten, taking into account $|\Delta k| \ll k$ as

$$\frac{d\beta}{dk} \Delta k = \frac{2\pi}{L} \tag{2.12}$$

Substituting $\beta = kN_{eff}$, where N_{eff} is the effective index of the guided mode propagating in the structure, into Eq.(2.12), we obtain

$$\frac{d\beta}{dk} = N_{eff} + k\frac{dN_{eff}}{dk} = N_{eff} - \lambda\frac{dN_{eff}}{d\lambda} = N_G \tag{2.13}$$

where N_G is the effective group index of the guided mode, not to be confused with group index of the bulk material constituting the waveguide. Since the frequency shift Δf and the wavelength shift $\Delta\lambda$ are related to the variation of the wavenumber Δk from $\Delta f = (c/2\pi)\Delta k$ and $\Delta\lambda =$

$-(\lambda^2/2\pi)\Delta k$, resonance spacings in terms of the frequency and wavelength are given by

$$\Delta f = \frac{c}{N_G L} \tag{2.14}$$

$$\Delta \lambda = -\frac{\lambda^2}{N_G L} \tag{2.15}$$

Both Δf and $\Delta \lambda$ can be referred to as the *free spectral range* (FSR). If the modal dispersion is neglected, then $N_G = N_{eff}$ and the intensity transmittance T is a periodical function of f with a period equal to $\Delta f = c/N_{eff}L$. However, taking into account the dispersion, T becomes a pseudo-periodical of the optical frequency.

2.3.3 FWHM and Finesse

The Full Width at Half Maximum (FWHM) $\delta\Phi$ is obtained after expanding the transmittance near $\Phi = 2m\pi$. It naturally implies that $\delta\Phi \ll \Phi$ which is easily verified since m is large. This expansion gives:

$$\delta\Phi = \frac{2(1-a\tau)}{\sqrt{a\tau}} \tag{2.16}$$

From $\delta\Phi$, we can define the finesse $\mathcal{F}$ of the resonator (not to be confused with the coefficient of finesse F defined earlier) given by:

$$\mathcal{F} = \frac{2\pi}{\delta\Phi} = \frac{\pi}{2}\sqrt{F} = \frac{\pi\sqrt{a\tau}}{1-a\tau} \tag{2.17}$$

FWHMs in terms of frequency and wavelength at the resonance peaks are given, from (2.17) and (2.10) as

$$\delta f = \frac{c}{\mathcal{F} N_G L} \tag{2.18}$$

$$\delta \lambda = -\frac{\lambda^2}{\mathcal{F} N_G L} \tag{2.19}$$

2.3.4 Q factor

The Q factor of a resonant cavity is generally defined as:

$$Q = 2\pi \frac{E_{st}}{\Delta E_{cycle}} \tag{2.20}$$

where E_{st} is the energy stored in the resonator and ΔE_{cycle} is the energy dissipated per cycle, which corresponds for a ring resonator to the field oscillation period $T_f = 1/f$. For large values of the Q factor ($Q \gg 1$), it can be approximated as:

$$Q = \frac{f}{\delta f} = \frac{\lambda}{\delta \lambda} \tag{2.21}$$

From (2.19), the Q factor of a ring resonator can be expressed as a function of its internal parameters

$$Q = \frac{N_G L}{\lambda}\mathcal{F} = \frac{N_G L}{\lambda}\frac{\pi\sqrt{a\tau}}{1-a\tau} \tag{2.22}$$

Comparison between variations of Q factor and contrast C as functions of τ is presented in Fig. 2.9. For a ring resonator, Q cannot be thought of as linearly dependent of L since the loss factor is proportional to the quantity $\exp(-\rho L)$ where ρ is the amplitude extinction coefficient in the ring, which also depends on L via the curvature of the ring. In Fig. 2.10 are plotted the Q factor and contrast as functions of the optical cavity length and τ.

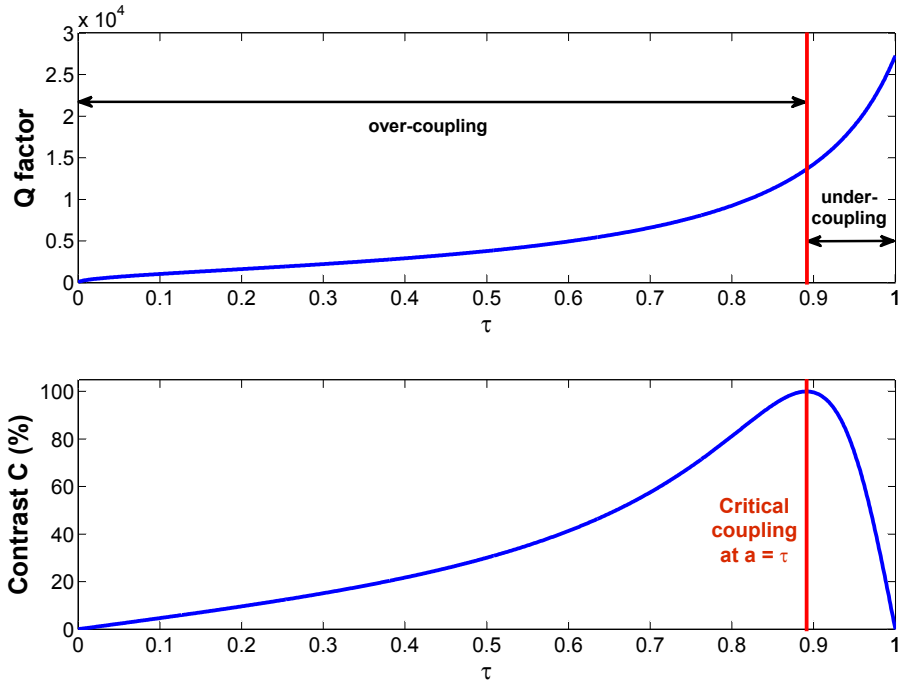

Figure 2.9: Q factor and contrast of a ring resonator for a linear attenuation of 1dB/cm with a cavity length L = 1mm vs the internal transmission coefficient τ. Critical coupling is obtained when $a = \tau = 0.89$ but does not correspond to the highest achievable Q factor.

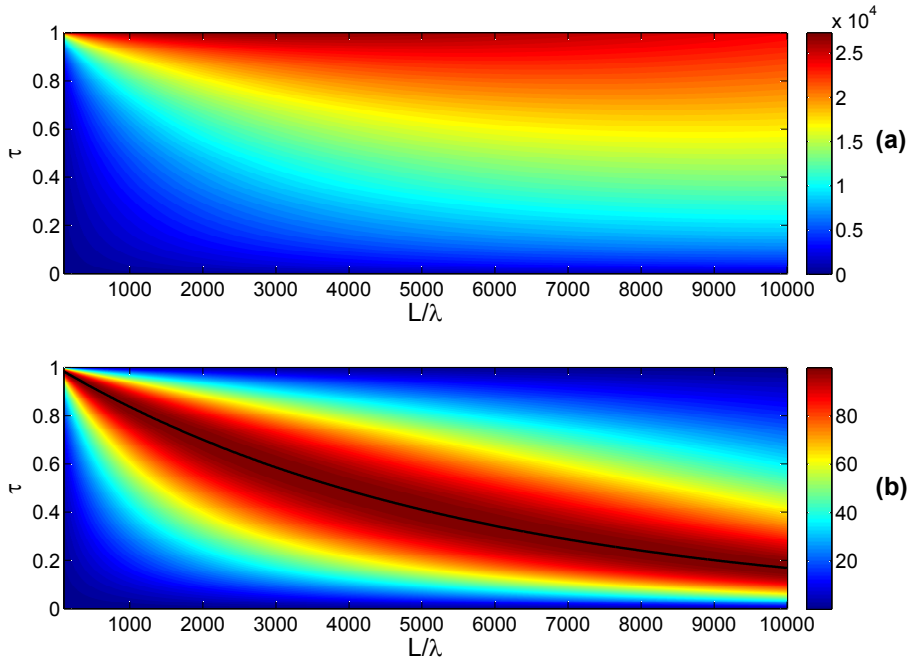

Figure 2.10: Q factor (a) and contrast (b) (in percents) of a ring resonator for a linear attenuation of 1dB/cm vs internal transmission coefficient τ and cavity length L. Critical coupling is obtained when $a = \tau$, represented by the solid black line.

2.3.5 Maximal intensity slope

Maximal intensity slope (MIS) of a measured transmittance is partly related to the absolute accuracy for the determination of a microresonator resonant wavelengths (cf. Chap.1). As a consequence, this characteristic of the intensity transmittance is of utmost importance in sensing applications.

To determine the value of the maxima of the slope Φ_C, we first need to determine their angular positions, corresponding to inflection points of the intensity transmittance. This is done by deriving Eq.(2.7) a first time:

$$\frac{dT}{d\Phi} = \frac{FA_0(1-\gamma)\sin(\Phi)}{2\left[1+F\sin^2\left(\frac{\Phi}{2}\right)\right]^2} \tag{2.23}$$

and a second time:

$$\begin{cases} \dfrac{d^2T}{d\Phi^2} = \dfrac{FA_0(1-\gamma)}{2\left[1+F\sin^2\left(\frac{\Phi}{2}\right)\right]^3}G(\Phi) \\ G(\Phi) = 2F\sin^4\left(\dfrac{\Phi}{2}\right) - (3F+2)\sin^2\left(\dfrac{\Phi}{2}\right) + 1 \end{cases} \tag{2.24}$$

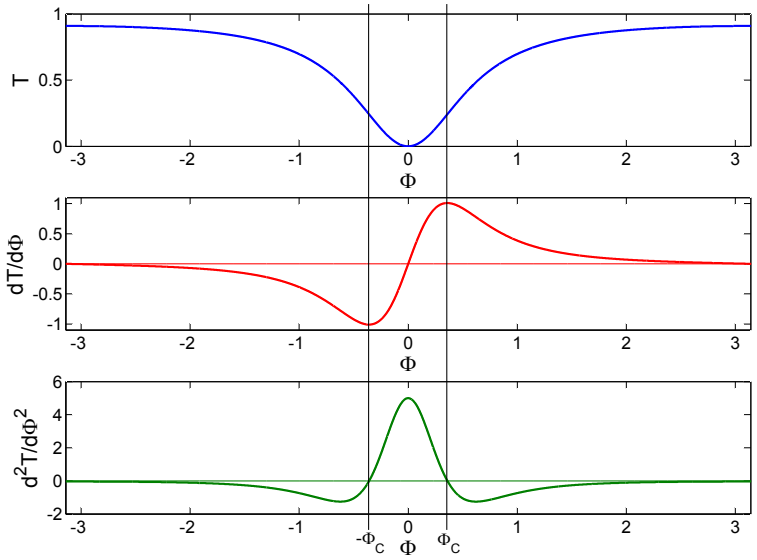

Figure 2.11: Intensity transmissions and its first and second order derivatives; F=10.

Setting $X = \sin^2(\Phi/2)$, we solve the following equation:

$$2FX^2 - (3F+2)X + 1 = 0 \tag{2.25}$$

In the range $[-\pi, \pi]$, the only two solutions of this equation corresponding to the resonance are:

$$\Phi_\pm = \pm\Phi_C = \pm 2 \arcsin \left[\frac{3F + 2 - \sqrt{9F^2 + 4F + 4}}{4F} \right]^{1/2} \tag{2.26}$$

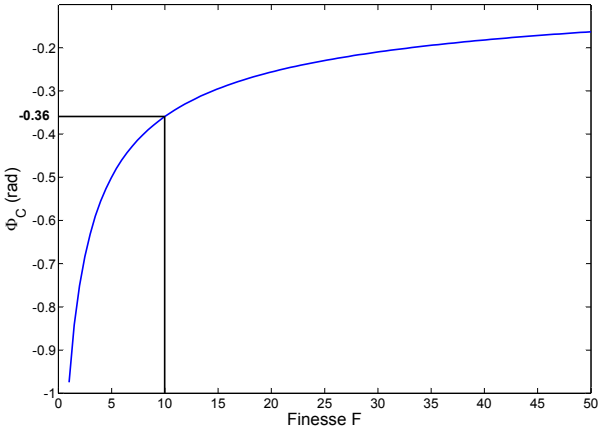

Figure 2.12: Angular position Φ_C of the maximum of intensity slope vs the coefficient of finesse F.

The maximal achievable slope for a set of parameters is then given, from Eq.(2.23), by:

$$\left(\frac{dT}{d\Phi}\right)_{max} = \frac{FA_0(1-\gamma)\sin(\Phi_C)}{2\left[1+F\sin^2\left(\frac{\Phi_C}{2}\right)\right]^2} \tag{2.27}$$

The complexity of the expression of the maximal slope as a function of a and τ makes its analysis difficult. A graphical representation is more suited to study the impact of loss coefficients a and transmission coefficient τ on the maximal slope value. Such a plot is presented in Fig. 2.13.

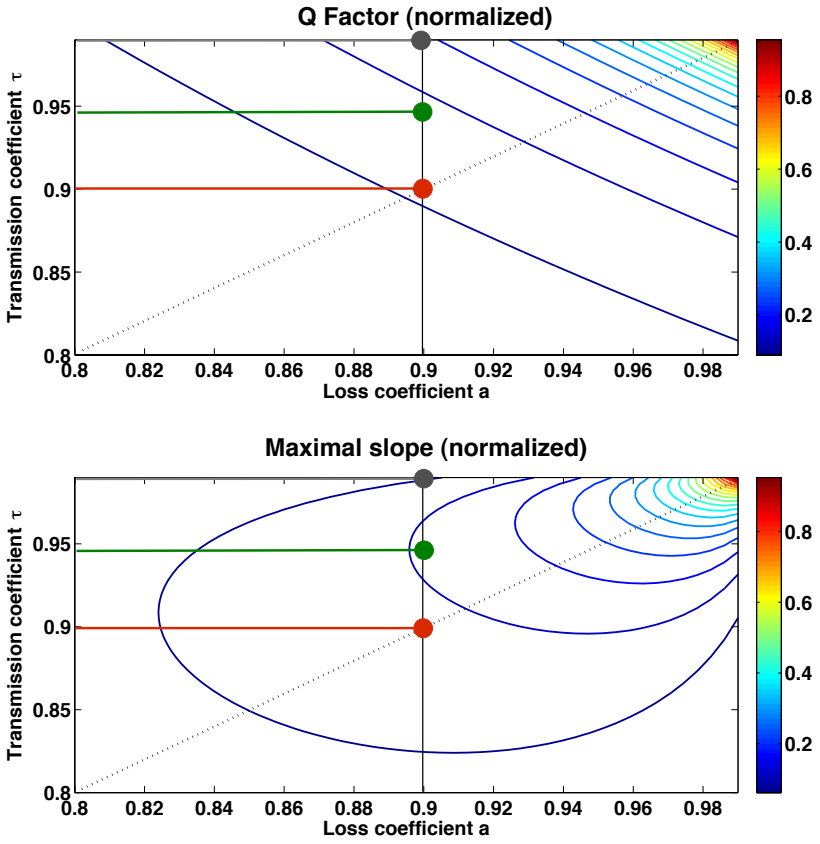

Figure 2.13: Contours for the Q factor and maximal slope as functions of loss coefficient a and transmission coefficient τ. Actual values are normalized by the highest Q factor and maximal slope, respectively. The dashed line represent the critical coupling condition. For a = 0.9, the red, green and grey spots correspond to maximal contrast, slope and Q factor, respectively.

In order to obtain the highest intensity slope, the coefficients a and τ have to be chosen carefully. It is clear from Fig. 2.13 that both internal parameters should have similar values, as close to unity as possible. For all characteristics A of the transmittance (A = F, Q, FSR, FWHM, ...),

$A(a,\tau) = A(\tau,a)$. Thus, the two parameters play identical roles. However, experimental achievement of targeted values is very different on the parameter. The transmission coefficient τ has the particularity to be easily adjustable, from variations of gap separation, radius of curvature and length of straight portions in microracetrack resonators. Specifically, values of τ near to 1 are easy to obtain since they correspond to situations where very little intensity is cross-coupled (cf. §3.4.1). In comparison, obtaining values of the loss coefficient a near unity requires a lot more efforts: optical loss is the limiting factor of the performances of optical resonators.

For this reason, the design of a microresonator is first oriented towards the reduction of optical losses. Then, the coupling coefficient must be adjusted to the loss coefficient in order to obtain the best characteristics of the resonator for the targeted application. As a careful noise analysis confirms (cf. Chap.1), the transmission coefficient needs to be chosen to obtain the highest possible slope for sensing applications. According to the contours in Fig. 2.13, for a given value of a, the optimal value for the transmission coefficient τ is roughly at half distance between $\tau = 1$, providing maximal contrast, and $\tau = a = 0.9$, corresponding to the highest achievable Q factor. It is clear that choosing the Q factor as reference characteristic for sensing applications would be a mistake: the highest Q factor does not correspond to a an optimal intensity slope.

3 Analytical formulation of internal parameters

3.1 Challenges

Until now, the ring resonator and its spectral characteristics were only studied as functions of internal parameters reflecting propagation, coupling and optical losses in the device. These parameters concentrate most difficulties in building an analytical model for microresonators. The previous study, although limited in many aspects, has still the great benefit to show what should be the design goals for a ring resonator, i.e. which value of the internal parameters it is best to achieve.

In order to find the maximal accuracy in the determination of the position of a resonance, or of the maximal intensity variation when the res-

onance shifts, the slope of the transmitted intensity at the inflection point needs to be maximized. According to the previous study, this is achieved for values of a and τ near unity. For the ring, τ can be easily adjustable by the design and also by the fabrication, especially in the case of vertically coupled ring resonators. As a consequence, the limiting factor is the loss coefficient a and one of the main efforts of the design is the minimization of the optical losses inside the ring resonator.

However, for sensing applications based on ring resonators, the accuracy in the measure of the resonance shift is not the sole aspect to consider. The second and equally important aspect is the sensitivity to the $measurand$ (cf. Chap.1). In the lucky situations where the optimization of the sensitivity to the $measurand$ coincides with the reduction of the losses, the design is straightforward. However, in most situations, the optimal configuration for the sensitivity is found when guided modes are poorly confined in the core of the waveguide, hence tending to correspond to important optical losses, and resulting in poor accuracy. In that case, a trade-off has to be found between the sensitivity and the resolution, based on the optimization of the detection limit which is the ratio of the resolution and the sensitivity.

Independently, an important gain on the resolution can be achieved through the sensing instrumentation, which means that the design paradigm for the ring resonator should be adapted to get the highest sensitivity while maintaining an intensity transmittance with resonance peaks compatible with the determination of the resonant wavelengths with high accuracy.

Anyhow, a good understanding of the optical phenomenons taking place in the ring resonator is very important to make decisive design choices. For the sake of simplicity, most expressions allowing to quantify the losses are written assuming that the study of a three-dimensional waveguide can be reduced to the study of a two-dimensional effective structure determined from the effective index method [10].

3.2 Effective index

Depending on the guiding structure, different solutions exist to determine the parameters of the guided modes. For rectangular waveguides, at least

two analytical methods can be used, Marcatili's method and the effective index method. Kumar's method can also be used in order to improve the accuracy in the calculations of the other analytical methods in the case of weakly guide modes [10]. Numerous numerical solutions also exist, in the form of commercial or homemade mode solvers. When it comes to determine the characteristics of the guided modes for curved waveguides as present in the ring resonator, different analytical methods exist and give result with good accuracy, though numerical methods provide results more easily. Calculation of the effective index and its variations will be further studied in Chap.6.

3.3 Loss mechanisms

3.3.1 Bending losses

A basic understanding of losses in bent optical waveguides can be achieved using the ray approximation for the propagation of light. In a straight waveguide, the angle of incidence of rays on sidewalls are the same since they are parallel. As consequence, if a ray undergoes total internal reflection on one side, it is also totally reflected on the other side, resulting in a theoretical lossless propagation.

The situation is different in a bent waveguide since, because of the curvature, the incidence angle is larger on the outward sidewall than on the in the inward sidewall. As consequence, two different propagation regimes can exist, with significant differences in bending losses.

In the first regime, light is totally reflected only on the inner sidewall and the total internal reflection criteria is not met for the outwards sidewall. From Fresnel laws, the ray is then only partially reflected at this interface which makes the mode inside the bent waveguide lossy, characterized by a complex propagation constant where the imaginary part relates to the loss and the real part to the actual propagation.

In the second regime, the criteria for internal reflections is met for both sidewalls and the bend losses become negligible compared to other sources of optical losses.

The bending loss is usually quantified by the power attenuation coeffiecient α_{bd} which can be be expressed as [41, 19]:

$$\begin{cases} \alpha_{bd} = \dfrac{2\gamma_s^2 k_y^2 \exp(\gamma_s W)}{(n_{core}^2 - n_{clad}^2)\, k_0^2 \beta (2 + \gamma_s W)} f(R_c) \\ f(R_c) = \exp\left\{ -\left[\dfrac{\beta}{\gamma_s} \ln\left(\dfrac{\beta + \gamma_s}{\beta + \gamma_s} \right) - 2 \right] \gamma_s R_c \right\} \end{cases} \tag{2.28}$$

where β is the propagation constant in the curved waveguide [43], k_0 is the wavenumber in vacuum, k_y is the propagation constant in the direction of the bend, R_c is the radius of curvature of the bend; γ_s is a coefficient describing the attenuation in a transverse cut of the waveguide.

It is easy to see from that formulation the benefit of high index contrast waveguides to reduce the bending losses. Also, from the exponential term, we see the existence, for a given guiding structure, of a critical radius of curvature $R_{critical}$ separating the two regimes of bending losses. An approximate but elegant expression for this critical radius was found by Marcatili [40]:

$$R_{critical} = \frac{\pi N_{core}^2 W^2}{\lambda^2} \tag{2.29}$$

Another important observation from [40] is that losses can be reduced by choosing the height of the guide large enough to confine the fields as much as possible within the core of the waveguide in the direction normal to the plane of curvature.

The value of this critical radius can be taken into account when designing the microring and its transverse guiding structure. By choosing a radius close to the critical value, the bending loss can be effectively reduced without too much compromise on the circumference of the microring which plays an important role in the some of its spectral characteristics. Moreover, the issue of compactness of microrings is an important one for many applications of these devices. This motivates designers to find a good compromise between compactness and optical losses from the bends.

3.3.2 Surface roughness scattering

Surface roughness scattering is also an important source for optical loss in all waveguide portions, not only the bent ones. However, guided mode in bent portions being slightly unconfined, bending tends to increase the effect of surface scattering.

In analogy to the part on bending losses, the optical losses from surface roughness scattering can be quantified in straight and bent waveguides by attenuation coefficients $\alpha_{srs,straight}$ and $\alpha_{srs,curved}$ are given by[19]:

$$\begin{cases} \alpha_{srs,straight} = 2\sigma^2 \left(N_{eff}^2 - N_{clad}^2\right) k_0^2 \dfrac{k_{y,straight}}{\beta_{straight}} E_s^2 \\ \alpha_{srs,curved} = \sigma^2 \left(N_{eff}^2 - N_{clad}^2\right) k_0^2 \dfrac{k_{y,curved}}{\beta_{curved}} \left(E_1^2 + E_2^2\right) \end{cases} \tag{2.30}$$

where σ is the variance of surface roughness; E_s is the electric field at the core-cladding interface in the case of the straight waveguide, and E_1 and E_2 are the electric field at the inner and outer boundaries, respectively, in the case of the curved waveguide.

From these expressions, two important observations can be made. First, the attenuation coefficients for both straight and curved waveguide are proportional to the square of the variance of surface roughness. This confirms how important is the quality of the surface of the microring, and the necessity to select materials and fabrication processes that minimize the surface roughness of the device in order to reduce the optical losses.

The second observation is that the attenuation coefficients are proportional to the difference between the squares of effective and cladding indices. Direct consequence is that surface roughness scattering will be more important in waveguides with high index contrast, typically SOI waveguides, than those with lower contrasts such as waveguides made from polymer materials. Compared to optical losses from the waveguide curvature, where polymer materials have inherently higher losses, the situation is reversed for surface roughness scattering losses.

At this point, it would be difficult to tell which technology, SOI or polymer, will result in the lower optical losses. From the expressions mentioned above, an actual comparison of both technologies will require to know the

constraints on the radius of curvature, and more importantly to know precisely what is the lowest achievable surface roughness at fabrication for each technology.

Another point to consider is that surface roughness scattering can couple light from a mode propagating in a microresonator to a counter-propagating mode [50]. Because of the slight asymmetry of the coupling region and the strong sensitivity of the position of resonances to the optical path, the presence of a counter-propagating mode modifies the intensity transmittance of the microresonator by creating a splitting of the resonances. The same effect can also be observed when a defect from fabrication induces a strong but local variation of the geometry of the microring.

3.3.3 Substrate and cladding losses

The origin of these losses is the physical limitation of the real guiding structure, as compared to the ideal structure where cladding and substrate occupy semi-infinite volumes. In that view, portions of the evanescent field that are guided in the ideal structure can be lost in the real, limited, structure if the materials beyond the guiding structure have stronger refractive indices than the cladding and/or the substrate materials. In most cases, this situation occurs for devices where the substrate is a thin layer of silica deposited upon on a silicon wafer. However, in situations where the cladding is a liquid flowing in a microfluidic channel built with PDMS, PMMA, or any material that has strong index and/or that absorbs light at the working wavelength, cladding losses can also have a strong influence on the microresonator performances.

Different methods can be used to reduce these losses. A first method is to reduce the dimension of the evanescent field, so that less optical power can leak. This is most effectively achieved by increasing the height of the waveguide. However, the height of the waveguide cannot be increased infinitely, since a larger waveguide will support more than one mode. Furthermore, for applications of microresonators such as biochemical sensing, a large evanescent field is preferable, for sensitivity issues. A better method is then to reduce the losses to the substrate or the cladding by increasing the widths of these regions, since the reduction of the losses will be achieved without modifying the evanescent field. It is also possible to choose ma-

terials surrounding the core of the waveguide with low refractive indices to increase optical isolation in the core. This solution is particularly interesting in surface sensing where it is advantageous to have a symmetrical waveguide, hence to have a waveguide where the substrate index is as low as the cladding index. However, this is difficult to obtain with conventional fabrication techniques and materials.

With several approximations, the power attenuation coefficients due to substrate and cladding losses can be expressed as [19]:

$$\begin{cases} \alpha_{sub} = \dfrac{\lambda^3 k_x \gamma_{sub}^2 \sin^2(k_x d_{core})}{\pi^3 N_{core} \left(N_{core}^2 - N_{sub}^2\right) d_{core}} \exp\left(-2\gamma_{sub} d_{sub}\right) \\ \alpha_{cladding} = \dfrac{\lambda^3 k_x \gamma_{clad}^2 \sin^2(k_x d_{clad})}{\pi^3 N_{core} \left(N_{core}^2 - N_{clad}^2\right) d_{core}} \exp\left(-2\gamma_{clad} d_{clad}\right) \end{cases} \tag{2.31}$$

where γ_{clad} and γ_{sub} are the attenuation constants in the cladding and substrate regions, respectively; d_{core} is the height of the waveguide core and k_x is the propagation constant in the direction perpendicular to the interfaces.

From the exponential decay of the loss coefficients with increasing thicknesses of the cladding and substrate regions d_{clad} and d_{sub}, we see as expected that these optical losses can be significantly reduced with larger zones corresponding to the cladding and substrate.

3.3.4 Absorption losses

Another source of optical loss in the waveguide is the material absorption. The first idea that comes to mind is to select materials that do not absorb in the wavelength range we plan on using. However, though very important loss could be fatal to the decent spectral characteristic we aim at, optical absorption may be an interesting property to use in order to produce thermal linear and non-linear effects [35, 36].

3.3.5 Modal mismatch losses

In a bent waveguide, the distribution of modal intensity as well as the effective index are slightly modified compared to that of a straight waveguide. This modification of the characteristics of the guided modes between bent

and straight waveguides has two principal effects on the spectral characteristics of the microresonator. When the resonator is a microring, the modal mismatch between the straight bus waveguide and the bent waveguide constituting the ring triggers coupling or insertion losses characterized by the coefficient $\alpha_i = (1-\gamma)^{1/2}$ as defined before (cf. §2.2.1). One possibility in order to reduce α_i is then to adopt the racetrack configuration where coupling occurs between waveguides with similar modal characteristics. However, in that configuration, loss is added in the microring because of the modal mismatch at the junctions between straight and curved portions of the microresonator. This is quantified by the junction transmission coefficient [51]:

$$T_j = 4\cos^2(k_y\delta)\left(1+\frac{\beta_{curved}}{\beta_{straight}}\right)^{-2} \tag{2.32}$$

where $\beta_{straight}$ and β_{curved} are the propagation constants in the straight and curved waveguides, respectively, δ is the lateral shift of the electric field peak in the bent waveguide and k_y is the propagation constant in the direction of the bend at straight/bent interfaces of the waveguide. Different methods can be used to calculate δ.

3.4 Coupling mechanisms

In order to calculate the coupling coefficients between two waveguides, the characteristics of the guided modes inside these waveguides need to be known. This makes the calculation of the coupling coefficient between a straight waveguide and a bent waveguide quite tricky since it is difficult to calculate the mode in a bent waveguide. For this reason, it can be more preferable to work with rings with large radii of curvature since, in that case, the mode in the bent waveguide can be approximated with that of the straight waveguide with sufficient accuracy.

The choice of the racetrack geometry is also a good solution to solve this problem, since coupling coefficients are largely determined by the length of the straight portions, $i.e.$ the parameter L_{str} of the resonator (cf. Chap.1). In addition, a panel of microracetrack resonators with various straight lengths L_{str} can be fabricated to determine the optimal value of this geometric parameter.

Another solution is to realize the coupling between the bus and the ring waveguides via multi-mode interference (MMI) coupler. For the micro-racetrack configuration with evanescent coupling or MMI coupling, the coupling coefficient can be easily calculated from analytical models or numerical methods such as BPM. This numerical method, very limited when the waveguide is curved compared to FDTD, provide more accurate results for straight portions of the waveguides.

3.4.1 Evanescent coupling

Let us consider two co-directional rectangular waveguides, z being the common direction of propagation. It is assumed that the electromagnetic fields of the coupled waveguides can be expressed as the sum of the guided modes in each waveguide:

$$\begin{cases} \vec{E} = A(z)\vec{E_1} + B(z)\vec{E_2} \\ \vec{H} = A(z)\vec{H_1} + B(z)\vec{H_2} \end{cases} \tag{2.33}$$

From Maxwell equations, considering that at z=0 the initial conditions are A(0)=A_0 and B(0)=0, it is then possible to show that the functions A and B describing the coupling between the two waveguides can be expressed as [10]:

$$\begin{cases} A(z) = \left[\cos(qz) + j\dfrac{\delta}{q}\sin(qz)\right] A_0 \exp(-j\delta z) \\ B(z) = -j\dfrac{\rho}{q}\sin(qz) A_0 \exp(+j\delta z) \end{cases} \tag{2.34}$$

where q is given by:

$$q = \sqrt{\rho^2 + \delta^2} \tag{2.35}$$

The constants ρ, the mode coupling coefficient of the directional coupler, and the difference of the propagation constants between the guided modes in each waveguides δ are defined by:

$$\delta = \frac{1}{2}(\beta_2 - \beta_1) = \frac{\pi}{\lambda}(N_{eff,2} - N_{eff,1}) \tag{2.36}$$

$$\rho = \rho_{12} = \rho_{21} = \frac{\omega\epsilon_0 \int_{-\infty}^{+\infty}\int_{-\infty}^{+\infty} \left(N^2 - N_2^2\right) \vec{E_1^\star} \cdot \vec{E_2} dxdy}{\int_{-\infty}^{+\infty}\int_{-\infty}^{+\infty} \vec{u_z} \cdot \left(\vec{E_1^\star} \times \vec{H_1} + \vec{E_1} \times \vec{H_1^\star}\right) dxdy} \tag{2.37}$$

where $\rho_{12} = \rho_{21}$ relates to the normalization of the eigenmodes $\vec{E_1}$ and $\vec{E_2}$.

From these (2.36) and (2.37), we can write the evolution of the optical power flow along the propagation direction:

$$\begin{cases} P_a(z) = \dfrac{|A(z)|^2}{|A_0|^2} = 1 - \eta \sin^2(qz) \\ P_b(z) = \dfrac{|B(z)|^2}{|B_0|^2} = \eta \sin^2(qz) \end{cases} \tag{2.38}$$

where ν denotes the maximum power-coupling efficiency, defined by:

$$\eta = \left(\frac{\rho}{q}\right)^2 = \frac{1}{1 + (\delta/\rho)^2} \tag{2.39}$$

From the expression of the maximum power-coupling efficiency, we see that an optimal directional coupler is obtained when the propagation constants of the coupled modes β_1 and β_2 are equal, corresponding to a phase matching. Another important parameter of the directional coupler is the coupling length L_c defined as

$$L_c = \frac{\pi}{2q} = \frac{\pi}{2\sqrt{\rho^2 + \delta^2}} \tag{2.40}$$

This parameter corresponds to the minimal length of the waveguides required for the power in the second waveguide to reach its maximal value.

In Fig. 2.14 we see the different phenomena which depend on the coupling coefficient ρ and the difference between the effective indices of the guided modes in the coupler. It is noticeable in case (b) that a slight phase mismatch between the coupled guided modes can limit the maximal obtainable coupling coefficient, whatever the coupling length could be. Also, from case (c) we observe a similar limitation when the coupling coefficient gets too small. These effects are important for the design of the microring particularly because in order to achieve critical coupling, the internal amplitude transmission coefficient $\tau = \left[1 - \eta \sin^2(qL_c)\right]^{1/2}$ needs to be adjusted to the loss coefficient a inside the ring. In the case where important optical losses apply, the coupling efficiency η needs to be sufficiently large so that is possible to find a coupling length L_c achieving τ near a, which might be impossible because of the limitation of the power-coupling possibilities.

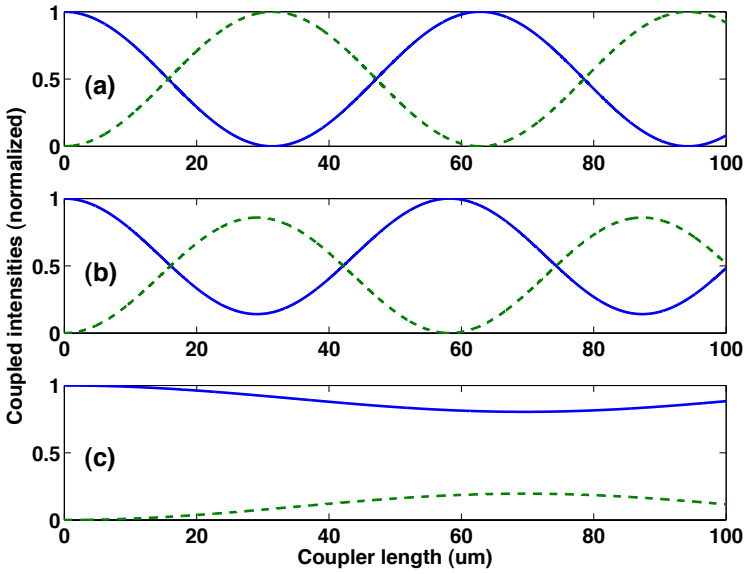

Figure 2.14: Transmitted (solid blue line) and coupled (green dashed line) optical powers with λ = 1.55 μm and $N_{eff,1}$ = 1.56. (a) ρ = 0.05 μm^{-1} and $N_{eff,2}$ = $N_{eff,1}$ resulting in η = 1 and L_c = 31.4 μm; (b) ρ = 0.05 μm^{-1} and $N_{eff,2}$ = 1.57 resulting in η = 0.86 and L_c = 29.1 μm; (c) ρ = 0.01 μm^{-1} and $N_{eff,2}$ = 1.57 resulting in η = 0.196 and L_c = 69.5 μm

In order to further visualize the power-coupling limitations due to the structure of the coupling region, the maximum power-coupling efficiency η is represented as a function of the modal mismatch δ and the coupling coefficient ρ (Fig. 2.15).

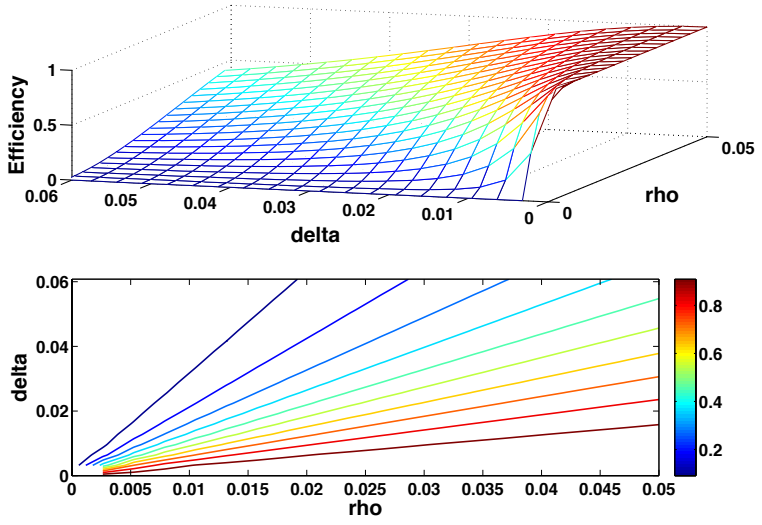

Figure 2.15: 3D representation of the power-coupling efficiency η as a function of ρ and δ and associated level curves from η = 0.1 (dark blue) to η = 0.9 (dark red).

From the contour plots, we can visualize the conditions on ρ and δ that must be verified in order to obtain specified cross-coupling and internal transmission coefficients κ and τ. The value of the coupling efficiency η defines the highest value of κ^2 that can be achieved for a coupler characterized by the couple (ρ, δ), whatever the coupling length L_c is. As a consequence, the higher the optical losses, the more difficult it is to achieve critical coupling or optimal transmission slope (cf. Fig. 2.13). Indeed, higher losses require to obtain either higher mode coupling coefficients ρ or lower phase mismatches δ or both.

To obtain high values of ρ, the distance between the waveguides must be very small, in the range of hundreds of nanometers, or under. Increasing cross-coupling coefficients κ will be then possible to some extent but will be inherently limited by the resolution of the technology adopted for fabrication of the devices. The constraint on phase mismatch is also important. However, it is not difficult to achieve low values of δ from a careful design of the waveguides, by matching the effective index of the guided modes.

3.4.2 MMI coupling solution

Obtaining large coupling coefficients is important for the performance of a microring resonator. It is usually achieved by reducing the distance between the waveguides in the coupling zone to a few hundreds of nanometers. In a lateral coupling configuration, this means that the resolution of the fabrication technique for the waveguides needs be well under the hundred of nanometers in order to accurately control the coupling coefficient. This fact itself requires the use of fabrication methods such as electron-beam (e-beam), focused-ion-beam (FIB) or nanoimprint lithographies.

Both e-beam and FIB lithographies are very expensive, and have a very low throughput as they are serial production methods. With reduced cost and higher throughput due to parallel fabrication, Nanoimprint lithography is a better solution. However, it often creates important surface roughness resulting in significant optical losses in the microring, and requiring further processing steps to reduce the roughness [52]. To that regard, the use of UV lithographies is preferable but the resolution they allow is usually not sufficient to obtain adequate coupling coefficients via evanescent coupling. An interesting solution to this technical limitation is to replace evanescent

coupling by creating a MMI coupler. In that configuration, the waveguides from the bus and the resonator are in contact in the coupling zone. In this case, during fabrication, the constraint on gap separation does not exist anymore [53].

4 Additions to the analytical model

4.1 Modal Dispersion

In most situations, the intensity transmittance of microring resonators is plotted not as a function of the single trip phase delay, but as a function of the wavelength or frequency in vacuum. It is based on the following relation:

$$\Phi = \frac{2\pi}{\lambda} N_{eff} L \tag{2.41}$$

As long as the effective index can be considered as a constant, the intensity transmittance expressed as a function of frequency is strictly periodical, which means that all resonances will be equally spaced. In comparison, the transmittance expressed as a function of wavelength is not strictly periodical since the single trip phase delay is inversely proportional to the wavelength. However, on a small wavelength range $\Delta\lambda$ as compared to the center wavelength λ_0, it is possible to make the following approximation:

$$\Phi = \frac{2\pi}{\lambda_0} N_{eff} L \left[1 + \frac{\lambda - \lambda_0}{\lambda_0}\right]^{-1} \simeq \frac{2\pi}{\lambda_0} N_{eff} L \left(1 - \frac{\lambda - \lambda_0}{\lambda_0}\right) \tag{2.42}$$

Typical wavelength in this work being 1550 nm, and the typical wavelength range being 100 nm or smaller, this equation shows that the transmittance, expressed as a function of wavelength can also be treated as periodical when the effective index is constant. For guided modes inside the waveguides constituting the microring, material and modal dispersions will affect the single-trip phase delay via the effective index. In the situation where these dispersion effects cannot be neglected, the effective index has to be treated as wavelength (or frequency) dependent. This is common to fit intensity transmittance of microrings with slight dispersion over large wavelength ranges (cf. Chap. 3) but more importantly when the dispersion is high, in small radii silicon microresonators for instance [54].

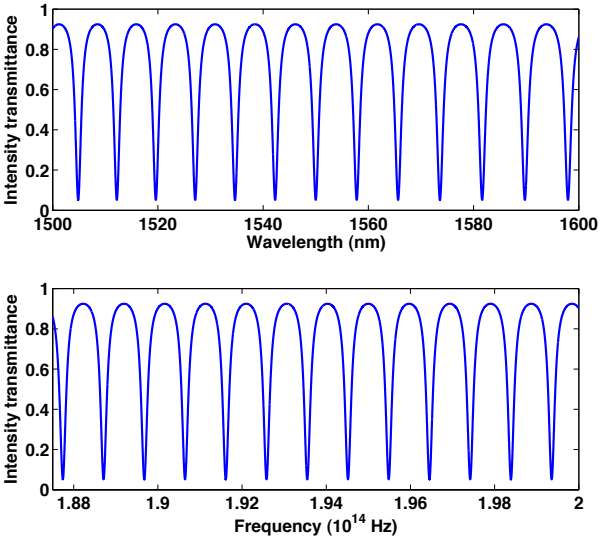

Figure 2.16: Intensity transmittances as functions of wavelength and frequency on corresponding ranges for a cavity length L = 100 μm and N_{eff} = 1.55

In such cases, the dependency of the effective index N_{eff} on the wavelength can be expressed in form of a Lagrange expansion, with one or more orders depending on the dispersion and the required accuracy of the approximation. In polymer microrings, a first order expansion is usually sufficient to properly describe the modal dispersion:

$$\begin{aligned} N_{eff}(\lambda) &= N_{eff}(\lambda_0) + (\lambda - \lambda_0)\frac{\partial N_{eff}}{\partial \lambda}(\lambda_0) \\ &= N_G(\lambda_0) + \left[\frac{\partial N_{eff}}{\partial \lambda}(\lambda_0)\right]\lambda \end{aligned} \tag{2.43}$$

where N_G is the group effective index.

According to this expression, the intensity transmittance expressed as a function of the frequency or wavelength is not longer strictly periodical. Thus, a measurable effect of dispersion in microring resonators is the variation of the spacings between resonances $i.e.$ of the free spectral range (FSR). These variations of the FSR, according to Eq.(2.14), are directly related to variations of the group effective index. In microrings where the dispersion coefficient is large, the group effective index can be more than twice the effective index, which means that neglecting dispersion will cause huge discrepancies between the required and obtained values of FSR. Specific effects of a wavelength-dependent effective index on positions of

the resonances are presented in Fig. 2.17, where the dispersion is moderate, and in Fig. 2.18 where the dispersion is high.

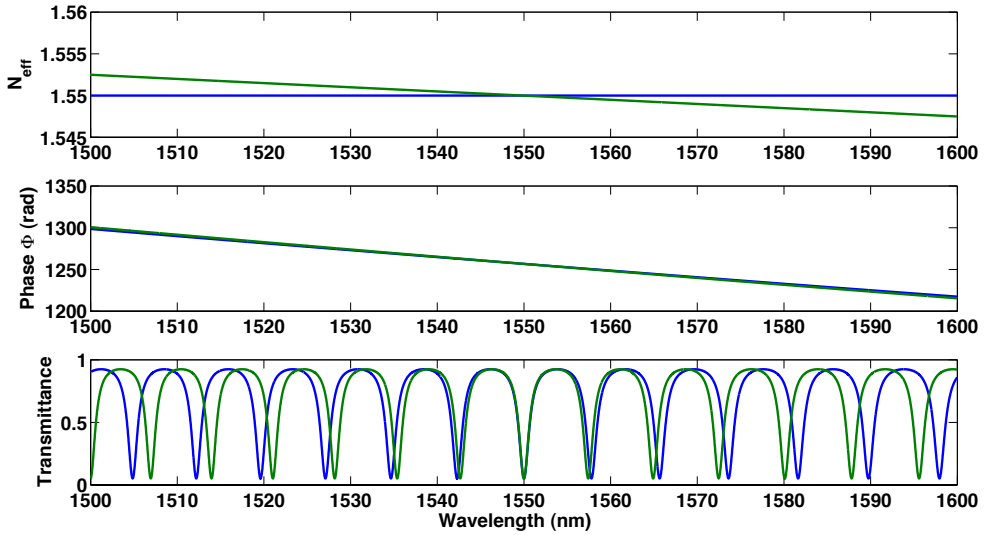

Figure 2.17: Effective index, single trip phase delay and intensity transmittances with (green dots) and without (blue line) first-order dispersion as function of the wavelength for a cavity length L = 200 μm, $N_{eff,0}$ = 1.55 and $\frac{\partial N_{eff}}{\partial \lambda}(\lambda_0)$ = -0.05 UIR/μm corresponding to $N_G(\lambda_0)$ = 1.628

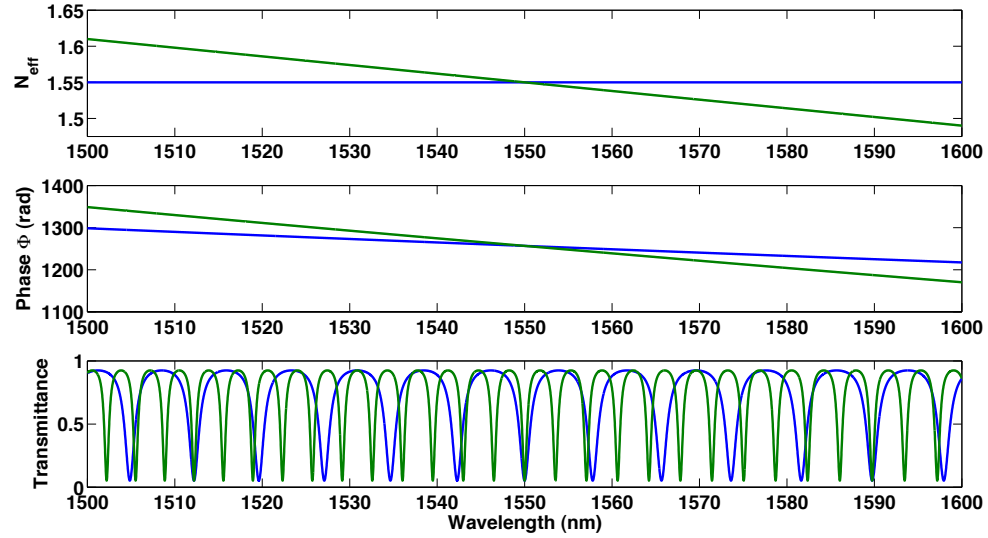

Figure 2.18: Effective index, single trip phase delay and intensity transmittances with (green dots) and without (blue line) first-order dispersion as function of the wavelength for a cavity length L = 200 μm, $N_{eff,0}$ = 1.55 and $\frac{\partial N_{eff}}{\partial \lambda}(\lambda_0)$ = -1.2 UIR/μm corresponding to $N_G(\lambda_0)$ = 3.41

Until now, it was assumed that the only effect of dispersion on the

intensity transmittance occurred via the single trip phase delay, affecting only the positions in wavelength or frequency of the resonances. However, though not explicitly, the other internal parameters a and τ also depend on the effective index of the guided modes, in both bus waveguide and microresonator [55]. As consequence, dispersion will not only affect the positions of the resonances, but also their lineshapes. As a direct consequence of dispersion, there is a difficulty to achieve critical coupling, optimal Q factor or optimal intensity slope for several resonances. The effect of dispersion on the progressive deformation of the resonances lineshapes in ring resonators can be accounted for by substituting in the expression of the intensity transmittance the constant coefficients a and τ by wavelength or frequency dependent functions. Similarly to the case of the effective index, these functions can be written in a form of Lagrange expansions:

$$\begin{cases} a(\lambda) \simeq a(\lambda_0) + (\lambda - \lambda_0)\dfrac{\partial a}{\partial \lambda}(\lambda_0) \\ \tau(\lambda) \simeq \tau(\lambda_0) + (\lambda - \lambda_0)\dfrac{\partial \tau}{\partial \lambda}(\lambda_0) \end{cases} \tag{2.44}$$

Depending on the variations of a and τ as functions of the wavelength, the effects on the modulation of the resonances envelope may be different. In Fig. 2.19, the case where a and τ have opposite slopes and cross is presented.

4.2 Modal Birefringence

As explained before in §1.2.3, a typical single-mode waveguide supports two quasi-orthogonal modes: a fundamental quasi-TE mode and a fundamental quasi-TM mode. Due to the differences in phase velocity and transverse intensity repartition between these guided modes, whether within the bus waveguide or within the microring, internal parameters corresponding to each mode can be quite different, resulting in distinct intensity transmittances. As a result, a measured intensity transmittance will strongly depends on the polarization state of the input wave.

We can assume in a first approximation that polarization coupling and polarization rotation effects can be neglected. This means that quasi-TE and quasi-TM modes can be considered as completely independent from one another. Also, as major electric field components of quasi-TE and

quasi-TM modes are orthogonal, we can neglect interference effects between the two modes.

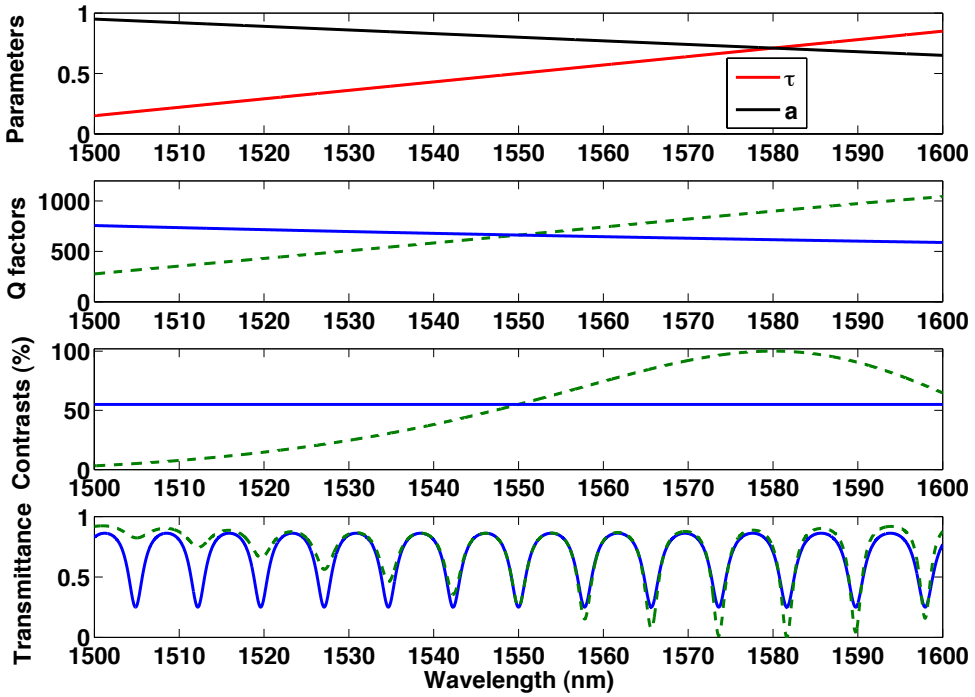

Figure 2.19: On top, arbitrary variations of parameters a and τ due to dispersion are presented. Q factors, contrasts and transmittances as functions of the wavelength are computed in presence (green dashed line) or without (blue solid line) these specific dispersion effects (variations in the positions of the resonances are not displayed). Taking into accounts variations of a and τ due to dispersion, the shape of the resonance strongly varies from one extremity to the wavelength range to the other.

Let us consider the situation where light inserted in the single-mode bus waveguide is linearly polarized in a given direction. After a short propagation length in the waveguide, only guided modes remain so that is is possible to write the input field as:

$$\begin{cases} E_1 = \sqrt{\alpha} E_1^{TE} + \sqrt{\beta} E_1^{TM} \\ I_1 = \alpha I_1^{TE} + \beta I_1^{TM} \end{cases} \tag{2.45}$$

where α and β appear as constants describing the intensity repartition between the two modes.

After the coupler, from the hypothesis of strict modal orthogonality, the output intensity can simply be written as the sum of two independent contributions:

$$I_4 = \alpha I_4^{TE} + \beta I_4^{TM} = \alpha T^{TE} I_1^{TE} + \beta T^{TM} I_1^{TM} \tag{2.46}$$

where T^{TE} and T^{TM} are respectively the intensity transmittance for the fundamental quasi-TE and quasi-TM modes. After normalization of the above expression by the input intensity, we obtain an expression for the resulting transmittance:

$$T = \alpha^{\star} T^{TE} + \beta^{\star} T^{TM} \tag{2.47}$$

where $\alpha^{\star} + \beta^{\star} = 1$, as a result of the normalization. In Fig. 2.20, the plotted total intensity transmittance of the device is the superposition of the transmittances of each polarization mode. As a result, the contrast of the resonances is affected. Also, the interpretation of the transmittance is more difficult. As we will see on the chapter dedicated to the instrumentation, TE and TM transmittances can be measured separately using a polarization controller before coupling to the bus waveguide. Also, both transmittances can be measured simultaneously by controlling the input polarization state and by separating both polarizations at the output of the bus waveguide (cf. Chap.5).

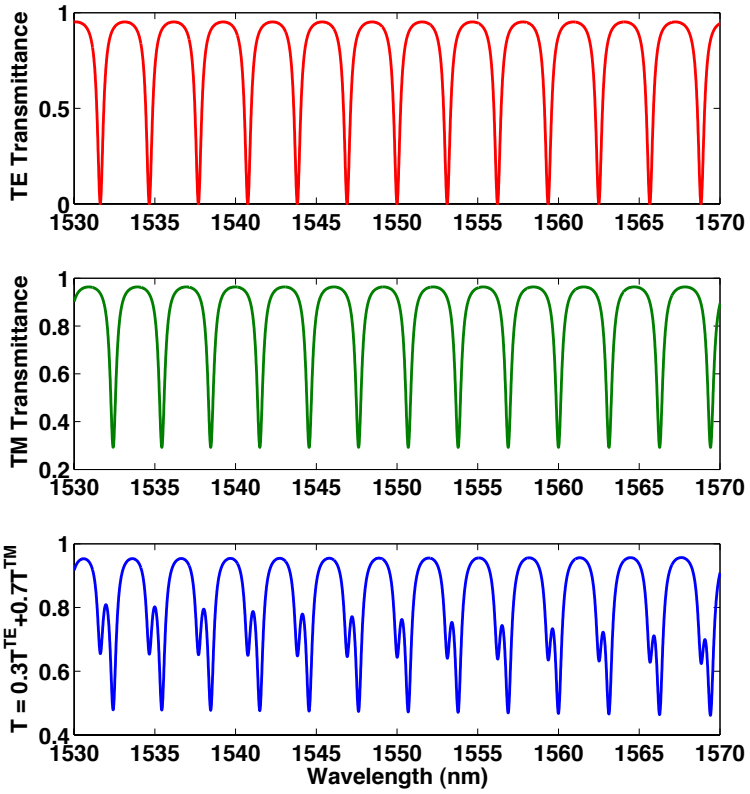

Figure 2.20: TE and TM transmittances as well as the total transmittance for $\alpha^{\star}$ = 0.3 and $\beta^{\star}$ = 0.7

4.3 Multimodal behavior

Until now, it was assumed that the bus waveguide and the microring could only support one transverse mode. Indeed, this is a convenient situation for sensing since the single-mode intensity transmittance can be analyzed in a straightforward fashion. However, in some sensing applications, it can be interesting to work with waveguides that have strongly confined fundamental modes, where most of the intensity of the guided mode is in the core. Higher and higher confinement factor modes can be easily obtained by building larger and larger waveguides, or increasing the index contrast between the core and the surrounding materials. The undesired consequence of this is an increasing number of modes supported by the waveguides. It is interesting for the design to determine if the presence of additional modes will make the sensing by analysis of the intensity transmittance more difficult or impossible, or if the influence of higher order modes on measurements is neglectable, and/or manageable. In order to do so, a model was developed to predict measurement results of intensity transmittances from microrings supporting two transverse modes. This model could easily be generalized to microrings with an unspecified number N of supported transverse modes.

In the following, the input field E_1 is replaced by a superposition of two input fields with identical polarization state $E_1^{(A)}$ and $E_1(B)$ with

$$\begin{cases} |E_1^{(A)}|^2 = \alpha |E_1|^2 \\ |E_1^{(B)}|^2 = \beta |E_1|^2 \\ \alpha + \beta = 1 \end{cases} \tag{2.48}$$

where α and β are modal ratios of the total input power. The field E_4 at the output of the resonator can be written as a superposition of the two modes

$$E_4 = E_4^{(A)} + E_4^{(B)} = t_A E_1^{(A)} + t_B E_1^{(B)} \tag{2.49}$$

where t_A and t_B are the amplitude transmittances for modes (A) and (B), defined in §2.2.2. The total amplitude transmittance t can then be written as:

$$t = \frac{E_4}{E_1} = \frac{E_1^{(A)}}{E_1} t_A + \frac{E_1^{(B)}}{E_1} t_B = \sqrt{\alpha} t_A + \sqrt{\beta} t_B \tag{2.50}$$

From this expression, we deduce the total intensity transmittance:

$$T = |t|^2 = \frac{1}{2}\left[\alpha |t_A|^2 + \beta |t_B|^2 + \sqrt{\alpha\beta}(t_A t_B^* + t_A^* t_B)\right] \tag{2.51}$$

We now define $T_A = |t_A|^2$ and $T_B = |t_B|^2$ as the independent intensity transmittances for modes (A) and (B). In addition, we define Φ_A and Φ_B as arguments of the complex amplitude transmittances t_A and t_B. These arguments are the sums of two contributions: propagation of the mode in the bus waveguide $\Phi_{A,B}^{(\mathrm{WG})}$, and propagation of the waves in the resonator $\Phi_{A,B}^{(\mathrm{RES})}$, expressed from Eq.(2.5) as:

$$\begin{cases} \Phi_{A,B}^{(\mathrm{WG})} = \dfrac{2\pi}{\lambda} N_{A,B} L_{\mathrm{WG}} \\ \Phi_{A,B}^{(\mathrm{RES})} = \arg\left(\dfrac{\tau_{A,B} - a_{A,B} e^{j\phi_{A,B}}}{1 - a_{A,B}\tau_{A,B} e^{j\phi_{A,B}}} \right) \end{cases} \tag{2.52}$$

where $\phi_{A,B}$ is the single trip phase delay in the resonator for mode (A) and (B), respectively. From eq.(2.51), the intensity transmittance measured by a photodetector can be written as a weighted sum of T_A, T_B and an interference term T_{A-B}.

$$\begin{cases} T = \dfrac{1}{2}\left[\alpha T_A + (1-\alpha) T_B + T_{A-B}\right] \\ T_{A-B} = 2\sqrt{\alpha(1-\alpha) T_A T_B}\cos(\Phi_A - \Phi_B) \end{cases} \tag{2.53}$$

Examples of computed transmittance are displayed on Fig. 2.21. The difference between the effective indices of both guided modes is at the origin of a modulation of the enveloppe in the total transmittance. In experimental transmittances, such modulation reveals the existence of multiple modes in the microring and/or in the bus waveguide. This observation can also be confirmed by the presence of smaller, secondary or tertiary resonance peaks in the intensity transmittance.

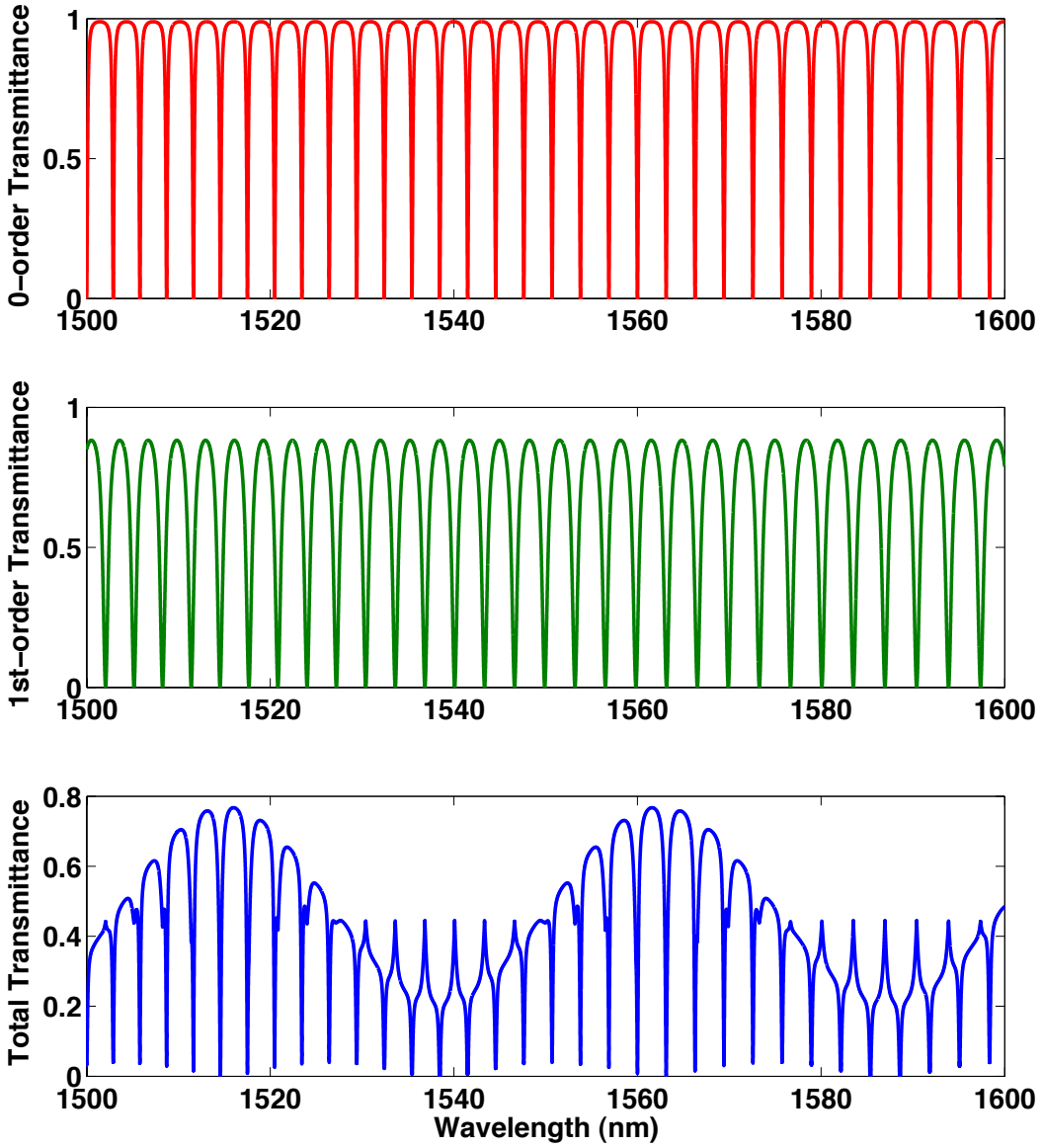

Figure 2.21: Transmittances of the fundamental and first-order propagation modes, and resulting total transmittance.

5 Numerical simulations of microring resonators

5.1 Challenges

Several numerical methods are used to simulate the behavior of light in photonic devices. the two most prominent methods are the Beam Propagation Method (BPM) where the propagation of light along an axis is determined via transfer matrices, and the Finite-Difference Time Domain (FDTD) method used in integrated optics to solve Maxwell equations in the simulated structure. BPM is interesting to use for straight waveguides because it is much faster and requires less memory than the FDTD method. For waveguides that are slightly curved such as in the arms of a Mach-Zehnder interferometer, BPM can provide accurate results using Padé approximants operators. However, for the study of ring resonators with circularly bent waveguides, BPM is not accurate enough to obtain satisfying simulation results. The FDTD method is currently the only method liable to provide accurate results for the response of a microring resonator and its application will be described in this section.

The FDTD method can be used firstly in a two-dimensional (referring to spatial dimensions) simulation, where a 3D guiding structure is transformed, via the effective index method, into a two-dimensional effective structure. The advantage of doing so is to considerably reduce the time of computation and the memory requirements in comparison to the direct simulation of a three-dimensional structure. Despite this simplification, the 2D-FDTD method is efficient to accurately model radial bending losses in the ring, and the exchange of optical power in the coupling region for lateral coupling configurations. However, the method does not take into account effects that are related to the vertical expansion of the evanescent field, mainly the losses to the substrate and cladding, which are particularly important in bended regions.

Also, the 2D-FDTD method is inherently unable to model the coupling region when the microresonator is vertically coupled to the bus waveguide. In such vases, where important phenomena take place in the vertical direction, only 3D-FDTD can provide accurate results. In situations when the use of the three-dimensional method is not entirely necessary, it is still interesting to some extent since this method provides higher accuracy. How-

ever, some phenomena such as surface roughness scattering are difficult to take into account because of the very high spatial resolution they require to model properly. As a consequence, even if the 3D-FDTD is probably the most accurate method for simulating microring resonator, experimental results are expected to differ from simulation results.

5.2 Application of FDTD method to ring resonators

5.2.1 Description

The FDTD method is a numerical method developed in its general formulation to solve sets of spatio-temporal differential equations, and is used in various fields of physics. In photonics, the FDTD method is used for the full resolution of Maxwell equations with associated boundary conditions applied to the components of the electromagnetic field. As a consequence, this method is extremely powerful to model a wide variety of linear or non-linear electromagnetic effects. In order to illustrate how the method is used, let us consider the simple case where the propagation of light in a waveguide is simulated. Typical preparatory procedure would be:

1. The structure of the waveguide, *ie* the refractive index distribution, or profile, is defined in two or three dimensions, depending on the simulation. Also, the refractive index distribution in the structure can be real or complex.

2. The computation grid is defined. This sets the spatial resolutions in each direction, the total number of calculation points and, partially, the memory requirements for the resolution.

3. The input electromagnetic field is defined. The envelope of field components can be chosen constant or time-dependent. It is also possible to choose between a point source or a plane source, where field distribution can be chosen to be Gaussian, or to match a mode of the waveguide, or any other distribution.

4. Observation points and observation planes are placed in the simulation window. Since the amount of memory required to record temporal evolutions of the field components during the simulation at each point of the grid would be too great, this is only performed for specified observation points. Once the simulation is complete, all neces-

sary information for a thorough analysis of the field structure at these specified locations can be retrieved.

Once the preparatory procedure is completed, the actual simulation can be launched. The final step is the analysis of simulation results. This step is particularly important and difficult because of the existence of several bias due to the numerical procedure. To that regard, some knowledge is required to properly interpret simulation results. In the following, the simulation procedure, choice of parameters and analysis of the results are further discussed.

5.2.2 Spectral and temporal responses

In FDTD simulations, an important choice is the control of the envelope of the input field. It can be constant or time-dependent.

In the case where the envelope of the input field is chosen as constant corresponds to the situation where the structure is excited by a continuous wave (CW) laser working at a specified wavelength and with a narrow spectral linewidth. These simulations are helpful to characterize the stationary phenomena, optical losses and coupling for instance, taking place in the simulated structure around a working wavelength. More generally, these simulations are well suited to study the distribution of light in the structure, which is of course of interest for the study of microring resonators. Also, it is possible to plot the intensity transmittance of such devices by repeating similar simulations with a varying wavelength for the CW input. However, this method would be far from optimal since it would require numerous repetitions of simulations that are already vastly time-consuming.

In order to study the spectral response of a device, it is much more appropriate to use an input field with a time-varying envelope, usually Gaussian-shaped. This corresponds to the experimental situation where the structure is excited by a pulsed laser with a specified center wavelength, and with a pulse duration that can be chosen arbitrarily small. At the specified observation points, the temporal evolutions of the components of the electromagnetic field will be recorded. These signals can be directly exploited in studying resonant structures to determine the value of

the single-trip optical path and of the phase delay at the center wavelength, and also to determine attenuation and coupling coefficients. Moreover, the Fourier Transform (FT) of the temporal signal can be used to determine, after normalization, the intensity transmittance of a structure. This method is much more time-efficient as the one using CW input and provides the same accuracy, provided that precautions are taken to avoid biases. Also, with observation planes, where the temporal signals are recorded, covering the entire structure, the simulations with a time-varying envelope induce then in one shot the equivalent of several CW simulations with varying wavelength. Thus, it can be used for microresonators to identify and study resonant and anti-resonant behaviors.

Simulations with a Gaussian-shaped time envelope input are associated with several conditions to guarantee the accuracy of the result. The first condition is to choose a pulse width in accordance with the wavelength bandwidth we want to study. The larger the bandwidth, the shorter the pulse which imposes the choice of a high resolution in time.

Secondly, when computing the Fourier transform of the time-dependent signals, the size of the time window, i.e. the time window during which the simulation takes place at the scale of the light propagating in the photonic circuit, is important. Indeed, from Fourier analysis it is well known that windowing biases the actual intensity transmittance: the multiplication between the time response and the window function result in the the convolution between the intensity transmittance of the device and a sinus cardinal (sinc) function, which is the Fourier Transform of the associated window function. Depending on the typical spectral width of the *sinc* function, inversely proportional to the width of the time window, characteristics of the intensity transmittance can be more or less distorted. For instance, intensity transmittances of straight waveguides will not be severely distorted because of their smooth appearance. On the other hand, intensity transmittances for resonant structures such as ring resonators can be strongly biased by windowing since the narrow resonance peaks they exhibit are particularly sensitive to the convolution with a *sinc* function, especially if the sinc function is larger than the resonance peak.

Another way to understand this effect on resonant structures is based

on the observation of the temporal signals corresponding to the transmitted waves. Those signals typically exhibit equally-distanced bumps corresponding to waves arriving at the observation point after traveling in the resonator for different amounts of cavity revolutions, with amplitudes exponentially decaying with time. No matter the resonator characteristics, if the simulation lasts (optical propagation time scale) only long enough to see the first two waves on the temporal signal, then the calculated intensity transmittance will be a sinus function, such as the one obtained in a two-wave interferometer. In the opposite situation, with a high number of bumps present on the simulated temporal signal, the calculated intensity transmittance will be close to the result obtained in the ideal situation where the time window for the simulation is infinitely long. An optimal choice of time window corresponds to the situation where the last bump before the end of the simulation window is barely above the noise level of the simulated signal. In that case, there is a guarantee that windowing will not affect the intensity transmittance more than numerical noise.

Because of windowing, the amount of simulation time necessary for a resonant structure with high quality factor can be several units to several tens of times larger than for non-resonant structure with comparable size. The direct consequence is the very large amount of computation time required to perform optimizations with limited hardware capacities.

5.2.3 Spatial and temporal grids

The spatial grid can be defined in the FDTD method applied to integrated optics as the set of points where the electric field is determined, while the magnetic field is distinctly determined at intermediary points, in equal number. In its simplest form, the spatial grid will be cubic, with equal or distinct spatial resolutions depending on the direction. However, it is possible to build a grid where more emphasis, in terms of simulation points, is given to specific regions that specifically require high resolution to model. This is particularly useful to optimize memory requirements and computation time. Indeed, these physical limitations of the hardware used for simulations make the use of FDTD difficult when resources are limited. In order to perform simulation in a realistic time scale, it is often necessary to make a trade-off between accuracy and resource use, and a good knowledge of the simulated structure is crucial to an adequate choice of grid,

limiting the amount of points while providing a good accuracy.

The first aspect to consider is the simulation volume, or spatial extension of the grid. The numerical bias of concern herein is that all components of the electromagnetic field are assumed to be zero outside the simulation volume. Because of this, a simulated wave propagating towards a border of the simulation volume will be reflected. This artificial reflection can subsequently interact with the simulated structure, creating important bias in the result. However, in state-of-the-art softwares performing the FDTD method, this specific problem is solved thanks to a technique called Perfectly Matched Layers (PML). The idea behind this technique is to automatically add thin layers at the borders of the simulation volume in order to cancel the reflection, the system of thin layers acting as a broadband, multilayer anti-reflector. However, PML technique does not change the fact that the electromagnetic field is set to zero outside the simulation volume. This is a problem if, for instance, the border of the simulation zone is too close to a waveguide supporting guided modes with large evanescent fields. In that case, the presence of the border will have two detrimental effects to the accuracy. The first effect is that the evanescent field of the weakly guided mode will be truncated, being arbitrarily set to zero at the border. Secondly, in addition to this distortion of the intensity distribution related to a guided mode, the presence of the border will modify its effective index, thus biasing the temporal signals. As consequence, in applications of microring resonators where large evanescent fields are essential, the volume of simulation should be carefully chosen, for instance so that truncated portions of the evanescent fields of guided modes do not exceed, for instance, 1% of the total modal intensity.

The second aspect is the spatial resolution of the grid. To that regard, ring resonators have very specific constraints to consider. If we consider the cases of straight or slightly curved waveguides, the spatial resolutions need to be high in the transverse directions of the waveguide, but the constraint is looser in the direction of propagation. Indeed, in these structures, variations of the field components along the propagation axis are small. However, for a strongly curved waveguides such as those constituting ring resonators, variations on small length scales occur in every direction. Then, if the simulated structure is a ring resonator coupled to a

straight bus waveguide, the resolution along the propagation axis of the straight waveguide will have to match those in the transverse directions. Also, an inherent difficulty of simulating planar resonators evanescently coupled to straight waveguides is that the resolution in the direction where the waveguides are close needs to be smaller than the gap separation. If not, the simulator will see the coupled waveguides as if they were in contact, which will significantly alter the properties of the coupler. In order to simulate a device with 100 nm gap separation, be it lateral or vertical, this means that the resolution in the gap direction should be in the range of 10 nm for accurate modelization and optimization. This range of spatial resolution would result, in most instances, in a number of simulation points too great to perform optimization procedures in a reasonable period of time, the optimization of the simulation procedure itself taking potentially several weeks for an ordninary computing station. Luckily, the ability to define a simulation grid with varying resolution allows one to perform simulations where the density of simulation points can be greatly increased in regions of interests: coupling regions and more generally regions where strong variations of the field components occur.

From these two considerations, we can partially conclude that in order to perform satisfying simulations of microring resonators, the simulation volume must be chosen large enough, and the spacings between the points constituting the simulation grid must be small enough, at least in regions with important variations of the refractive index distribution and/or field components. Thanks to grids with varying space steps, an accurate simulation of the evanescent coupling zone for microring resonators seems possible without too much influence on hardware resources consumption. However, a particularity of the FDTD method applied to integrated optics is the use of Yee's algorithm to solve discretized Maxwell equations, whose numerical stability is contingent on the respect of the Courant limit [56]:

$$\Delta t \leq \frac{1}{c\sqrt{(\Delta x)^{-2} + (\Delta y)^{-2} + (\Delta z)^{-2}}} \tag{2.54}$$

where Δx, Δy and Δz are the spatial steps, or resolutions, in the x, y and z directions respectively and Δt is the time step. From this expression, we see that if one of the three spatial steps is small compared to the others, then its effect will be dominant, and the smaller it is, the smaller the time step will have to be. As the time step can not vary from point to point,

this means that Δt will be chosen according to the smallest space step of the simulation grid. For the simulation of a ring resonator where the time duration should be chosen according to the time response of the device, the consequence of the Courant limit is the necessity to perform simulations with a very large number of time steps, increasing the actual time consumption of the simulation but not the memory requirements.

5.2.4 Gains and limitations

The use of the 3D-FDTD method on ring resonators is mainly limited by the high memory and time consumptions necessary to perform accurate simulations of these devices. These limitations mainly come from a particularly bad conjunction between the necessities of the numerical method and the accuracy requirements for the simulated devices. Because of this, the time requirement to simulate a device with typical size of 100 microns with sufficient accuracy on a personal computer at disposal was roughly from several days to one week's time. Moreover, a positive result, where the simulated device exhibits good intensity transmittance is often not obtained at the first trial. Even if finding a structure with decent characteristics does not require good accuracy, it can still take several weeks to achieve.

It was also noticed on several occasions that when trying to simulate structures that were subsequently fabricated and presented good experimental properties, the simulation results were very different from the measurements, and *vice versa*; and thus despite careful and precise measurements of the real structures during the fabrication process. Discrepancies between simulated and actual structures are easily explained by the fact that a small mismatch between coupling and losses tend to have important repercussions on the typical resonance contrast. Then, sources of optical losses that are difficult to simulate with FDTD, such as surface roughness scattering, are important for device fabrication as they will modify the fragile equilibrium between coupling and losses, thus creating large differences in behavior between simulated and fabricated devices.

From these observations, the idea to optimize a device using 3D-FDTD simulations might be wrong. In any case, related difficulties are strong motivations to look for other efficient techniques to simulate microring

resonators. It was also clear that in most cases, it was probably much easier and more efficient to optimize devices by repetitions of prototypes in fabrication-characterization cycles than via numerical simulations. However, the use of simulation tools is probably relevant for further understanding of various effects taking place in the structure, and can be of interest in its applications, such as nonlinear effects. The development of analytical tools can allow to model very specific aspects of the microrings, the sensitivity to a modification of the surrounding refractive index for instance, or optical loss sources. Indeed, simulation methods such as 3D-FDTD can yield reference results for the validation of analytical models [57].

5.3 Numerical simulation of internal parameters

Simulations of microring resonators can be roughly reduced to the calculation of three key elements: waveguides dispersion, coupling and optical losses. In order to quantify these effects, analytical expressions exist and can be used to orientate the design of the device: geometry, materials, radius of curvature, etc ... However, the accuracy of these expressions is difficult to evaluate, making accurate predictions on the behavior of a modeled device not realistic. To that regard, state-of-the-art numerical methods such as 3D-FDTD may achieve accurate simulations, but discrepancies between the simulated and fabricated structures are too great for validation or contradiction. Still, numerical methods might be of great help, not in the optimization of a proposed structure, but in the test and comparison of very different structures for microresonators. They can be used to determine which coupling configuration should be chosen, or what waveguide or cavity shape minimizes the optical losses. The problems raised before with 3D-FDTD, the only method that can provide accurate results for all possible configurations, are related to computation facilities at disposal. These limitations require to seek time and cost-efficient ways to model microresonators.

5.3.1 General approach

The overall description presented at the beginning of this chapter shows that the knowledge of the coupling coefficient, the attenuation factor and the waveguide dispersion are required to determine the intensity transmittance of a microresonator. Instead of calculating these parameters from

analytical expressions, it is possible to use various numerical methods to fully or partially determine them, so that they can be injected in the analytical expressions for the intensity transmittances and related parameters: Q factor, FSR, finesse and contrast.

5.3.2 Effective indices

The dispersion of the waveguides constituting the microresonators are probably the easiest aspect to model. Analytical models such as the effective index method can be applied to various guiding structures: rectangular, rib, ridge, etc ... Moreover, they can also manage to determine the complex effective index of guided modes in curved waveguides [58], with a good accuracy. But beyond the effective index of guided modes in straight or curved waveguides, it is important for the determination of optical losses and coupling properties to calculate the modal distribution of intensity in the waveguides, which is in most cases only possible with numerical mode solvers.

Among numerical methods used to solve modes, the Alternating Direction Implicit (ADI) method - a finite difference method for solving parabolic and elliptic partial differential equations - proved effective to determine the entire modal structure of most straight waveguides. The method, thanks to a conformal transformation [59], can be also efficiently applied to curved waveguides.

5.3.3 Estimation of optical losses

Via BPM The BPM method is only accurate to simulate straight or slightly curved waveguides, with angles roughly smaller than 10 degrees. Accordingly the method cannot be used to study the propagation of light and losses in an entire ring resonator. However, the method can be easily used to model the transmission of the straight bus waveguide, and the associated propagation losses as well as the parasitic reflections that occur on both ends of the waveguide.

Via FDTD The FDTD method can be used to determine the sum of bending losses, cladding and substrate losses in ring resonators by adequately positioning observation planes perpendicular to the waveguide constituting

the ring. Associated intensity attenuation factor is determined by comparing values of the intensity distribution integral in the selected observation planes. These simulations are fast since they do not require large amount of points and a long propagation time. In addition, the optical loss at the junction between a straight and a curved waveguide, in a microracetrack resonator, can be determined thanks to the calculated value of the loss coefficients due to the propagation in the bended region.

Concerning the coupling losses, they can be determined by placing observation planes perpendicular to the waveguides before and after the coupling region. In a method similar to the one used to calculate propagation loss, the integration of optical intensity distribution in both observation planes will provide after comparison an estimated value of the coupler intensity-insertion-loss coefficient γ (2.2).

5.4 Estimation of coupling coefficients

Via BPM BPM is efficient to model the coupling between straight waveguides, which occurs in microracetrack resonators. The method can also be used to optimize a MMI coupler replacing evanescent coupler. However, it cannot be used to study the delicate matter of the evanescent coupling between the bus waveguide and the curved portions of the racetrack resonators, or the curved waveguide forming a ring resonator, which can only be numerically solved by the FDTD method.

Via FDTD With FDTD, calculating the transmitted and coupled intensity at the coupler is also achieved by positioning observation planes and spatially integrating the intensity distribution computed at these planes. For the transmission coefficient, planes are positioned on the straight waveguide before and after the coupler. For the coupling coefficient, planes are positioned on the straight waveguide, before the coupler, and along the microresonator, as far as possible from the coupler. Retrieving the value of the coupling coefficient is more complicated than the transmission coefficient since it is necessary to take into account for the latter the propagation loss coefficients, the loss at the junctions in the case of microracetracks. However, for boths, the accurate value is only obtained if the intensity-insertion-loss coefficient is taken into account.

Conclusion

In this chapter were presented models and simulations of passive microring and microracetrack resonators. A comprehensive list of effects susceptible to occur in such photonic devices was established, and a rough estimation on how each effect influence the microresonators response in various situations was performed.

Following this study, typical analytical model for the microring resonator, providing expressions for the intensity transmittance and its characteristics as functions of internal parameters, was presented and discussed. Roles of the total amplitude loss factor a and the internal amplitude transmission coefficient τ on the main optical characteristics: contrast, Q factor and maximal intensity slope were specifically examined. Conclusions on the values these two parameters should have to yield the best performances of microresonators, depending on the application, were drawn.

Since a and τ play significant roles in optimization of the devices, parts of the chapter were dedicated to establishing analytical expressions and numerical simulation techniques, in order to calculate and predict their experimental values.

Analytical expressions of the internal parameters suggest wavelength-dependent behaviors of the microresonators that are not accounted for in a typical "starting-point" model. As consequence, additions to the initial model were suggested, and corresponding effects were simulated.

Finally, the use of both Finite-Difference Time-Domain (FDTD) and BPM methods applied to the study of microresonators, specifically microrings and microracetracks, was discussed. One of the major conclusion emerging from this part is the absolute necessity to confront models and simulations to experimental results.

The experimental verification of the developed models of microring and microracetrack resonators has to do with both fabrication and analysis of the experimental data. These aspects are the subjects of the next two chapters.

Chapter 3

Fabrication of microring resonators

Introduction

Fabrication plays a decisive role in the performances of microring resonators, with consequences on the quality of the device for any kind of application. In many cases, large defects of the guiding structure, introduced during the fabrication process, require to modify the design of the resonators. Necessary changes can be related to materials, to patterning techniques and also to the geometry of both waveguides (height, width, ...) and microcavity (radius, coupling length, ...). Moreover, the quality of hand-made micrometric devices can be inconsistent because of the difficulty to exactly reproduce decisive steps of the fabrication procedure, such as thin-film deposition or mask alignment. Consequently, the main challenge related to fabrication is to find a working combination between design and fabrication technique. A second challenge is then to gain enough control of the whole fabrication procedure to obtain repeatable optical performances of the microresonators. Another important aspect to consider is the repeatability of experimental results, more specifically in bio-chemical sensing experiments. For these applications, the physico-chemical state of the surface is very important, and can be very easily deteriorated. In these situations, careful handling of the devices after fabrication is equally important to obtain repeatable experimental behavior of the microresonators.

In order to demonstrate the relevance of a microresonator design and of the associated fabrication procedure, performances of a device as well as the repeatability of its behavior in application are necessary, and sufficient. However, for the next levels of device development, towards a working prototype that could meet potential customer needs, constraints may be

different. For instance, the performances of a device are always to be examined in relation to its fabrication cost, which is *in fine* mostly dependent on the materials and the fabrication procedure required by the design. To that regard, though the question: "Is it really worth it ?" is difficult to answer in some cases, it should be at least part of the design considerations. Robustness of the fabricated devices can also be an important issue for targeted applications.

Also, depending on the application, the microresonator can only be a small part of a much more complex system. When the resonator is the key element, the fabrication of the whole system is dependent on the design of the microresonator. As consequence, another design consideration related to the fabrication should be the ease of integration, especially for label-free biosensors, requiring an association of the optical device with microfluidics and thus forming an optofluidic device. A design achieving promising preliminary results but that would not be suited for integration in larger systems would have to be rejected for most applications.

1 Fabrication Procedures

1.1 Introduction

Over the last years, numerous techniques have been proposed to produce microring resonators. The variety of existing procedures is related to the variety of materials that can be used, and also to the numerous options available in terms of profiles of the waveguide geometry (rectangular, rib, ridge, slot, ...) and of coupling configurations (evanescent or MMI, lateral or vertical).

In this work, for practical reasons, but also with the idea to build high-quality and low-cost prototypes of microring devices, all fabrication procedures were based on near-UV lithographies as patterning technique. The main limitation of near-UV lithography is the poor lateral resolution (500 nm at best) of the technique for patterning. In consequence, fabrication of laterally-coupled microring resonator, requiring lateral resolutions in the 100 nm range, is practically impossible with this technique. As discussed before, lateral MMI coupling configuration could however be used. This

limitation rapidly appeared to be more of an advantage than a constraint. Near-UV lithography is cost efficient and easy to handle, but more importantly very versatile. Indeed, there is a large variety of photoresists with excellent optical and mechanical properties. Also, thanks to lithography mask aligners, three-dimensional patterning of the structure is relatively easy, specifically for the fabrication of vertically-coupled microring resonators. This is particularly important for bio-chemical sensing applications where the gap between the ring and the bus waveguide should not be modified by the analyte [18]. In addition, near-UV lithography introduce very moderate surface roughness, which can be the dominant source of optical loss in the microresonator. Other lithography techniques such as e-beam or nanoimprint, in comparison, produce much more surface roughness, and usually require additional steps such as thermal reflow [52] in order to achieve good optical characteristics of the microrings.

The fabrication of planar microresonators using UV lithography as presented in this chapter, is based on the conjunction of several procedures: spin coating, UV lithography direct or indirect patterning, Reactive Ion Etching (RIE) and, as an usual final step, wafer slicing.

1.2 Spin coating

1.2.1 Presentation

Spin coating is a very well established method used to deposit uniform thin films (over 200 nm) and ultrathin films (under 200 nm) of polymer materials to planar substrates. It is most often employed in the microelectronics industry to produce photoresists films with thicknesses in the micrometer range. A machine used for spin coating is usually called a spin coater.

Before the spin coating process, an excess of diluted solution containing monomers, building block of the selected polymer, is first deposited on the substrate, typically from a syringe. Then, the substrate is accelerated to a desired, high rotation speed. Owing to the centrifugal force, the solution flows radially and excess is ejected off the edge of the substrate. During this ejection phase, the film thinning can be considered to be only due to the radial, outward flow [60]. After this initial stage, the film becomes essentially immobile because of a dramatic rise in viscosity due to solvent

evaporation. Further thinning of the film is then due solely to solvent evaporation. Once spinning is complete, the substrate can be deposited on a hot plate to the small quantity of solvent remaining in the thin film.

Since the thinning is related to both fluid rheology and solvent evaporation, the final thickness of the film will depend on numerous physicochemical parameters of the solution: concentration, viscosity, volatility of the solvent, ... The final thickness will also logically depend on the three parameters of the spin: the acceleration phase, the stationary rotation speed and the spinning time duration applied to the substrate. Depending on these parameters, the range of achievable thicknesses with spin-coating, depending on the material, can go from 10 nm to 200 μm.

Several models of thin film deposition by spin coating exist [60, 61, 62] and are successful in predicting experimental thicknesses. These models are useful in order to optimize spin coating procedures with custom made solutions. For commercial solutions, optimization usually starts from provided technical information, where typical process is explained in details and graphs indicate which rotation speed shall be chosen to obtain a targeted thickness, with usually sufficient accuracy. Further control of the deposited film thicknesses and quality rely on experiential knowledge.

1.2.2 Undesired effects

During a spin coating procedure, a few undesirable effects always occur and special care is required to diminish their consequences. The first class of undesirable effects produce defects in the films at random locations, such as typical comet-shaped inhomogeneities. These defects can be created by the presence of small bubbles in the solution. Also, they can occur in the presence of impurities such as dusts or particles trapped in the film. These are usually present initially on the surface of the substrate, or can be introduced during the spinning steps.

In Fig. 3.1, pictures show that impurities create large local variations of thickness, which is particularly detrimental in (b) and (c) because defects are located on the waveguides. The worst case scenario is presented in picture (c) where a defect on the surface caused a nitrogen (N_2) or air bubble to be trapped in the deposited film during the spin coating. It is also

noticeable that previous irregularities of the surface, for instance due to the presence of rectangular waveguides, have a tendency to trap impurities during the spin coating procedure, which is the most problematic point.

In Fig. 3.2 are presented examples of defects introduced by the presence of bubbles from different sizes. In picture (a), a large number of tiny bubbles created by the syringe filter used to transfer the solution to the substrate cause important surface roughness, each bubble being at the origin of a typical comet-shaped defect. In picture (b), larger bubbles caused almost periodic defects in an insulating thin film. Far from the waveguide, they have little consequence, but defects located on the waveguide can cause severe alterations of the propagation of light such as backward reflections and strong stress-induced birefringence. A few useful precautions to reduce the number of occurrences of these defects are described in 3.4.

A second class of undesirable effects are related with non-uniformity of the film thickness, and with the spatial distribution of the deposited material on the substrate. For instance, a resist volume which is too small to cover the whole surface of the wafer can result in uncoated areas on the substrate, also called striations. A more recurrent problem is the formation of so-called edge beads forms, *ie* zones located near the edges of the substrate where film thickness dramatically increase because of border effects. Edge bead formation can infer numerous detrimental effects. For instance, it creates a variation of film thickness from the center to the outer part of the substrate that can be relatively important. Also, for photoresist layers, edge beads can stick to the lithography mask, making the achievement of a minimal gap separation between the mask and the resist during exposure impossible, with a reduced lateral resolution as a result.

Ultimately, the spin coating procedure can only work if there is enough adhesion between the substrate and the solution, which is classically obtained when both are hydrophobic or hydrophilic. Adhesion issues can specifically occur when producing multi-layer structures, since the different materials may not be compatible. Insufficient adhesion can result in strong non uniformity of the thickness of the film, with regions, usually in the outer parts of the substrate, where no material is deposited. In the worst case scenario, no material is actually deposited on the surface. In order to

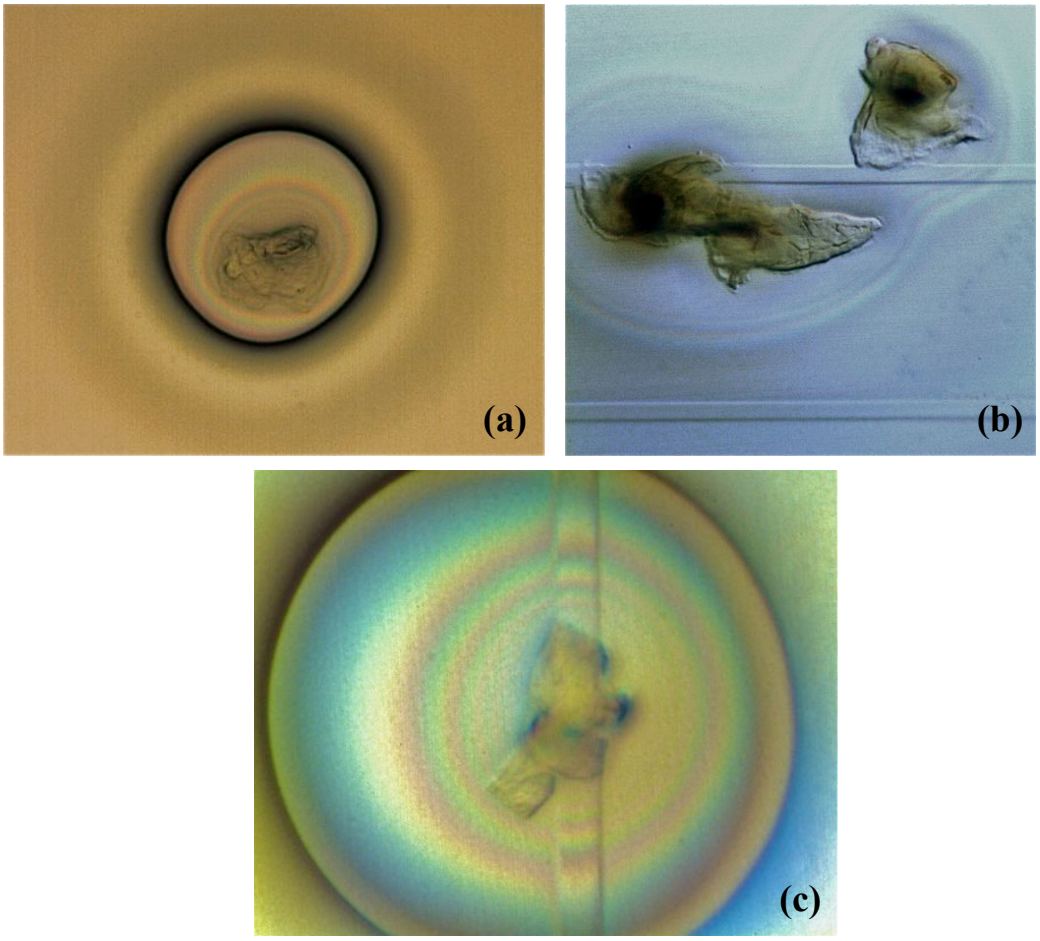

Figure 3.1: Examples of thin film defects produced by impurities.

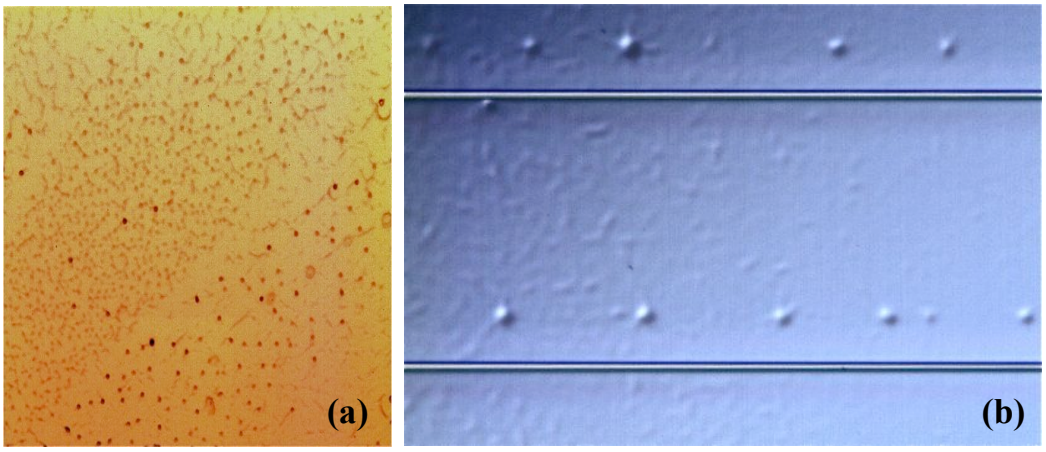

Figure 3.2: Fabrication steps for a SU-8 vertically-coupled ring resonator

improve adhesion between incompatible materials, an adhesion promoter such as Hexamethyldisilazane (HMDS) can be used. Other satisfactory solutions consist in modifying the surface state of the substrate via low power plasma treatment for surface activation.

1.2.3 Typical procedure

All polymer films produced in the scope of this dissertation where so from commercial solutions. The thin films where fabricated from a Karl Suss RC8 spin coater, in ENS Cachan cleanroom facility. Different class of materials where deposited: SU-8 for negative photoresists, S18 for positive photoresists, silica sol-gels (SOG), and fluoropolymers (CYTOP). For each solution, the starting point in finding an optimal procedure was to rely on the technical information. Then, procedures were individually adapted to each solution in order to meet specific requirements: optimal adhesion, stronger solvent evaporation, better thickness uniformity, etc ... To do so, theoretical and empirical knowledge were equally important.

In general, the SU-8 photoresist [63] was extensively used in the scope of this dissertation. First as core material for the waveguides, it was deposited in thin films with thicknesses varying between 500 nm to 5 microns, then was either directly (rectangular waveguides) or indirectly (rib waveguides) patterned with near UV lithography (see 1.3). The specificity of the procedure optimization was in that case to control thicknesses of the fabricated films. It was also to obtain, with good reproducibility, surfaces with minimum defects, those being very detrimental to the waveguides, and difficult to detect from control tools. This material was also used to build molds for the fabrication of microfluidic channels. Compared to the "optical" films, the SU-8 films fabricated for microfluidics applications were much larger, with thicknesses between 20 and 150 microns. It implied to use SU-8 solutions with much higher viscosities, thus requiring adaptation of the fabrication process. However, as compared to optical elements, the advantage of microfluidic elements is their relatively large scale, which make the constraints on film uniformity and cleanliness less severe. Also, defects of microfluidics elements have usually much less impact on the overall behavior of an optofluidic device than defects on optical elements, especially on microresonators. Finally, non patterned layers were fabricated in order to perform experiments on the surface functionnalization of

SU-8, where the thickness did not matter, but where the regularity and perfect cleanliness of the surface was crucial for reproducibility of the results.

In the following, a typical spin coating procedure to produce 2-μm-thick SU-8 films for optical elements is roughly presented:

1. The starting point of any spin coating procedure is to know which material to deposit, and which value of the film thickness to obtain. This questioning may extend to additional parameters, such as density of the film and thickness homogeneity.

2. The targeted thickness gives usually enough information to select a solution with appropriate monomer concentration and solvent type. From technical information or self-obtained measurements, an adequate rotation speed can then be chosen. Situations where two or more solutions are known to provide the targeted thickness can occur. In such case, the selected solution should be the one that achieves the targeted thickness with the higher rotation speed, usually corresponding to the solution with the higher viscosity. This choice optimizes thickness uniformity of the film on the substrate.

3. As part of the preparation of spinning, the substrate is positioned on the holder and maintained in place thanks to aspiration from a vacuum pump. It is important to center the substrate on the holder to obtain a thin film with radial symmetry. The solution, previously loaded in a syringe, is filtered to remove impurities and transferred to the surface of the substrate. Additionally, specificities of the spin coating process (speeds and durations) are entered in the spin coater. Then, the spinning procedure can be started.

4. The "spread" step is a phase where the rotation speed is low (500 rpm, typically). The solution is spread on the wafer so that it uniformly covers the whole substrate surface. The time duration of this "spread" step, in the range of seconds, depends on the viscosity of the solution. The acceleration is usually chosen as low, typically 100 rpm/s.

5. The "spin" step corresponds to the phase of high speed rotation. For the "spin", typical acceleration is chosen between 300 rpm/s and 1000 rpm/s. Depending on the targeted thickness, the stationary rotation speed can extend from 800 to 4000 rpm. Using speeds lower than

800 rpm usually results in poor thickness homogeneity, whereas 4000 rpm corresponds to a limit of the spin coater. The duration of the spin is about few tens of seconds, which is usually long enough for the solvent to almost completely evaporate.

6. The "soft-bake" step. After deceleration, substrate is removed from the holder and deposited on a hot plate at temperatures from 65 to $115°$C, for one to three minutes. On some occasions, the soft-bake step can be skipped but for photoresists, it is quite important for stabilizing the surface and to evaporate solvent remains trapped in the thin layer.

7. If the thin layer is meant to be kept as is at the end of the soft-bake, the substrate goes directly into a oven for an hard-bake step, where it is cooked at temperatures between $100°$C to $200°$C for durations from 30 minutes to 3 hours. The purpose is to fully cross-link the polymer material, hence to make it very resistant to degradations from further fabrication steps, or from utilization. However, if the film is meant to be patterned by UV lithography, the hard bake step will be realized after patterning.

The higher is the speed, the best is the homogeneity. The last parameter is the duration of the coating step. This parameter has an effect on the solvent evaporation. As a result, depending on this parameter, it is possible to modify the amount of solvent that will remain in the layer. This has both an effect on the refractive index of the layer and its thickness, though both modulations are not strong (few percents).

1.3 UV lithography patterning

1.3.1 Presentation

UV lithography (also called "photolithography" or "optical lithography") is a fast, versatile and low-cost method used in microfabrication for patterning bulk substrates or thin films, typically deposited by spin coating and with thicknesses up to 100-150 μm. It uses UV radiation to transfer a two-dimensional geometric pattern previously imprinted on a "photomask", or lithography mask, to a light-sensitive chemical "photoresist", usually a polymer, in the form of a thin film deposited on a substrate. After exposition, the photoresist film is plunged in a developer bath, where the

three-dimensional pattern engraved in the film is revealed. In analogy to photography, a photoresist is said to be positive if only the portion exposed to UV is soluble in the developer, and thus removed. In opposition, a photoresist is qualified as negative when its exposed portions become insoluble in the developer. Thus, only the unexposed parts are removed. Comparison between two typical negative and positive tone resists is presented in Tab. 3.1 [1].

Characteristic	**Microchem SU8-2000**	**Shipley S18**
Tone	Negative	Positive
Relative Cost	Less expensive	More expensive
Developer Base	Organic	Aqueous
Lateral Resolution	1	0.48
Step Coverage	Lower	Higher
Wet Chemical Resistance	Excellent	Fair
Adhesion Strength Si/Glass	Higher	Lower
Aspect ratio	> 20	Higher

Table 3.1: Comparison between two typical negative and positive photoresists.

Patterning positive or negative photoresists from photolithography is a straightforward technique and can be referred to as direct patterning (cf. Fig 3.3).

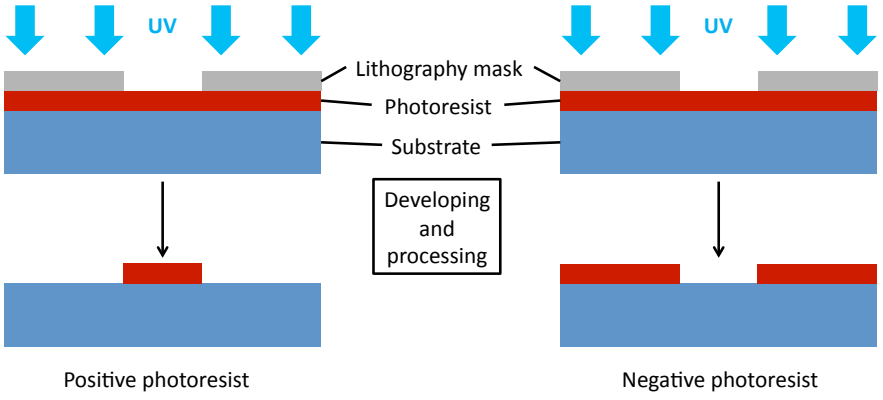

Figure 3.3: Direct patterning of a photoresist material.

UV lithography is also used to indirectly transfer a pattern to any material, not just photoresists, that can be chemically etched by a liquid ("wet"

[1]Comparison is made from technical information and generalizations usually accepted in the MEMS fabrication industry, physical properties of photoresists being in most instances unavailable

etching) or a plasma ("dry" etching), using RIE for instance. In that case, a photoresist is deposited on top of the layer to be patterned. A first pattern is transferred via lithography to the photoresist. Then, the whole surface is put in contact with a physical or chemical etchant. During the etching steps, only the parts of the initial layer that are not covered by the photoresist will be removed, the other regions being physically protected from the etchant by the photoresist (cf. Fig 3.4). After etching, the remaining photoresist is removed with an adequate solvent. The final pattern obtained on the film is complementary to the one applied to the photoresist.

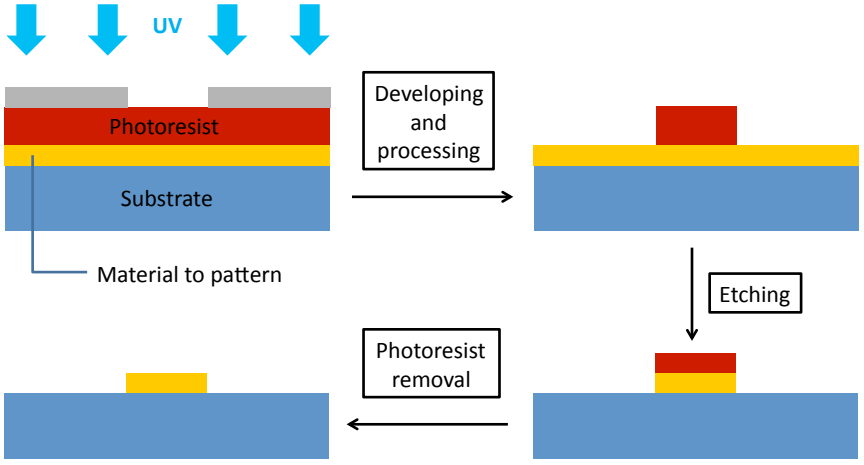

Figure 3.4: Undirect patterning of a etchable material via negative photoresist.

1.3.2 Limitations

The actual limitations of photolithography in terms of resolution are almost entirely related to the diffraction that takes place in the exposure system. In maskless lithography, which includes laser writing and interference lithography, the resolution is limited by the focusing volume. This is also the case in projection exposure, where current state-of-the-art photolithography systems use deep ultraviolet (DUV) light from excimer lasers with wavelengths under 250 nm, and large NA optical systems allowing resolutions down to 50 nm. Projection systems are specifically used for Very-Large-Scale-Integration (VLSI) systems, mostly because of the large size of the substrates that makes other techniques difficult to use.

In research, contact or proximity lithography is often employed since it uses inexpensive hardware and can nevertheless result in high optical res-

olution. In such lithography, the photomask, usually a square fused quartz substrate covered with a patterned layer of chromium, is positioned in direct contact or near the photoresist thin film, covering the entire surface of the substrate. The chromium layer blocks the collimated light from the source, thus positively or negatively transferring (depending on the tone of the photoresist) its pattern to the thin film.

The optical resolution in contact or proximity lithography is limited by Fresnel diffraction on the edges of the individual chromium patterns, and can be roughly expressed as:

$$\Delta x = \sqrt{\lambda D} \tag{3.1}$$

where Δx is the lateral resolution, λ is the limiting wavelength, and D is the distance between the chromium layer and the photoresist. According to this expression, a better resolution is obtained with shorter wavelengths, and when the film is thin and as close to chromium as possible. Fresnel diffraction has a typical distortion effect on the vertical edges, waveguides sidewalls for instance, in the patterned film. In Fig. 3.5, a SEM image partially shows the distorted sidewall of a 2 μm thick fabricated rectangular waveguide approximately.

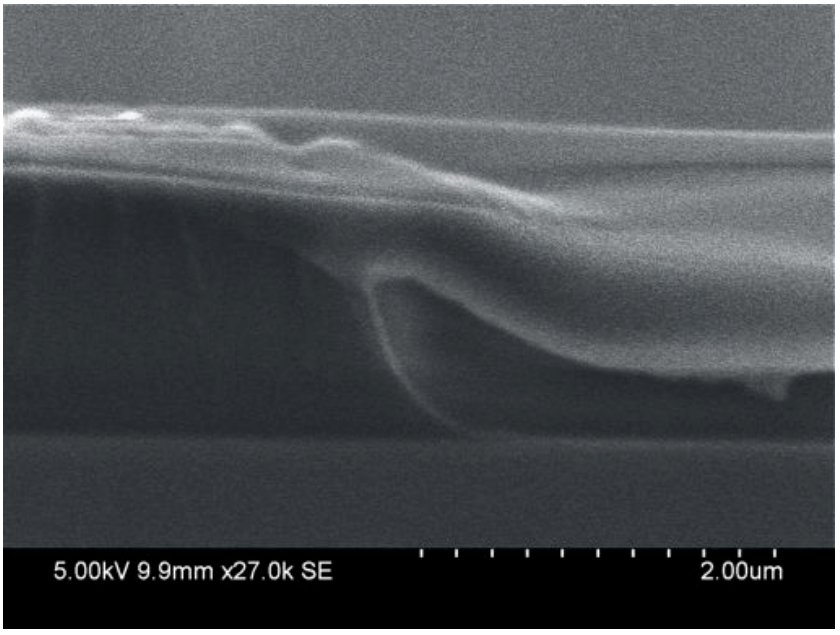

Figure 3.5: SEM image of an edge of a rectangular waveguide produced by direct photolithography patterning

The actual shape of the waveguide sidewall is due to a combination of Fresnel diffraction and of the photoresist threshold, *ie* the minimal optical power applied to the resist so that the exposed region remains (when negative), or is removed (when positive), during development. As a consequence, distortion of the edge and lateral resolution will depend on the resist itself, on the exposure system, on the the exposure duration, on development duration, and finally on the thickness of the photoresist film.

When patterning is indirect, the final result will also depend on the etching method used to remove unwanted regions of the thin film or bulk material. Naturally, wet etching is an isotropic process (for isotropic materials), tending to etch the material in any direction, thus resulting in negative sidewalls: base of the waveguide is thinner than the top. However, such isotropic etching, well controlled by etching duration, can be used to produce waveguide pedestals in order to reduce optical losses to the substrate for rectangular waveguides. In opposition, any plasma etching techniques, if the parameters are chosen correctly, are strongly anisotropic and etch the film mostly vertically, thus reproducing the pattern on the photoresist with a better fidelity.

Besides the issue of lateral resolution, a very important aspect of this fabrication procedure applied to waveguides is the adhesion between the photoresist, and/or the material to indirectly pattern, and the substrate. The quality of adhesion is generally quantified by the adhesion strength, a surfacic force usually expressed in Pascals (Pa). Thus, for a given adhesion strength, the total force maintaining an individual pattern on its substrate is proportional to its surface. Because they are usually long (few cm) and laterally thin (1 to few μm), waveguides are particularly sensitive to any force that may apply locally to them, such as stress due to the expansion or contraction of the waveguide material and/or the substrate, and even buoyancy in the developer solution. For waveguides with widths that are too small relatively to the adhesion strength, the insufficient adhesion will result in a partial of full detachment of the waveguide, either during development or during later stages of fabrication. The adhesion strength, if small, can thus be a more crucial limiting factor to the smallest achievable waveguide width than the lateral resolution of the lithography.

With the equipment available in our clean room facility, the minimal width obtained for 2 μm thick SU-8 waveguides constituting the microrings was three microns, several times larger than the value allowed by lateral resolution of near UV-lithography.

1.3.3 Typical procedure

Photolithography was mainly employed to pattern SU-8 or S18 films, either directly or indirectly, using mask aligners from Karl Suss, the MJB3 for microfluidic elements and the MJB4 for optical elements, the latter allowing easier and more reproducible alignment of different levels of patterning, necessary to build vertically coupled microresonators. These apparatus perform lithography by shining UV radiation, for a controlled exposure duration, through a photomask (cf. Fig. 3.6) in contact with the photoresist film. Depending on the applied pressure between the substrate and the mask, the contact can be soft or hard. Hard contact yields better lateral resolution but can deteriorate the mask more rapidly than soft contact.

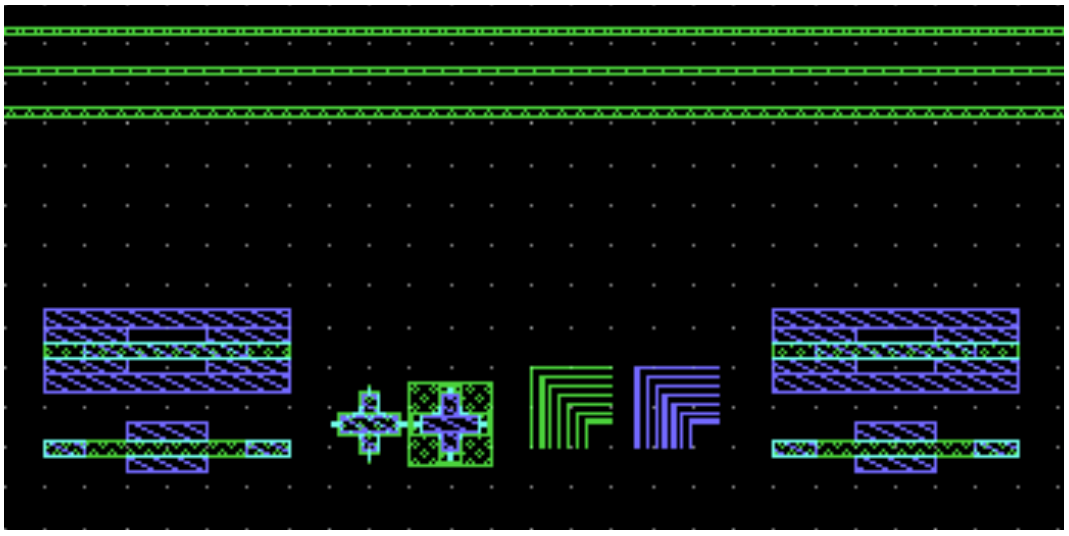

Figure 3.6: Schematics of two superimposed photomasks for the fabrication of vertically-coupled microresonator. In the bottom, marks are applied to both masks in order to align the first green patterns to the blue patterns on the second-level mask.

In all situations, the resist films where obtained from spin coating procedures such as described in 1.2. Exposure to UV takes place right after pre-bake of the resist where solvent remains are driven off. When needed,

the photomask is then aligned with patterns previously formed on the substrate using alignment marks (cf. Fig. 3.6).

For a two-micrometer-thick photoresist layers, the exposure duration is typically around ten seconds. Exposure duration is particularly important when patterning waveguides on negative resists. Indeed, if it is too short, corresponding to under-exposure, a thin layer of resist in contact with the substrate will not be sufficiently exposed and will be removed during development, thus detaching the whole waveguide. The consequence of over-exposure is less dramatic: an exposure duration that is too long results in a widening of the base of the waveguide due to Fresnel diffraction (cf. Fig. 3.5).

After exposure, a second bake, the *post-exposure bake* (PEB), is performed in order to catalyze either the chemical reactions responsible for the cross-linking of negative resists [64], or the deprotection reactions making the exposed positive resists soluble in their developer. SU8-2000 commercial solutions are composed of SU8 dissolved in an organic solvent, the gamma-butyrolacton (GBL), and photosensitized with triaryl sulfonium salt in propylene carbonate solvent, allowing protolysis in the wavelength range of conventional broadband mask aligners [65]. The photo-acid thus formed during exposure is responsible for the cross-linking of SU8 molecules. The reaction kinetics of the cross-linking reaction is very slow at room temperature. The temperature of the PEB is chosen as high enough to substantially increase the reaction kinetics, but not so high that cross-linking may occur in unexposed regions of the film. The typical PEB applied to exposed SU-8 films was 1 minute at $65°C$ followed by 1 minute at $95°C$. In thick SU-8 structures, PEB is also known to reduce the effects of interferences occurring in the photoresist film due to partial reflections of the exposure light, by increasing the diffusion length of the photo-acid.

Before developing the film, it is usually necessary to let it cool down after PEB in order to avoid strong thermal variations when it is plunged in the developer solution. Typical duration of the developer bath is one minute, during which the developer solution can be smoothly agitated above the film. Then, the development is stopped by plunging the film in a second bath, isopropanol for SU-8 films and DI water for S-18 films.

In the case of a direct patterning, the subsequent and final step is a hard-bake of the resist, which is meant to further solidify the resist in order to make it more resistant to chemical or physical degradation. In case of indirect patterning, the resist first undergoes an etching procedure. Potential remains are then removed by a resist stripper. Contrary to direct patterning, the procedure does not need to end with a hard-bake since the patterned layer already underwent such a step before resist deposition.

1.4 Reactive Ion Etching (RIE)

1.4.1 Generalities on etching

Etching is commonly used in microfabrication to chemically remove full or partial layers of materials from the surface of a wafer during manufacturing. For many etching steps, a part of the wafer is protected from the etchant by a protective material which protects the material underneath from the etchant. As described before in an indirect patterning procedure, the protection layer can be a photoresist previously patterned using photolithography.

If the purpose of etching is to remove a thickness of a material, control of the depth of the etch is achieved using the etching time and the etch rate, known from calibration. In most situations, it is preferable that etching does not affect the protection layer. This ability, referred to as selectivity of the system, depends on the ratio between etch rates of the material to etch and that of the protecting layer material.

Another issue in etching is the sharpness of the sidewalls in the etched material. In most situations, straight sidewalls are desired to produce well-controlled features, which means that the etch needs to be anisotropic. A perfectly anisotropic etching will have a non-zero etch rate only in the direction normal to the substrate.

Wet etching techniques, using liquid-phase etchants, are mostly isotropic when applied to isotropic materials. This characteristic usually disqualifies them from any use in the fabrication of optical waveguides, where the control of the transverse geometry is important. For the same reason, modern

VLSI processes avoid wet etching, and use plasma etching instead. Indeed, plasma etchers can control etching anisotropy by adjusting parameters of the plasma.

Ordinary plasma etchers, with typical pressures between 0.1 and 5 Torr (1 Torr $\cong$ 133.3 Pa), produce energetic, free and neutrally charged radicals that react with the surface of the wafer. The source gas for the plasma usually contains small molecules rich in chlorine or fluorine. For instance, carbon tetrachloride (CCl_4) etches silicon and aluminium, and trifluoromethane etches silicon dioxide and silicon nitride. Since neutral particles attack the wafer from all angles, the etching process obtained is isotropic. In opposition, ion milling, or sputter etching, uses lower pressures, often as low as 10^{-4} Torr (10 mPa). Materials are bombarded with energetic ions of noble gases, such as Argon, which hit atoms from the substrate by momentum transfer. The ions tending to approach the surface from one direction, this process is more anisotropic than regular plasma etching [66].

1.4.2 Description

With operating pressures between 10^{-3} and 10^{-1} Torr, Reactive-ion etching (RIE) can be considered an intermediate between sputter and plasma etching, and is commonly used in microfabrication.

A parallel plate RIE system consists of a cylindrical vacuum chamber, with a wafer platter located in the bottom portion of the chamber. The wafer platter is electrically isolated from the rest of the chamber, which is usually grounded.

A RIE system such as the one available in ENS Cachan clean-room facility is composed of a cylindrical vacuum chamber with a wafer platter located in its bottom. Gas enters through small inlets in the top of the chamber, and exits to the vacuum pump system through the bottom. Types and amount (quantified by flowrate) of gas vary depending upon the etch process. Typically, oxygen is used to etch polymers. The pressure in the vacuum or plasma chamber is typically maintained between a few mTorr to few hundreds of mTorr, integrating gas flowrates in a valve position control of an exhaust orifice. The plasma is generated by applying a RF powered

electromagnetic field to the wafer platter, with a power of few hundreds Watts. Gas molecules, stripped of their electron, are ionized, creating a plasma. From the action of the oscillating electric field, liberated electrons are moving up and down in the chamber. Meanwhile, the movements of the much heavier ions are not affected by the RF electric field. When electrons are absorbed into the chamber walls, they are simply fed out to ground and do not alter the electronic state of the system. However, electrons stripped from the wafer platter cause the platter to build up a large positive electric potential, typically 300 volts, due to its DC isolation. On the contrary, the plasma develops a slightly negative charge due to the higher concentration of negative ions compared to free electrons. Because of the large voltage difference, negative ions tend to drift toward the wafer platter and collide with the surface.

At this point, two etching processes coexist. The negative ions can chemically react with the materials on the surface, or can also knock off (sputter) material particles by impact. Thanks to the mostly vertical delivery of the ions, this technique can produce very anisotropic etch profiles, hence sharp waveguide sidewalls. However, etch anisotropy strongly depend on the many process parameters, such as pressure, gas flows, and RF power.

RIE can also be used for the activation of the surface of a substrate, to achieve good adhesion between the substrate and a material to be deposited. For this application, parameters are usually selected so that the etch rate is low.

1.4.3 Typical procedure

Typical procedure was to etch SU8 thin films covered with S18 patterns to fabricate rib SU-8 waveguides. This was achieved with oxygen gas. A first step of RIE etching is to produce vacuum around 10^{-5} Torr in order to clean the chamber from possible remains of previous etching procedures. This guarantees the reproducibility of the procedures. Then, the vacuum is broken and the chamber returns to ambient pressure, at which point the wafer can be placed in the chamber. In order to prepare for the etch, a vacuum similar to the initial one is created again. Then, the pressure of the chamber and the flowrate of O_2 were typically set at 30 mTorr and 10

sccm[2], respectively. Once these parameters are stabilized, which usually takes one minute or so, the RF electromagnetic field is applied, which creates the plasma. The duration of the etch is measured from this moment. The etching is stopped when the RF field is shut down, after which pressure regulation and oxygen flow are stopped so that high vacuum can once again be created in the chamber. After a sufficient time, vacuum can be broken so the chamber returns to ambient pressure. At this point, the etched surface can be retrieved.

Though not essential to the etching procedure, it can be important to determine precisely the etching rates of the various etched materials for each procedure, especially when new parameters are tried, but also to make sure that the RIE system functions normally. This means that thicknesses of the layers must be measured before and after the etching procedure. Such measures are achieved with a profilometer (cf. 2.2).

1.5 Wafer slicing

Wafer slicing consist in breaking the silicon wafer at specific locations to obtain an adequate size of the photonic device. This step can be very delicate if done manually since the wafer can easily break to multiple pieces, making the fabricated device impossible to use. The quality of the slicing can also be very important. Indeed, for microresonators with bus waveguides in which light is coupled and retrieved at the output from microscope objectives, or from butt-coupled fibers, the quality of the transverse cut performed to the waveguides at input and output plays an important role in the coupling loss and source to detector transmission. If the cut is sideways, high amounts of optical power can be lost at input and output facets of the waveguides. Also, the straightness of the cut is important for practical reasons, whatever the coupling scheme.

[2]The *sccm* flowrate unit stands for "standard cubic centimeters per minute"

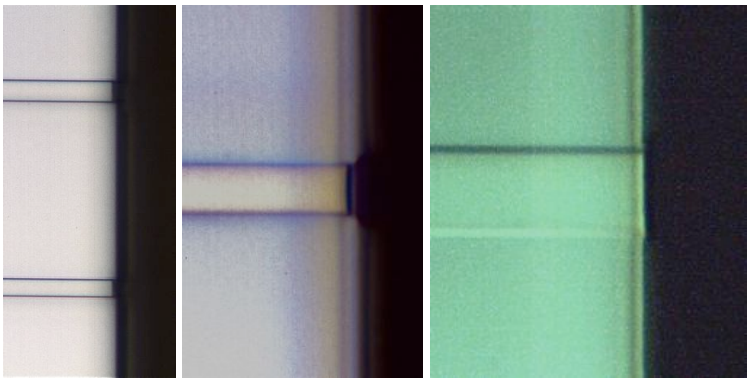

Figure 3.7: Successful slicing of the wafer resulting in a clean break of SU8 waveguides all along the cut.

To achieve a good slicing, we have to rely on the crystalline planes of the silicon wafer. The best result is achieved when a cut is achieved by propagating a break along a crystalline plane (cf. Fig 3.7), which requires some experience. Also, it is important for a good cut of the waveguide that these waveguides are built well perpendicular to the crystalline planes corresponding to the slicing direction.

2 Control tools

In the development of a fabrication process, using several fabrication procedures, controlling the device after each fabrication step is particularly important since it is the only way to control the cleanliness of the fabricated devices, and also its conformity to the specifications of the design. These verifications take time, and, as measurements are submitted to numerous biases, a good knowledge of the control tools is necessary to perform accurate observations. Once a fabrication process is well established and controlled, precise measurements of the thicknesses of deposited layers, width of waveguides, and other such parameters become less necessary and time can be saved. In such case, with a good knowledge of the process, a direct visual control between fabrication steps is usually sufficient.

Hereafter are described some the control tools used inside or outside the cleanroom facility.

2.1 Optical microscopy

Optical microscopy is an easy to use tool in clean room to verify if one given fabrication step went according to plan. It is possible to accurately check the widths of the patterned waveguides as well as the homogeneity of the surface. Also, small defects are usually visible with a regular microscope with objectives from x5 to x100 magnitudes. Many illumination techniques such as cross-polarized light and dark field illuminations improve image contrast, making the observation of defects easier.

2.2 Contact profilometer

A profilometer is a common appellation for a measuring apparatus whose purpose is to characterize the profile of a surface, mainly to quantify its roughness or geometry. Initially, profilometers where only contact profilometers, where the relative movement of a stylus in contact with the surface is used to characterize it. Nowadays, numerous non-contact profilometry techniques exist, such as laser triangulation, confocal microscopy, low coherence interferometry and digital holography [67]. Despite their interesting qualities, contact-profilometers are usually preferred as control tools in most microfabrication processes.

In recent contact profilometers, a diamond point (or *stylus*) is slowly moved downwards until it contacts the sample to characterize. Then, the sample moves along a given lateral direction and for a specified distance and with a specified speed, thus scanning a part of the surface. The scanning speed has a role in the lateral resolution, but also in the fidelity of the measured steps. Lower speeds provide the best accuracy, and also prevent the stylus from damaging the surface. This also depends on the tracking force. The contact or tracking force is the force that maintains the stylus in contact with the surface, and is commonly expressed in its weight equivalent, from 1 to 50 mg. When the contact force is low, the stylus as less chance to damage the surface, but then a brutal variation of the surface to measure is more likely to make the stylus bounce.

State-of-the-art contact profilometers can work on very large vertical ranges, from few nm to few hundreds of μm, with very good vertical resolutions, down to 0.1 nm. Also, they allow to scan the profile of a surface

on distances as high as few cm. Regarding the lateral (or horizontal) resolution, it is mainly limited by the radii of the stylus, which can be chosen in most systems from 200 nm to 25 μm to meet specific requirements, the smallest radii providing the best resolution.

3 Fabrication of vertically-coupled microresonators

The aim of this section is to present all the techniques employed successively to obtain the ring resonators that were used in most experiments described later in the dissertation. We present here some of the fabrication issues that can be encountered as well as tricks to obtain better quality. This section presents a thorough fabrication procedure that others could apply without having to understand all of its imbrications.

3.1 Materials

Main properties of materials used in the typical fabrication of the microresonators are presented in Tab.3.2.

Characteristic	SU8-2000	Cytop	Silica	Silicon
Class	epoxy-based photoresist	perfluoro-polymer	amorphous glass	crystal
Refractive index (at 1550 nm)	1.56	1.3335	1.444	3.48
Transmittance (% at 1550 nm)	100	100	92	poor
Specific heat (kJ/kg / K)	1.5	861	703	0.71
Thermal conductivity (W/m/K)	0.3	0.12	1.38	149
Linear CTE (ppm/K)	52	115-120	0.55	2.6
Young Modulus (GPa)	2.0	1.4-1.6	73	130-188
Tensile strength (MPa)	60	40	50	7000

Table 3.2: General properties of fabrication materials.

3.2 Description of the fabrication steps

3.2.1 Starting point

The starting point of the device fabrication is a 3 inches (7.62 cm in diameter) silicium wafer covered with a 5 μm-thick silica layer. These wafers are commercially available. Such a (relatively) thick layer of silica, with

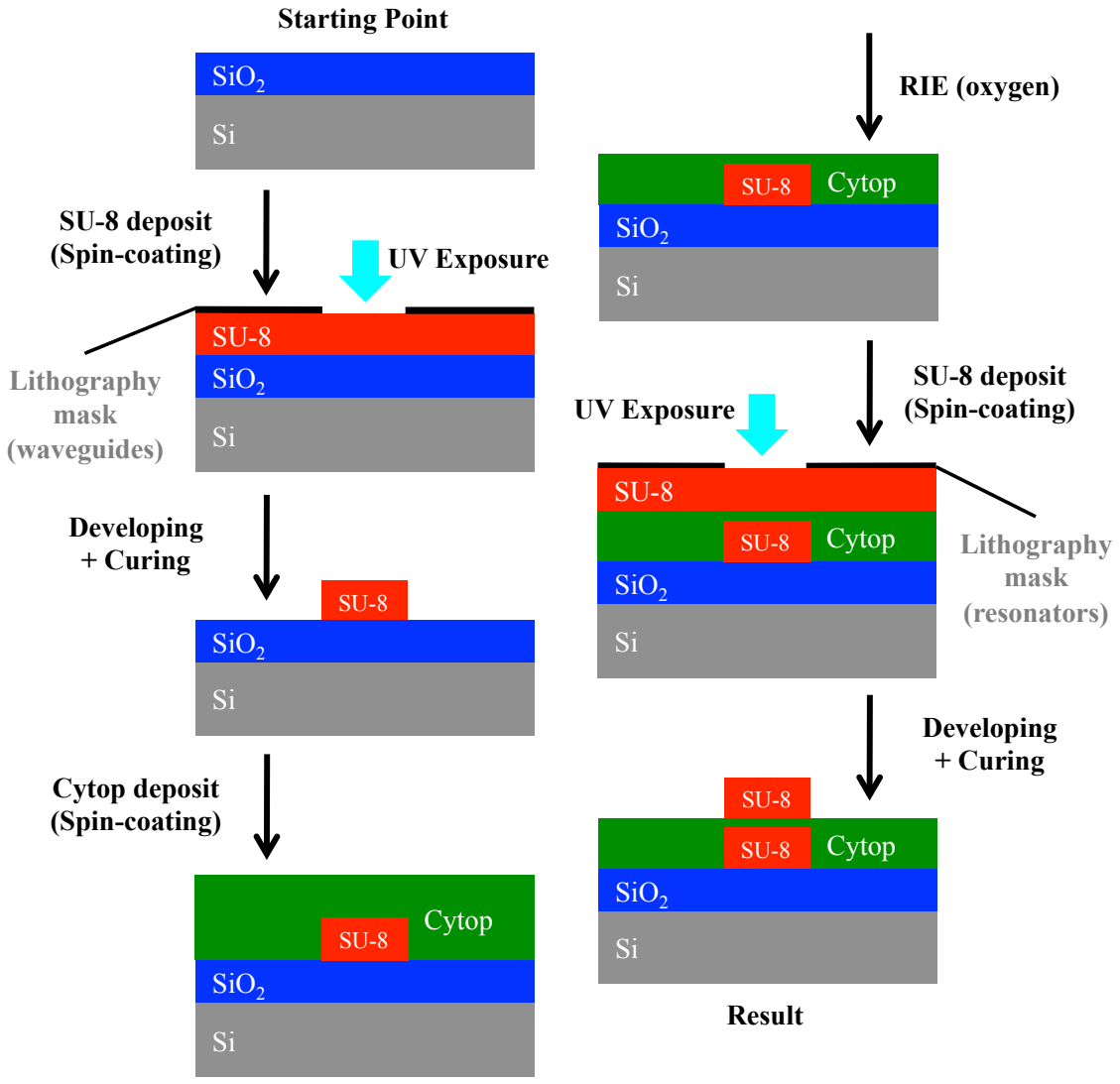

Figure 3.8: Fabrication steps for a SU-8 vertically-coupled ring resonator

a refractive index of 1.444 at 1550 nm, is aimed at the reduction of substrate loss in bus waveguides. Some fabrication procedures include a thorough cleaning of the silicon surface for process reproducibility but it was noticed that these procedures, implemented in a lower grade clean room facility than that of the wafer manufacturer, tends to lower the quality of the surface. For this reason, commercial wafers were directly used without any additional procedure for surface preparation.

3.2.2 First SU-8 deposition

A first fabrication step consist in depositing a first layer of SU-8 negative photoresist. In fabrication procedures, three commercial solutions were used: SU-8 2000.5, SU-8 2002 and SU-8 2005 by Microchem. This was done in order to test different waveguides widths, and also to compare the quality of surfaces with similar thicknesses obtained from different solutions. The SU8-2002 solution, allowing typical thicknesses between 1.5 and 3 μm has been the most used, thus procedures described are adapted to this specific solution, though they can be largely reproduced with the others. The solution is typically transferred from a small glass bottle stored in a dark storage cupboard to a 10 mL syringe. Though all this solution volume is not actually needed, it is better to have large excess in order to control bubble contamination.

A 2 μm filter is then applied to the syringe. Pressure is applied to wet the filter until few drops of the solution go through. Meanwhile, the spin-coater is programmed to operate two distinct cycles. The first cycle, with the spin-coater cap shut, is the spread step. In order to obtain a 2 μm-thick SU-8 layer, parameters of this step where an acceleration at 100 rpm/s, to arrive at the stationary speed of 500 rpm and stay at this speed for 7 seconds. Then, the spin-coater proceeds with the second cycle: cap shut, acceleration at 300 rpm/s, stationary rotation speed at 2000 rpm for a duration of 30 seconds, which may slightly vary depending on the exact thickness targeted.

Once the spin-coater is programmed and the content of the program is checked, the substrate, in that case the silicon wafer with the silica layer, is deposited on the spin-coater which is designed to immobilize the wafer thanks to a vacuum pump providing aspiration under the wafer. In sit-

uations when the shape of the wafer does not entirely coincide with the holder, it might be important to check on a similar trial wafer is the aspiration is strong enough to maintain the wafer during the high-speed spinning, otherwise one might risk to destroy the device. However, in the case of a entire 3" wafer set on the 2" holder of our spin-coater, aspiration issues where never reported.

After the wafer is placed on the holder, with careful alignment between wafer center and spin coater rotation axis, aspiration under the wafer to maintain it in position can be activated. This can be done by starting the spinning procedure and stopping it immediately. In that case the machine maintain the aspiration until the user decides to end it. The solution is deposited drop by drop through the filter at the center of the wafer. The rule of thumb is usually to verse 1 mL of solution per inch of wafer diameter. Once the correct volume of solution has been versed on the substrate, it is better to wait for the solution to wet the surface from the center of the wafer to the outer parts, progressively, in order to minimize the risk of having small air bubbles stuck between the solution and the substrate. Depending on the viscosity of the solution, this works for varying areas of the wafer and takes various amounts of time. With SU8-2002, this only takes one minute. Also, to finalize the repartition of the solution on the whole area of the substrate, it is possible to provide small angular momentum to the holder via manual rotation until the solution wets the surface from center to the extreme outer parts. That way, the user is sure of the reproducibility of the spin, whereas launching the spin procedure without this step might induce variations in the outer regions from one wafer to another.

Once the solution entirely wets the surface of the substrate, the spin procedure can be launched. During the procedure, it is always good to check the dials for the speed values to make sure that the procedure is as planned.

After the spin procedure is complete, the wafer is retrieved from the holder and deposited on a hot plate at 65°C for 1 minute (typically) and then on a second hot plate at 95°C, typically for 1 minute. Different durations can be applied to modulate the remaining quantity of solvent in the deposited layer which will slightly affect the thickness and the optical properties of the film. This step is usually referred to as the soft bake.

What directly follows is a temporizing step where we allow the temperature of the substrate to get back to room temperature. This is important to make sure that each time the fabrication procedure is repeated, the initial conditions before a subsequent step are the same. Typical duration is 5 minutes, which is more than enough for the temperature of the substrate to stabilize to room temperature, and can be used to prepare following procedures.

3.2.3 First lithography

This step consists in patterning the photoresist film by contact UV lithography, using a first photomask to obtain rectangular bus waveguides. The equipment used for this step, an MJB4 apparatus from Suss Microtec, is switched on well before the start of the exposition to make sure that the lamp is at its nominal temperature and thus, that the emission spectrum is always the same.

A first sub-step is to make sure that the mask holder is well aligned with the wafer holder, and that the angle of the z-rotation stage is set to zero. This is important to easily produce the alignment in the second UV lithography procedures where patterns from the substrate have to be aligned with patterns from the second photomask.

The second sub-step is to put the photomask in place. At this point, the cleanliness of the mask should be checked. Indeed, dust or resins from previous exposures can remain on the mask and have undesirable effects. In such case, photomask may be cleaned, with lots of care, in acetone, then rinced with isopropanol and finally dried with nitrogen gas. After cleanliness check, it is important for the resolution of the technique to place the chromium patterns downwards so that they are as close as possible to the photoresist during this exposition. Position of these patterns on the quartz plate that constitutes the mask can be observed by looking at the sides of the mask.

The third sub-step is to place the substrate on the wafer holder. This positioning should also be executed with special care, making sure that the wafer is well aligned with the circles engraved on the wafer holder. In-

deed, a good repeatability in the positioning of the wafer makes subsequent alignment procedures a lot easier.

The fourth sub-step is to set the z-translation stage so that once the lever is pushed, the photoresist layer will be in close contact with the patterns from the mask. This is achieved during a semi-automatic procedure which is done as follow. The initial height of the wafer holder is set so that once the contact lever is pushed, the wafer will not be in contact with the mask. Then, the contact lever is pushed. Then, the distance between the layer and the mask is slowly reduced until the equipment, thanks to an air balloon system under the holder, whose pressure is controlled, detects that the layer is in contact with the mask. Once this contact is realized, the lever can be pushed back and the contact setup is finished.

In the fifth sub-step, the duration of the exposition is set. The chosen time depends on several factors: the nature of the substrate and the thickness and type of the photoresist layer. This duration needs to be very well adjusted to achieve good geometry of the waveguides and good adhesion to the substrate. For negative resins such as SU-8, if the exposure time is too short, the base of the waveguide, where the intensity is lower than in the upper regions, will be under-exposed, which means that the action of the developer will tend to remove the base of the waveguide. Typical result of under-exposure is the observation of formed waveguides detached from the substrate and retrieved in the developer solution. On the opposite, if the exposition time is too long, because of Fresnel's diffraction on the chromium patterns, the sidewalls of the waveguides will be slanted. Slanted waveguide sidewalls engenders polarization conversion (cf. Chap. 2), which can severely affect the transmittance of the final device. As far as the adhesion of the waveguide is concerned though, it is always better to over-expose than to under-expose, because of the dramatic effect of the latter. For a 2 μm-thick SU-8 film deposited on 5 micron-thick silica layer and for waveguides from 3 to 5 microns wide, an exposition time of 12 seconds was found to be a good trade-off between optical quality and surface adhesion of the waveguides.

The purpose of the sixth sub-step is to align the waveguides with the crystalline lines of the silicon wafer. This will guarantee that when cutting

the wafer pieces to separate the devices, the cut will be as much as possible perpendicular to the section of the waveguide, which is very important to get the best optical coupling efficiency from the laser source to the waveguide. With the MJB4 exposition unit, possessing two separate microscope objectives to observe simultaneously both right and left sides of the wafer, this alignment can be achieved thanks to the following procedure: playing with the z-rotation knob of the microscope element, separation between the optical left and right fields can be aligned with the waveguide patterns from the mask. The mask holder can never move from its position, so this makes the dark line marking the field separation as a reference line for the waveguides that will be imprinted on the photoresist layer. Then, the microscope can be moved in the plane of the substrate to image the wafer notch which is the reference line for the crystalline lines. The angle between the notch and the field separation is then set at 90 degrees which virtually makes the future waveguides perfectly perpendicular to the crystalline lines of the silicon wafer. This is done by playing with the z-rotation knob of the wafer holder.

After these preparative sub-steps, the actual exposure can be performed. When processing SU-8, it is directly followed by the Post Exposure Bake (PEB). This step was typically completed by putting the wafer on a hot plate at 65 °C for one minute and then at 95 °C for two minutes, after which the wafer was let to cool down to room temperature for 10 minutes. This also allows for the surface of the layer to capture oxygen which supposedly increase the quality of the patterning after developing. Letting the temperature cool down is important for the same reason as before, so that the initial steps of the fabrication procedure are always the same. Also, it is important to avoid thermal shocks when immersing the wafer in the developer solution. Thermal shocks at this stage usually provoke critical loss of adhesion of the waveguides to the substrate. During temporization, the developer solution is prepared. The wafer is immersed in the developer solution for 1 minute. If the adhesion between resist and substrate is poor, which was the case with SU-8 on silica, this step needs to be realized with a lot of care. For the first 30 seconds, the user can let the developer work on the unexposed photoresist. Then, the user provides a slight agitation to the developer solution to refresh the developer solution near the waveguides. If the adhesion is strong, at this point, the user can provide strong agitation

to remove all the unexposed photoresist. Then, the wafer is retrieved from the developer bath and rinsed with isopropanol to remove all the developer solution of the surface. Finally, the substrate is thoroughly dried with nitrogen gas.

The quality of the patterning can then be observed either directly or through a microscope. This step is particularly important to check if the parameters of the exposition and the PEB were well chosen. On some occasions, it is possible to see parts of waveguides that lost their adhesion to the surface in the developer bath, then stabilized and fixated a little further from their initial position. This is a sign that the exposure was slightly too brief, and/or that the agitation during developing was too strong.

It is also possible to check the waveguide height at this point with a profilometer. However, this is not advisable since the stylus of the profilometer can deteriorate the waveguides during measurement. It is preferable to wait for after the hard bake to measure the profile of the waveguides. Indeed, this step makes the SU-8 waveguides much more resistant, and also give their definitive shape to the waveguides.

The hard bake step consist in fully cross linking the polymeric layer. It is realized in a oven with temperatures between 90 °C and 200 °C. Temperature and duration have an impact on the roughness of the surface, which is important for the optical loss in the waveguide. It also plays a role on the state of the surface. This aspect will be discussed further concerning the microring patterning. Typical parameters for the hard bake of the waveguides are 3 hours at 120 °C, without any discontinuity in temperature, which means that the wafer is positioned in the oven before it is switched on and removed when the temperature of the oven is back to room temperature. Once the duration is over, oven is stopped and the wafer is let to slowly cool down to room temperature in the oven.

At this point, profiles of the patterned waveguides can be measured without risk of deterioration. Measurements at different regions of the waveguides, and for different widths of waveguides, are useful to determine the homogeneity of the deposited layer. For reference, it is then important to mark down exactly where the heights measurements were made

to be able to compare from sample to sample, or for the etching procedure and gap control discussed in § 3.2.5. Once the profiles of the waveguides are determined, wafer moves to the next step which is the deposition of a Cytop thin film by spin coating.

3.2.4 Cytop deposition

Cytop is a perfluoropolymer material with a refractive index (RI) of around 1.3335 at 1550 nm. Because of its low RI, it is optically well suited as substrate material for microresonators, since it provides a good confinement layer for the ring waveguides that reduces loss to the substrate in comparison to silica. Secondly, the material can be deposited in thick layers to provide a good homogeneity of the surface despite the presence of the waveguides, and can be then easily and accurately etched to obtain the wanted gap separation between the bus waveguide and the ring resonator.

The inhomogeneity of the upper Cytop surface induced by the presence of waveguides is reduced as the deposited thickness of the layer gets larger. As a consequence, the parameters of the spin-coating are chosen so that a thick layer is obtained while maintaining a decent homogeneity on the outer parts of the wafer. If the layer is too thin, waveguides will create strong local variations of the height of Cytop which will create deformations of the ring resonators sitting on top. Also, a thin layer does not provide a strong optical insulation of the waveguide constituting the ring resonator, hence increasing the optical loss of the guided modes. On the opposite, if one wants to obtain a thick layer, the only parameter to play with is ultimately the stationary rotation speed during the spin-coat. If the speed is low, the layer will be thicker but the material can build up massively in the outer parts of the wafer, because of the edge bead phenomenon. This is detrimental to the control of the vertical gap since because of the wedge, waveguides have variable heights depending on their position on the waver. It is then impossible to achieve the same gap separation for all devices. Also the wedge is problematic since it will prevent one from achieving a close contact between the upper photoresist layer on the second lithography mask when patterning the microresonators.

In a typical procedure, a 2 microns thick layer of Cytop was achieved with the following parameters: 500 rpm - 100 rpm.s^{-1} - 10s for the spread

and 1000 rpm - 300 rpm.s^{-1} - 20s for the spin. For waveguides with typical height of 1.8 μm, typical inhomogeneity of deposited Cytop layer due to the waveguides was around 500 nm. The procedure for the spin-coating of Cytop is similar to the one followed for SU-8, except that after the spin-coating, the substrate is directly transferred to an oven for a hard bake at 180°C for two hours.

3.2.5 Cytop etching procedure

Once the Cytop film is hard-baked, it is necessary to etch it in order to obtain a well-controlled vertical gap separation between the bus waveguides and the microresonators, usually between 50 and 200 nm. This is efficiently achieved from an RIE procedure using oxygen gaz.

For the gap to be well-controlled, it is necessary to determine accurately how long the etching procedure needs to last. Two parameters need to be determined: the thickness of the Cytop film above a SU-8 waveguide (cf. Fig 3.9, and the etch rate of Cytop under selected RIE parameters.

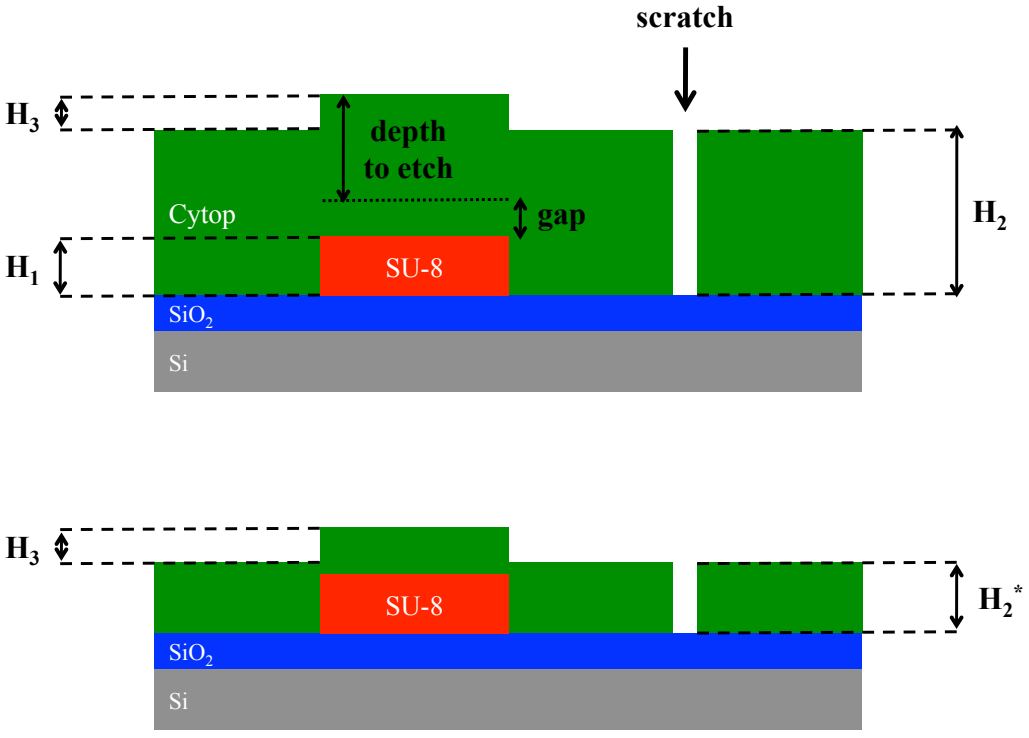

Figure 3.9: Thickness measurements for the control of the vertical gap separation.

The former parameter can be precisely determined from three contact profilometer measurements. The first measurement is that of the average height of the rectangular SU-8 waveguides H_1. Measuring this specific geometric parameter is not possible after Cytop deposition.Therefore it must be performed beforehand, right after the SU-8 hard bake. The second measurement is that of the thickness of the deposited layer of Cytop H_2. It is performed by scratching the surface with the tip of a tweezer, preferably in a region of the wafer where the thickness is homogeneous. After the scratch is cleaned, the difference of height between the low surface (top of the silica layer, too hard to be scratched) and the high surface (top of the Cytop layer) is measured. An important trick is to try to make the scratch as thin and short as possible and not too close to the waveguides. Indeed, the presence of the scratch causes perturbation of the flow of the photoresist during the second spin-coating of SU-8 that creates local modulation of the thickness of the photoresist near the scratch. The last measurement is that of the thickness step H_3 of the Cytop layer caused by the waveguide. This shall be performed in the same region where the thickness of the waveguides was determined. From these measurements we can deduce the thickness of Cytop above a waveguide, hence, from the targeted gap separation, the thickness of Cytop to be etched:

$$\text{depth to etch} = H_2 + H_3 - (H_1 + \text{gap}) \tag{3.2}$$

The duration of the oxygen plasma etch is then calculated from the previously measured value of the etch rate of Cytop. It is important to know that the etch rate is not constant during the procedure. The average etch rate for a long etching duration is lower than the average etch rate for shorter durations. To obtain the targeted gap separation, it is then necessary to retrieve the etch rate that was measured for procedures with comparable Cytop thicknesses to etch. It is also possible to separate the etching procedure in two steps. First, the duration is determined from average etch rate determined in previous procedures. Than, a first etching procedure is performed with a duration of half what is estimated. After the first etch, thickness of the Cytop layer is measured from the scratch used to measured H_2 and value of the actual etch rate is determined. Then, from this new value, the duration of the second part of the procedure is calculated. Though this procedure takes more time, it provides very accurate control of the gap separation, with relative accuracy under 5%. The typical set of

parameters used for the RIE removal of Cytop was:

- Power = 55 W
- Oxygen flowrate = 10 sccm
- Chamber pressure = 30 mTorr
- DC bias = 300 V

For a one-minute-long etching, the average etch rate obtained from this set of parameters was around 420 nm/min. It was measured that shorter durations led to larger averages for the etch rate. For example, a 440 nm/min etch rate was obtained for a 30 seconds etching duration, and a 380 nm/min rate was measured for a 2-minute etch duration.

The oxygen plasma, in addition to performing the necessary etch of Cytop, activates the surface of Cytop for the deposition of the second SU-8 layer. As a consequence, it is preferable, in order to achieve maximum adhesion between SU-8 and Cytop, to perform the spin-coating of the photoresist shortly after the etching procedure is complete.

3.2.6 Second lithography

Deposition of the second layer of SU-8 is very similar to the procedure used for the waveguide layer. The main difference between the two procedures is the alignment of the patterns imprinted in SU-8 at the level of the waveguides with complementary patterns found on both left and right sides of the second lithography mask (cf. Fig. 3.10) This step is very important for the final quality of the optical resonators and will be discussed further in §3.4. The other difference is in the exposure duration, which has to be slightly longer during the second lithography.

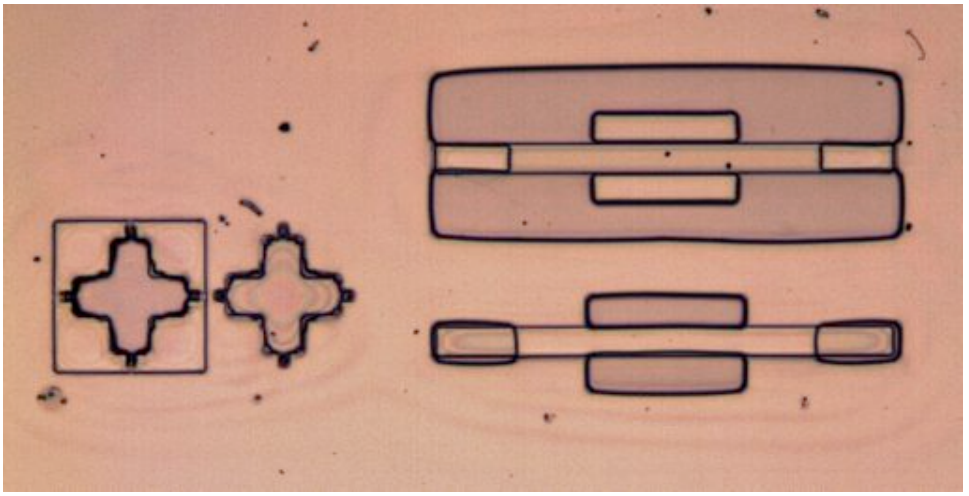

Figure 3.10: Alignment between patterns from first and second lithographies.

When exposing the photoresist layer to UV, the optical properties of the substrate have to be taken into account. UV radiation is well reflected by the silicon layer because of its high refractive index. This way the exposition of a photoresist layer directly deposited on silicon is shorter than the exposure of the resist where a layer of silica is present between the silicon and the resist. Typical ratio between the exposition time is 1.5 in that case, because of the absorption of UV radiation in the silica layer. As the deposited layer of Cytop also absorbs UV radiation during the exposure, the second exposure needs to be slightly longer that the first one because of the presence of Cytop. Typically, exposition time goes from 12 to 15 seconds from the first to the second exposure.

3.2.7 Final hard bake

After development of the resonators pattern, the wafer is finally hard-baked at $120°C$ for three hours. It was observed with FTIR spectroscopy that temperatures under $100°C$ where not enough to further cross link the SU-8 during the hard bake process. At temperatures higher than $150°C$, the polymer is fully cross-linked but the surface has a higher level of roughness. These measures, performed by Marion Salsac, Aleksandra Bernardska and Claude Nogues from LBPA, also showed that $120°C$ was an adequate temperature for cross-linking, surface roughness and further functionalization of the surface of the ring resonators which is particularly important for biological applications of SU-8 microresonators.

After the final hard bake, the profiles of the waveguides constituting the ring resonators are studied with a profilometer and analysis of the surface and the devices, especially in the coupling region, is achieved through microscope observation. Usually, photographs are taken to be able to link fabrication procedure modifications to the results in terms of apparent quality of the devices. This approach is complementary to the optical characterization of the devices. The final step is often the one that requires the most care in its realization. It consist in separating the wafer in smaller rectangles corresponding to the size of the support of the devices on the characterization and sensing bench. To obtain the best coupling to the bus waveguide when focusing the laser beam from the source, the cut needs to be perfectly perpendicular to the section of the waveguide. The problem is that manual cut, if not careful, can very easily break the wafer sideways, or break all devices altogether. And efficient procedure for this step is as following. First, the position of the cuts to realize are precisely determined. Best solution for this is to add lines of arrows on the second level of patterns in SU-8 to precisely localize where the cuts need to be performed. With a diamond tip, a very shallow scratch, one millimeter long, is made on the top layer, at the extremity of the wafer. Then, this shallow scratch is made deeper and deeper by gently applying pressure with the tip up and down the initial scratch. After a while, pressure can be applied in the scratch, at the extremity of the wafer, to break a small piece of wafer. This will result in a V defect on the side of the wafer. Then, by applying a moderate pressure with the side of the tip at the scratch and near the defect, a small break along a single crystalline line will appear. By maintaining some pressure at the same position, slowly, the break will spread in straight line from one side of the wafer to other. At this point, even if the silicon layer is cut, the two wafer parts are still attached because of the polymer layer. For a clean cut of the polymer layer, the wafer can be lifted with tweezers positioned on the break. After a 10 cm fall on a hard surface, both parts will be separate and the cut will appear very clean.

3.3 Technical defects

3.3.1 Localized defect

In a fabrication procedure of microresonators such as described before, most impurities present in the thin films will not affect the behavior of the optical devices, since the overall surface occupied by the waveguides is small compared to the size of the wafer. However, when a localized defect such as the one pictured in Fig. 3.11 occurs, the optical transmittance of the device will be strongly affected, often showing stress-induced birefringence effects.

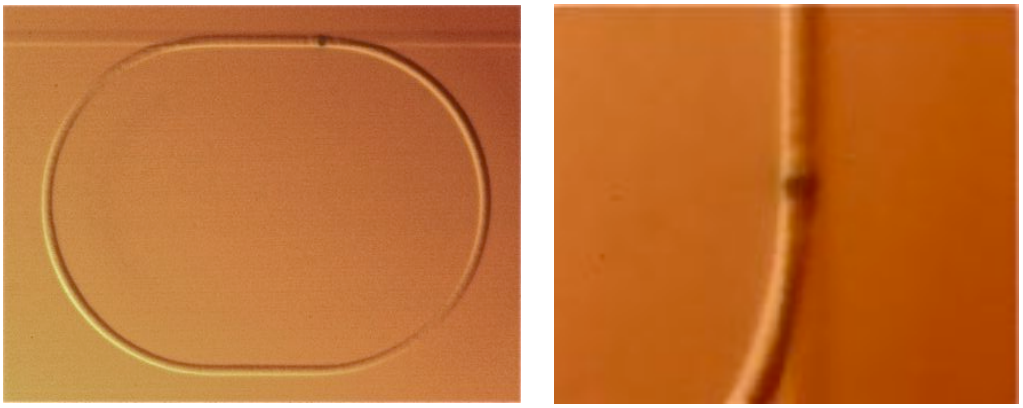

Figure 3.11: Single defect localized in the coupling region of a microring resonator.

With thorough impurities removal procedures such as described in §3.4.1, the risk of such events is minimized.

3.3.2 Waveguide breaks

There are two categories of waveguide "breaks", as depicted in Fig. 3.12. The first category, presented on the left, is due to the presence of dust or small bubbles in the photoresist film. Such defects can prevent some regions of a waveguide to be correctly exposed. At development, the defect is removed with the unexposed photoresist, and a permanent break of the waveguide appears.

The second kind of break is different in nature and can be referred to as an elongation break. It is presented in the right in Fig. 3.12. During the final hard bake step, at high temperature, Cytop laterally expands more than

twice as much as SU-8. This owes to the fact that Cytop has a higher coefficient of thermal expansion than SU-8 (cf. Tab. 3.1). Thus, the waveguide constituting the resonator, with Cytop as cladding, is submitted to an important stress. In the case where this stress overcomes the tensile strength of SU-8, then the waveguide breaks. Elongation breaks can be prevented by making sure that the device does not undergo strong temperature variations, which favor higher stress applied to the fragile microring resonators.

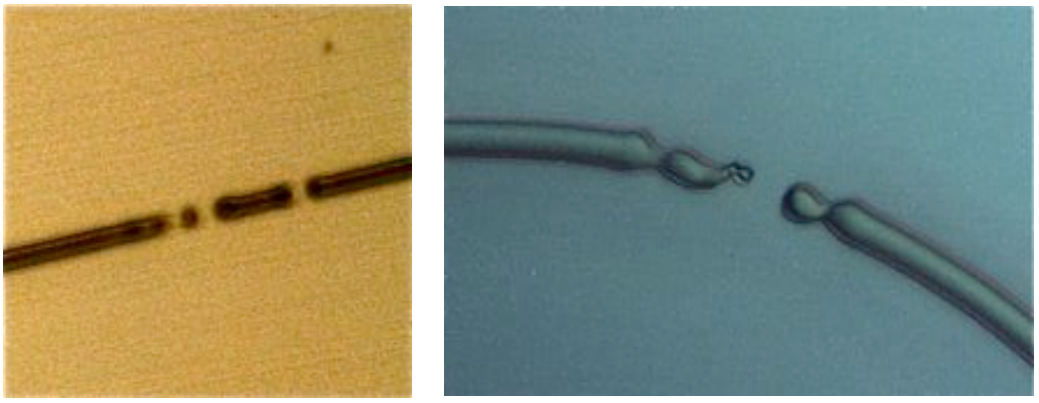

Figure 3.12: Dust or bubble-related (left) and elongation breaks (right) on fabricated waveguides.

3.3.3 Vertical step

Because of the rectangular profile of the waveguides, the surface of the Cytop film after deposition and solidification is not planar, and presents variations of height up to 500 nm due to the presence of the bus SU-8 waveguides. This planarity defect is not modified by the anisotropic etching procedure. The presence of these steps create vertical distortions of the ring waveguide at one side of the bus waveguide (cf. Fig. 3.13). These defects create additional optical loss in the microresonator, and create extra stress on the resonator in the coupling region which results in induced birefringence.

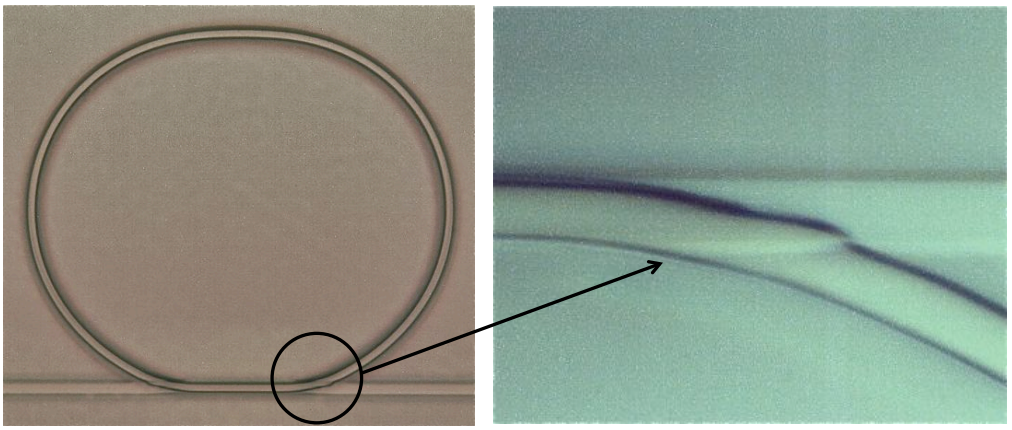

Figure 3.13: Vertical steps of the microresonator due to planarity defect of the Cytop upper surface.

A first effort to reduce this step consisted in replacing the rectangular bus waveguide by a rib waveguide. Since rib waveguides have smaller vertical edges, this design was successful at reducing the vertical distortion of the resonators. However, the presence of a thick SU-8 layer close to the resonator waveguide dramatically increased the optical loss, at a point where no modulation of the transmittance was repeatably visible.

Subsequent efforts were targeted at increasing the planarity of the Cytop surface built over rectangular bus waveguides. The best solution was to deposit thicker films of Cytop to diminish the height of the vertical steps.

3.3.4 Surface roughness

A large advantage of photolithography patterning of films is the very low surface roughness obtained on all processed surfaces. However, on rare occasions, surface roughness of the Cytop layer was observed (cf. Fig. 3.14), resulting in a small corrugation of the waveguide forming the microresonator. Effect of waveguide corrugation in cavity can result in counter propagation coupling, and splitting of the resonances in the intensity transmittance of the device.

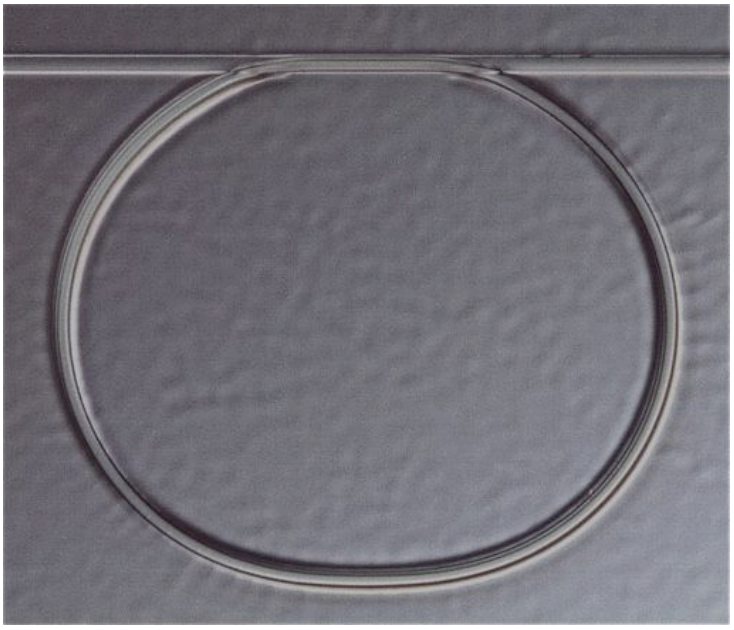

Figure 3.14: Visible surface roughness and waveguide corrugation on a fabricated device.

The origin of this surface roughness is not clear, although it may be related to an inadequate (too fast) thermal relaxation after Cytop hard bake.

3.3.5 Lateral waveguide distortion

As pictured in (cf. Fig. 3.15), in some devices, usually those with thin rectangular waveguides (3 μm and lower), parts of the waveguides can be laterally misplaced due to adhesion related stress. However, from the optical characterization of such microresonators, this phenomenon does not seem to affect the intensity transmittance.

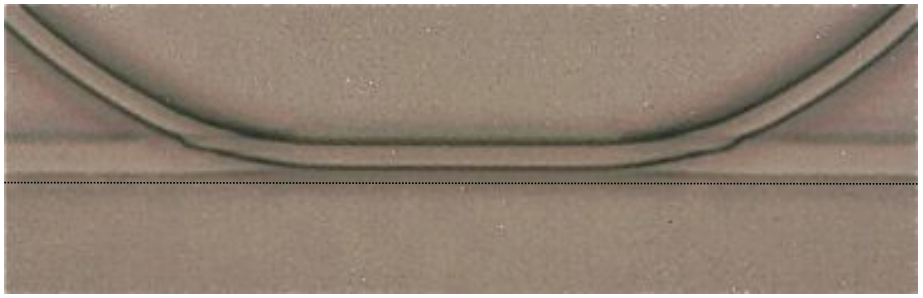

Figure 3.15: Lateral distortion of the bus waveguide near the coupling region.

3.3.6 Curvature discretization

Curvature discretization, which can be observed on microrings with large radii (few hundreds of microns), arise from the design of the photomask. At this step, a drawing software is used to create the pattern to be physically reported to the mask. In these softwares, circular lines are approximated by polygon sections, with a number of facets depending on the resolution of the drawing. This polygonal shape of the circular portions of the resonators are reported to the mask, and finally to the resist.

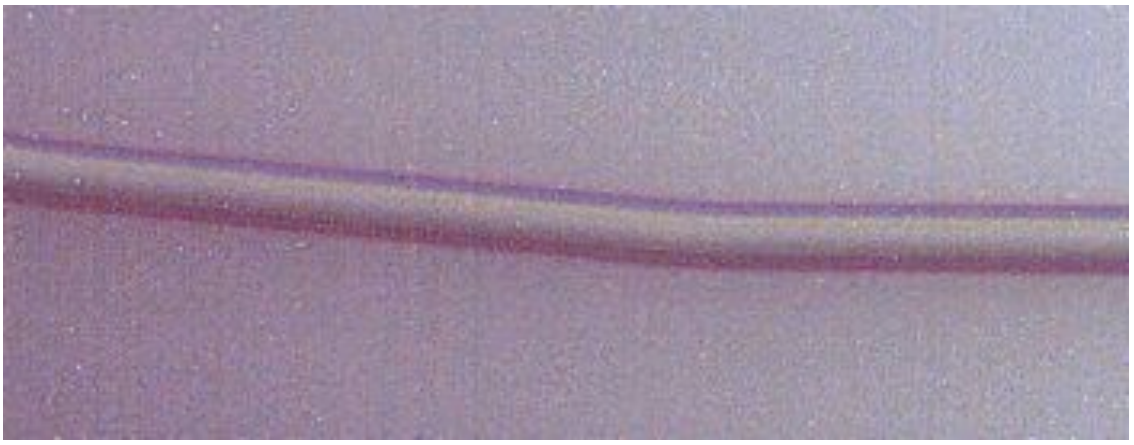

Figure 3.16: "Circularly curved" waveguide with clear discretization of the bend.

The presence of these slight changes of the direction of the waveguide should create more bending losses than a perfectly circular waveguide, but effects are not expected to be important. However, this observation led us to modify the resolution in the drawing software used for mask design.

3.4 Fabrication challenges

3.4.1 Avoiding dusts

Despite the fact that all fabrication steps take place in clean room, dust can always be found and are extremely detrimental to the quality of the fabricated device. Thin layers are particularly subject to dust pollution before they are polymerized, because in this situation, dusts can be imprisoned in the layer and are subsequently impossible to remove without destroying the layer. The problem is mainly due to the use of two equipments that easily collect dust: the spin-coater and the mask aligner. Most dusts accumulated in the spin-coater are residuals of previous depositions of polymer

layers. Also, tissue fibers from inadequate cleaning of the spin-coater can be present inside the chamber of the spin-coater. To avoid the accumulation of these dusts on the layer during polymer deposition, it is very important to clean thoroughly the spin-coater before (and after) use. A first step in the cleaning consists in blowing nitrogen in the chamber to remove all polymer dusts and tissue fibers. Then, the chamber, especially the wafer holder and its plate, and the cover of the chamber, need to be cleaned with specific paper towels[3] wet with acetone.

High attention must be paid at the handling of the wafer near the spin-coater. First, the wafer needs to be stored permanently in a clean Petri dish or similar reservoir. After the wafer is deposited on the wafer holder of the spin-coater, and before starting to put the solution on the substrate, it is necessary to make sure that its surface is perfectly cleaned. If not, a gentle blow of nitrogen has to be applied to the surface to remove dusts. Then, once the spin-coating and soft bake is finished, before putting the wafer back in the Petri dish, it is preferable to blow nitrogen in the Petri dish to ensure its cleanliness. Thanks to this scheme, the wafer is safely transported to the mask aligner. This kind of equipment can also attract dust. As the operator is quite close to the wafer, there is a high probability that the operator will bring dust to the freshly deposited layer. First thing is to make sure that hands, arms or face of the operator are never positioned over the wafer. For this reason, it is preferable to sit one meter away from the equipment and to manipulate the wafer with stretched arms. Also, the lithography mask, if not spotless, needs to be cleaned. This has to be performed very carefully because the mask can easily be damaged with scratches and must be replaced, which is expensive. However, photomasks can be cleaned quite efficiently only using acetone, isopropanol and nitrogen gun. Q-tips can also be used to remove material on parts of the mask that are not covered with chromium. Finally, dusts hidden in the mechanical parts of the mask aligner can be also removed with nitrogen flow.

Although all these procedures might not seem entirely necessary, their addition to the overall fabrication procedure greatly enhanced the optical quality and the reproducibility of the results. Moreover, techniques im-

[3] paper towels designed not to lose fibers during cleaning

ported from biological engineering to produce and maintain similar surface states had to be eventually employed on the photonic circuits destined to biological experiments. In the surface characterization and functionalization experiments on SU-8 surfaces realized at LBPA, it was duly observed that the cleanliness of the surface, relative to the presence of dust, has a significant role in the reproducibility of the tests.

3.4.2 Avoiding bubbles

Bubbles present in the solution deposited on the substrate just before spinning can also be very detrimental to the optical quality of the fabricated devices. A few tricks can be used to diminish or eradicate the presence of these bubbles:

- The solutions used for deposition via spin-coating are usually stored in small glass bottles which are frequently refilled from a main bottle stored in a fridge. When the small glass bottle is refilled, small bubbles are formed. It is then important to avoid bringing air bubbles to the solution used for the deposition, and to wait for a few hours for the bubbles thus formed to disappear. Another solution is to put the glass bottle in a sonic bath for few minutes, and then in a vacuum chamber for 30 minutes to remove all air bubbles from the solution.
- Very tiny air bubbles, the more dangerous ones, are also produced when the solution in the syringe is pushed through the filter. For that reason, it is necessary to put the first drops that go through the filter directly in the bottle. Then, as applying pressure on the piston of the syringe creates few extra bubbles, the first two or three drops must be emptied in the recipient surrounding the wafer holder. Only then, and while maintaining constant pressure on the piston of the syringe, the user can finally let the drops fall on the surface of the substrate.

3.4.3 Achieving good alignment

A good alignment between the ring resonators and the bus waveguide is crucial for the quality of the devices. Furthermore, it is also important to have a well established procedure for the alignment since slight variations of the operation will result in different characteristics for the devices.

The alignment procedure on the MJB4 equipment for mask alignment is relatively easy due to the presence of two microscope objectives to image

simultaneously both left and right sides of the substrate. This is particularly important for the setting of the angle for the z-rotation stage of the substrate. Alignment marks are patterned on the waveguide level on each side of the wafer and complementary patterns are present on the lithography mask for the resonators.

The first difficulty is to have the alignment marks from the substrate and of the mask in the same region where imaging takes place. This is not easy since the lithography mask is not globally transparent where the patterns are supposed to be seen. To correct this, windows were patterned on the second lithography mask so that alignment patterns from the substrate could be found more easily. The other difficulty can come from the fact that in between the two lithographies, modifications where made on the position of the substrate holder in regards to the mask holder. An important step before trying to align, even before placing the mask and the substrate is to check if the equipment have visibly the same alignment as for the first exposition. If not, the user needs to approximately reproduce the same initial alignment as done for the first exposition. This is usually enough to find substrate alignment patterns in the windows near the mask alignment patterns. It is important to make the alignment patterns asymmetric in the plane of the wafer. Indeed, with symmetric patterns, it can potentially occur that alignment marks from the substrate patterns are matched to inverted patterns of the mask.

Conclusion

In this chapter, usual tools and techniques employed in microfabrication were first presented. From a careful analysis of these techniques, their advantages and limitations in the fabrication of microring and microracetrack resonators were discussed. Finally, a comprehensive method to fabricate high-quality vertically-coupled microracetrack resonators with good reproducibility is proposed.

Devices resulting from this fabrication method are optically characterized in the next chapter. Then, they are used to perform sensing experiments in subsequent chapters.

Chapter 4

Optical characteristics of microring resonators

Introduction

In the two previous chapters, models of microring resonators were presented, then, fabrication methods of specifically vertically-coupled microring resonators made of SU-8 were reviewed. Before studying the sensor applications of these devices, where sensitivity issues are crucial, it is important to focus on the basic optical characteristics of the fabricated devices.

This chapter is dedicated to all aspects related to the study of passive microresonators: characterization methods, methods for filtering and fitting intensity transmittances, and methods to extract critical information in order to further understand the physical system and to optimize it for specific applications.

1 Characterization Methods

1.1 Cavity Ring Down (CRD) Techniques

Cavity Ring Down (CRD) Techniques are commonly used to characterize ultra high-Q and/or high-finesse optical resonators such as whispering-gallery modes (WGM) resonators, microtoroids and microspheres, photonic crystal resonators, fiber-loop resonators, and mirror-based optical cavities. A common feature of all CRD techniques is the measurement of the time-dependent intensity response(s) at output port(s) of the resonator

after excitation.

A basic CRD setup uses a tunable CW laser as input source and a fast photodetector. First, the laser is tuned so that the emission wavelength matches a resonance of the resonator. Depending on the output port, this is achieved when the transmitted intensity is either at maximum, or at minimum. Then, the input beam is shut down, and the resulting time-dependent intensity is measured by the photodetector, with a signal acquisition synchronized with the shutter. In most cases, shutters are electro or acousto-optic modulators, in order to reduce the transition period.

For a microresonator coupled to a single bus waveguide, the transmitted intensity is initially at its minimum and rises instantly from the moment the shutter is on. Then, intensity decays exponentially until it reaches zero, with a characteristic time referred to as the ring-down time T_{RD}. The ring-down time characterizes the energy decay in the cavity, and thus integrates optical losses due to the propagation in the resonator, and to coupling to the bus waveguide. As a consequence, this basic setup can provide the Q factor of the entire resonant device, $\{\text{resonator} + \text{bus}\}$, but cannot provide the individual in-cavity propagation loss coefficient a and cross-coupling coefficient.

In more recent CRD techniques, an optical pulse emitted by a pulsed laser or a modulator, is used to probe the resonator. The analysis of the time-dependent intensity response measured at output can then provide further information on the propagation of light in the structure, and does not require wavelength tuning of the laser source to reach one resonant wavelength of the cavity. In the coupling region, the initial pulse is parted in two: one pulse is directed towards the output, and the other pulse towards the cavity. After a round trip, the latter pulse is parted in two: one is cross-coupled to the bus waveguide and thus directed to the output, the other makes a second round-trip in the resonator, so on and so forth.

The recorded intensity is a series of equally time-distributed pulses with exponentially-decaying peak intensities. The time between the arrival of two neighboring pulses is equal to the effective group length of the cavity, which results of the product between the average geometrical length of

the resonator and the group effective index of the resonator at the center wavelength of the input pulse. In addition, ratios of the peak intensities of successive pulses and typical decay time provide the values of the two internal parameters $a = \sqrt{1-\gamma}e^{-\rho L_{mc}}$ and τ (cf. Chap.2 §2.2.1).

Let us consider I_1, I_2 and I_3, the peak intensities of the three first pulses arriving to the photodetector, and I_0 the initial peak intensity in the bus waveguide before the coupling region. To simplify the calculations, we set $a_L = e^{-\rho L_{mc}}$ as a partial in-cavity amplitude loss factor. The first pulse arriving to the photodetector is directly transmitted through the coupler. The second pulse is cross-coupled two times and makes a single trip in the resonator. The third pulse is also cross-coupled two times, and is transmitted one time through the coupler, between the two trips around the resonator. As a consequence, using $\tau^2 + \kappa^2 = 1$ (cf. Chap.2 §2.2.1), we can express the peak intensities as:

$$\begin{cases} I_1 = \tau^2 (1-\gamma) I_0 \\ I_2 = \kappa^4 (1-\gamma)^2 a_L^2 I_0 = \left(1-\tau^2\right)^2 (1-\gamma)^2 a_L^2 I_0 \\ I_3 = \kappa^4 \tau^2 (1-\gamma)^3 a_L^4 I_0 = \left(1-\tau^2\right)^2 \tau^2 (1-\gamma)^3 a_L^4 I_0 \end{cases} \tag{4.1}$$

After the first pulse, the following relation between the peak intensities of two neighboring pulses can be written as:

$$I_{n+1} = (1-\gamma) a_L^2 \tau^2 I_n = (a\tau)^2 I_n \,, \quad n \geq 2 \tag{4.2}$$

From Eq.(4.1) and Eq.(4.2), the normalized peak intensities $I_n^\star = I_n / \left[(1-\gamma) I_0\right]$ of all pulses, where $(n-1)$ stands for the number of round trips performed, can be deduced from:

$$\begin{cases} I_1^\star = \tau^2 \\ I_n^\star = \left(\dfrac{1}{\tau} - \tau\right)^2 (a\tau)^{2(n-1)} \,, \quad n \geq 2 \end{cases} \tag{4.3}$$

We can now introduce R_1 and R_2, two ratios that can be determined experimentally, and defined by:

$$\begin{cases} R_1 = \sqrt{\dfrac{I_2^\star}{I_1^\star}} = \sqrt{\dfrac{I_2}{I_1}} = \dfrac{a\left(1-\tau^2\right)}{\tau} \\ R_2 = \sqrt{\dfrac{I_{n+1}^\star}{I_n^\star}} = \sqrt{\dfrac{I_{n+1}}{I_n}} = a\tau \,, \quad n \geq 2 \end{cases} \tag{4.4}$$

According to the expressions above, experimental values of a and τ can be deduced from:

$$\begin{cases} a = \sqrt{R_2\left(R_1 + R_2\right)} \\ \tau = \sqrt{\dfrac{R_2}{R_1 + R_2}} \end{cases} \tag{4.5}$$

It is important to notice that from this method, a_L and γ cannot be determined separately. Because only two independent equations are available, it is only possible to determine τ and $a = \sqrt{1-\gamma}a_L$.

1.2 Optical Low-Coherence Interferometry (OLCI)

OLCI allows the measurement of the reflectivity or transmittivity of a photonic device as a function of the optical propagation length, with an excellent spatial resolution and a large dynamic range. For that reason, the technique was mainly used for the detection, the localization and the quantification of refractive index discontinuities in optical waveguides, and for the determination of local absorption coefficients.

Moreover, Fourier transform analysis of the generated interferogram provides the complex spectral reflectivity (or transmittivity) of the device under test (DUT). Thus, it can be used to determine the intensity reflectance (or transmittance) of a device, and the accumulated phase which is particularly useful to characterize the dispersion inside optical resonators. This ability to measure the accumulated phase is an important specificity of OLCI.

An OLCI setup is based on a Michelson interferometer combined with a broadband source. This source (typically 100 nm in bandwidth) is divided via a 2x2 coupler and sent to a reference arm, in which the optical path is scanned via a translating mirror, and to a test arm containing the DUT. This setup can be used in two configurations: reflection and transmission modes. In reflection mode, waves reflected from both reference and test arms are recombined by the coupler and directed to a photodetector recording a reflectogram (Fig. 4.1), *ie* the variations of the intensity in the detection arm as a function of the varying optical length of the reference arm. Intensity sampling is triggered on the rising edge of a synchronization signal obtained by a coupled coherent interferometer that produces self-referencing

of optical length.

As interferences only occur when the optical path of the reference arm matches[1] one optical path generated in the DUT, it is possible to analyze the sources of optical losses very accurately. Also, provided that dispersion is taken into account, it is possible to accurately quantify quality factors and finesses of optical microresonators as well as coupling and loss coefficients[2]. The reflection mode of OLCI is not suitable for specific applications such as the study of polymer-based optical resonators. Since only a small fraction of the wave intensity (4% for a fiber or polymer waveguide) is routed to the photodetector, and thus used for the measurement, the signal-to-noise ratio (SNR) is not optimal.

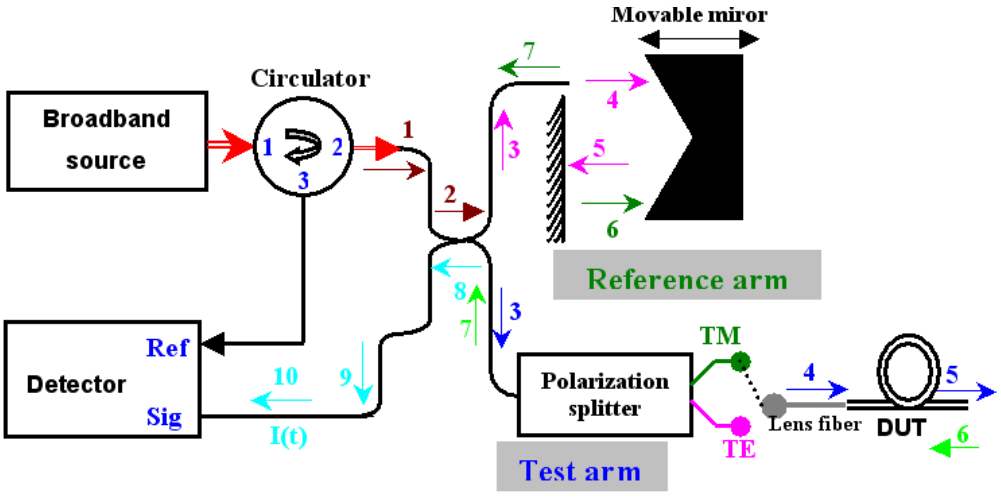

Figure 4.1: OLCI setup in reflection mode

In transmission mode, the reflection from the reference arm is combined specifically to the waves exiting the DUT, which contains most of the incoming intensity (Fig. 4.2). Compared to the reflection mode and thanks to the large improvement in the signal-to-noise ratio, more optical paths generated in a resonator-based device can be observed, which leads to an increased accuracy in the determination of the parameters of these devices.

[1] within the coherence length of the source
[2] the parameters a and τ cannot be determined via a typical wavelength scanning method

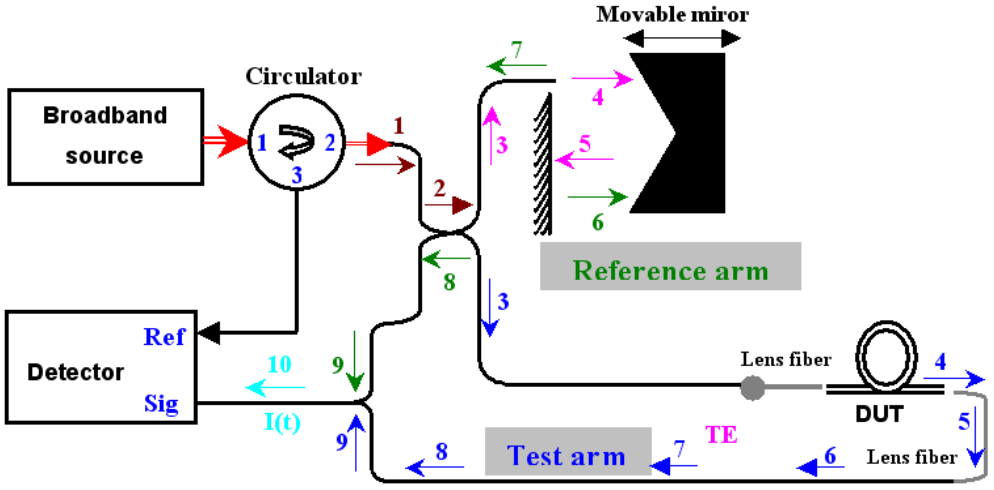

Figure 4.2: OLCI setup in transmission mode

The general mathematical expression of OLCI-generated interferograms is given by:

$$I(x) \propto \mathrm{Re}\left\{ \int_{-\infty}^{+\infty} S(\nu) t(\nu) \exp\left(-j2\pi \frac{x}{c}\nu\right) \mathrm{d}\,\nu \right\} \tag{4.6}$$

where ν is the optical frequency, $S(\nu)$ is the PSD (Power Spectral Density) of the broadband source, $t(\nu)$ the complex transmission (or reflection) amplitude coefficient of the device, x is the optical path in the reference arm and c the speed of light in vacuum.

For a ring resonator of geometrical cavity length L coupled to a straight waveguide of total geometrical length L_T, the complex amplitude transmittance, is expressed as:

$$\begin{cases} t(\nu) = (1-\gamma)^{1/2} \dfrac{\tau - a e^{j\Phi}}{1 - a\tau e^{j\Phi}} e^{j\Phi_T} \\ \Phi_T = \dfrac{2\pi L_T}{c}\nu N_{eff}(\nu)\,, \text{ and } \Phi = \dfrac{2\pi L}{c}\nu N_{eff}(\nu) \end{cases} \tag{4.7}$$

where $N_{eff}(\nu)$, the frequency-dependent phase effective index of the guided mode, is assumed to be identical in both straight and curved portions of the waveguides of the device. The expression can be rewritten using a geomet-

ric series:

$$\begin{cases} t(\nu) = (1-\gamma)^{1/2}\left(\tau - ae^{j\Phi}\right)e^{j\Phi_T}\sum_{p\geq 0}(a\tau)^p e^{jp\Phi} \\ \qquad = (1-\gamma)^{1/2}\sum_{p\geq 0}(a\tau)^p\left\{\tau\exp\left[j\Phi_p(\nu)\right] - a\exp\left[j\Phi_{p+1}(\nu)\right]\right\} \\ \Phi_p(\nu) = \dfrac{2\pi}{c}\nu N_{eff}(\nu)\left(L_T + pL\right) \end{cases} \tag{4.8}$$

We now assume that the PSD of the broadband source is constant over its whole bandwidth $\Delta\nu$ centered on the frequency ν_0. Its total power is K. This is summarized in the piecewise expression of the DSP:

$$\begin{cases} S(\nu) = \dfrac{K}{\Delta\nu}, \quad \nu \in [\nu_0 - \Delta\nu\,, \nu_0 + \Delta\nu\,] \\ S(\nu) = 0\,, \quad \text{elsewhere} \end{cases} \tag{4.9}$$

Consequently, the OLCI interferogram for a ring resonator can be expressed as:

$$\begin{cases} I(x) = (1-\gamma)^{1/2}\sum_{p\geq 0}(a\tau)^p\left[\tau I_p(x) - aI_{p+1}(x)\right] \\ \qquad = (1-\gamma)^{1/2}\left[\tau I_0(x) - a(1-\tau^2)\sum_{p\geq 1}(a\tau)^{p-1}I_p(x)\right] \\ I_p(x) = \dfrac{K}{\Delta\nu}\displaystyle\int_{\nu_0-\Delta\nu}^{\nu_0+\Delta\nu}\cos\left\{\frac{2\pi}{c}\left[(L_T+pL)N_{eff}(\nu) - x\right]\nu\right\}\mathrm{d}\,\nu \end{cases} \tag{4.10}$$

From this expressions, $I_p(x)$ represent the intensity of waves performing p round trips in the resonator. In the case where dispersion can be neglected, corresponding to a constant effective index $N_{eff}(\nu) = N_0$, I_p takes the simpler form:

$$I_p(x) = -K\,\mathrm{sin}_c\left\{\frac{\pi}{c}\left[L_p^\star - x\right]\Delta\nu\right\}\cos\left\{\frac{2\pi}{c}\left[L_p^\star - x\right]\nu_0\right\} \tag{4.11}$$

where $L_p^\star = (L_T + pL)N_0$ and $\mathrm{sin}_c(x) = \frac{\sin x}{x}$.

From this simplified expression, few observations can be made. First, each I_p function is the product of a high (spatial) frequency signal of period $T_{s,HF} = c/\nu_0$ and of a low frequency signal in form of a sin_c function

with a period $T_{s,LF} = 2c/\Delta\nu_0$. For a source with a 100 nm bandwidth emitting around 1550 nm, $T_{s,HF}$ is 15.5 times shorter than $T_{s,LF}$. As a consequence, the $\sin_c$ signal appears as a low frequency envelope signal representing interferences between the waves from the reference arm and the waves having made p round trips.

The $\sin_c$ modulation is actually the result of the Fourier transform (FT) of the DSP, and has a typical width inversely proportional to the source bandwidth $\Delta\lambda$. The function $I(x)$ can thus be viewed as the convolution between a sum $\Sigma(x)$ of equally spaced Dirac functions and a narrow-envelope, peak-shaped, form factor function $\mathcal{F}(x)$, which is the product between the FT of the DSP and the high frequency sinusoidal modulation:

$$I(x) = \{\mathcal{F} * \Sigma\}(x) \tag{4.12}$$

where:

$$\begin{cases} \Sigma(x) = (1-\gamma)^{1/2}\left[\tau\delta(x) - a(1-\tau^2)\sum_{p\geq 1}(a\tau)^{p-1}\delta(x-L_p^\star)\right] \\ \mathcal{F}(x) = \{\mathbf{FT}(DSP)\}(x)\cos\left(2\pi\frac{\nu_0}{c}x\right) \end{cases} \tag{4.13}$$

A Hilbert Transform is usually applied to the recorded interferogram signal I to remove the high frequency modulation so that the signal can be more easily analyzed.

These results can be compared to those obtained with the CRD technique employing laser pulses as described in §1.1. The positions of the envelope peaks provide the optical length of the resonator. Also, internal parameters a and τ can be deduced from the respective heights of the peaks. In fact, the same equation system, Eq.(4.5), can be used to determine these parameters, R_1 being the height ratio between the first two peaks and R_2 between any subsequent neighbour peaks.

In addition to the determination of the internal parameters, the recorded OLCI signal also provides the intensity transmittance and the accumulated phase shift as functions of the wavelength in a range defined by the bandwidth of the source. These two functions correspond to the squared modulus and the argument of the FT of the recorded signal, respectively.

1.3 Wavelength-Scanning Method

1.3.1 Introduction

The wavelength-scanning method (WSM) was previously described as a detection scheme to track the resonant wavelengths of a microresonator (cf. Chap.1). In this chapter, we study the use of the same method to determine the optical characteristics of the microresonator.

The WSM is straightforward to measure the intensity transmittance of a microresonator as a function of the wavelength. Light from a tunable laser is coupled to the bus waveguide and optical power at the output is measured as the emission wavelength of the laser varies. The wavelength scan is either performed step-by-step, or continuously. The main advantage of a step by step method is the absolute accuracy obtained due to measurement signal averaging. The continuous method[3] is much faster, and liable to measure a transmittance over 100 nm in 1 second. However, obtaining the same accuracy[4] with a continuous scan of the wavelength requires very fast acquisition channels. Also, in comparison to the step-by-step method, where the wavelength is known at each step, the continuous method requires an additional wavelength referencing system.

The choice between a step-by-step or continuous method is in fact mainly determined by budget issues, an accurate implementation of a continuous method being more expensive. With adequate acquisition channels and internal referencing of the tunable laser, the continuous method can provide very accurate results for a minimal measurement duration. This aspect is particularly important for microring resonators where the position and shape of resonances can greatly vary with device temperature. Therefore, if the room temperature is not perfectly stable, intensity transmittance measurements of long durations, typical of step by step methods, can be largely biased because of temperature variations.

1.3.2 Intensity transmittance of a microresonator as a function of wavelength

It was established in Chap.2 (§2.2.1) that the intensity transmittance of a microring resonator can be expressed as:

[3] where the source is continuously swept between two wavelengths
[4] as that achieved with a step-by-step method

$$T(\Phi) = (1-\gamma)\left[1 - T_{\text{FP}}(\Phi)\right] \tag{4.14}$$

where $T_{\text{FP}}(\Phi)$ is analogous to the intensity transmittance of a Fabry-Pérot interferometer.

$$\begin{cases} T_{\text{FP}}(\Phi) = \dfrac{A_0}{1 + F\sin^2(\Phi/2)} \\ A_0 = \dfrac{\left(1-a^2\right)\left(1-\tau^2\right)}{(1-a\tau)^2} \\ F = \dfrac{4a\tau}{(1-a\tau)^2} \end{cases} \tag{4.15}$$

The single-trip phase delay Φ can be written either as a function either of the optical frequency ν, or of the wavelength in vacuum λ:

$$\Phi = \frac{2\pi}{c}\nu N_{eff}(\nu)L = \frac{2\pi}{\lambda}N_{eff}(\lambda)L \tag{4.16}$$

Because Φ displays a nonlinear dependence on λ, it would be best to use the optical frequency ν to analyze intensity transmittances. However, in the literature, intensity transmittances are most commonly written as functions of the wavelength. Accordingly, in the following, the intensity transmittance will be written as:

$$T(\lambda) = (1-\gamma)\left\{1 - \frac{A_0}{1 + F\sin^2\left[\pi N_{eff}(\lambda)L/\lambda\right]}\right\} \tag{4.17}$$

1.3.3 Determination of the resonant wavelengths

The measurement of the resonant wavelengths of a microresonator and of their variations is the basic operating principle of all optical-resonator-based sensors. The advantage of those devices in sensing applications is the strong sensitivity of the spectral position of a single resonance to the effective index of the mode propagating in the resonator, which is itself sensitive to numerous physical quantities, including the nature and composition of the external medium to be characterized.

For sensing purposes, resonant wavelengths have to be measured with a maximal accuracy. Thus, specific attention must be paid to the measurement techniques. As outlined in Chap.1, a suitable technique is to measure

the resonant wavelength[5] $\lambda_m^{(R)}$ is to determine first the wavelengths corresponding to the inflection points[6], $\lambda_{m,inf}^{L}$ and $\lambda_{m,inf}^{R}$. Indeed, because the intensity slope is at its highest at these points, the accuracy in the determination of these wavelengths is maximal (cf. Chap.2). Then, from the symmetry of the resonance, we have:

$$\lambda_m^{(R)} = \frac{\lambda_{m,inf}^{L} + \lambda_{m,inf}^{R}}{2} \tag{4.18}$$

All characteristic wavelengths and intensities related to a resonance of order m are presented in Fig. 4.3.

Besides sensing applications, spectral positions of the resonances can provide interesting information on the dispersion of the guided mode in the microresonator.

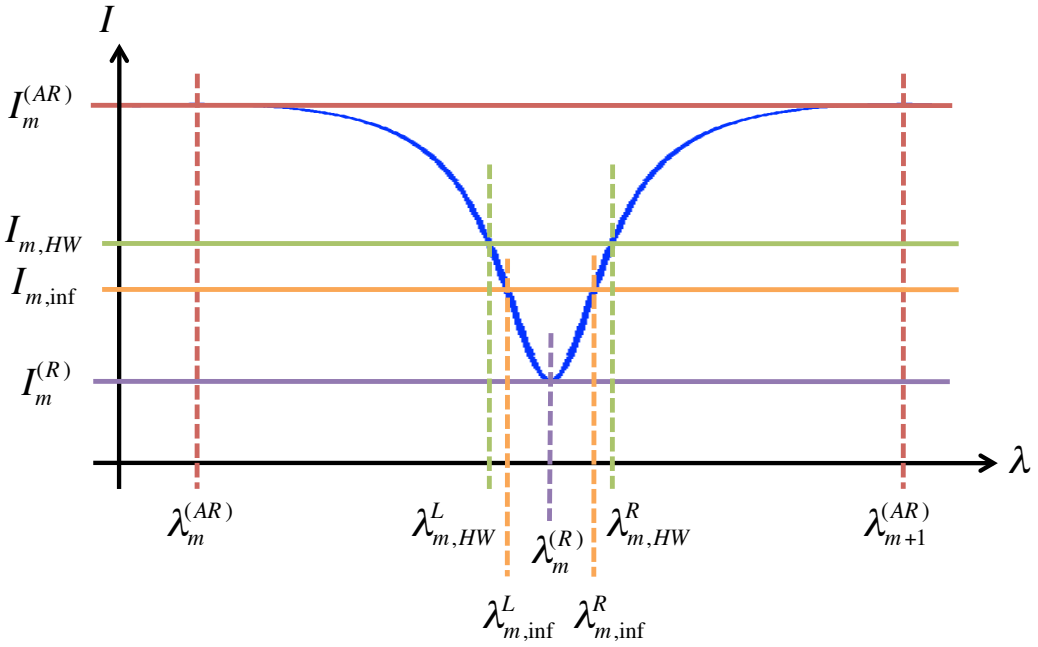

Figure 4.3: Diagram of characteristic intensity levels and wavelengths of a resonance

From Eq. 4.17, a resonant wavelength λ_m of order m, corresponding to

[5] "(R)" for Resonant
[6] "L" for Left and "R" for Right

a local minimum of transmitted intensity, verifies the following equation:

$$\frac{\lambda_m^{(R)}}{N_{eff}(\lambda_m^{(R)})} = \frac{L}{m+1/2} \tag{4.19}$$

From this equation, and because the order of interference m cannot be determined, it is clear that the effective index $N_{eff}(\lambda_m^{(R)})$ cannot be calculated from the sole measurement of $\lambda_m^{(R)}$. However, the spacings between the resonant wavelengths, commonly used to measure the free spectral range (FSR), can be used to determine dispersion properties.

1.3.4 Determination of the FSR

In a straightforward fashion, the evaluation of the FSR can be performed by measuring two neighbouring resonant wavelengths near the center λ_c of the wavelength range:

$$\text{FSR} \simeq \text{FSR}(\lambda_c) = \lambda_{m+1}^{(R)} - \lambda_m^{(R)} \tag{4.20}$$

The FSR value itself is, for many applications, of little interest as compared to the finesse, the contrast and the Q factor. However, its relation to the group effective index is particularly important to determine dispersion properties. Indeed, the FSR, on a neighbourhood of a wavelength λ_0, can be expressed as (cf. Chap.2):

$$\text{FSR}(\lambda_0) = \frac{\lambda_0^2}{N_G(\lambda_0)L} \tag{4.21}$$

where $N_G(\lambda_0)$ is the group effective index near λ_0 and L is the average geometrical length of the microresonator.

1.3.5 Determination of the dispersion properties

Generally speaking, for a measured intensity transmittance, an integer number N of resonant wavelengths can be measured; N depends on $\Delta\lambda$, the wavelength range scanned, on the FSR, and on dispersion properties. In the following, these resonant wavelengths will be written as a series of wavelengths $\{\lambda_1^{(R)}, \lambda_2^{(R)}, \ldots, \lambda_N^{(R)}\}$ in ascending order. Then, (N-1) values of the anti-resonant wavelengths $\lambda_m^{(AR)}$, corresponding to a single-trip

phase delay that is a multiple of 2π, can be approximately[7] determined from the values of the resonant wavelengths according to:

$$\lambda_m^{(AR)} = \frac{\lambda_m^{(R)} + \lambda_{m+1}^{(R)}}{2} \tag{4.22}$$

Spectral positions of the anti-resonances are merely used as indicative values, or as starting points for searching local maxima, and consequently do not need to be determined very accurately.

The local value of the FSR at $\lambda_m^{(AR)}$ can be written as:

$$\text{FSR}\left(\lambda_m^{(AR)}\right) = \lambda_{m+1}^{(R)} - \lambda_m^{(R)} \tag{4.23}$$

From these equations, the group effective index can be calculated at each of the (N-1) anti-resonant wavelength according to:

$$N_G\left(\lambda_m^{(AR)}\right) = \frac{\left(\lambda_m^{(R)}\right)^2}{L\left(\lambda_{m+1}^{(R)} - \lambda_m^{(R)}\right)} \tag{4.24}$$

The phase effective index, or simply the effective index N_{eff} can then determined by solving the differential equation:

$$N_{eff} - \lambda \frac{\mathrm{d}\, N_{eff}}{\mathrm{d}\, \lambda} = N_G \tag{4.25}$$

1.3.6 Determination of the contrast and the FWHM

The measurement of the contrast C is simply based on the measurements of local minimum T_{min} and maximum T_{max} of intensity transmittance. These values are injected in the expression defining the contrast:

$$C = \frac{T_{max} - T_{min}}{T_{max} + T_{min}} \tag{4.26}$$

In presence of parasitic modulations of the intensity transmittance envelope, or of modulations due to variations of the internal parameters[8], it is

[7] The approximation lies in the fact that, since the effective index is wavelength dependent, the actual spectral position of anti-resonance is not strictly at an equal distance between the two neighbouring resonant wavelengths. However, if the dispersion is moderate, it can be considered that the effective index does not change significantly over a wavelength range corresponding to one FSR, especially if it is small.

[8] as described in Chap.2 §4.1

preferable to define T_{min} and T_{max} locally as:

$$\begin{cases} T_{min} = T\left(\lambda_m^{(R)}\right) \\ T_{max} = \dfrac{1}{2}\left[T\left(\lambda_m^{(AR)}\right) + T\left(\lambda_{m+1}^{(AR)}\right)\right] \end{cases} \tag{4.27}$$

From these values, the calculated value of the contrast C is local, depending on the chosen resonant wavelength $\lambda_m^{(R)}$. For a further characterization of the global behavior, determining the average value of the contrast can also be of interest. This can be easily done from an algorithm calculating all values of $\lambda_m^{(R)}$, $\lambda_m^{(AR)}$, $T\left(\lambda_m^{(R)}\right)$ and $T\left(\lambda_m^{(AR)}\right)$, and then infers all local values of the contrast $C\left(\lambda_m^{(R)}\right)$. Finally, the average contrast $\overline{C}$ can be calculated from:

$$\overline{C} = \frac{1}{N}\sum_{m\geq 1}^{N} C\left(\lambda_m^{(R)}\right) \tag{4.28}$$

Such averaging can also be applied to all characteristics deduced from intensity transmittance - FWHM, Finesse, Q factor, ... - as described in the following.

The extinction ratio (ER) sometimes replaces resonance contrast C to characterize the depth of a resonance, especially in optical filter applications. Whereas contrast is conventionally expressed in percents (%), the extinction ratio can be expressed in ratio, decibels (dB) or percents. Is is mathematically defined as:

$$\begin{cases} \text{ER} = T_{max}/T_{min} \\ \text{ER}_{\%} = 100\,\text{ER} \\ \text{ER}_{dB} = 10\log_{10}\left(\text{ER}\right) \end{cases} \tag{4.29}$$

The full width at half maximum (FWHM) can be determined locally, at the vicinity of a wavelength $\lambda_m^{(R)}$, by searching for the wavelengths $\lambda_{m,HW}^{R,L}$ (cf. Fig. 4.3) verifying:

$$T(\lambda) = \frac{1}{2}\left[T_{max}\left(\lambda_m^{(R)}\right) + T_{min}\left(\lambda_m^{(R)}\right)\right] \tag{4.30}$$

The local FWHM is then deduced from:

$$\text{FWHM}_{\lambda}\left(\lambda_m^{(R)}\right) = \lambda_{m,HW}^{R} - \lambda_{m,HW}^{L} \tag{4.31}$$

Another method to measure the FWHM is to use the fact that, at the vicinity of the resonant wavelength, a part of the intensity transmittance is equivalent to a Lorentzian.

1.3.7 Lorentzian equivalent

In physics, the general expression of a three-parameter Lorentzian distribution is:

$$D_{Lor}(x) = \frac{\Gamma^2}{\Gamma^2 + (x - x_0)^2} D_0 \tag{4.32}$$

where D_0 is the Lorentzian peak height, corresponding to $x = x_0$. The peak is centered on x_0, and its FWHM is Γ.

In comparison, the part of the intensity transmittance of a microresonator analogous to the intensity transmittance of a FP etalon is written as:

$$T_{\text{FP}}(\Phi) = \frac{A_0}{1 + F \sin^2(\Phi/2)} \tag{4.33}$$

Close to $\Phi = 0$, the following asymptotic expansion can be made :

$$\sin^2(\Phi/2) \sim \frac{\Phi^2}{4} \tag{4.34}$$

As as a result, T_{FP} can be written with near Φ near 0 as:

$$T_{\text{FP}}(\Phi) \sim \frac{4A_0/F}{4/F + \Phi^2} \tag{4.35}$$

This equivalent of T_{FP} can be identified as a Lorentzian distribution with $D_0 = A_0$ and $\Gamma = 2/\sqrt{F}$, which matches the expression of the phase FWHM [9], and of the intensity transmittance in Chap.2 (§2.3.3). Comparison between intensity transmittance, Lorentzian equivalent, and polynomial equivalents is plotted in Fig. 4.4.

[9] $\Delta\Phi$

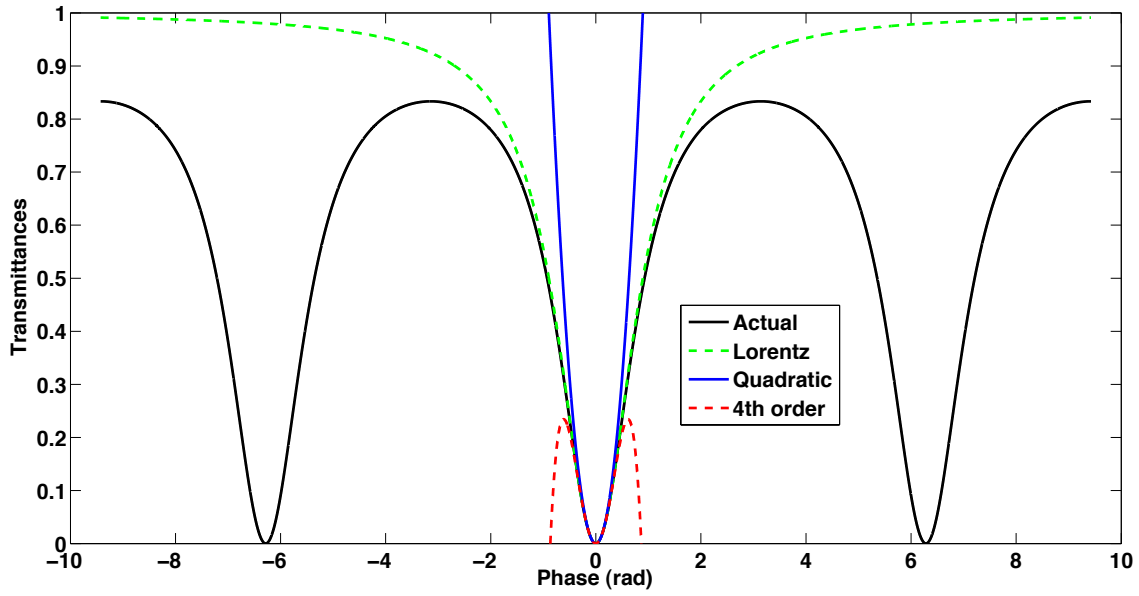

Figure 4.4: Comparison between Lorentzian, quadratic and 4th-order polynomial equivalents of the intensity transmittance for a coefficient of finesse $F = 5$.

A rapid analysis of Fig. 4.4 shows that the Lorentzian equivalent is a very good approximation of the intensity transmittance near $\Phi = 0$, and is much better suited for curve fitting than polynomial equivalents. Since the intensity transmittance expressed as a function of phase is 2π-periodical, each resonance peak can be approximated by the same Lorentzian distribution, translated in phase by a multiple of 2π.

In Fig. 4.5, the accuracy of the Lorentzian approximation is evaluated as a function of the coefficient of finesse F. The plots of residuals[10] clearly show that the Lorentzian approximation is better for narrower peaks, with significant variations depending on the Finesse $\mathcal{F} = \pi\sqrt{F}/2$ of the optical cavity.

One of the property of the Lorentzian distribution is the constant ratio between the FWHM and the distance between the inflexion points, which is equal to $\sqrt{3}$. Thus, a good approximation of the FWHM can be deduced from the positions of the inflexion points following:

$$\mathrm{FWHM}_\lambda\left(\lambda_m^{(R)}\right) \simeq \sqrt{3}\left(\lambda_{m,inf}^{R} - \lambda_{m,inf}^{L}\right) \tag{4.36}$$

[10] residuals are the absolute differences between transmittances and their Lorentzian equivalents

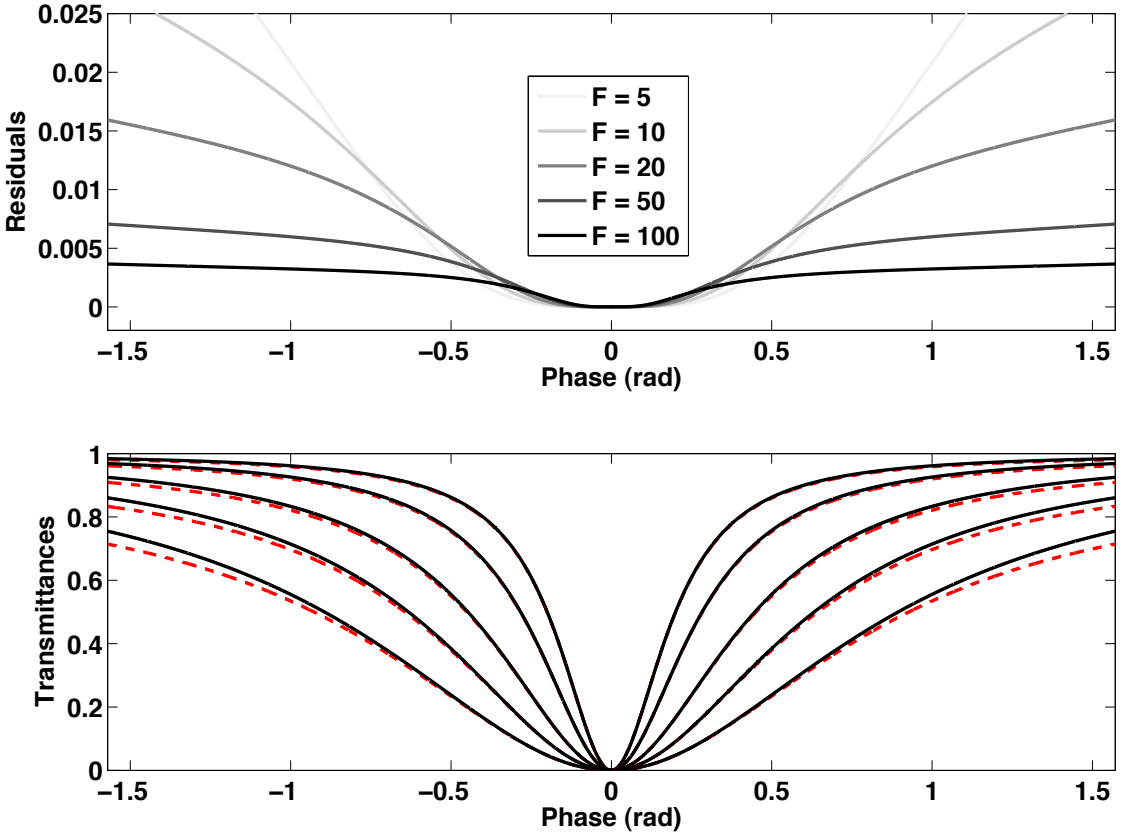

Figure 4.5: Evaluation of the accuracy of the Lorentzian approximation as a function of the coefficient of finesse F. In the transmittance plots, solid black lines are the Lorentzian equivalents, and red dashed lines are the theoretical transmittances for F values ranging from $F = 5$ (largest resonance) to $F = 100$ (narrowest resonance).

1.3.8 Determination of the Q factor and the finesse $\mathcal{F}$

The Q factor can be almost directly calculated knowing the value of the FWHM, from the expression:

$$Q\left(\lambda_m^{(R)}\right) = \frac{\lambda_m^{(R)}}{\text{FWHM}_\lambda\left(\lambda_m^{(R)}\right)} \tag{4.37}$$

Finally, the local finesse $\mathcal{F}\left(\lambda_m^{(R)}\right)$ can be directly evaluated from the local values of the FSR and the FWHM, from:

$$\mathcal{F}\left(\lambda_m^{(R)}\right) = \frac{\text{FSR}\left(\lambda_m^{(R)}\right)}{\text{FWHM}_\lambda\left(\lambda_m^{(R)}\right)} = \frac{\lambda_{m+1}^{(AR)} - \lambda_m^{(AR)}}{\text{FWHM}_\lambda\left(\lambda_m^{(R)}\right)} \tag{4.38}$$

1.3.9 Determination of the internal parameters

In the expression of the intensity transmittance, as in the expressions of all its characteristic factors, the internal parameters a and τ play perfectly symmetrical roles. Thus, unless the critical coupling condition is satisfied, resulting in $a = \tau$, no measurement or fit of a single intensity transmittance can provide the actual values of a and τ. This constitutes a basic limitation of the wavelength scan method for the characterization of passive microresonators.

However, as it will be demonstrated, a quantity that can be determined uniquely from the single knowledge of the transmittance is the product $a\tau$. In addition, it is possible to determine two numerical values α and β ($\alpha < \beta$), that relate to a and τ. More specifically, either $a = \alpha$ and $\tau = \beta$, or $\tau = \alpha$ and $a = \beta$. Still, it is impossible from the sole analysis of the intensity transmittance to know if it is the first or the second situation that applies[11].

The $a\tau$ product, and α and β values can be determined from two methods. The first one is based on a numerical fit of the intensity transmittance, providing directly the values of α and β, then $a\tau = \alpha\beta$. The fit can be performed on a single resonance to provide local values of the parameters. For that purpose, the full expression of the intensity transmittance, or its Lorentzian equivalent near resonance, can be used.

It can also be of interest to study how these internal parameters vary with wavelength. Then, a first method could be to provide wavelength-dependent expressions of the parameters used in the intensity transmittance to perform a fit on a large wavelength range. However, this implies a previous knowledge of the form of the wavelength-dependent expressions. A better method is to fit each resonance independently to determine all local values of the internal parameters, directly providing their wavelength dependence with a sampling period equal to the FSR.

[11] The former situation corresponds to under-coupling, whereas the later is characteristic of over-coupling. Because of this, knowing if the resonator is under or over coupled allows the determination of a and τ. Such knowledge may be acquired by comparing the properties of two or more microresonators which differ from each other by only their optical loss or by their cross-coupling coefficient. This can be achieved, for instance, by building two neighbouring microracetrack resonators with a small difference in their respective coupling lengths.

The local values of α, β and $a\tau$ can also be calculated without the use of a fitting algorithm. This can be achieved using several schemes. The most efficient scheme is to determine $a\tau$ from a local value of the finesse, then α and β from a local value of the contrast. Further details on the necessary calculations are presented below.

At this point, it is preferable to perform a variable change, setting $X = a\tau$. The finesse can be expressed as:

$$\mathcal{F} = \frac{\pi\sqrt{X}}{1-X} \tag{4.39}$$

Knowing $\mathcal{F}$, X appears as a solution of the following quadratic equation:

$$X^2 - \left(2 + \frac{\pi^2}{\mathcal{F}^2}\right) X + 1 = 0 \tag{4.40}$$

With a positive discriminant Δ, the two distinct solutions of this equation are:

$$X_{\pm} = 1 + \frac{\pi^2}{2\mathcal{F}^2} \pm \frac{\pi}{2\mathcal{F}^2}\sqrt{4\mathcal{F}^2 + \pi^2} \tag{4.41}$$

Because $X = a\tau$ needs to be inferior to unity, the only solution and final expression is:

$$a\tau = 1 + \frac{\pi}{2\mathcal{F}^2}\left[\pi - \sqrt{4\mathcal{F}^2 + \pi^2}\right] \tag{4.42}$$

Then, the contrast C can be written as a function of X and τ:

$$C = \frac{(X+\tau^2)^2(1-X)^2 - (X-\tau^2)^2(1+X)^2}{(X+\tau^2)^2(1-X)^2 + (X-\tau^2)^2(1+X)^2} \tag{4.43}$$

This equality can be re-written as a fourth-order equation where τ is the unknown, and C and X are parameters. The positive solutions of this equation are α and β, expressed as:

$$\begin{cases} \alpha = \dfrac{\left[1+\sqrt{1-C^2}\right]X + 2CX^2 + \left[1-\sqrt{1-C^2}\right]X^3}{\sqrt{C+2X+CX^2}} \\ \beta = \dfrac{\left[1+\sqrt{1-C^2}\right]X + 2CX^2 + \left[1+\sqrt{1-C^2}\right]X^3}{\sqrt{C+2X+CX^2}} \end{cases} \tag{4.44}$$

1.3.10 Fourier transform analysis of the intensity transmittance of a ring resonator

In order to determine the Fourier Transform of the transmittance, we will start by calculating the FT of the following function:

$$h(z) = \frac{(1-a^2)(1-\tau^2)}{(1-a\tau)^2 + 4a\tau\sin^2(z)} \tag{4.45}$$

This function is π-periodical and can accordingly be written as:

$$h(z) = \sum_{n=-\infty}^{+\infty} c_n e^{+2jnz}\,, \text{where } c_n = \frac{1}{\pi}\int_{-\pi/2}^{\pi/2} h(z)e^{-2jnz}dz \tag{4.46}$$

To determine the expressions of the c_n coefficients, we set:

$$\Sigma_n = \alpha c_{n-1} + \beta c_n + \gamma c_{n+1}\,, \quad n \in \mathbb{Z} \tag{4.47}$$

From Eq. 4.46, this quantity can be written as:

$$\Sigma_n = \frac{(1-a^2)(1-\tau^2)}{\pi}\int_{-\pi/2}^{\pi/2} \frac{e^{-2jnz}\left[\alpha e^{+2jz} + \beta + \gamma e^{-2jz}\right]}{(1-a\tau)^2 + 4a\tau\sin^2(z)}dz \tag{4.48}$$

where $\sin^2(z)$ can be written in a complex exponential form:

$$\sin^2(z) = -\frac{1}{4}\left[e^{2jz} + e^{-2jz} - 2\right] \tag{4.49}$$

The denominator of the rational fraction can then be written as:

$$1 + (a\tau)^2 - a\tau\left[e^{2jz} + e^{-2jz}\right] \tag{4.50}$$

To simplify the fraction, we have to set

$$\begin{cases} \alpha = \gamma = -a\tau \\ \beta = 1 + (a\tau)^2 \end{cases} \tag{4.51}$$

so that the final expression of Σ_n is

$$\Sigma_n = \frac{(1-a^2)(1-\tau^2)}{\pi}\int_{-\pi/2}^{\pi/2} e^{-2jnz}dz\,, \quad n \in \mathbb{Z} \tag{4.52}$$

From that expression, values of Σ_n are determined:

$$\begin{cases} \Sigma_n = 0, \quad n \in \mathbb{Z}^* \\ \Sigma_0 = (1-a^2)(1-\tau^2) \end{cases} \tag{4.53}$$

For $n \in \mathbb{Z}^*$, c_n verifies the characteristic equation (C):

$$\alpha c_{n-1} + \beta c_n + \gamma c_{n+1} = 0 \tag{4.54}$$

We know then that c_n is of the form $c_n = \lambda r_1^{|n|} + \mu r_2^{|n|}$ where r_1 and r_2 are the solutions of (C). We can rewrite the characteristic equation as:

$$-a\tau X^2 + \left[1 + (a\tau)^2\right] X - a\tau = 0 \tag{4.55}$$

After expanding and refactoring, the discriminant of (C) can be expressed as:

$$\Delta = \left[1 - (a\tau)^2\right]^2 \tag{4.56}$$

In this expression, a and τ only have a physical meaning if their values range between 0 and 1, which means that in our case, Δ is always superior to 0. The two solutions of (C) can then be deduced from:

$$r_{1,2} = \frac{\left[1 + (a\tau)^2\right]^2 \mp \left[1 - (a\tau)^2\right]}{2a\tau} \tag{4.57}$$

After simplification, we find $r_1 = (a\tau)^{-1}$ and $r_2 = a\tau$. r_1 being superior to 1, c_n has only a physical meaning if $\lambda = 0$. which means that $c_n = \mu(a\tau)^{|n|}$. We use then the value of Σ_0 to determine the expression of the constant μ:

$$\Sigma_0 = (1-a^2)(1-\tau^2) = 2\alpha c_1 + \beta_0 = \mu\left[-2(a\tau)^2 + 1 + (xy)^2\right] \tag{4.58}$$

The final form for c_n is then

$$c_n = \frac{(1-a^2)(1-\tau^2)}{1-(a\tau)^2}(a\tau)^{|n|}, \quad n \in \mathbb{Z} \tag{4.59}$$

From this expression, the phase-dependent intensity transmittance of a micro-resonator can be written as its Fourier series:

$$T(\Phi) = (1-\gamma)\left[1 - h(\Phi/2)\right] = \sum_{n=-\infty}^{+\infty} d_n e^{+jn\Phi} \tag{4.60}$$

where we simply have

$$\begin{cases} d_0 = (1-\gamma)(1-c_0) \\ d_n = -(1-\gamma)\dfrac{(1-a^2)(1-\tau^2)}{1-(a\tau)^2}(a\tau)^{|n|}, \quad n \in \mathbb{Z}^* \end{cases} \tag{4.61}$$

Since the intensity transmittance $T(\Phi)$ is a real function, $d_n = d_{-n}$ is verified. We can then finally write the intensity transmittance as function of the single-trip phase delay:

$$T(\Phi) = (1-\gamma)\left\{1 - \frac{(1-a^2)(1-\tau^2)}{1-(a\tau)^2}\left[1 + 2\sum_{n=1}^{+\infty}(a\tau)^n \cos(n\Phi)\right]\right\} \tag{4.62}$$

1.3.11 Spectrum of recorded intensity transmittance

From Eq. 4.62, the unilateral spectrum of the intensity transmittance is composed of equally spaced Dirac functions. However, the actual spectrum from the measured intensity has to be related to wavelength, and not to the single-trip phase delay. Also, because of a windowing effect, the limited wavelength range on which the intensity transmittance was measured will bias the calculated spectrum.

In order to simplify calculations, the use of the wavenumber $\sigma = \lambda^{-1}$ is preferred in the following. The single-trip phase delay Φ can be written as a function of σ:

$$\Phi(\sigma) = 2\pi\sigma L N_{eff}(\sigma) \tag{4.63}$$

The optical power at the output of the tunable laser does not usually depend on wavelength. Therefore, the spectral density $\mathcal{I}_S$ of the optical source can be defined for $\sigma \in \mathbb{R}$ as a boxcar function:

$$\begin{cases} \mathcal{I}_S(\sigma) = \dfrac{dI_S}{d\sigma}(\sigma) = \mathcal{I}_0 = \dfrac{I_0}{\Delta\sigma}, \quad \sigma \in [\sigma_1, \sigma_2] \\ \mathcal{I}_S(\sigma) = 0 \quad \text{elsewhere} \end{cases} \tag{4.64}$$

where σ_1 and σ_2 are the lower and upper limits of the measured wavenumbers. When the spectrum of the intensity transmittance is calculated from a FFT algorithm, the signal to consider is the transmitted intensity $\mathcal{I}_{Tr}$ defined as:

$$\mathcal{I}_{Tr}(\sigma) = \text{Mod}(\sigma) T(\sigma) \mathcal{I}_S(\sigma) \tag{4.65}$$

where Mod(σ) is a envelope modulation function from the photodetector.

A calibration of the transmittance from the source to the photodetector can be performed so that this modulation can be removed. At this stage, the measured intensity transmittance can be written as:

$$T_{Meas}(\sigma) = \frac{T(\sigma)\mathcal{I}_S(\sigma)}{I_0} \tag{4.66}$$

In the Fourier domain, the reciprocal variable of the wavenumber σ is the optical distance x, *ie* the product between a phase index and a geometrical length. Because of the limited wavelength range of the measurement, the Fourier transform (FT) of the measured intensity transmittance will result from a convolution between the FT of the transmittance and the FT of the source spectrum:

$$\widetilde{T}_{Meas}(x) = \frac{\widetilde{T}(x) \otimes \widetilde{\mathcal{I}}_S(x)}{I_0} \tag{4.67}$$

The actual form of the spectrum will finally strongly depend on the wave dispersion in the resonator.

Case of zero dispersion

Zero dispersion corresponds to $N_{eff}(\sigma) = N_0 =$ constant. This scenario is the most simple to solve since all waves travel at the same speed. For all wavenumbers, the optical distance corresponding to a single trip inside the resonator is $x_0 = LN_0$. From Eq.(4.60), the spectrum of the transmittance $\widetilde{T}$ can be written as:

$$\widetilde{T}(x) = \sum_{n=-\infty}^{+\infty} d_n \delta(x - nx_0) \tag{4.68}$$

The windowing effect, result of the convolution, now appears in the expression of the measured spectrum:

$$\widetilde{T}_{Meas}(x) = \sum_{n=-\infty}^{+\infty} d_n \, \mathrm{sinc}\left[\pi(x - nx_0)\Delta\sigma\right] \tag{4.69}$$

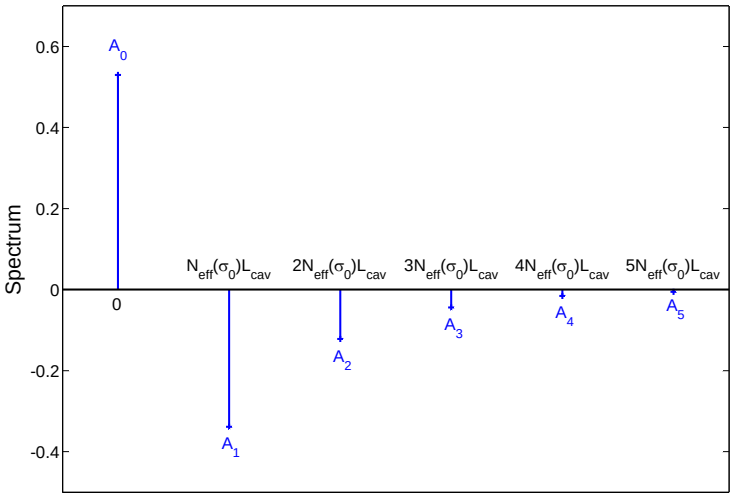

Figure 4.6: Spectrum of the transmitted intensity when dispersion is neglected. $a = \tau = 0.6$ and $\gamma = 0$.

Case of non-zero dispersion

This scenario is more subtle to understand since each wavenumber has an associated optical distance $x_0(\sigma) = LN_{eff}(\sigma)$ corresponding to a single trip in the resonator. As a result, the spectrum of the transmission is a superimposition of the spectra of zero dispersion transmission for each wavenumber:

$$\widetilde{T}(x) = \frac{1}{\Delta\sigma} \sum_{n=-\infty}^{+\infty} d_n \int_{\sigma_1}^{\sigma_2} \delta(x - nx_0(\sigma))\,\mathrm{d}\,\sigma \tag{4.70}$$

After integration of the distribution, the spectrum of the transmission can be expressed as:

$$\widetilde{T}(x) = \sum_{n=-\infty}^{+\infty} \frac{d_n}{n\left[x_0(\sigma_2) - x_0(\sigma_1)\right]} \mathrm{Rect}\left\{\frac{x - nx_0(\sigma_0)}{n\left[x_0(\sigma_2) - x_0(\sigma_1)\right]}\right\} \tag{4.71}$$

where σ_0 is the center of the bandwidth.

2 Measurement setup

2.1 Basic Setup

2.1.1 Presentation

The key element of our basic setup for intensity transmittance measurements is a TUNICS tunable laser source working in the 1500-1640 nm wavelength range. Its output is connected to a SMF-28 optical fiber. The output of this fiber is collimated by a x20 NACHET NIR[12] microscope objective. Then, the polarization of the beam is controlled with a polarizer (P) and half-wave plate ($\lambda/2$).

The polarizer defines the linear polarization state, and the half-wave plate is used to rotate the direction of the linear polarization after the polarizer. The beam is then coupled to the DUT, more precisely to the bus waveguide coupled to a microresonator, with a x40 NACHET NIR microscope objective. The silicon wafer on which the DUT was built is placed on a temperature-controlled mount to prevent temperature drift effects during characterization. The beam at the output of the bus waveguide is collimated by a x20 NACHET NIR objective, then directed to a photodetector, such as an optical power-meter or a photodiode.

2.1.2 Tunable laser source

The basic component of the tunable laser sources of the Tunics series is an external laser cavity in a modified Littman-Metcalf configuration (cf. Fig. 4.8). The emission wavelength, among others resonant wavelengths of the external cavity, is spatially selected by the incidence of the collimated beam on the diffraction grating. The controlled rotation of the dihedral reflector modifies the cavity length and simultaneously shifts the selectivity of the grating so that the order of the laser mode remains constant while the emission wavelength is tuned.

[12]NIR for near infrared

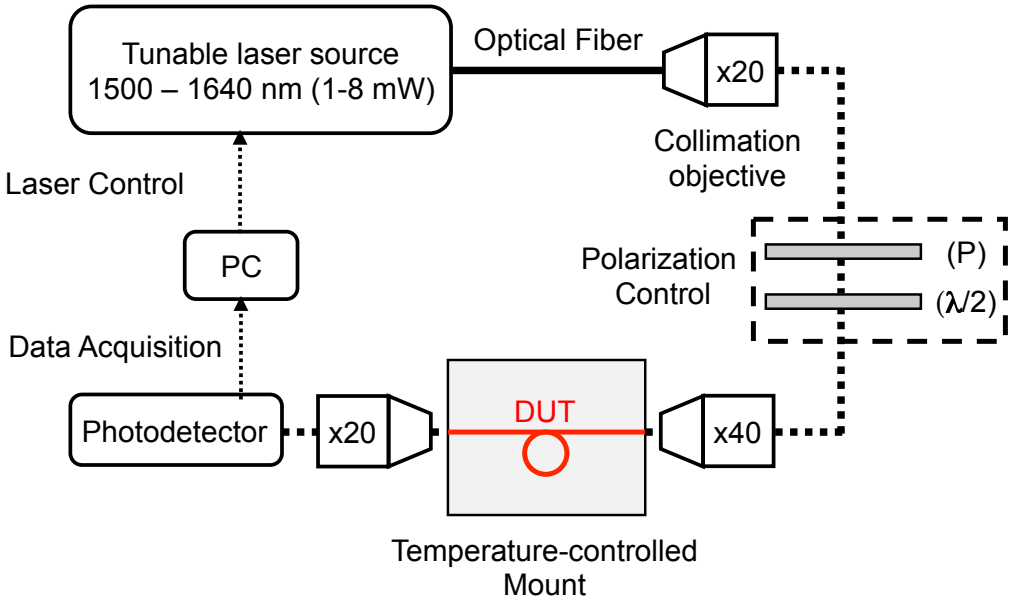

Figure 4.7: Schematic diagram of the basic setup for intensity transmittance measurements.

This configuration ensures a mode-hop free operation when tuning the emission wavelength, continuously or step-by-step. Some performances of the tunable laser are particularly relevant to the intensity transmittance measurements:

- The absolute wavelength accuracy (AWA) can be defined as the resolution on the emission wavelength after self-calibration. The wavelength error follows, on the whole spectral range, a normal distribution. The AWA is equal to three times the standard deviation of the emission wavelength. Consequently, the probability that the emission wavelength is within the displayed wavelength $\pm$ the AWA is approximately 99.7 %. Depending on the tunable laser source, the AWA can vary, from a few pm to a few tens of pm.

  The AWA is important for the absolute characterization of resonance positions of a microresonator. It combines uncertainties on the emission wavelength due to both systematic and random errors. However, if the aim of the wavelength scans is to measure the variations of the resonant wavelengths, then, as described in Chap.1, the uncertainty on the wavelength variation is not directly related to the AWA.

- Wavelength stability (WS) measures the drift with time of the emission wavelength from the user-specified value. This drift is caused by temperature variations of the room and/or by internal temperature variations of the optical elements. The value of WS applies to describe the uncertainty for the measurement of resonant wavelength variations. With Tunics laser source, values of WS is typically a few pm per hour.

- The tuning range (TR) is the wavelength range on which the tunable laser source can achieve mode-hop free operation. it is essentially dependent on the output optical power, whatever the source. Both FSR of the microresonator under study, and TR of the laser sources define how many resonances can be measured in one scan.

  optical power dependent emission wavelength range that can be selected without presence of mode hop. With the FSR of a microresonator, the TR defines how many resonances can be observed.

- The spectral width (SW), defined as a FWHM, is the typical linewidth of the laser emission around the selected wavelength. The SW defines the coherence length of the radiation, and can have an influence on parasitic modulations due to interferences from partial reflections in the DUT.

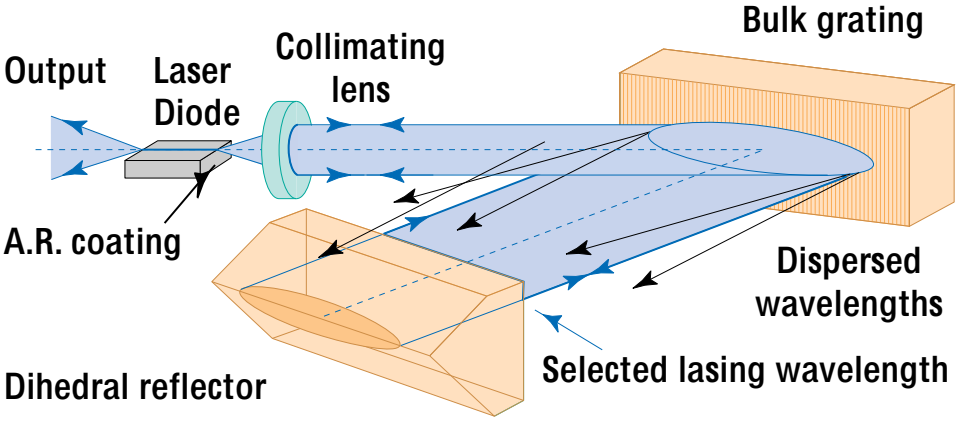

Figure 4.8: Schematic diagram of the self-aligned external laser cavity in a Tunics-Plus tunable laser source.

2.1.3 Polarization control

The polarization controller, composed of a polarizer (P) and a half-wave plate ($\lambda/2$), is necessary to define the polarization state of the input field, which is particularly important for the characterization of guided optics devices such as planar microresonators where the anisotropy is strong.

The role of the polarizer is to deliver a linearly polarized field from the slightly elliptical output of the optical fiber connected to the tunable laser. The ellipticity of the polarization state mainly comes from stress-induced birefringence in the fiber. It can be corrected by a slight twist applied to the connector of the fiber, in order to optimize the optical power after the polarizer.

The half-wave plate rotates the linear polarization after (P). It is thus used to control the polarization direction of the field coupled to the DUT. This direction can be chosen to exactly match the specific dominant field direction of TE or TM modes of the DUT. It can also be chosen so that both TE and TM modes of the DUT are excited. Rotation of the half-wave plate can then be used to control the intensity ratio between excited TE and TM modes.

In order to limit parasitic reflections, both polarizer and half-wave plate are coated with anti-reflective layers for 1500 nm. In addition, the half-wave plate is specifically chosen with highly a spectrally flat retardance so that input polarization state does not depend on the wavelength on the measurement bandwidth.

2.1.4 Temperature-controlled mount

The temperature-controlled mount was designed to reduce effects of external temperature variations on the intensity transmittance of the microresonators, especially on the resonances positions. The thermal regulation system is composed of a thermistor, two thermo-electric (Peltier) actuators and a controller. In real-time, the controller measures the temperature-dependent resistance of the thermistor and compares it to the resistive equivalent of the temperature set point.

The difference is fed to a proportionnal-integral-derivative (PID) controller whose output controls a symmetric current amplifier connected to the two thermo-electric devices in series configuration. This system can both cool down and warm up the microresonators. PID coefficients are set so that their response time is minimal, but with sufficient phase and gain margins so that the system remains stable under all circumstances.

The thermistor is in contact with the silicon wafer. A thin film of thermal paste between the copper plate and the silicon wafer, and surrounding the thermistor, ensures optimal thermal conduction between the different elements. As the silicon is a very good thermal conductor, temperature variations of microresonators are quickly detected by the controller. The thermo-electric devices are placed under the copper plate where the silicon wafer is placed. Copper was chosen for its high thermal conductivity, so that the response delay is minimal.

This thermal regulation setup, very efficient to stabilize the temperature of the DUT, was also used to measure the sensitivity of microresonators to temperature. This was done by modifying the temperature set points and measuring the intensity transmittance in both transient and stationary regimes.

2.1.5 Photodetector

The photodetector employed was either a large aperture commercial powermeter based on a Germanium photodiode, or a small aperture photodetector integrating a InGaAs photodiode. Both photodetectors can be used to perform step-by-step measurements, characterized by slow intensity variations. However, continuous measurements, with wavelength scanning speeds up to 100 nm/s, required the much higher bandwidth of the small aperture photodetector. Because of the small aperture, a 50 mm lens was specifically coupled with the fast detector to focus the output beam on the photodiode.

2.1.6 Data acquisition

Analogous signals from the temperature controller, from the laser source and from the photodetectors where routed to a National Instruments BNC-

2120 connector block, itself connected to a PCI-6133 data acquisition board, embedded in the control PC via a PCI port. The maximum sampling rate is 2.5 MSamples/s per channel, with a 14 bits resolution. A software was developed from the NI LabWindows environment to perform intensity transmittance measurements, controlling both the laser source and the data acquisition from the board.

2.1.7 Beam alignment

Because of the small section of the waveguides, a good alignment of all optical elements is necessary to achieve good source-to-detector transmission. Using the setup described and the alignment scheme developed in the following, an overall transmission rate up to 12 % were achieved.

The source block, where the beam is collimated first, needs to be adjusted so that the beam is parallel to the optical table (constant height), and parallel to one of the direction defined by the screw holes grid of the table. Then, the photodetector can be positioned on the course of the beam at the other end of the setup, and an iris can be placed in front to materialize the right position of the beam. Then, the elements of the polarization controller can be placed.

The x40 objective is placed so that the light intensity on the focusing region shows a good radial symmetry. For that purpose, parasitic reflections can be used to align the objective axis with the beam. The second objective can then be placed and aligned so that the output beam hits precisely the aperture hole. This scheme ensures a permanent alignment of the two objectives.

2.1.8 Optimization of the output intensity

Once the position of the focusing objective is defined, it shall not be moved when trying to couple the beam to the bus waveguide. Indeed, this would deteriorate the alignment between the beam and the optical axis of the objective. Instead, it is better to search for coupling by moving the wafer, hence the bus waveguide input, laterally and/or vertically.

A good alignment between the focusing objective and the input of the

bus waveguide is important for several reasons. The first reason is that the overall transmission will strongly depend on it. But, more importantly, a non-optimized alignment will result in a biased estimation of the resonance contrast in the measured intensity transmittance. This happens specifically if the focusing point is too close or too far from the input of the waveguide in the direction of the optical axis. In such a situation, light is coupled in the waveguide, but also in the silicon layer which acts as a slab waveguide. This results in measurement of optical power that did not propagate in the DUT. Moreover, light from the input beam can be reflected on the surface of the wafer, resulting in additional optical transmission. Because of this effect, all measured intensity levels are biased, which makes the observation of critical coupling impossible.

Before measuring the intensity transmittance from a device, the beam is routed via a mirror placed on a flip-mount to an IR camera with a 50 mm lens. Combined to the x20 collimation objective, a microscope is formed, allowing the observation of the distribution of IR radiation at the output of the waveguide. A good alignment of the waveguide is obtained when only light coming out of the waveguide is detected.

2.2 Acquisition method

2.2.1 Step-by-Step Scan

In a step-by-step scan, the emission wavelength is modified by discrete steps $\delta\lambda$ at every period T_s between a start wavelength λ_{start} and a stop wavelength λ_{stop}. After the instruction to change the wavelength is received, the source takes a typical duration T_d to tune and stabilize to the new wavelength. The value of T_d, depending on the wavelength step $\delta\lambda$ and on the scanning speed, can be determined from an analog output providing a signal proportional to the set wavelength. The minimal value of T_d for our tunable lasers was around 100 ms, and applies to all wavelength steps under 100 pm, being an intrinsic limit due to the motor. Because of this delay, acquisitions with high resolutions on large wavelength ranges would last several hours.

The acquisition of the data is triggered so that after proof that the instruction was properly received by the source, and after a time T_d, a num-

ber N_{avg} of samples of the transmitted intensity are acquired. These samples are directly averaged to produce one measurement point of the intensity transmittance as function of the wavelength. After the data points are recorded, a new wavelength setpoint is sent to the source. The other component of the measurement point to determine is the actual wavelength corresponding to the measured intensity transmittance. The wavelength can be precisely measured by an external lambda-meter. However, the characterization of planar microresonators with limited Q factors does not require a very high wavelength accuracy. In step-by-step measurements, the wavelength of the measured point was assumed to be equal to the set wavelength.

2.2.2 Continuous Scan

In a continuous scan, the emission wavelength is continuously swept from λ_{start} to λ_{stop}, with a speed defined as the scanning speed $(d\lambda/dt)$, which can be up to 100 nm/s. Then, after a specified time delay of at least 100 ms, the wavelength is continuously swept back, from λ_{stop} to λ_{start}. After stabilization at λ_{start}, a new cycle can be launched after a minimal delay of 100 ms.

In such a measurement scheme, the duration of the measurement depends on the wavelength range $\Delta\lambda = |\lambda_{start} - \lambda_{stop}|$, but does not depend on the wavelength resolution $\delta\lambda$. The wavelength resolution, depending only on the scanning speed and the sampling rate of the acquisition board, can interestingly be set at much lower values than the wavelength setting resolution of the source.

During a continuous scan, the analog output providing the set wavelength is not operational since it is continuously modified during the cycle. The challenge is then to trigger the acquisition, and to measure or extrapolate the wavelengths corresponding to the acquired transmitted intensities.

Continuous scan without wavelength referencing

The first developed method for continuous scan did not require an external wavelength measurement module. The idea was to trigger the acquisition of the intensity data from the rise of a synchronization signal,

corresponding to the voltage applied to the motor. An average time delay between the rising edge of this signal and the start of the sweep was evaluated, and was used to determine the instant, in the acquired data, where the wavelength was equal to λ_{start}. The wavelength corresponding to each acquired intensity was than calculated from the scanning speed, assumed to be constant during the scan, and from the value and position (in samples) of the start wavelength.

The main problems encountered with this technique is that the scanning speed is not constant during the scan: in the beginning, the motor accelerates to its nominal speed, and the motor slows down before arriving to λ_{stop}. This means that the actual scanning speed is lower than the nominal scanning speed at the beginning and at the end of each scan. Because the wavelength points are calculated from the nominal speed, the record intensity transmittance is importantly distorted in wavelength near λ_{start} and λ_{stop}.

The second problem of this technique is the repeatability of the determination of the wavelength. Indeed, each wavelength position relies on the time delay between the rise of the synchronization signal and the beginning of the sweep. Because this time delay is never exactly the same for each scan, the estimated wavelength positions are randomly varying around the actual wavelength positions, with a typical amplitude around 20 pm. This is particularly detrimental to sensor applications of microresonators where the accuracy in determining the position of the resonance has a strong influence on the sensing performances.

Continuous scan with wavelength referencing

Wavelength referencing in continuous measurements of intensity transmittances as a function of the wavelengths solves the two problems related to the inhomogeneity of the scanning speed during a scan, and to the inconsistency of the time delay from one scan to another. In a new setup, a wavelength referencing module inside a Tunics T100-R tunable laser provided an analog signal proportional to the wavelength during continuous scans.

The wavelength referencing is based on a Michelson interferometer integrating an acetylene cell. During a continuous scan, the analog signal is at 0V (V for volts) when $\lambda = \lambda_{start}$ and at 5V when $\lambda = \lambda_{stop}$. Due to the limitation of the resolution of the internal referencing module, the analog signal could only take a limited number of values from 0 to 5V. This separates the use of the continuous scan into two categories:

1. The first category of scan corresponds to the situation where the required resolution in wavelength for the acquisition of the intensity transmittance is larger than the resolution of the internal wavelength referencing. In that situation, the intensity transmittance as a function of the wavelength can be directly plotted as a XY plot of the measured intensity and the measured wavelength.

   Because of the direct measurement of the wavelength, motor acceleration and deceleration phases have no effect on the plot and the repeatability of the measured wavelength is not affected by variations of the time delay, allowing very good accuracy on the determination of the position of a resonance.

2. In the second category of scan, the required resolution is lower than that of the internal referencing. In such situation, because the actual wavelength is rounded up to the nearest level, the measured wavelength signal is a staircase function and cannot be directly used to plot the intensity transmittance.

   A solution to match the resolution was found by applying a linear regression to the staircase function, thus reconstructing the actual wavelength values. The only limitation of this technique is related to the non-uniformity of the scanning speed $(d\lambda/dt)$ along the scan duration, resulting once again in a wavelength distortion of the plot near λ_{start} and λ_{stop}. This was partially solved by limiting virtually the range of the source. When a scan between λ_{start} and λ_{stop} is required, the source actually scans the wavelength between $\lambda^{\star}_{start}$ and $\lambda^{\star}_{stop}$ de-

fined as:

$$\begin{cases} \lambda^{\star}_{start} = \lambda_{start} - \dfrac{V_{\lambda}}{V_{\lambda\,,\,\max}} \cdot \dfrac{\Delta\lambda_{\max}}{\Delta\lambda} \cdot M_N \\ \lambda^{\star}_{stop} = \lambda_{stop} + \dfrac{V_{\lambda}}{V_{\lambda\,,\,\max}} \cdot \dfrac{\Delta\lambda_{\max}}{\Delta\lambda} \cdot M_N \end{cases} \tag{4.72}$$

where V_{λ} is the specified scanning speed, $V_{\lambda\,,\,\max}$is the maximal scanning speed; $\Delta\lambda = |\lambda_{start} - \lambda_{stop}|$ is the specified scanning range and $\Delta\lambda_{\max}$ is the maximal scanning range; M_N is a nominal margin, equal to 5%, 10%, 20%, ... depending on the allowed level of wavelength distortion.

3 Optical characteristics

3.1 Experimental characterization of a microring resonator

3.1.1 Presentation

In this part, we present the method for characterizing a microring resonator from its measured intensity transmittance. The measured microresonator is a vertically-coupled microracetrack resonator with R = 180 μm and L_{str} = 120 μm, with 18 MΩ de-ionized (DI) water. It is a good example to study because of its single-mode behavior over the whole wavelength range of the source.

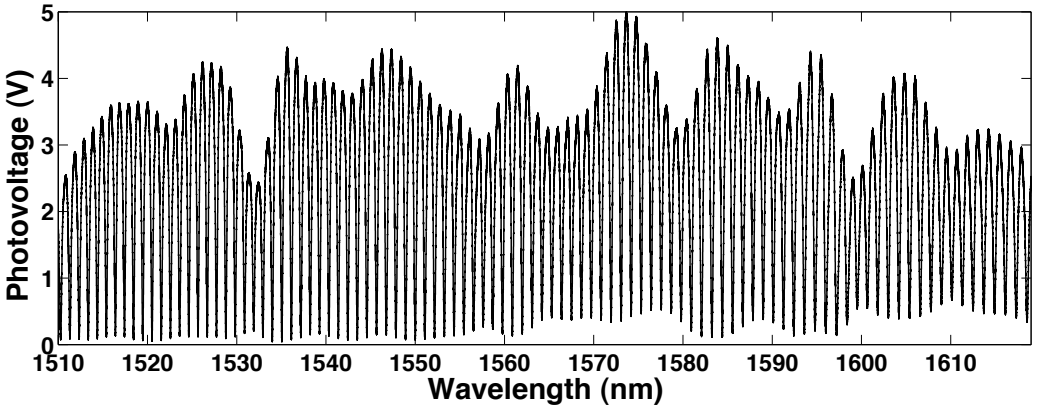

Figure 4.9: Photodetection voltage measured at the output of the DUT for an input optical power of 10 mW and a TE polarization state.

3.1.2 Smoothing the data

The intensity transmittance of the DUT was measured from a continuous wavelength scan, roughly between 1510 nm and 1620 nm with a resolution of 0.5 pm. With this very high resolution, noises from numerous sources are visible in the signal. From that point, smoothing the data can be useful to prevent noises from interfering with the algorithms that are used to determine the characteristics of the microresonators from intensity transmittances.

In Fig. 4.10, where different spans are used in the moving average filter for smoothing the data, specific results for the filtered signal are presented. In the raw data, a specific high frequency noise is detected. This noise can come from the optolectronic detection chain, and/or the intensity transmittance itself, from parasitic reflections of the waves. In the signal filtered with a span equal to 20 points, corresponding to 1 pm, the high-frequency noise disappears, and a lower frequency modulation, with a period of 40 pm, becomes obvious.

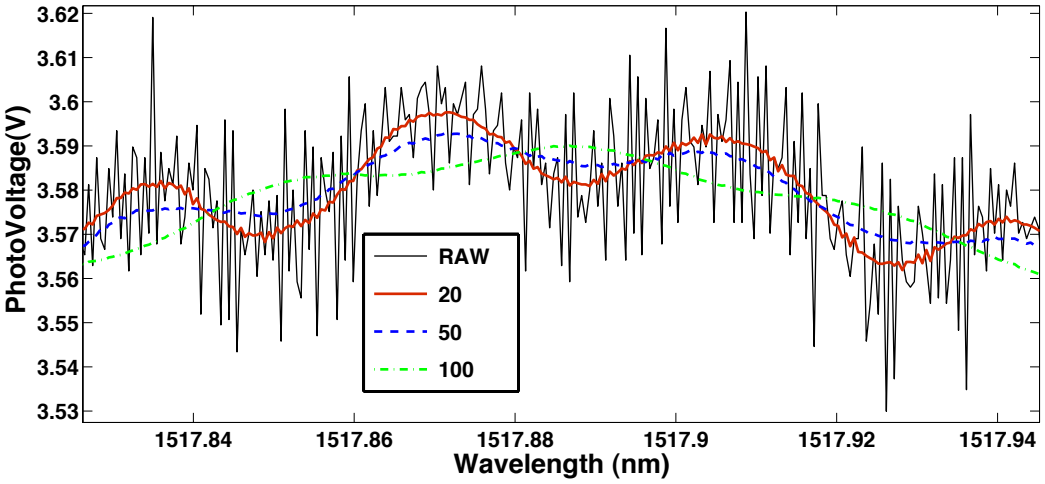

Figure 4.10: Photodetection voltage around a maximum of transmitted intensity and smoothed signal from a moving average filter with various spans.

This period corresponds to an interferometer with an optical length of approximately 6 cm while the geometric length of the bus waveguide is approximatelys 2 cm. The group effective index of propagation in the bus waveguide being near 1.5, this modulation appears to come from the interferences between waves travelling directly out of the bus waveguide and

waves reflected on both output and input before being directed to the reflector.

The small amplitude of the modulation is also consistent with the low reflection coefficients at the SU-8/air interfaces (4.8% at normal incidence). With the higher spans of 50 and 100, corresponding to 25 and 50 pm, respectively, the high-frequency modulations disappear and only the low frequency modulation remains, with a decreasing amplitude. When the moving average filter has a span of 100 points, its cutoff period as low-pass filter is 50 pm. As a consequence, the phase of the modulation with a period of 40 pm, under the cutoff period, is shifted by π.

It would be tempting to increase the span even more in order to get rid of the external perturbations and noises, and so to reveal the behaviour of the microresonator alone. However, as can be seen in Fig. 4.11, the moving average filter has a slight effect on the position of the resonances, and on their depths. Hence, the span of the filter should be adjusted so that high-frequency noise is removed, and so that the filtered signal remains roughly centered on the noise of the raw signal. In subsequent treatments, the span was set at 35.

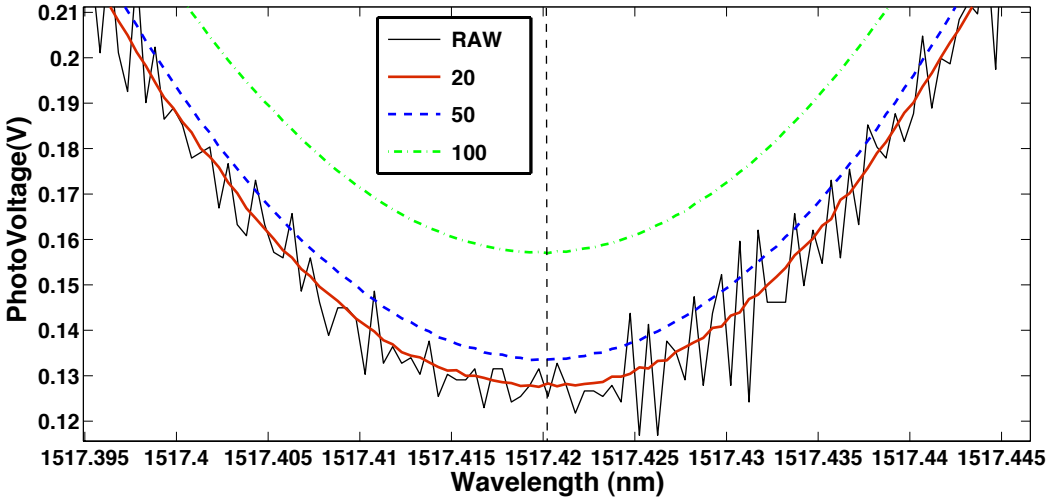

Figure 4.11: Influence of the span of the moving average filter on the measured signal near resonance.

3.1.3 Peak detection

The peak detection relies on a peak finding algorithm applied to the smoothed data. Local minima are found as being the zeros of the first-order differentiation of the data. Because of external modulations and noises, many irrelevant minima can be found by the algorithm. This issue is answered by filtering the peaks by height and periodicity constraints. A specified level sets a threshold value for "real" minima, *ie* for a maximal height that minima can have and which can be still considered as corresponding to a resonance peak. The periodicity constraint corresponds to a minimal distance separating the peaks. From these two additional parameters, the algorithm finds the most relevant peak system (cf. Fig. 4.12). Such a scheme can also be used to filter sets of resonances that are due to higher-order guided modes in the resonator.

From the positions of the resonances gathered from the peak finding algorithm, the positions of the anti-resonances can be deduced, and a second algorithm can easily find the values and positions of the local maxima of transmitted intensity (cf. Fig. 4.13).

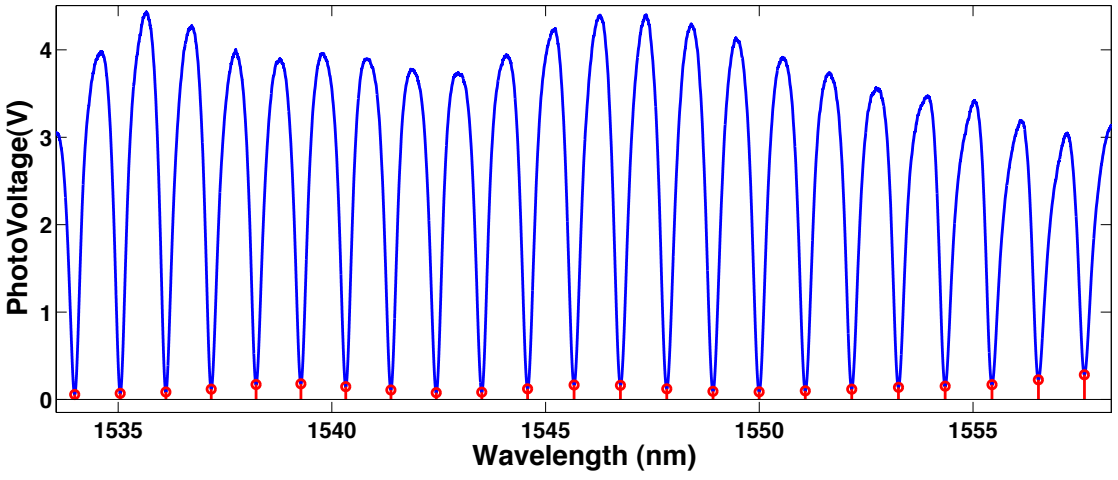

Figure 4.12: Smooth signal and resonant wavelengths found from a peak finding algorithm.

It is noticeable that the positions of the anti-resonances deduced from the positions of the resonances does not correspond to the local maximum of transmitted intensity. This shift can be explained in part by dispersion, with a group index decreasing with the wavelength. However, the main

contribution comes from the modulation of the envelope of the resonance peaks, well visible in Fig. 4.9 and Fig. 4.12.

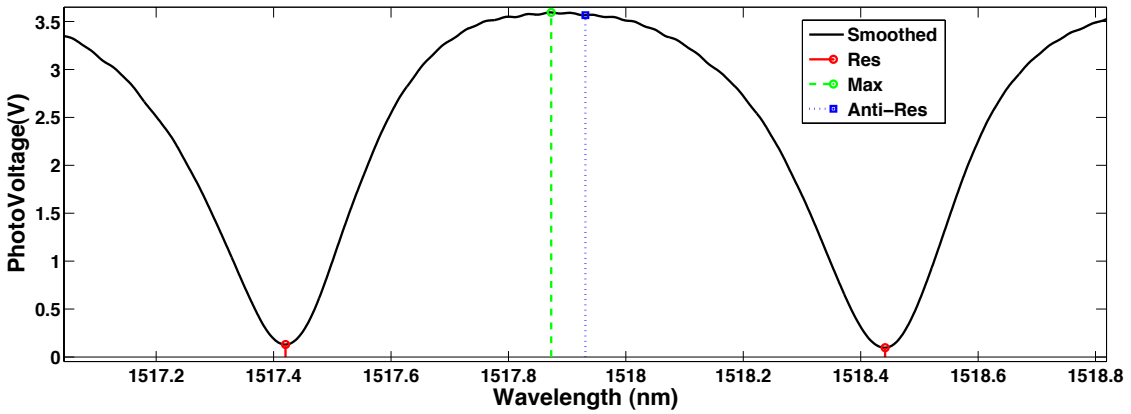

Figure 4.13: Positions of the resonances, anti-resonance and maximum of intensity determined from the smoothed signal.

3.1.4 Normalizations

Until now, the data was presented as a photodetection voltage providing the measured transmitted intensity. As a consequence, the data, smoothed or not, integrates the input optical power, which may depend on the wavelength, the responsivity of the photodetector and finally the intensity transmittance of the bus waveguide.

Assuming a linear behaviour, these functions are not related to the microresonator response, and should be divided by the measured signal to obtain the true intensity transmittance of the microresonator. In this part, we discuss which normalizations can be applied to retrieve some specific aspects of the microring response.

First Normalization

If we assume that the optical power of the source is constant over the whole measured wavelength range, a first normalization (N_1), resulting in a curve (C_1) where the overall maximum is set to 1 and the overall minimum is set to 0, provides a transmission curve which does not depend on the

input power. It is described by:

$$C_1(\lambda) = \frac{C_0(\lambda) - \min(C_0)}{\max(C_0) - \min(C_0)} \tag{4.73}$$

where C_0 is the raw or smoothed signal. It can be noticed that the multiplication of C_0 by a factor K does not modify C_1.

This simple normalization can be used to compare data gathered with different input powers, and could specifically be interesting to track nonlinear effects related to the level of input power. However, the responsivity of the photodetector and the transmittance of the waveguide are still present in (C_1), resulting in a modulation of the envelope of the resonances.

Second Normalization

A second normalization (N_2) consist in putting all minima at 0 and all maxima at 1, thus providing a normalized curve C_2 which is a lot easier to fit from a numerical model of the microresonator, and also easier for the determination of FWHM, Q factor and finesse from an algorithm.

For this normalization, the method described forthe normalization (N_1) is applied sequentially to each wavelength range $\Delta\lambda_k$ corresponding to a resonance $\lambda_k^{(R)}$, in between the two surrounding maxima. After these local transformations, all local minima are at 0, but the resulting signal C_{2p1} shows discontinuities at local maxima.

For each wavelength range $\Delta\lambda_k$, a linear correction is then applied: the equation of the straight line joining the two neighbouring maxima is determined and a corresponding value is subtracted to C_{2p1} so that after correction, all local maxima are equal in the C_{2p2} signal. However, the linear correction slightly modifies the value of the minima.

In order to obtain the final normalized signal C_2, the transformation applied to C_0 to obtain C_{2p1} is re-applied to C_{2p2}. In Fig. 4.14 are compared C_1 and C_2.

Application of the local normalizations and linear corrections does not modify the position of the resonances from C_0 to C_2. However, (N_2) sets all

the contrasts of the resonances to 100 %, making the retrieving of the internal parameters from C_2 impossible. In comparison, the values of FWHM, Q factor and finesse are not affected by (N_2) and are easier to determine than from C_1.

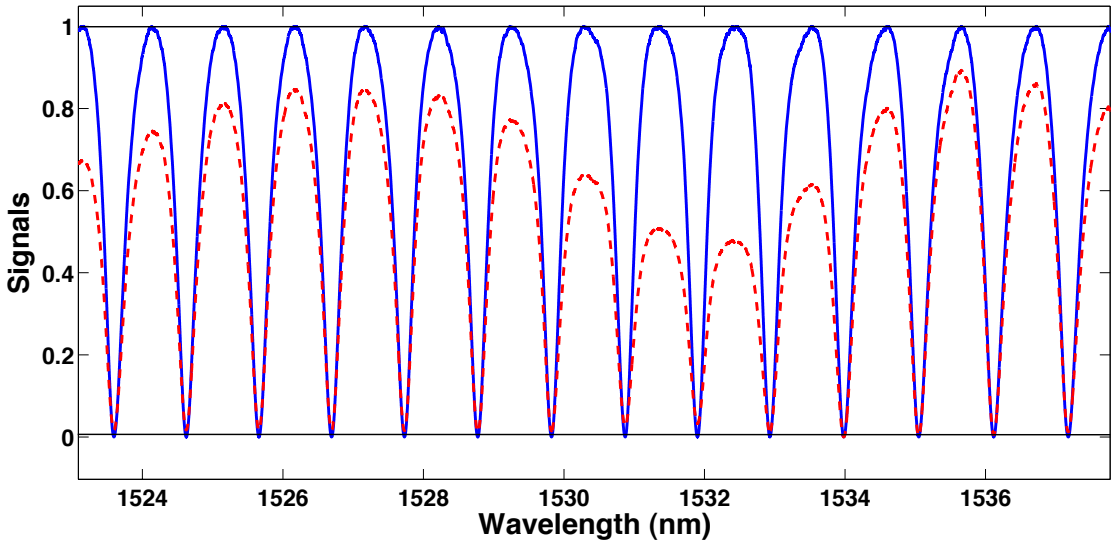

Figure 4.14: Comparison between partially normalized (dashed red line) and fully normalized (solid blue curve) signals C_1 and C_2.

Third Normalization

The idea behind the third normalization (N_3) is to retrieve an envelope function from the maxima and the minima and to divide the data by an interpolated curve of the retrieved envelope. Whereas the second normalization proceeds to linear corrections of the envelope, the correction applied in (N_3) is from a cubic spline interpolation of the envelope, providing a more accurate result in terms of true resonance shape.

From the expressions of the maxima and minima of transmittance are inferred the functions representing the values of the maxima and minima

of measured intensity:

$$\begin{cases} I_{max}(\lambda) = [1-\gamma(\lambda)]\left[\dfrac{a(\lambda)+\tau(\lambda)}{1+a(\lambda)\tau(\lambda)}\right]^2 I_0(\lambda) = A(\lambda)I_0(\lambda) \\ I_{min}(\lambda) = [1-\gamma(\lambda)]\left[\dfrac{a(\lambda)-\tau(\lambda)}{1-a(\lambda)\tau(\lambda)}\right]^2 I_0(\lambda) = B(\lambda)I_0(\lambda) \end{cases} \tag{4.74}$$

where $I_0(\lambda)$ is the product between the intensity response of the source, the intensity transmittance of the bus waveguide, and the responsivity of the photodetector.

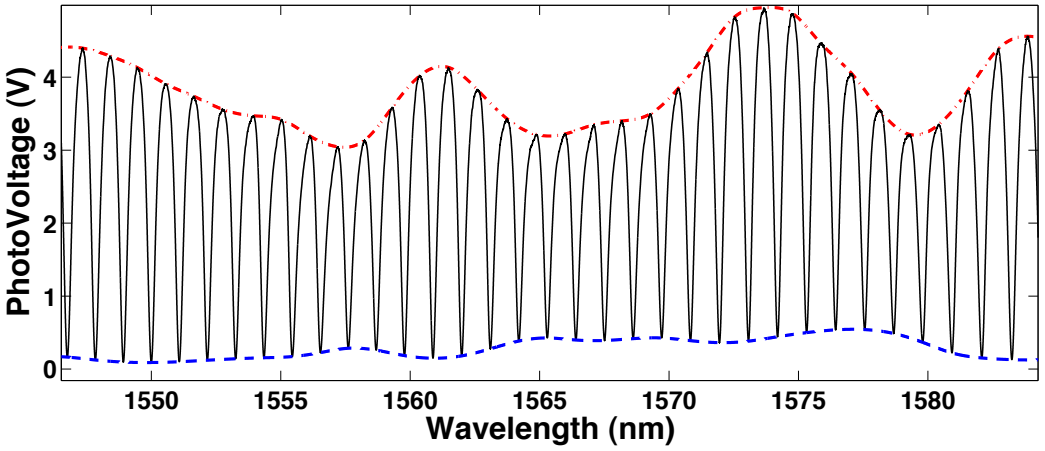

Figure 4.15: Upper (red dot-dash line) and lower (blue dash line) envelope of the transmitted intensity interpolated from the positions of the maxima and minima, respectively.

In these expressions, it appears that $I_0(\lambda)$ cannot be directly retrieved from the upper and lower envelopes of the resonances. Indeed, the modulation of the envelope potentially comes from variations of the internal parameters a, τ and γ as functions of the wavelength. Proof of the dispersion of internal parameters can be observed in Fig. 4.15: if the internal parameters were constant, upper and lower envelopes would have identical variations, which is clearly not the case.

In order to obtain a normalized curve C_3 similar to C_2, but with a better correction of the shape of the resonances, the signal C_0 is first divided by the upper interpolated upper envelope. The resulting signal C_{3p1} has all its maxima at 1. Then local normalizations are performed in the wavelength ranges $\Delta\lambda_k$. The resulting curve C_3 is displayed in Fig. 4.16 and compared to C_2.

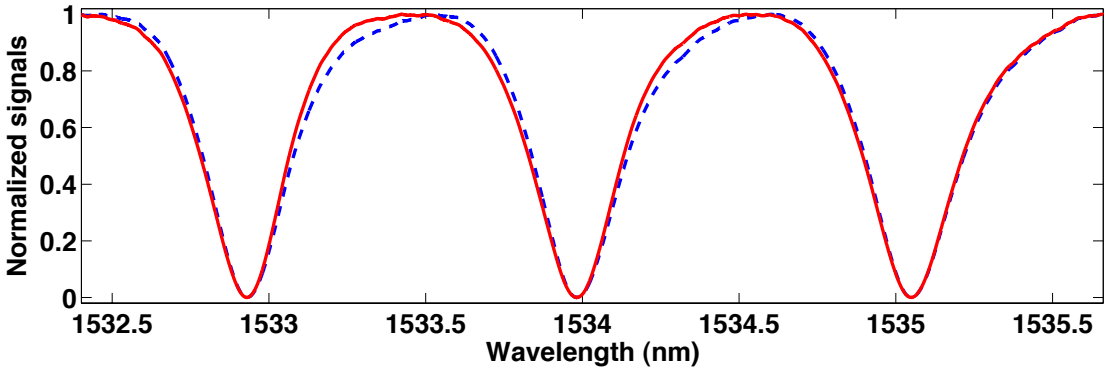

Figure 4.16: Comparison between the results of the second (dotted blue line) and the third (red solid line) normalizations C_2 and C_3, respectively.

A general observation of the curves show that both normalizations have very similar results where envelope variations are not large: the linear correction matches the cubic spline interpolant. In the case of are large envelope variations, differences between the two methods appear clearly. It is noticeable that the result of the third normalization, C_3, is flatter than C_2 near anti-resonances, thus with further resemblance to an ideal behaviour of the microresonator.

In addition, the correction with the cubic spline interpolant has the specificity to modify the positions of maxima. In C_3, these positions are shifted to the left and are closer to their expected position of the maxima, approximately at half-distance between two resonant wavelengths. The appearance of C_3 is very close to that of a ideal intensity transmittance. However, the result is limited in fidelity by the presence of a shallow modulation due to the presence of resonances from a second-order mode. Because the effective index of the second propagation mode differs from that of the fundamental mode, an additional envelope modulation is due to the beating between the two sets of resonances.

Because of this phenomenon, more sophisticated methods would have to be employed to study both modes separately. Such a method may be based on a curve-fitting algorithm liable to identify all resonances, specifically those that are hidden behind the resonances from the fundamental mode.

3.1.5 FSR and effective group index dispersion

The FSR values can be easily deduced from the positions of the detected resonances. Results for the DUT are presented in Fig. 4.17.

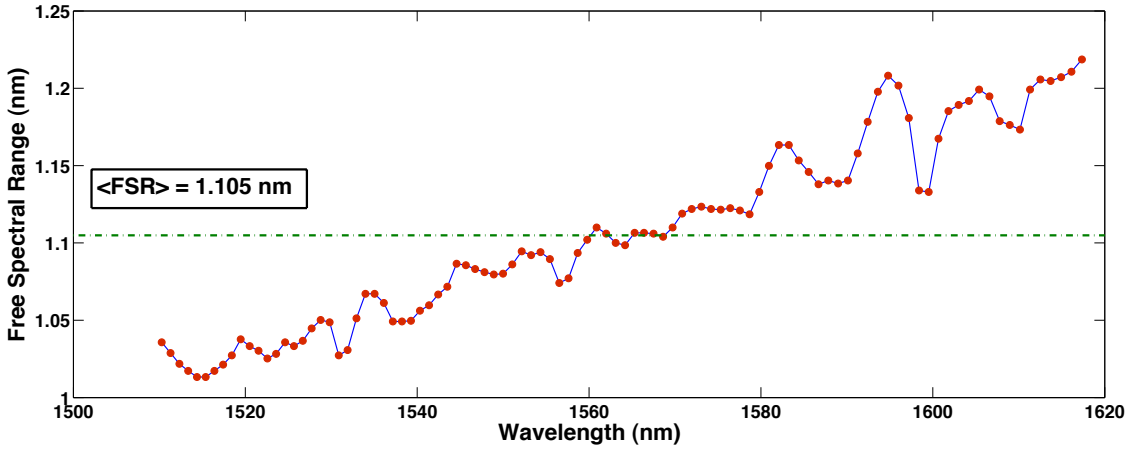

Figure 4.17: Wavelength-dependent Free Spectral Ranges for the DUT.

From the measured values of wavelength-dependent FSRs, and from the estimated circumference of the microresonator, the dispersion of the group effective index is obtained, and presented in Fig. 4.18.

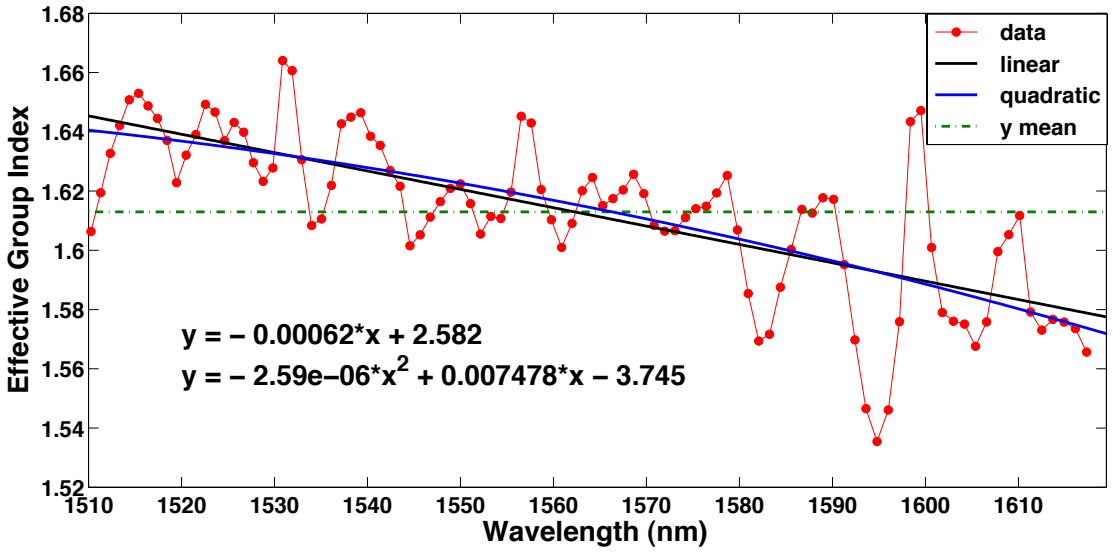

Figure 4.18: Effective group index dispersion in the DUT.

Two contributions are visible in the variations of the group effective index. The first contribution corresponds, as expected, to the typical dispersion in an optical waveguide. It is well fitted by a linear or quadratic curve. The second contribution, a slight modulation of the group index around the expected behavior, is more difficult to explain.

Because of their apparent periodicity, the most probable origin of these oscillations is the presence of resonances from a second propagation mode in the microresonator. The oscillation period can then be correlated to the difference of effective indices between the two modes. Because of secondary resonances, the measured positions of the resonant wavelengths corresponding to the fundamental mode are slightly modified as compared to their actual values.

3.1.6 FWHM, Q factor and Finesse

The determination of the FWHM of each resonance peak is easily made by the normalizations (N_2) and (N_3). By applying a zero-finding algorithm to the curve C_4 = (C_3-1/2) for instance, all wavelengths at half-resonances are determined and subtracted to calculate FWHMs. From these values and those of the FSRs, the Q factor and the finesse for each resonance are calculated. Results are presented in Figs. 4.19 and 4.20.

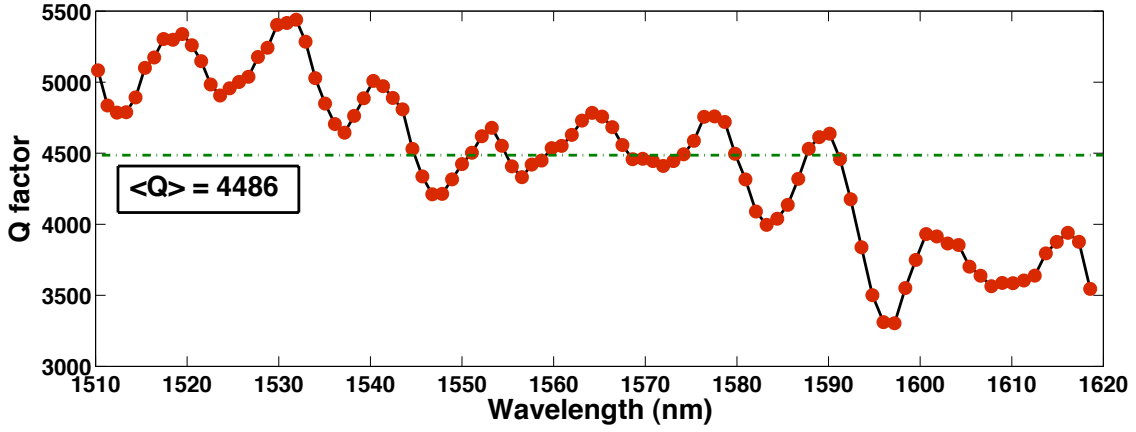

Figure 4.19: Wavelength-dependent Q-factor for the DUT.

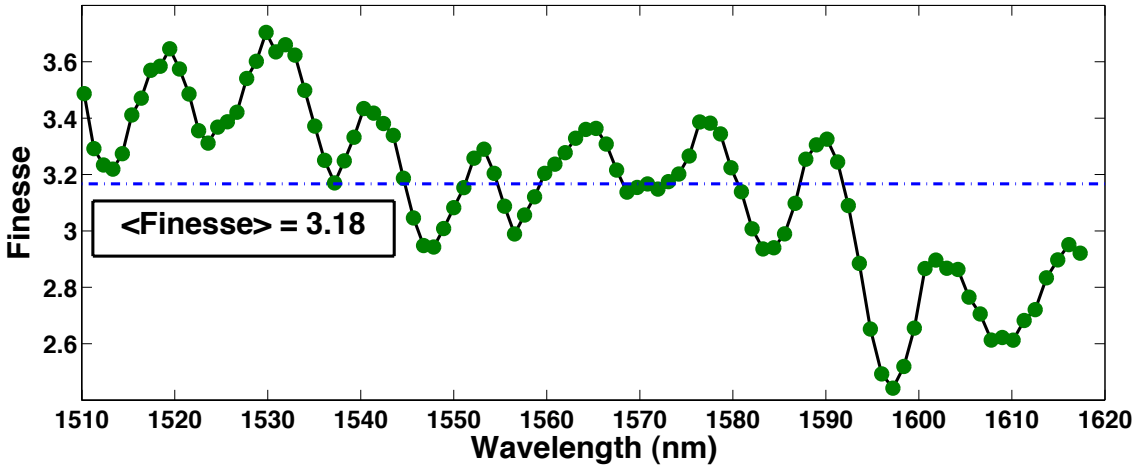

Figure 4.20: Wavelength-dependent Finesse for the DUT.

Similarly to the group index, the wavelength dependence of Finesse and Q factor seem to have two origin: a slow, almost linear variation, and fast oscillations with a noticeable periodicity, estimated to 11 nm at 1550 nm.

Assuming that another set of resonances corresponding to a higher-order propagation mode is hidden by the first resonance peak, its period will be defined by $FSR_2 = \lambda^2/N_{G,2}L$. The beating between the two sets of resonance will produce two new periods:

$$\begin{cases} T_\lambda^{(+)} = \dfrac{\lambda^2}{L} \cdot \dfrac{1}{N_{G,1} + N_{G,2}} \\ T_\lambda^{(-)} = \dfrac{\lambda^2}{L} \cdot \dfrac{1}{N_{G,1} - N_{G,2}} \end{cases} \tag{4.75}$$

It is expected than the group effective index $N_{G,2}$ of the higher-order mode will be lower than that of the fundamental mode $N_{G,1}$, and the difference between both indices will not be very large. Assuming $N_{G,1} = N_{G,2}$, the estimated value for $T_\lambda^{(+)}$ is 0.54 nm. This period, close to that of the noise due to parasitic reflections, cannot be observed. From the estimated magnitude of $T_\lambda^{(+)}$, it seems clear that the period observed in the curves of the Q-factor and the finesse corresponds to $T_\lambda^{(-)}$. In this situation, $T_\lambda^{(-)}$= 11 nm at 1550 nm corresponds to a difference of effective group indices $(N_{G,1} - N_{G,2})$ equal to 0.16. From Fig. 4.18, $N_{G,1}$ is approximately equal to 1.62, corresponding to $N_{G,2} = 1.46$ which is consistent for a higher-order

propagation mode (cf. Chap.6).

Another observation that can be made from the Finesse and Q factor curves concerns the slopes of their linear decay when the wavelength increases. The Q factor explicitly depends on the group effective index. Because of this relationship, it is not surprising to see that Q factor creases when N_G decreases. In comparison, the dependence of the Finesse on the group index, or wavelength, can only be implicit. The decay of the finesse would then be related to variations of the internal parameters of the resonator with respect to wavelength. Also, the relative linear slope of the Q factor decay is around 0.3 % when the same factor is equal to 0.2% for the Finesse. This comparison shows that the dependence of the Q factor and Finesse with respect to wavelength are similar, therefore, the implicit contribution of the dispersion on these characteristics is larger than the explicit contribution.

3.1.7 Resonance contrast

With normalization techniques, it was observed that any measured resonance could be arbitrarily transformed in a resonance with 100 % contrast, corresponding to infinite extinction ratio. Because of this, the resonance contrast could be considered by as an unimportant characteristic compared to the Q factor. It is generally assumed in sensor applications of microresonators that the accuracy in the determination of the position of a resonance only depends on the Q factor. However, a better understanding of what limits the accuracy is provided by an analysis of the measurement noise (cf. Chap.1).

In that regard, the importance of the maximal intensity slope (MIS) was outlined. In a first approximation, the maximal slope can be thought as proportional to the product between the contrast, the Q factor and the maximal transmitted intensity:

$$MIS = \left(\frac{d\lambda}{dT}\right)_{max} \propto Q \cdot C \cdot I_{max} \tag{4.76}$$

Because the normalization procedures have no effect on the SNR, the raw contrast C appears as important as the Q factor in sensing applications[13].

[13] as far as the uncertainty on the resonant wavelength is concerned

The contrasts are determined for each resonance from the signal C_0. Because of the variations of the upper envelope of the resonances, they cannot be calculated exactly as defined. For each resonance, the unique maximum of intensity from the contrast formula can be replaced by the average between the two local maxima at the left and right of the resonance peak. However, it can be simpler to define the contrast for all wavelengths, as the relative difference between the interpolated upper and lower resonance envelopes:

$$C(\lambda) = \frac{\mathrm{UpEnv}(\lambda) - \mathrm{LowEnv}(\lambda)}{\mathrm{UpEnv}(\lambda) + \mathrm{LowEnv}(\lambda)} \tag{4.77}$$

Results form these calculations are presented in Fig. 4.21. As expected from the visualization of the measured transmitted intensity, the contrast strongly depends on wavelength. From the expression of the contrast, the plotted contrast curve cannot depend on the $I_0(\lambda)$ function, representing all external perturbations.

The contrast variations can only be explained by internal phenomena: dispersion of internal parameters and presence of resonances from higher-order propagation modes. It can be observed that the contrast can be better fitted by a quadratic curve. In comparison, a linear fit is sufficient to describe the wavelength dependence of the Q factor and the Finesse. This is consistent with the dependence of the contrast to the square of the product $a\tau$ and confirms that the dispersion of these parameters plays a key role in the wavelength-dependence of the characteristics.

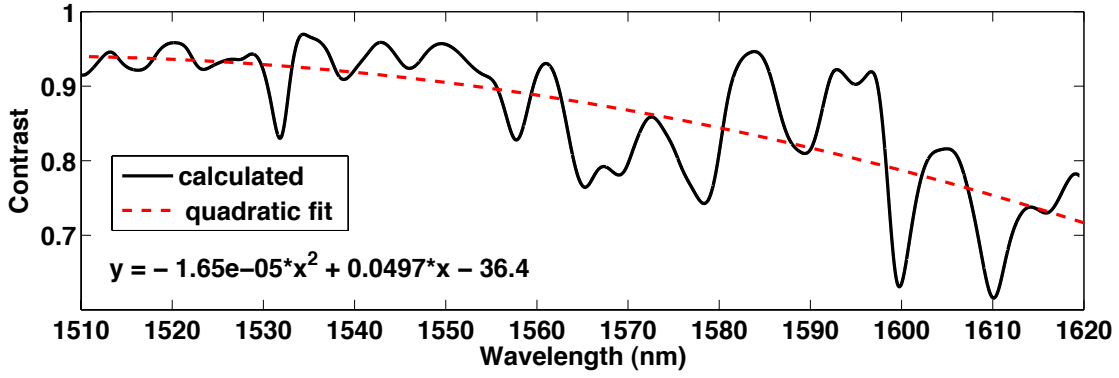

Figure 4.21: Wavelength-dependent resonance contrast for the DUT.

3.1.8 Determination of MIS and optimal σ_{λ}^{res}

In order to determine the maximal intensity slope (MIS), the signal can be numerically derived (cf. Fig. 4.22). Relying on algorithmic schemes similar to those described before, local maxima and minima of the first-order derivative are deduced. They correspond to the maximal intensity slopes, located at inflection points on the right and left sides of the wavelength-dependent intensity transmittance, respectively.

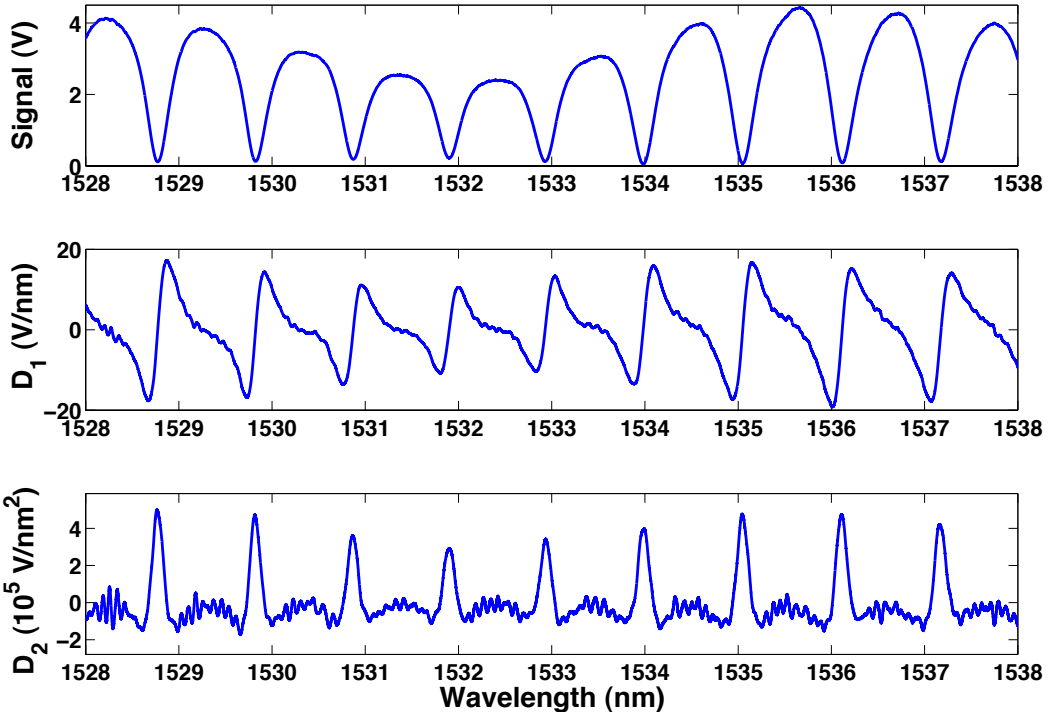

Figure 4.22: Signal C_0 and its first and second-order derivatives D_1 and D_2.

In the frequency domain, the derivation acts as a high-pass filter, increasing the amount of noise in comparison to the signal. By applying moving average filters to the raw signal and to the first-order derivative, as it was performed to plot the curves in Fig. 4.22, the maximal intensity slope can be determined with sufficient accuracy.

Results of these calculations are displayed in Fig. 4.23. It is particularly visible that the maximal slope is strongly diminished in regions where the contrast is low.

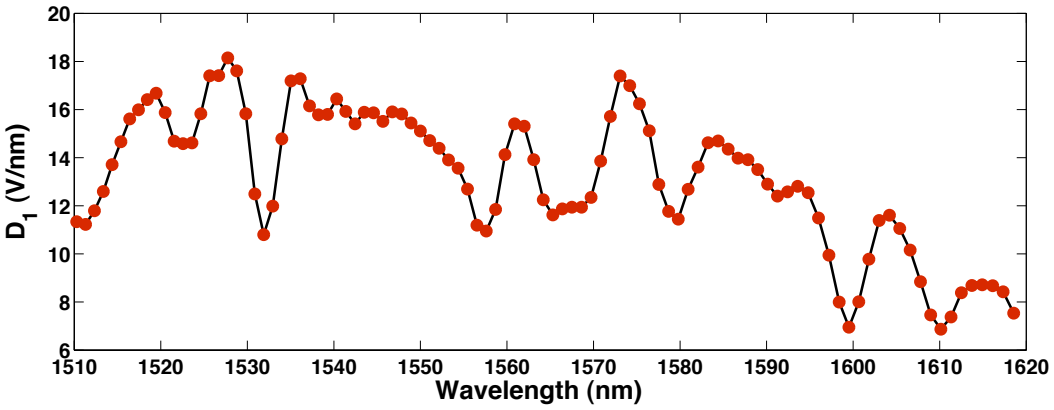

Figure 4.23: Wavelength-dependence of the maximal intensity slope for the DUT.

Also, even if the highest Q factors are measured between 1530 and 1535 nm, the optimal resonant wavelengths for sensing applications are near 1527 nm and 1575 nm. The worst resonances are at larger wavelengths, where both contrast and Q-factor curves have low values.

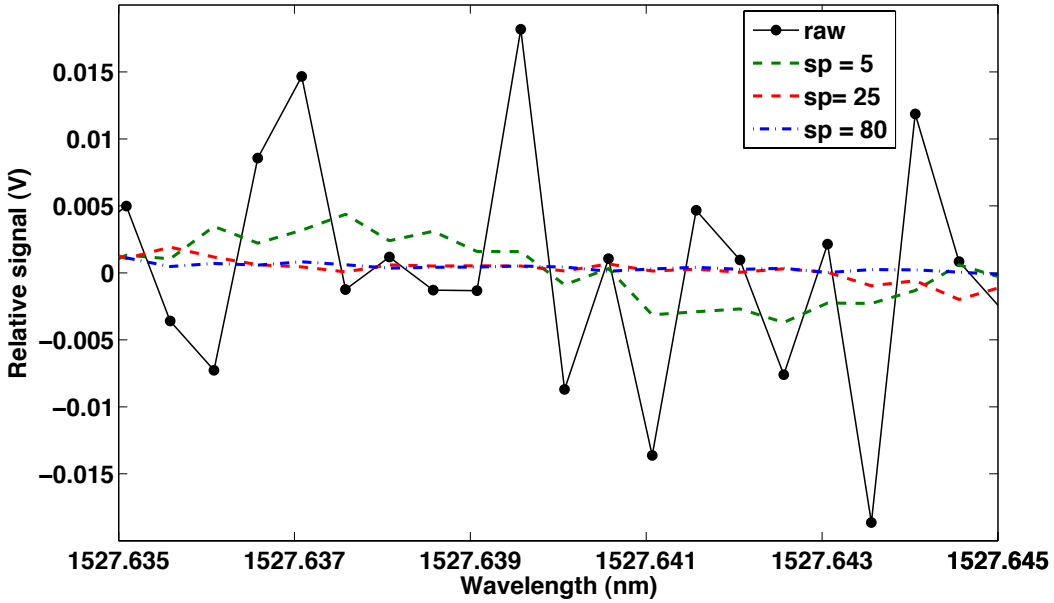

Figure 4.24: Photodetection noise for different spans of the moving average filter.

The value of the uncertainty on the resonant wavelength $\sigma[\lambda](I)$ due to intensity fluctuations depend on the intensity slope and the standard deviation of intensity σ_I, which includes noise from parasitic interferences. Therefore, for a given slope, $\sigma[\lambda](I)$ can be optimized by averaging, or

by applying a moving average filter to the raw data. Effect of the filtering for different spans is presented in Fig. 4.24 and estimated values of σ_I and $\sigma[\lambda](I)$ depending on the moving average filter span are compiled in Tab. 4.1.

Span	0	5	10	25	50	80
$\sigma_I(mV)$	11.8	3.25	2.71	2.19	1.54	0.45
$\sigma[\lambda](I)$ (pm)	0.66	0.18	0.15	0.12	0.08	0.02

Table 4.1: Estimated values of the accuracy for the determination of the resonant wavelength

With averaging, $\sigma[\lambda](I)$ can be very low. In addition, the moving average filter does not affect the response time in such a case, since it is only limited by the wavelength scanning speed. From this analysis, the contribution of intensity fluctuations in the combined uncertainty for the measurement of resonant wavelengths could be cancelled by applying an adequate movering average filter to the raw data.

3.1.9 Determination of the internal parameters a and τ

As explained before, the exact determination of a and τ from measured intensity transmissions is not directly possible. However, the product X = $a\tau$ can be deduced from the Finesse. In addition, two values corresponding to a and τ, α and β where $\alpha < \beta$ can be calculated from the resonance contrast.

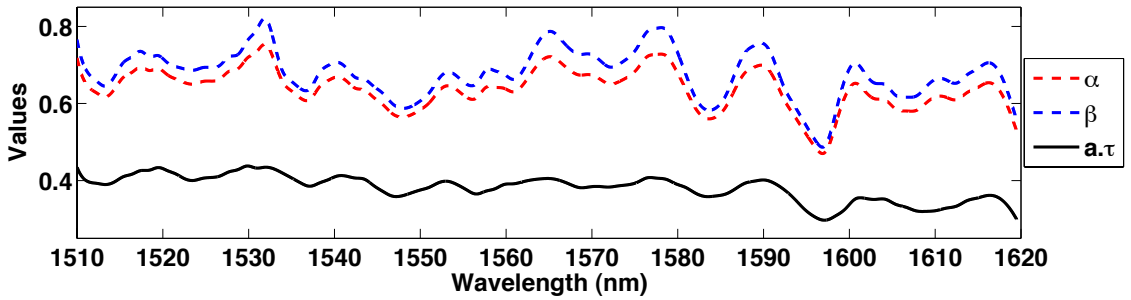

Figure 4.25: Wavelength-dependent values of $a\tau$, α and β for the DUT.

From the plotted curve in Fig. 4.25, it is observed that values of a and τ for the DUT with TE polarization roughly vary between 0.5 and 0.8 over

the whole wavelength range. Because it is not possible to determine from α and β the exact values of a and τ at each wavelength, the variations of a and τ are not visible. The only available information is that both parameters have variations in between the curves of α and β. Another observation is related to the near-to-linear decay of the $a\tau$ curve.

To some extent, it can be stated that the resonant contrast mostly depends on the difference between a and τ, and characteristics such as the Finesse and the Q factor mostly depend on the $a\tau$ product. The validity of these "rules of thumbs" is examined in Fig. 4.26.

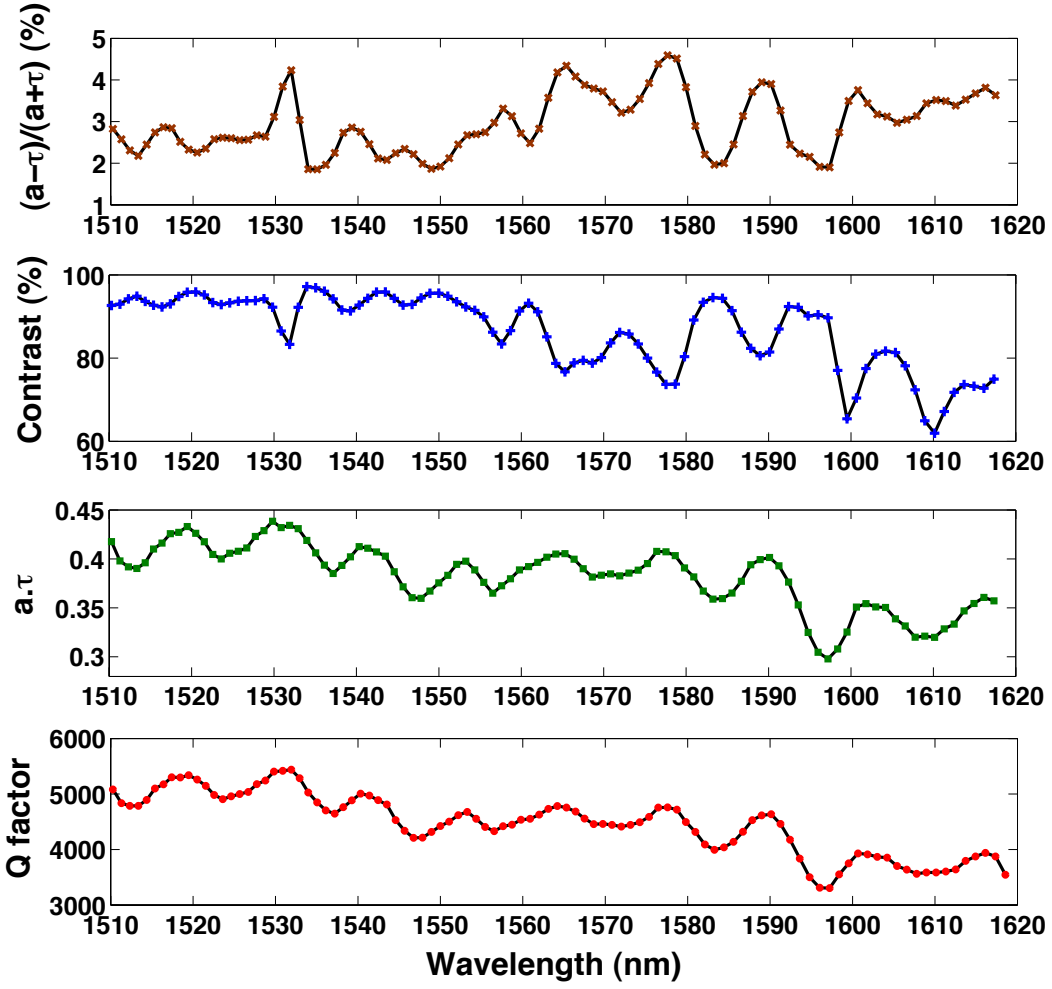

Figure 4.26: Comparison between the wavelength-dependences of the (absolute) relative difference between a and τ, the contrast, the product $a\tau$ and the Q-factor.

It is clearly visible that variations of the contrast are specifically correlated to variations of the relative difference between a and τ. Curves of $a\tau$

and Q-factor are also well correlated.

Chapter 5

Sensing properties of microring resonators

Introduction

As outlined in Chap.1, the detection principle of microresonator-based sensors is the direct or indirect measurement of $\delta\lambda$, the wavelength shift of the cavity resonances related to a variation δM of the measurand. More specifically, δM induces a modification of the phase velocity of the guided waves propagating in the microresonator, described by a variation δN_{eff} of the phase effective index.

In Chap.1, the accuracy on $\delta\lambda$ measurements was the main concern about the LOD to achieve a measuring instrument integrating optical microresonators. In that respect, an essential point, which is the relation between δM and δN_{eff}, was not discussed in depth.

In this chapter, we focus on the relations between the measurand and the effective index, depending on the sensing configuration, and their consequences on the LOD achieved by the measuring instrument.

1 Sensitivity, resolution and LOD

1.1 First expression for the limit of detection (LOD)

1.1.1 Resolution in wavelength shift

In order to model the measurement of the quantity δM from microring resonators using either a fixed-wavelength, or wavelength-scanning method[1], a simple coefficient K was introduced as the ratio between δM and δN_{eff}. Because of the relation between the measurand and the effective index, the resolution $R[\delta M]$ of such measuring instruments is intrinsically related to the resolution $R[\delta N_{eff}]$ achieved in the measurement of the quantity δN_{eff}:

$$R[\delta M] = K \cdot R[\delta N_{eff}] \tag{5.1}$$

It is assumed here that K is strictly constant. Since the equation $\delta\lambda/\lambda = \delta N_{eff}/N_{eff}$ is verified, the resolution $R[\delta\lambda]$ in $\delta\lambda$ measurements is directly related to $R[\delta N_{eff}]$:

$$R[\delta\lambda] = \frac{\lambda}{N_{eff}} R[\delta N_{eff}] \tag{5.2}$$

where λ and N_{eff} are the central values of the wavelength and the effective index, respectively.

1.1.2 Relation to the LOD

In Chap.1, the resolution $R[\delta M]$ was also referred to as the limit of detection (LOD) of the measuring instrument. It is important to point out that the term *resolution* can be associated to the measurement of any value in the system, whereas LOD is specifically the resolution associated to the measurand, more specifically its variation, which is *in fine* the only value of interest.

Consequently, the LOD of a measuring instrument based on a microresonator can be expressed, from the expressions above, as:

$$\text{LOD} = \frac{K N_{eff}}{\lambda} R[\delta\lambda] \tag{5.3}$$

However, this expression, using unspecified parameters, does not provide a very clear view of how a lower LOD can be obtained.

[1] FWM and WSM, respectively

1.2 Microresonator sensivitity and LOD

1.2.1 Definition of the microresonator sensitivity

The microresonator, as a transducer, is generally viewed as a device that converts the measurand M into a value of resonant wavelength λ. Therefore, the transfer function $\mathcal{T}_{\text{res}}$ of the microresonator can be defined, independently from the detection scheme, as the relation between the two quantities: measurand as input and resonant wavelength as output. This transfer function can be reduced to a scalar function F, verifying $\lambda = F(M)$. The corresponding *microresonator sensitivity* S_{res} can then be locally defined, on a neighbourhood of a point [2] (M_0, λ_0), as:

$$S_{res}(M_0) = \frac{d\lambda}{dM}(M_0) \tag{5.4}$$

1.2.2 Relation to LOD

Consequently, the relation between the variations δM and $\delta\lambda$ around M_0 and λ_0, respectively, can be simply written as:

$$\delta\lambda = S_{res}(M_0) \cdot \delta M \tag{5.5}$$

If we assume that the transfer function does not deviate during measurements, and can be linearised over the measurement span, $S_{res} = S_{res}(M_0)$ is strictly constant, resulting in the relation:

$$R[\delta\lambda] = S_{res} \cdot R[\delta M] \tag{5.6}$$

Therefore, the LOD can be directly expressed as the ratio between the resolution in the measurement of the shift $\delta\lambda$ and the sensitivity of the microresonator:

$$LOD = \frac{R[\delta\lambda]}{S_{\text{res}}} \tag{5.7}$$

1.3 Optimization of the LOD

The last expression allows an analysis on the limit of detection (LOD) of a sensor integrating an optical microresonators, but more generally on any waveguide or plasmonic-based sensor.

[2] $\lambda_0 = F(M_0)$

1.3.1 Optimization of the resolution

LOD is proportional to the resolution in the measurement of the wavelength shift of the optical device spectral signature[3]. It is important to point out that, as demonstrated in Chap.1, this resolution depends on the optical device itself and on the instrumentation. More specifically, the only intrinsic parameter to the signature of the optical device that is directly related to $R[\delta\lambda]$ is MIS, *ie* the maximal slope of the intensity transmittance as function of the wavelength[4]. Beyond considerations on MIS, the resolution $R[\delta\lambda]$ depends on uncertainties on the values of parameters related to both optical device and instrumentation. In that respect, an ideal instrument would be achieved with an optical device whose internal parameters are perfectly stable during measurements, and/or an instrumentation that minimizes the variations of the device internal parameters, while, as an independent source of uncertainty, contributing as little as possible to the combined uncertainty.

1.3.2 Optimization of the sensitivity

LOD is inversely proportional to the microresonator sensitivity S_{res}, or more generally to the sensitivity in wavelength per measurand unit of the spectral signature of the waveguide-based or plasmonic-based devices[5]. This sensitivity has the particularity, as compared to the resolution and to all other specifications of the measuring instrument, to be absolutely intrinsic to the optical microcavity. More specifically, it relates to the interaction between (optical) electromagnetic waves and measurand. This interaction occurs at the device surface in label-free sensors. Typically, the measurand modifies the distribution of electric permittivity, thus modifying the propagating wave velocity. Hence, two distinct factors have a role in the sensitivity. The first factor is the ratio between local measurand variation and local permittivity variation, or the related local refractive index variation. Since a local variation of the permittivity around a point P_0 in space can only have an effect on the velocity of the light waves if their energy is non-zero at P_0, a second factor must be related to the superposition of the

[3]Spectral signatures of optical devices are the resonances for microcavities, the plasmon resonance for plasmonic devices, and the sinusoidal modulation of the transmitted intensity for MZI or DPI-based sensors.

[4]With higher values of MIS, parasitic modulations of the intensity transmittance have less influence on the measure (cf. Chap.1)

[5]We assume here that, for these devices, the transfer function can be written as $\lambda = F(M)$, where λ is any wavelength position that can be used to characterize the spectral signature.

spatial distributions of permittivity variations and energy of the propagating waves.

1.3.3 Relation to the waveguides

Considering the main dependencies of the LOD for the optimization of sensors integrating microring resonators, two aspects, concerning the waveguides, are particularly interesting: one being relevant to the resolution $R[\delta\lambda]$, the other one to the microresonator sensitivity S_{res}.

A part of the uncertainties limiting the resolution $R[\delta\lambda]$ are related to the variations of the optical characteristics of the microresonators. These characteristics, as outlined in Chap.2 and demonstrated in Chap.4, are mainly dependent on the dispersion of microring waveguides. Thus, it seems interesting to study waveguide dispersion, a specific issue being to design a waveguide so that its dispersion properties are, as much as possible, independent from environmental perturbations, such as temperature and pressure.

From the discussion on the sensitivity S_{res} and its importance for LOD, it was pointed out that this parameter was dependent on the spatial superposition of two distributions: the optical energy of the mode propagating in the microring, and permittivity variations due to the measurand. The latter distribution can be significantly modulated by the geometry of the microring waveguide. This constitutes a second motivation to study the guided modes in microring resonators.

1.4 Analysis of the microresonator sensitivity

1.4.1 General expression

The microresonator sensitivity S_{res} to the measurand is defined as the total derivative of the resonant wavelength λ with respect to the measurand M:

$$S_{res} = \frac{d\lambda}{dM} \tag{5.8}$$

The exact relation between λ and the effective index of the propagation mode inside the microresonator N_{eff} is:

$$N_{eff}L = m\lambda \tag{5.9}$$

where m is a constant[6] and L is the mean circumference of the microresonator.

According to the above relation, the sensitivity S_{res} can be written as:

$$S_{res} = \frac{\lambda}{N_{eff}} \cdot \frac{dN_{eff}}{dM} + \frac{\lambda}{L} \cdot \frac{dL}{dM} \tag{5.10}$$

1.4.2 Contributions to the overall sensitivity

Two contributions to the sensitivity appear in the expression above. The first term, proportional to the derivative of the effective index with respect to the measurand, is classical in the sense that most waveguide-based sensors only rely on this term. The second term, proportional to the derivative of the mean circumference L with respect to the measurand, is more exotic since measurands are rarely considered to have an impact on L. However, if the measurand is a pressure or a temperature for instance, the variations of the measurand can induce a significant variation of L via dilation or contraction of the material. Thus, for a general study, the second term should be taken into account. To simplify further expressions, we will define $S_{N_{eff}} = (dN_{eff}/dM)$ as the sensitivity of the effective index to the measurand, and $S_L = (dL/dM)$ as the sensitivity of the cavity length to the measurand, resulting in:

$$S_{res} = \frac{\lambda}{N_{eff}} \cdot S_{N_{eff}} + \frac{\lambda}{L} \cdot S_L \tag{5.11}$$

As S_L only depends on the optical materials of the waveguide, its expression can be straightforward. In comparison, expressing $S_{N_{eff}}$ is much more challenging.

1.4.3 Effective index and measurand

The effective index can be expressed as an implicit function of all the parameters characterizing the propagation of the guided mode in the resonator. These parameters can be separated into two categories. The parameters of the first category, written down as $(A_i)_{i\in[1,N]}$, are independent of the measurand. Those of the second category, written down as $(B_j)_{j\in[1,P]}$,

[6] m is the half of a large integer (cf. Chap. 2)

depend on the measurand. Accordingly, an infinitesimal variation of the effective index can be expressed as:

$$dN_{eff} = \sum_{i=1}^{N} \frac{\partial N_{eff}}{\partial A_i} dA_i + \sum_{j=1}^{P} \frac{\partial N_{eff}}{\partial B_j} dB_j \tag{5.12}$$

In the above equation, only the second sum relates to the sensitivity to the measurand M. Assuming that all parameters (B_j) can be written as functions of the measurand, the *effective index sensitivity* $S_{N_{eff}}$ can be written as:

$$S_{N_{eff}} = \frac{dN_{eff}}{dM} = \sum_{j=1}^{P} \frac{\partial N_{eff}}{\partial B_j} \cdot \frac{\partial B_j}{\partial M} \tag{5.13}$$

In this sum, the partial derivatives $S[N_{eff}/B_j] = (\partial N_{eff}/\partial B_j)$ are defined as partial sensitivities of the effective index to the waveguide parameters, whereas the partial derivatives $S[B_j/M] = (\partial B_j/\partial M)$ are defined as sensitivities of the parameters (B_j) to the measurand. It is important to point out that the latter sensitivities are dependent on the interaction between the guiding structure and the measurand, hence they only depend on the properties of the optical materials. Consequently, they will be referred to as *material sensitivities*. In comparison, the former sensitivities are only functions of the parameters of the guiding structure: wavelength, waveguide geometry and refractive index of materials. Hence, they will be referred to as *waveguide sensitivities*.

2 Evaluation of the waveguide sensitivities

As waveguide sensitivities play an important part in the sensitivity of the microresonator, it is important to study ways to evaluate these quantities, from numerical or analytical methods. In order to determine how the variation of a single parameter of the waveguide modifies the effective index (indices) of its guided mode(s), the first task is to develop an accurate model to calculate modal effective indices.

Since optical waveguides are commonly used in a wide variety of photonic devices [68, 25], numerous studies were led to model, both analytically [69, 70, 71], and numerically [72, 73], the guided modes; in terms of

effective index and spatial distribution of modal intensity[10].

Analytical studies are relatively simple for very basic structures such as slab waveguides, or other structures where the effective index of a guided mode is directly determined from the resolution of a single dispersion equation. This is usually the case for structures with high levels of symmetry, specificity that is in most instances associated with a reduced number of parameters, which further simplifies their optimization[7]. However, for 2D[8] or 3D[9] guiding structures, with several independent parameters, the analytical evaluation of the modal effective indices requires the resolution of several dispersion equations, often obtained at the cost of several simplifying hypotheses. Consequently, it is often preferred to use numerical simulations for such complex structures. Still, as it will be demonstrated, analytical models are much more suitable to study the waveguide sensitivities, provided that an adequate formalism is developed.

Amongst the above stated structures, rectangular waveguides are both the simplest ones to model and the most straightforward ones to fabricate. For these reasons, we chose this particular structure for further discussions, also for developing our analytical formalism later on. Nevertheless, the presented method is general enough to be applied to all guiding structures as long as they can be sufficiently well described by a set of dispersion equations.

2.1 Use of numerical tools: application to glucose sensing

To illustrate how to use numerical waveguide simulations to evaluate the waveguide sensitivities, we consider the optimization of a microring waveguide geometry for the homogeneous detection of glucose in aqueous solution, as cladding of the waveguide.

2.1.1 Microresonator sensitivity for homogeneous sensing

The waveguide parameters are the refractive indices of the core N_{core}, of the substrate N_{sub} and of the cladding N_{clad} materials; the width w and

[7] Good examples are fiber optics, guiding spheres and disks.
[8] Such as rectangular, rib, ridge, and slot waveguides
[9] photonic crystals

height h of the core of the waveguide, the average radius R of the ring and the wavelength λ. Amongst all these parameters, only N_{clad} depends on the measurand, which is glucose concentration C. The sensitivity of N_{clad} to the measurand depend on the optical properties of water and glucose molecules. Hence, the sensitivity of the effective index N_{eff} to N_{clad} is to optimize. As a matter of fact, since the variations of glucose concentration are not likely to modify the geometry of the waveguide, the sensitivity of the microresonator for this sensing experiment can be written:

$$S_{res} = \frac{d\lambda}{dM} = \frac{\lambda}{N_{eff}} \cdot \frac{\partial N_{eff}}{\partial N_{clad}} \cdot \frac{\partial N_{clad}}{\partial C} = \frac{\lambda}{N_{eff}} \cdot S_{wav} \cdot S_C \qquad (5.14)$$

In this expression, S_C needs to be treated as a constant. Overall, the key quantity to optimize is $S^{\star}_{wav}$, defined as:

$$S^{\star}_{wav} = \frac{\lambda}{N_{eff}} \cdot \frac{\partial N_{eff}}{\partial N_{clad}} \qquad (5.15)$$

2.1.2 Optimization procedure

For such optimization, the parameters are N_{core}, N_{sub}, w, h, R and λ. These parameters can be combined in a vector $\mathbf{V}$ = (N_{core}, N_{sub}, w, h, R, λ), that characterizes one trial configuration. For one configuration $\mathbf{V}_0$, $S^{\star}_{wav}$ has to be calculated as a function of the the cladding index N_{clad}, which may vary between unity and N_{core}. Each value of $S^{\star}_{wav}(N_{clad})$ requires the evaluation of two values of the effective index: $N_{eff}(N_{clad} + \delta N)$ and $N_{eff}(N_{clad} - \delta N)$ where δN is an index increment.

In order to calculate P values of $S^{\star}_{wav}$ for $\mathbf{V}_0$, at least (P+1) values of the effective index needs to be evaluated. Then, to test all independent configurations, assuming that each independent parameter is sampled on P points, the total number of effective index evaluations to perform is (P+1)P^n where n is the number of independent optimization parameters. For the microring resonator described, $n = 5$[10]. For P = 5, it amounts to 18,750 calculations, and for P = 10, it amounts to 900,000 calculations. This has to be combined to the fact that one accurate evaluation of the effective index of a configuration can take up to several minutes with a standard PC.

[10]We can show that w, h, and λ can be replaced by two independent parameters $w^{\star} = w/\lambda$, $h^{\star} = h/\lambda$

2.1.3 Conclusion

It must be pointed out here that this optimization is almost the simplest one. Clearly, the direct use of numerical waveguide simulations is not suitable, and other solutions are necessary to reduce, as much as possible, the actual number of accurate numerical solutions to perform for optimization.

2.2 Use of analytical models

What is expected here of an analytical model of the waveguide is the ability to derive expressions for waveguide sensitivities. Partial sensitivities can then be calculated by injecting results of the resolution of the dispersion equations in the analytical formulas. After presenting the principle of the method, an example of its implementation to the simple case of a slab waveguide will be proposed. The method is then applied to the case of the rectangular waveguide, using dispersion equations from both effective index and Marcatili's methods. Sensitivity results are compared to those obtained with a commercial mode solver software using the ADI method. Finally, we will show how this approach can be used to predict and optimize IO devices performances with a focus on evanescent wave sensors.

2.2.1 Description of the general approach

For most three-dimensional guiding structures, such as rectangular, rib or ridge waveguides, the effective index method [70], also Marcatili's method in the case of rectangular waveguides [69], provides a set of dispersion equations whose resolution gives a good estimate of the effective indices of TE and TM guided modes [10]. As for slab waveguides, a unique dispersion equation provides an exact solution for any propagating mode.

Total derivative of the effective index

For such guiding structures, with a set of N parameters $(a_1, a_2, ..., a_N)$, it is then possible, by deriving all dispersion equations, to obtain the total derivative of the effective index N_{eff} of any guided mode as a function of all parameters such as expressed in the following equation:

$$dN_{eff} = \sum_{i=1}^{N} \frac{\partial N_{eff}}{\partial a_i} da_i = \sum_{i=1}^{N} S_i da_i \tag{5.16}$$

where S_i are the waveguide sensitivities defined before.

Evaluation of the waveguide sensitivities

Sensitivity calculations for a given structure and various sets of parameters can be reduced to four steps:

1. The dispersion equations are determined for the given structure. Several cases were already treated in the literature making these equations easily obtainable for usual configurations.

2. The formulas for the S_i coefficients are determined as functions of all parameters for the studied structure, from the total derivatives of the dispersion equations. This can be very efficiently achieved using a formal calculation software.

3. The effective indices of the studied propagating modes are obtained for each set of parameters, either by solving the same dispersion equations, or using a numerical mode solver.

4. Values of the parameters and calculated effective indices are finally injected in the formulas obtained at step one to calculate the values of the S coefficients.

2.2.2 Implementation to a slab waveguide

Basic description

In order to determine the expressions of the sensitivities S_i, we need to write down the dispersion equations of TE and TM modes of the slab waveguide as $f(N_{eff}, N_{core}, N_{sub}, N_{clad}, w, \lambda_0) = 0$, where N_{eff}, N_{core}, N_{sub} and N_{clad} are the effective, the core, the substrate and the cladding indices, respectively, and where w is the width of the core (cf. Fig 5.1). λ_0 stands for the wavelength in vacuum.

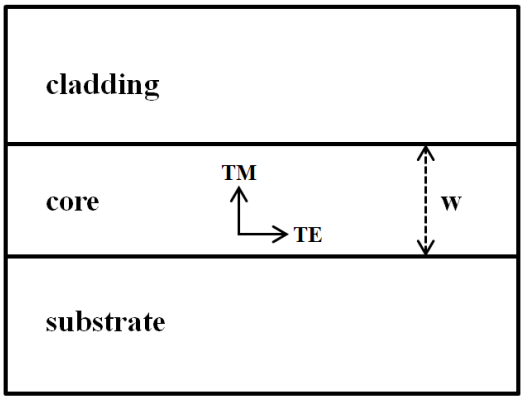

Figure 5.1: Schematic drawing of an asymmetrical slab waveguide. Directions of the dominant electric field components corresponding to TE and TM modes are represented

Normalized parameters

To display the dispersion equations in a form that is easily solvable, three normalized, dimensionless, parameters are usually introduced: the normalized propagation constant b, the normalized frequency v and the asymmetry factor γ, defined herein as:

$$b = \frac{N_{eff}^2 - N_{sub}^2}{N_{core}^2 - N_{sub}^2} \tag{5.17}$$

$$v = k_0 w \left(N_{core}^2 - N_{sub}^2\right)^{1/2} \tag{5.18}$$

$$\gamma = \frac{N_{sub}^2 - N_{clad}^2}{N_{core}^2 - N_{sub}^2} \tag{5.19}$$

where k_0 is the wavenumber in vacuum.

Dispersion equations for an asymmetrical slab waveguide

We can write the dispersion equation $f_{TE}(m)$ for the TE guided modes, where m is a positive integer indicating the order of the mode[11]:

$$\begin{aligned} f_{TE}(m) = 0 = v\sqrt{1-b} - m\pi \\ - \arctan\left(\sqrt{\frac{b}{1-b}}\right) - \arctan\left(\sqrt{\frac{b+\gamma}{1-b}}\right) \end{aligned} \tag{5.20}$$

[11] m=0 corresponding to the fundamental mode

For the TM guided modes, the dispersion equations $f_{TM}(m)$ are slightly different:

$$\begin{aligned} f_{TM}(m) = 0 = v\,(1-b)^{1/2} - m\pi \\ - \arctan\left[\frac{N_{core}^2}{N_{sub}^2}\sqrt{\frac{b}{1-b}}\right] - \arctan\left[\frac{N_{core}^2}{N_{clad}^2}\sqrt{\frac{b+\gamma}{1-b}}\right] \end{aligned} \tag{5.21}$$

We assumed here that the substrate index is larger than the cladding index. In the opposite situation where $N_{clad} > N_{sub}$, both variables must be exchanged in the above definitions and dispersion equations.

Derivation of waveguide sensitivities

Each equation, applying for a single propagation mode in a slab waveguide, can be derived to obtain its identically zero total derivative:

$$\begin{aligned} df = 0 = \frac{\partial f}{\partial N_{eff}}dN_{eff} + \frac{\partial f}{\partial N_{core}}dN_{core} + \frac{\partial f}{\partial N_{sub}}dN_{sub} \\ + \frac{\partial f}{\partial N_{clad}}dN_{clad} + \frac{\partial f}{\partial w}dw + \frac{\partial f}{\partial \lambda}d\lambda \end{aligned} \tag{5.22}$$

from which we obtain :

$$\begin{aligned} dN_{eff} = S_{core}dN_{core} + S_{sub}dN_{sub} \\ + S_{clad}dN_{clad} + S_w dw + S_\lambda d\lambda \end{aligned} \tag{5.23}$$

The expressions of the slab waveguide sensitivities are obtained as ratios of partial derivatives of the dispersion fonctions:

$$\begin{cases} S_{core} = -\left(\dfrac{\partial f}{\partial N_{eff}}\right)^{-1}\dfrac{\partial f}{\partial N_{core}} \\ S_{sub} = -\left(\dfrac{\partial f}{\partial N_{eff}}\right)^{-1}\dfrac{\partial f}{\partial N_{sub}} \\ S_{clad} = -\left(\dfrac{\partial f}{\partial N_{eff}}\right)^{-1}\dfrac{\partial f}{\partial N_{clad}} \\ S_w = -\left(\dfrac{\partial f}{\partial N_{eff}}\right)^{-1}\dfrac{\partial f}{\partial w} \\ S_\lambda = -\left(\dfrac{\partial f}{\partial N_{eff}}\right)^{-1}\dfrac{\partial f}{\partial \lambda} \end{cases} \tag{5.24}$$

Discussion

Since all partial derivatives of a dispersion equation can be written using N_{eff}, N_{core}, N_{sub}, N_{clad}, w and λ, a formal calculation engine is very handy to determine the expressions of the S_i coefficients as functions of these parameters. Once the effective index N_{eff} is obtained from the resolution of either dispersion equation, or from another method, values of the waveguide sensitivities are easily calculated.

The resulting expression of S_{clad} is similar to that presented in [74]. The novelty of the approach is the possibility to model phenomena related to external parameters thanks to the above equations.

2.3 Sensitivities of rectangular waveguides

2.3.1 Analytical models for rectangular waveguides

To obtain analytical dispersion equations for relatively complex guiding structures such as step index rectangular, rib or ridge waveguides, it is necessary to assume the validity of simplifying hypotheses. First, some vector components of the electromagnetic field, depending on the studied polarization and the studied region, are assumed to be identically zero [10]. The second hypothesis is related to the resolution of the propagation equations in each region of the waveguide[12]. For ridge and rib structures, only the effective index method (EIM) can provide dispersion equations. However, for rectangular waveguides, two other methods can be used. Marcatili's method (MM) is the simplest one but as we will see, its accuracy for the determination of the effective index is limited. The second, Kumar's method [71], uses a perturbation approach to deal with corner regions of the waveguides, with an improved accuracy - compared to other methods - as a result. However, the formalism developed in Kumar's method is hardly compatible with the approach we propose. Also, the accuracy obtained with simpler methods is sufficient in most cases. As a consequence, we only focus here on EIM and MM for the analysis of rectangular waveguides.

[12]The choice of simplifying hypothesis distinguishes the different existing methods to obtain dispersion equations for the guided modes.

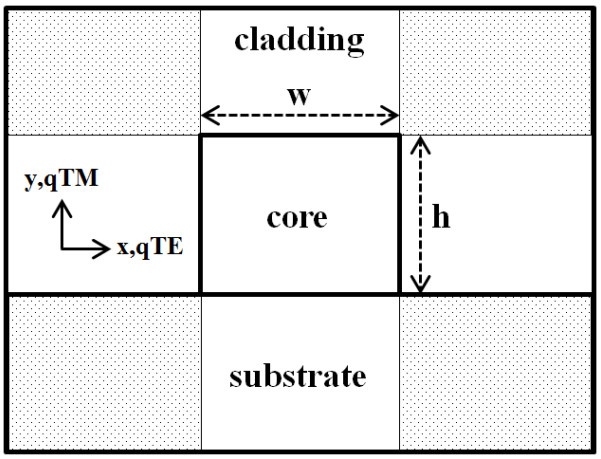

Figure 5.2: Schematic drawing of a rectangular waveguide. Directions of the major electric field components corresponding to quasi-TE and quasi-TM modes are represented. Corner regions appear as dashed zones

2.3.2 Effective index method (EIM)

Description

In the effective index method, both directions of optical confinement are treated subsequently. It is based on the assumption that the electromagnetic field can be expressed with a separation of the spatial variables [10]. In the simple case of a rectangular waveguide, the effective index of a guided mode is obtained by solving a first 1D dispersion equation, similar to those of the slab waveguide, for a confinement direction - lateral or vertical - providing $N_{eff,\,I}$. This is followed by the resolution of a second dispersion equation, for the perpendicular confinement direction, in which the core index is replaced by $N_{eff,\,I}$.

Normalized parameters

In this treatment we need to introduce normalized constants for both directions. Initiating the EIM on the vertical confinement direction, the propagation constant b_V and the normalized frequency v_V related to this confinement direction are expressed as:

$$\begin{cases} b_V = \dfrac{N_{eff,\,I}^2 - N_{sub}^2}{N_{core}^2 - N_{sub}^2} \\ v_V = kh\left(N_{core}^2 - N_{sub}^2\right)^{1/2} \end{cases} \tag{5.25}$$

Then, their equivalent b_L and v_L for the lateral direction are expressed as:

$$\begin{cases} b_L = \dfrac{N_{eff}^2 - N_{clad}^2}{N_{eff,\,I}^2 - N_{clad}^2} \\ v_L = kw\left(N_{eff,\,I}^2 - N_{clad}^2\right)^{1/2} \end{cases} \tag{5.26}$$

With this set of parameters, the guided modes of the rectangular waveguides are determined by a polarization and mode-order dependent set of two identically zeros functions.

Sets of dispersion equations

For quasi-TM modes, also referred to as $E_{p,\,q}^{y}$ modes this set of dispersion equations is written:

$$\begin{cases} f_{L,\,qTM}^{(p)} = 0 = v_L\sqrt{1-b_L} - p\pi - 2\arctan\sqrt{\dfrac{b_L}{1-b_L}} \\ f_{V,\,qTM}^{(q)} = 0 = v_V\sqrt{1-b_V} - q\pi \\ \qquad - \arctan\left[\dfrac{N_{core}^2}{N_{sub}^2}\sqrt{\dfrac{b_V}{1-b_V}}\right] - \arctan\left[\dfrac{N_{core}^2}{N_{clad}^2}\sqrt{\dfrac{b_V+\gamma}{1-b_V}}\right] \end{cases} \tag{5.27}$$

For quasi-TE modes, also referred to as $E_{p,\,q}^{x}$ modes this set of dispersion equations is written:

$$\begin{cases} f_{L,\,qTE}^{(p)} = v_L\sqrt{1-b_L} - p\pi - 2\arctan\left[\dfrac{N_{eff,\,I}^2}{N_{clad}^2}\sqrt{\dfrac{b_L}{1-b_L}}\right] \\ f_{V,\,qTE}^{(q)} = v_V\sqrt{1-b_V} - q\pi \\ \qquad - \arctan\left(\sqrt{\dfrac{b_V}{1-b_V}}\right) - \arctan\left(\sqrt{\dfrac{b_V+\gamma}{1-b_V}}\right) \end{cases} \tag{5.28}$$

In analogy with the case of slab waveguides, we again assumed that $N_{clad} < N_{sub}$. Due to the fact that the lateral direction of confinement always relate to a symmetric slab waveguide, the case where the cladding

index is larger than the substrate index can be treated by exchanging both parameters in expressions related to the vertical (asymmetrical) direction: b_V, v_V, f_V and γ.

Expressions for waveguide sensitivities

Similarly to the case of the slab waveguide, the derivation of a set of dispersion equations for a given mode determines the relation between the quantity dN_{eff} and the elementary variations of all other parameters of the rectangular waveguide:

$$\begin{aligned} dN_{eff} = S_{core} dN_{core} + S_{sub} dN_{sub} + S_{clad} dN_{clad} \\ + S_w dw + S_h dh + S_\lambda d\lambda \end{aligned} \tag{5.29}$$

The difference with the case of the slab waveguide is that, in order to obtain the expressions of the sensitivities, the derivation of two dispersion equations, f_V and f_L, is necessary. As a consequence, the resulting expressions are somewhat different in form, with one or two components, depending on the coefficient.

$$\begin{cases} S_{core} = \left(\dfrac{\partial f_L}{\partial N_{eff}}\right)^{-1} \cdot \dfrac{\partial f_L}{\partial N_{eff,\,I}} \cdot \left(\dfrac{\partial f_V}{\partial N_{eff,\,I}}\right)^{-1} \cdot \dfrac{\partial f_V}{\partial N_{core}} \\ S_{sub} = \left(\dfrac{\partial f_L}{\partial N_{eff}}\right)^{-1} \cdot \dfrac{\partial f_L}{\partial N_{eff,\,I}} \cdot \left(\dfrac{\partial f_V}{\partial N_{eff,\,I}}\right)^{-1} \cdot \dfrac{\partial f_V}{\partial N_{sub}} \\ S_{clad} = \left(\dfrac{\partial f_L}{\partial N_{eff}}\right)^{-1} \cdot \dfrac{\partial f_L}{\partial N_{eff,\,I}} \cdot \left(\dfrac{\partial f_V}{\partial N_{eff,\,I}}\right)^{-1} \cdot \dfrac{\partial f_V}{\partial N_{clad}} \\ \qquad\qquad - \left(\dfrac{\partial f_L}{\partial N_{eff}}\right)^{-1} \dfrac{\partial f_L}{\partial N_{clad}} \\ S_w = - \left(\dfrac{\partial f_L}{\partial N_{eff}}\right)^{-1} \cdot \dfrac{\partial f_L}{\partial w} \\ S_h = \left(\dfrac{\partial f_L}{\partial N_{eff}}\right)^{-1} \cdot \dfrac{\partial f_L}{\partial N_{eff,\,I}} \cdot \left(\dfrac{\partial f_V}{\partial N_{eff,\,I}}\right)^{-1} \cdot \dfrac{\partial f_V}{\partial h} \\ S_\lambda = \left(\dfrac{\partial f_L}{\partial N_{eff}}\right)^{-1} \cdot \dfrac{\partial f_L}{\partial N_{eff,\,I}} \cdot \left(\dfrac{\partial f_V}{\partial N_{eff,\,I}}\right)^{-1} \cdot \dfrac{\partial f_V}{\partial \lambda} \\ \qquad\qquad - \left(\dfrac{\partial f_L}{\partial N_{eff}}\right)^{-1} \cdot \dfrac{\partial f_L}{\partial \lambda} \end{cases} \tag{5.30}$$

Discussion

Using the expressions above, each waveguide sensitivity can be expressed as a function of normalized parameters (b_V, b_L, v_V, v_L, γ) or physical parameters (N_{eff}, $N_{eff,I}$, N_{core}, N_{clad}, N_{sub}, w, h, λ). Expressions can be very easily obtained with a formal calculation engine[13]. This scheme allows to calculate the sensitivity coefficients without being confronted to the complexity of their expressions.

2.3.3 Marcatili's method

Description

In Marcatili's method (MM), both directions of optical confinement are treated independently. The important assumption of this method is that the electromagnetic field in the corner regions of the structure can be neglected since it decays quite rapidly in these regions [69]. The separation of variables, used in EIM, is also assumed in MM. As a result, the effective index can be obtained by solving two independent 1D dispersion equations, one for lateral confinement, providing $N_{eff,\,L}$, and one for vertical confinement, providing $N_{eff,\,V}$.

The effective index of the guided mode is then determined from the expression:

$$N_{eff}^2 = N_{eff,\,L}^2 + N_{eff,\,V}^2 - N_{core}^2 \tag{5.31}$$

Normalized parameters

In the case of the rectangular waveguide, we will need, in analogy to the slab waveguide treatment, the following dimensionless parameters:

[13] typical expressions are extremely long and difficult to analyse without graphical analysis

$$\begin{cases} b_L = \dfrac{N_{eff,\,L}^2 - N_{clad}^2}{N_{core}^2 - N_{clad}^2} \\ v_L = kw\left(N_{core}^2 - N_{clad}^2\right)^{1/2} \\ b_V = \dfrac{N_{eff,\,V}^2 - N_{sub}^2}{N_{core}^2 - N_{sub}^2} \\ v_V = kh\left(N_{core}^2 - N_{sub}^2\right)^{1/2} \end{cases} \tag{5.32}$$

The asymmetry factor γ is defined in the same way as in Eq.(5.19). With this set of parameters, the guided modes of the rectangular waveguides are solutions of a set of two equations which depend on the polarization of the guided mode.

Sets of dispersion equations

For the quasi-TM polarization, we have:

$$\begin{cases} f_{L,qTM}(p) = 0 = v_L\sqrt{1-b_L} - p\pi - 2\arctan\left(\sqrt{\dfrac{b_L}{1-b_L}}\right) \\ f_{V,qTM}(m) = 0 = v_V\sqrt{1-b_V} - q\pi - \arctan\left[\dfrac{N_{core}^2}{N_{sub}^2}\sqrt{\dfrac{b_V}{1-b_V}}\right] \\ \qquad\qquad - \arctan\left[\dfrac{N_{core}^2}{N_{clad}^2}\sqrt{\dfrac{b_V+\gamma}{1-b_V}}\right] \end{cases} \tag{5.33}$$

As for the quasi-TE polarization, the set of dispersion equations is:

$$\begin{cases} f_{L,qTE}(p) = 0 = v_L\sqrt{1-b_L} - p\pi - 2\arctan\left[\dfrac{N_{core}^2}{N_{clad}^2}\sqrt{\dfrac{b_L}{1-b_L}}\right] \\ f_{V,qTE}(m) = 0 = v_V\sqrt{1-b_V} - q\pi - \arctan\left(\sqrt{\dfrac{b_V}{1-b_V}}\right) \\ \qquad\qquad - \arctan\left(\sqrt{\dfrac{b_V+\gamma}{1-b_V}}\right) \end{cases} \tag{5.34}$$

Expressions for the sensitivity coefficients

The total derivative dN_{eff} is calculated similarly to the case of the effective index method and provides the expressions of the sensitivity coefficients, first for the width w, height h and wavelength λ:

$$\begin{cases} S_w = -\dfrac{N_{eff,\,L}}{N_{eff}} \cdot \left(\dfrac{\partial f_L}{\partial N_{eff,\,L}}\right)^{-1} \cdot \dfrac{\partial f_L}{\partial w} \\ S_h = -\dfrac{N_{eff,\,V}}{N_{eff}} \cdot \left(\dfrac{\partial f_V}{\partial N_{eff,\,V}}\right)^{-1} \cdot \dfrac{\partial f_V}{\partial h} \\ S_\lambda = -\dfrac{N_{eff,\,L}}{N_{eff}} \cdot \left(\dfrac{\partial f_L}{\partial N_{eff,\,L}}\right)^{-1} \cdot \dfrac{\partial f_L}{\partial \lambda} \\ \qquad\quad - \dfrac{N_{eff,\,V}}{N_{eff}} \cdot \left(\dfrac{\partial f_V}{\partial N_{eff,\,V}}\right)^{-1} \cdot \dfrac{\partial f_V}{\partial \lambda} \end{cases} \tag{5.35}$$

Then, the waveguide sensitivities to the refractive indices of the structure are expressed as:

$$\begin{cases} S_{N_{core}} = -\dfrac{N_{eff,\,L}}{N_{eff}} \cdot \left(\dfrac{\partial f_L}{\partial N_{eff,\,L}}\right)^{-1} \cdot \dfrac{\partial f_L}{\partial N_{core}} \\ \qquad\quad - \dfrac{N_{eff,\,V}}{N_{eff}} \cdot \left(\dfrac{\partial f_V}{\partial N_{eff,\,V}}\right)^{-1} \cdot \dfrac{\partial f_V}{\partial N_{core}} - \dfrac{N_{core}}{N_{eff}} \\ S_{N_{sub}} = -\dfrac{N_{eff,\,V}}{N_{eff}} \cdot \left(\dfrac{\partial f_V}{\partial N_{eff,\,V}}\right)^{-1} \cdot \dfrac{\partial f_V}{\partial N_{sub}} \\ S_{N_{clad}} = -\dfrac{N_{eff,\,L}}{N_{eff}} \cdot \left(\dfrac{\partial f_L}{\partial N_{eff,\,L}}\right)^{-1} \cdot \dfrac{\partial f_L}{\partial N_{clad}} \\ \qquad\quad - \dfrac{N_{eff,\,V}}{N_{eff}} \cdot \left(\dfrac{\partial f_V}{\partial N_{eff,\,V}}\right)^{-1} \cdot \dfrac{\partial f_V}{\partial N_{clad}} \end{cases} \tag{5.36}$$

Limitations

In MM, the effective index is deduced from Eq.(5.31) after obtaining the two partial effective indices $N_{eff,V}$ and $N_{eff,L}$, this equation being a direct consequence of Marcatili's model. It can be observed that near cut-off, the calculated values of the effective index can become lower than the lowest refractive index of the structure. This absurd behavior is attributed

to the strong assumption that the electromagnetic field can be neglected in the corner regions, whose validity is seriously challenged when most of the mode intensity is propagating outside the core. However, when the effective index remains larger than the lowest refractive index, the accuracy of the method is sufficient for waveguide analysis.

A more important limitation of these analytical models is that they do not allow to model bent waveguides, such as microring waveguides. The evaluation of the effective index for a simple bent slab waveguide requires to solve equations that are much more complicated than those applying for a straight configuration [58]. A solution to this limitation is the use of a perturbational approach, allowing to calculate the correction to apply to the effective index due to the curvature of the waveguide. Also, for microrings with large radii (cf. Chap.2), it can be assumed in a first approximation that the curvature of the waveguide can be neglected in the analytical evaluations of the sensitivities.

2.3.4 Comparison with results from a numerical method

In this part, values calculated from the previously described methods are compared to those obtained from a commercial mode solver using the ADI method. These values are used as a reference to test the accuracy of proposed analytical methods for evaluations of effective indices and sensitivity coefficients.

Description of the simulated structure

The developed analytical methods are applied to the typical waveguide structure used in the scope of this dissertation: a rectangular waveguide with SU-8 as core material, silica as substrate material and water as cladding material, with a central wavelength chosen at 1550 nm.

The comparison, whose results are plotted in Figs. 5.3, 5.4 and 5.5, focuses on the values of the effective indices of the fundamental TE and TM modes of a 2 μm-large waveguide as well as on two key sensitivities for this mode, S_{core} to the core refractive index and S_{clad} to the cladding index, for a varying height.

Numerical evaluations of the waveguide sensitivities

The values relative to the ADI numerical method were obtained by comparing the values of the effective indices of the TE and TM modes when N_{core} and N_{clad} undergo a slight variation - $\delta = 0.001$ - of their value. Sensitivities are then deduced from:

$$S_{core}^{ADI} = \frac{N_{eff}^{ADI}\left(N_{core}+\delta\right) - N_{eff}^{ADI}\left(N_{core}\right)}{\delta} \tag{5.37}$$

$$S_{clad}^{ADI} = \frac{N_{eff}^{ADI}\left(N_{clad}+\delta\right) - N_{eff}^{ADI}\left(N_{clad}\right)}{\delta} \tag{5.38}$$

First observations

The first noticeable result of the comparison is that both analytical methods are less accurate when the height of the waveguide decreases, especially near cut-off (cf. Fig. 5.4 and Fig. 5.5). In this case, the common assumption of the separation of spatial variables for the electromagnetic field becomes questionable since for a weakly guided mode, a large part of the intensity is located in the corners of the waveguide where diffraction occurs.

It also seems that the additional assumption made in MM is detrimental to the accuracy of the calculated effective index. This is well explained since the assumption that the electromagnetic field is negligible in the corner regions is not valid for weakly-guided modes. Other important observations are listed below.

Comparison of evaluated effective indices

The effective indices calculated from both methods are very close to those obtained with ADI, which is especially true for EIM (cf. Fig. 5.3). This shows that numerical methods can be effectively replaced in most cases by EIM when it comes to calculate effective index values. Furthermore, the use of ADI method can be problematic in cases of very weak guidance since electromagnetic field components are arbitrarily set to zero at the border of the simulation window, biasing the characteristics of the

computed guided mode. This is particularly visible for the calculations of S_{clad} discussed below. The only solution to overcome this difficulty is to drastically increase the size of the simulation window for weakly guided modes while maintaining a constant grid density, which considerably increases computations durations and memory requirements.

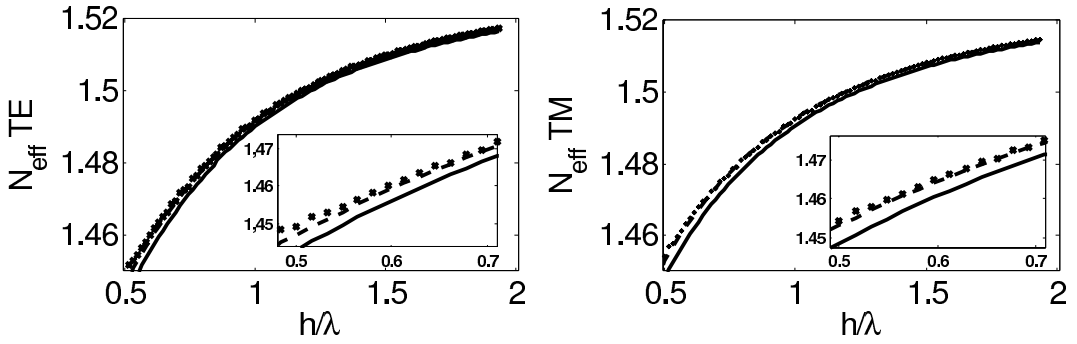

Figure 5.3: Comparison of effective indices of fundamental TE and TM modes of a typical polymeric rectangular waveguide with a varying height. Legend of the plot is: MM = solid, EIM = dash and ADI = cross

Comparison of waveguide sensitivities to the RI of the cladding material

Sensitivities to the cladding refractive index is particularly important for homogeneous and surface sensing applications. In our calculations, we notice a good agreement between results from analytical and ADI methods.

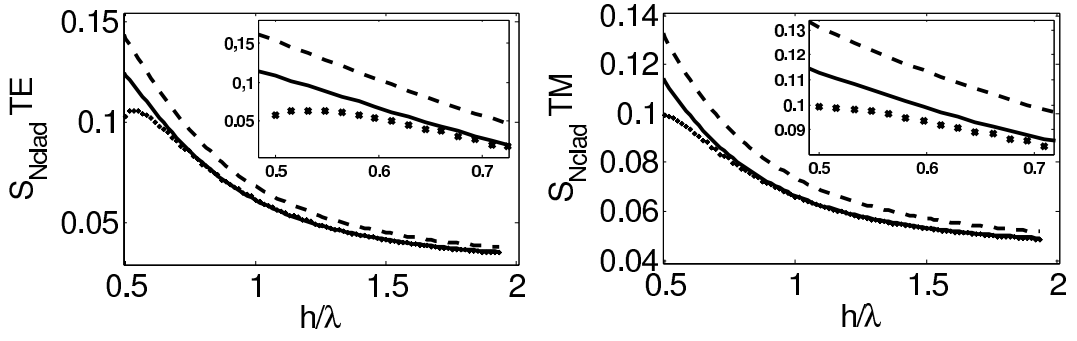

Figure 5.4: Comparison of waveguide cladding sensitivities for the fundamental TE and TM modes of a typical polymeric rectangular waveguide with a varying height. Legend of the plot is: MM = solid, EIM = dash and ADI = cross

It is particularly interesting to notice that for this coefficient, MM provides results that are more accurate than those obtained from EIM, for both

TE and TM modes. Since the values of the calculated effective indices are more accurately determined with EIM, this result appears odd. Nevertheless, the strong correlation in the data generated by ADI method and MM indicates that, the additional assumption made in MM makes it somehow more relevant to describe homogeneous sensing in this particular case.

Despite this puzzling effect, both analytical methods provide sufficient accuracy for waveguide design, within 5 % the values obtained from the numerical method. The major discrepancy between analytical and numerical methods for this coefficient is near the cut-off where the numerical method predicts a saturation of the cladding sensitivity. This effect, as discussed earlier, comes from the limited extent of the calculation window in the ADI method, and affects more the accuracy of the cladding sensitivity than for the calculation of the effective index. This is an additional limitation of the numerical methods for sensitivity studies.

Comparison of waveguide sensitivities to the RI of the core material

The core sensitivity can be the most important parameter for the study of thermal influence since the polymer core material has usually the largest TO coefficient. Analytical models provide values in good agreement - within 5% - with ADI method. Despite the slight difference obtained between analytical and numerical methods, they generate similar behavior when the height varies, which is important for the use of analytical methods for waveguide optimization (cf. Fig. 5.5).

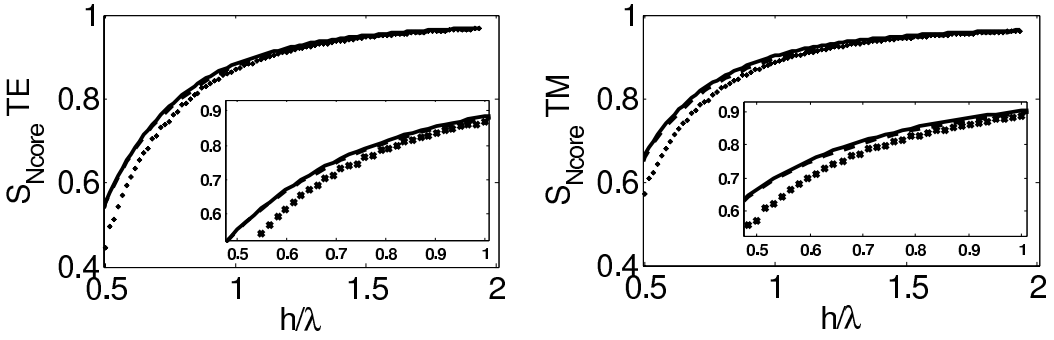

Figure 5.5: Comparison of waveguide core sensitivities for the fundamental TE and TM modes of a typical polymeric rectangular waveguide with a varying height. Legend of the plot is: MM = solid, EIM = dash and ADI = cross

2.3.5 Starting point for waveguide sensitivity analysis

Goals of a sensitivity analysis

As outlined before, the main goals of waveguide sensitivity analysis is to optimize the structure of the microring waveguide to achieve the best sensing performances. This implies to maximize the waveguide sensitivity to the measurand, while waveguide sensitivities to other quantities, or perturbations, must be minimal.

Combining analytical and numerical approaches

The analytical models developed to evaluate the sensitivities of a rectangular waveguide were proven to be quite accurate. However, they are limited when dimensions of the waveguide core become small. They are also unable to directly provide sensitivity evaluations for bent waveguides. In comparison, the ADI method can be applied to accurately evaluate effective indices and sensitivities of bent waveguides for any core dimension. However, as outlined in §2.1, numerical methods such as ADI cannot be realistically applied for full waveguide sensitivity analysis.

In consequence, the most relevant approach is to use analytical tools first, in order to orient numerical studies with a limited number and range of independent parameters to consider. With such a scheme, a very general case study can be performed, resulting nonetheless in accurate evaluations of the sensitivities.

Analytical approach as optimization starting point

In Fig. 5.6, a starting point of such a general study is presented, with the evaluation of waveguide sensitivities for the fundamental TM mode as functions of the normalized width $w^\star = w/\lambda$ and height $h^\star = h/\lambda$ of the SU-8 core of a waveguide with silica as substrate material and de-ionised (DI) water as cladding material.

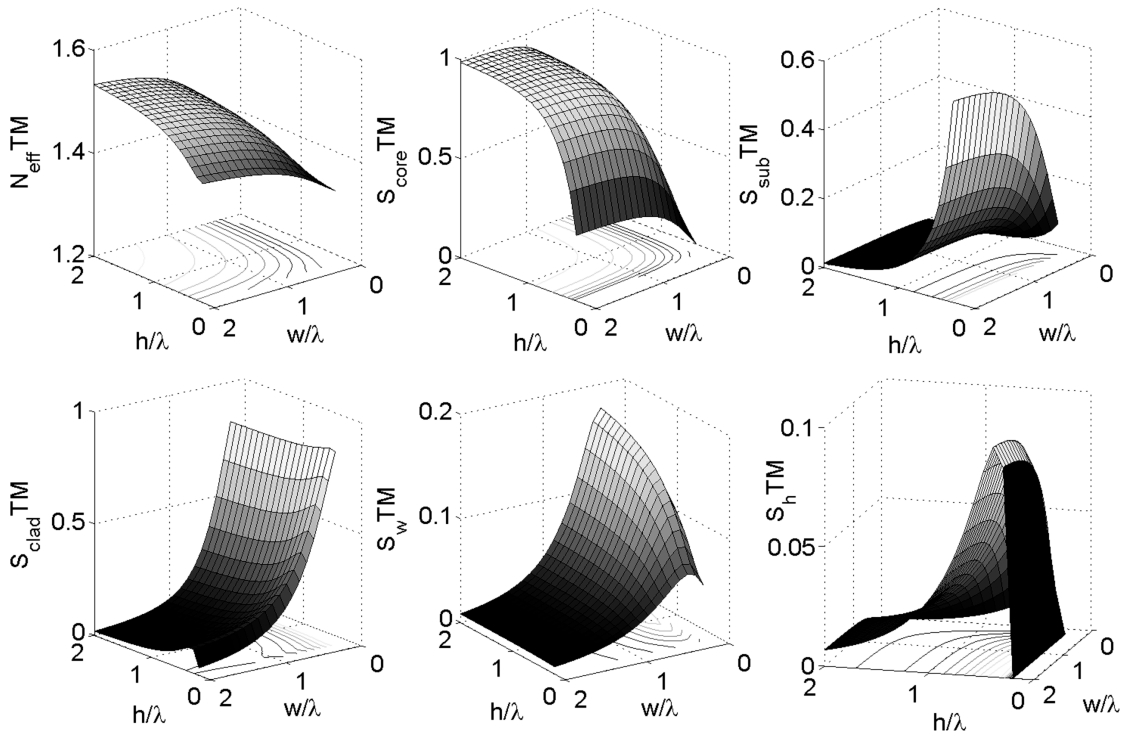

Figure 5.6: Full waveguide sensitivity analysis for the fundamental TM mode of a polymeric rectangular waveguide using the effective index method. $N_{core} = 1.56$ (SU-8), $N_{sub} = 1.444$ (silica) and $N_{clad} = 1.323$ (water).

3 Microresonator sensitivities in homogeneous sensing

3.1 Microresonator sensitivity

The sensitivity of the microresonator was previously defined as:

$$S_{res} = \frac{d\lambda}{dM} = \frac{\lambda}{N_{eff}} \cdot \frac{dN_{eff}}{dM} + \frac{\lambda}{L} \cdot \frac{dL}{dM} \tag{5.39}$$

where λ is the spectral position in wavelength of one of the microresonator resonances. The parameter L is the mean circumference of the microresonator, also referred to as cavity length.

3.1.1 General expression for homogeneous sensing

In homogeneous sensing, we can assume that the parameter L is not dependent on the measurand. We can also safely assume that the only parameter

modified by the measurand is the RI of the cladding material of the microresonator. Accordingly, in homogeneous sensing, the sensitivity of the microresonator can be simply expressed as[14]:

$$S_{res} = \frac{\lambda}{N_{eff}} \cdot \frac{\partial N_{eff}}{\partial N_{clad}} \cdot \frac{\partial N_{clad}}{\partial M} = \frac{\lambda}{N_{eff}} \cdot S_{wav} \cdot S_M \tag{5.40}$$

where S_{wav} is the waveguide sensitivity to the cladding RI, and S_M is the sensitivity of cladding RI to the measurand.

3.1.2 Application to a refractometer

The homogeneous sensing scheme can be applied to use the microresonator as a transducer for refractometry. In such an instrument, the aim is to measure the refractive index of a gaz, a liquid, or a solid as the cladding material of the microresonator. As discussed before, the detection scheme allows relative index measurements only. This means that an RI can only be determined in reference to another known RI, of a gas, or liquid or solid material.

For refractometry applications, the measurand is directly the RI of the cladding, hence the sensitivity of the microresonator is simply expressed as:

$$S_{res}^{(RI)} = \frac{\lambda}{N_{eff}} \cdot \frac{\partial N_{eff}}{\partial N_{clad}} = \frac{\lambda}{N_{eff}} \cdot S[N_{eff}/N_{clad}] \tag{5.41}$$

3.1.3 Application to a concentration sensor

Application of the microresonator as a transducer for homogeneous sensing of concentration is very similar. The working principle of such an instrument is to infer the concentration C of a solution from the measurement of its refractive index. The sensitivity of the microresonator can then be written as:

$$S_{res}^{(C)} = \frac{\lambda}{N_{eff}} \cdot \frac{\partial N_{eff}}{\partial N_{clad}} \cdot \frac{\partial N_{clad}}{\partial C} = \frac{\lambda}{N_{eff}} \cdot S_{wav} \cdot S_C \tag{5.42}$$

As described in the previous section, the coefficient S_{wav} and the effective index N_{eff} can be determined from numerical simulations, or from

[14] similarly to the the case study presented in §2.1

analytical models. Accordingly, the sensitivity of the microresonator can be evaluated via the coefficient S_C, *ie* the sensitivity of the cladding RI to the concentration C.

3.2 Sensitivity to the measurand

3.2.1 Refractive index of a dense medium

Lorentz-Lorenz formula

A relation between the refractive index n of a linear, homogeneous and isotropic medium, composed of N molecules per unit of volume, is the Lorentz-Lorenz formula, expressed in SI units[15], as:

$$\frac{N\alpha}{3} = \frac{n^2 - 1}{n^2 + 2} \tag{5.43}$$

where α is the mean polarizability of the molecules.

Molar refractivity

Instead of the mean polarizability α, another quantity, the *molar refractivity* A is often used. It is defined as:

$$A = \frac{1}{3}\mathcal{N}_A\alpha \tag{5.44}$$

where $\mathcal{N}_A = 6.02 \times 10^{23}\,\text{mol}^{-1}$ is the Avogadro number.

The molar refractivity A for many molecules can be found in the literature. However, this quantity is often measured at 589 nm, the wavelength corresponding to the D line of sodium lamps. In consequence, values of A near 1550 nm may be difficult to find.

3.2.2 Refractive index of a mixture

Modified Lorentz-Lorenz formula

[15]It is important to point out that sometimes, the Lorentz-Lorenz formula is expressed in Gaussian units, in which case the polarizability α is replaced in the formula by $4\pi\alpha$

For a mixture composed, per volume unit, of N_1 molecules of molar polarizability A_1 and N_2 molecules of molar polarizability A_2, a good approximation [75] of the resulting refractive index n is obtained from the expression:

$$\frac{n^2-1}{n^2+2} = \frac{N_1}{\mathcal{N}_A}A_1 + \frac{N_2}{\mathcal{N}_A}A_2 \tag{5.45}$$

Relation to analyte concentration

What is particularly interesting for concentration sensing is the relation between the refractive index of the solution N_{clad} and the concentration C of the solution. Let us consider an aqueous solution where the measurand relates to the concentration of a molecule X in the solution. The solution is a mixture of water (W) molecules and X molecules. The molar concentration $C_m^{(X)}$ of the solution is defined as:

$$C_m^{(X)} = \frac{n_m^{(X)}}{V} \tag{5.46}$$

where $n_m(X)$ is the number of moles of X and V is the total volume of the solution.

The density N_X of X molecules per volume unit verifies the expression:

$$N_X = \frac{\mathcal{N}_X}{V} = \frac{\mathcal{N}_a n_m^{(X)}}{V} = \mathcal{N}_a C_m^{(X)} \tag{5.47}$$

In the same manner, the density N_W of water molecules per volume unit can be expressed as:

$$N_W = \mathcal{N}_a C_m^{(W)} = \mathcal{N}_a \frac{\rho(W)}{M(W)} \tag{5.48}$$

where $\rho(W)$ is the density of water[16], and M(W) is molar mass of water, approximately equal to 18 g.mol^{-1}.

Refractive index of the cladding

[16] as mass per unit of volume

From the above expressions, the refractive of the cladding N_{clad} expressed as function of the concentration $C_m^{(X)}$ can be inferred from:

$$f(N_{clad}) = \frac{N_{clad}^2 - 1}{N_{clad}^2 + 2} = C_m(X)A_X + \frac{\rho(W)}{M(W)}A_W \tag{5.49}$$

where A_X and A_W are the molar polarizabilities of X and water (W) molecules, respectively.

3.2.3 Sensitivity of the cladding index to analyte concentration

In order to derive the expression of the sensitivity of N_{clad} to the concentration $C_m^{(X)}$, we define $N_{clad,0}$ as the value of the cladding RI when $C_m^{(X)} = 0$. From a differentiation of the above expression near $N_{clad,0}$, we obtain:

$$df(N_{clad,0}) = f'(N_{clad,0})dN_{clad} = A_X dC_m^{(X)} \tag{5.50}$$

where $f'(N_{clad,0})$ is the derivative of the function f at $N_{clad} = N_{clad,0}$. After calculation, is is expressed as:

$$f'(N_{clad,0}) = \frac{6N_{clad,0}}{\left(N_{clad,0}^2 + 2\right)^2} \tag{5.51}$$

Finally, the sensitivity of the cladding RI to the concentration of $C_m^{(X)}$ can be expressed, near $C_m^{(X)} = 0$, as:

$$S_{C[X]} = \frac{A_X}{f'(N_{clad,0})} \tag{5.52}$$

where $S_{C[X]}$ is in RIU per molar concentration unit.

3.3 Optimization of the cladding sensitivity

For both refractometer and concentration sensor applications, the waveguide sensitivity to the cladding has to be optimized. In the following, we apply the analytical expression of the waveguide sensitivity to the RI of the cladding material obtained with Marcatili's method to identify the key waveguide parameters to achieve the highest microresonator sensitivity.

3.3.1 Description of the study

In Fig. 5.7 are plotted the values of this sensitivity $S_{clad} = \partial N_{eff}/\partial N_{clad}$ for fundamental TE and TM modes as a function of the normalized width w/λ and height h/λ for two rectangular waveguides.

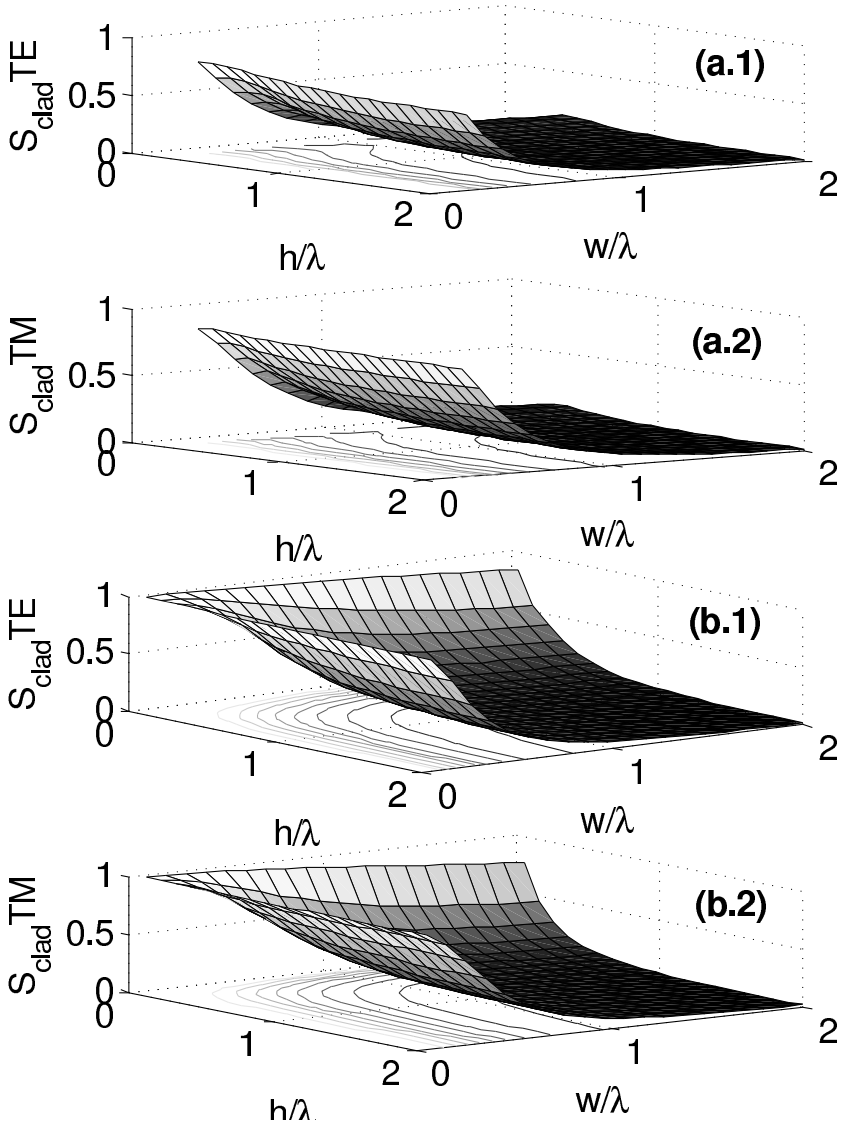

Figure 5.7: Sensitivities of the effective indices of fundamental TE and TM modes to the refractive index of the cladding of a rectangular waveguide vs normalized height and width. (a) asymmetric waveguide with $N_{core} = 1.56$, $N_{sub} = 1.444$ and $N_{clad} = 1.323$, (b) symmetric waveguide with $N_{core} = 1.56$ and $N_{clad} = N_{sub} = 1.323$

The first waveguide studied is an asymmetric rectangular waveguide with SU-8 as core material, silica as substrate and DI water as cladding. The second waveguide is a symmetric waveguide with SU-8 as core mate-

rial, where cladding and substrate are assumed to have the same refractive index, equal to that of DI water.

3.3.2 Analysis of the results

From these graphs (Fig. 5.7), it is visible that the sensitivity S_{clad} can be largely modulated according to the dimension of the waveguide. More specifically, the width w has clearly more influence than the height h on the cladding sensitivity. This can be explained by following the considerations.

Optimization with constant width

For a given width w_0, a reduction of the height h of the core of the waveguide will result in a less confined mode, characterized by a more important evanescent field in both cladding and substrate regions. Since, the additional intensity in the substrate region does not contribute to S_{clad}, the gain on the cladding sensitivity when reducing h is limited. In addition, smaller values of h result in higher optical losses to the substrate (cf. Chap.2).

Optimization with constant height

For a given height h_0, since the core of the waveguide is surrounded in the lateral direction by the cladding (cf.5.2), a reduction of the width w increases the intensity of the evanescent field primarily in the cladding region. Therefore, the gain of sensitivity when reducing the width is relatively higher that the gain obtained when reducing the height.

Another interesting observation comes from the comparison of the variations of the cladding sensitivity between the two configurations, (a) and (b), of rectangular waveguides. Clearly, for a given cross-section, the latter waveguide configuration is more advantageous. This can be simply explained by the fact that, when the refractive index of the substrate is lower, the intensity of the evanescent field in this region is relatively lower, which means that the same intensity is relatively higher in the cladding. In other words, the yield of the total evanescent field is at its highest for homogeneous detection when the refractive index of the substrate is as low as pos-

sible. The discussion and waveguide geometry optimization is illustrated in Fig. 5.8.

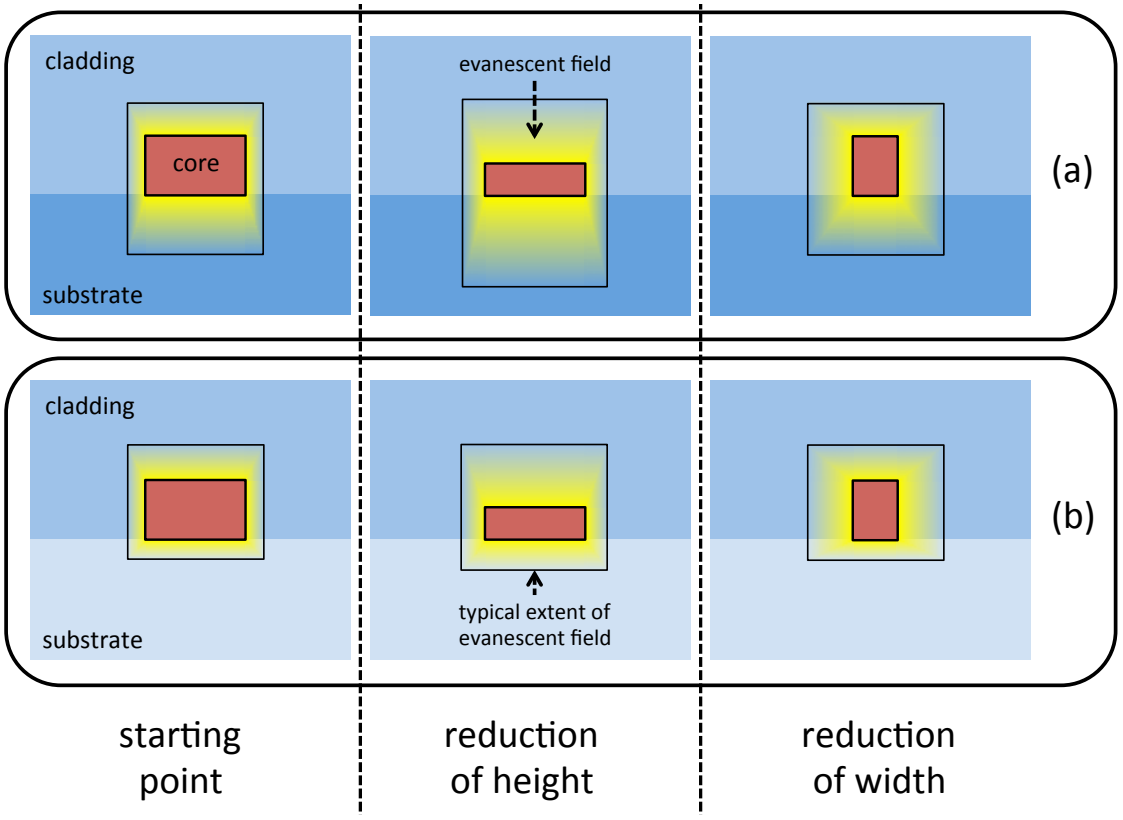

Figure 5.8: Evanescent field for various rectangular waveguide configurations. In (a), the cladding RI is higher than the substrate RI; the opposite situation is presented in (b).

According to the above considerations, a symmetric configuration, where cladding and substrate RIs are identical, is not necessarily optimal. However, symmetric waveguides theoretically support guided modes, even with very small core cross-sections. Thus, matching substrate and cladding RIs and adopting waveguides with very small cross sections could be another way to optimize the sensitivity.

4 Optimization for surface sensors

4.1 Introduction to surface sensing

In homogeneous sensing, as discussed before, the information on the measurand is carried by the refractive index N_{clad} of the cladding material,

which is assumed to be homogeneous. As a matter of fact, in the view provided by Lorentz-Lorenz equation, N_{clad} can be viewed as an average refractive index of a mixture over its all volume.

In surface sensing, the molecules to detect and/or quantify are bound on the microresonator surface. As a consequence, the situation differs from that of homogeneous sensing since variations of N_{clad} are only local, near the surface of the waveguide in contact with the cladding. In that respect, considering that shifts of the resonances during sensing are due to a variation of the average value of N_{clad} over the entire volume of solution[17] could be, in specific sensing configurations, a mistake. The error would be to consider all the solution volume, and not just the volume where the analyte molecules can effectively interact with the evanescent field of light propagating in the microresonator.

4.2 Sensitivity in surface sensing experiments

4.2.1 Expression of the microresonator sensitivity in surface sensing

General expression

We can use Eq.(5.10) to express the sensitivity of the microresonator to the surface detection of a measurand M:

$$S_{res}^{(SD)} = \frac{\lambda}{N_{eff}} \cdot \left(\frac{dN_{eff}}{dM}\right)_{(SD)} + \frac{\lambda}{L} \cdot \left(\frac{dL}{dM}\right)_{(SD)} \tag{5.53}$$

where λ is the spectral position (in wavelength) of one of the resonances of the microresonator. The parameter L is the mean circumference of the microresonator, also referred to as cavity length.

Case of WGM resonators

For WGM devices such as microspheres, microtoroids, microdisks, ... the adsorption of the molecules on the surface of the microresonator is liable to modify[18] the cavity length L [76]. Therefore, we have to consider that for a microring waveguide, the geometry of the microresonator will be modified by molecular adsorption.

[17] such consideration applies to homogeneous sensing
[18] on a scale dependent on the size of the molecules

Case of microring resonators

For microring resonators, L is defined as the average circumference of the ring. Therefore, assuming that the molecular layer is adsorbed symmetrically on the top and the sides of the waveguide, the cavity length L as average is not modified by the the presence of the molecules. The effective index is consequently the only parameter liable to vary according to the measurand. We can then express the sensitivity of the microring as:

$$S_{res}^{(SD)} = \frac{\lambda}{N_{eff}} \cdot \left(\frac{dN_{eff}}{dM} \right)_{(SD)} \tag{5.54}$$

Discussion

The major issue is now in the evaluation of $\left(\frac{dN_{eff}}{dM} \right)_{(SD)}$. In that respect, similarly to the case of homogeneous sensing, the questions to be addressed are:

- How the presence of analyte molecules modify the refractive index distribution in the cladding ?
- What is the influence of a local variation of refractive index in the cladding on the effective index a guided mode ?

4.3 Sensitivity of the RI distribution to the analyte

4.3.1 Position of the problem

In surface sensing, local variations of the refractive index distribution are to be considered. As a consequence, the first issue is to define what local means. The approach chosen in the following is to use a mesoscopic description of the cladding material.

4.3.2 Mesoscopic description of the cladding material

All properties of the material are hereafter defined as constant in an infinitesimal volume dV centred on a point M belonging to the space occupied by the cladding material.

Cladding refractive index distribution

The RI of the cladding can then be expressed at each point M as:

$$N_{clad} = n_{cl}(M) \tag{5.55}$$

The local index $n_{cl}(M)$ can be viewed as an average of the refractive index over the volume dV centered on M:

$$n_{cl}(M) = < n_{cl} >_{dV(M)} \tag{5.56}$$

Advantage of the mesoscopic description

The advantage of using a mesoscopic description is that the volume dV can be considered as small enough to accurately describe local variations of refractive index, and as large enough to apply macroscopic relations to the volume dV.

Mesoscopic scale

It must be pointed out that, consequently, the use of a mesoscopic scale is only relevant if waveguide dimensions are large as compared to the dimensions of the analyte molecules. If A_{wav} is a typical dimension of the waveguide, and A_{mol} is a typical dimension of a molecule, dV should verify:

$$A_{mol} \ll (dV)^{1/3} \ll A_{wav} \tag{5.57}$$

In the following, we assume that this relation is verified.

4.3.3 Derivation of cladding RI distributions

With $A_{mol} \ll (dV)^{1/3}$, we can consider that dV contains enough molecules so that the Lorentz-Lorenz formula for a mixture can be applied locally. Similarly to the description for homogeneous sensing, we consider a mixture of water (W) molecules and analyte molecules referred to as X molecules.

Local application of Lorentz-Lorenz formula for mixtures

In the volume dV centred on M, we can define the local molecular densities $N_W(M)$ and $N_X(M)$ of W and X molecules, respectively. From Lorentz-Lorenz formula applied to the volume dV, we have:

$$\frac{n_{cl}^2(M)-1}{n_{cl}^2(M)+2} = \frac{N_W(M)}{\mathcal{N}_A} A_W(M) + \frac{N_X(M)}{\mathcal{N}_A} A_X(M) \tag{5.58}$$

In this expression, the molar refractivities A_W and A_X, as defined from mean polarizabilities, need to be considered locally since the mixture cannot be considered as homogeneous.

A major assumption here is to consider that interactions between molecules in the mixture have no effect on their respective polarizabilities at the microscopic scale. However, as presented in [75], this model is quite efficient to describe RIs of basic mixtures.

Comparison with homogeneous mixtures

A major difference with homogeneous sensing is that, in such a situation, analyte molecules can have a specific orientation in space. Therefore, the interaction between the guided mode and the analyte molecules can depend on its polarization state[19]. Therefore, we have to replace the constant molar refractivity A_X used in homogeneous sensing by a local and polarization-dependent quantity.

Refractivity of water molecules

Concerning water molecules, event though they may bind to the microresonator surface via O-H bonds, we can assume that the orientation distribution of water molecules interacting with the surface will be random. Therefore, contrary to X molecules, the same molar refractivity A_W used for homogeneous sensing applies to surface sensing.

Polarization-dependent RI distributions

[19] If molecules have a spherical symmetry, we can assume that the orientation of the spheres will have no impact on the polarizability. However, if molecules are strongly asymmetric, such as DNA strands, a non-random orientation of the molecules at the surface of the microresonator will result in optical anisotropy

According to these considerations, we can introduce two distinct distributions of the cladding index, depending on the polarization state of the guide mode: $n_{cl,TE}(M)$ and $n_{cl,TM}(M)$. For instance, $n_{cl,TE}(M)$ can be viewed as the refractive index perceived by a TE guide mode in the volume dV centred on M. This simple model provides the following polarization-dependent Lorentz-Lorenz formula:

$$\begin{cases} \dfrac{n_{cl,TE}^2(M)-1}{n_{cl,TE}^2(M)+2} = \dfrac{N_W(M)}{\mathcal{N}_A}A_W(M) + \dfrac{N_X(M)}{\mathcal{N}_A}A_X^{(TE)}(M) \\ \dfrac{n_{cl,TM}^2(M)-1}{n_{cl,TM}^2(M)+2} = \dfrac{N_W(M)}{\mathcal{N}_A}A_W(M) + \dfrac{N_X(M)}{\mathcal{N}_A}A_X^{(TM)}(M) \end{cases} \tag{5.59}$$

4.3.4 Sensitivities of the RI distributions to the measurand

Local and polarization-dependent sensitivities

In analogy to the expressions derived in the case of homogeneous sensing, we can define local sensitivities of the cladding index distribution to the measurand, expressed with respect to the molar concentration $C_m^{(X)}$:

$$\begin{cases} S_{C[X]}^{(TE)}(M) = \dfrac{\partial n_{cl,TE}}{\partial C_m^{(X)}}(M) \\ S_{C[X]}^{(TM)}(M) = \dfrac{\partial n_{cl,TM}}{\partial C_m^{(X)}}(M) \end{cases} \tag{5.60}$$

In surface sensing, the molar concentration $C_m^{(X)}$ is the concentration of the analyte solution before contact with the microresonator.

Distribution of the analyte molecules in the cladding

Because of the surface functionalization of the microresonator, a specific chemical reaction, between analyte molecules[20] and recognition molecules[21], will occur at its surface. The direct effect of this chemical reaction is to convert an homogeneous distribution of the analyte into an inhomogeneous distribution, where part of the analyte molecules are adsorbed at the

[20] in the cladding
[21] on the waveguide surface

surface, and the other part is homogeneously distributed in the cladding. The effect of this chemical reaction can be modelled by a *binding function* $B(M)$ that relates the molecular density $N(M)$ to the concentration of the initial analyte solution $C_m^{(X)}$:

$$N_X(M) = \mathcal{N}_A \cdot B(M) \cdot C_m^{(X)} \tag{5.61}$$

Discussion on the binding function

For small concentrations, it can be assumed that the binding function $B(M)$ does not depend on the concentration $C_m^{(X)}$. This corresponds to the case where the amount of analyte molecules is small as compared to the number of binding sites on the surface. However, if the amount of molecules is very large as compared to the number of binding sites, resulting in a saturation of the surface in analyte, increasing the concentration $C_m^{(X)}$ would not modify in the same manner the distribution $N_X(M)$. In such a case, the binding function $B(M)$ is necessarily dependent on $C_m^{(X)}$.

Polarization-dependent expressions of sensitivities

In order to derive expressions for the local sensitivities, we can use a function f defined as:

$$f(x) = \frac{x^2 - 1}{x^2 + 2} \tag{5.62}$$

As a reference situation for surface sensing, we use the case where there are no analyte molecules in the cladding. Accordingly, for this situation, we have, at every point M in the cladding:

$$n_{cl,TE}(M) = n_{cl,TM}(M) = n_W = \text{constant} \tag{5.63}$$

The local sensitivities can be expressed from this reference point, similarly to homogeneous sensing, as:

$$\begin{cases} S_{C[X]}^{(TE)}(M) = \dfrac{A_X^{(TE)}(M)}{f'(n_W)} \cdot B(M) \\ S_{C[X]}^{(TM)}(M) = \dfrac{A_X^{(TM)}(M)}{f'(n_W)} \cdot B(M) \end{cases} \tag{5.64}$$

4.4 Waveguide sensitivity to the RI distribution

The second aspect to study is the relation between a local variation of cladding index, related to the concentration of the analyte $C_m^{(X)}$ by $S_{C[X]}^{(TE)}$ or $S_{C[X]}^{(TM)}$, and the variation of the effective index.

4.4.1 Derivation of the effective index from the refractive index distribution

A rigorous approach

From a rigorous point of view, the effective index of a guided mode, as solution of one or more dispersion equations, can only be expressed as an implicit function of the waveguide parameters. With such a view, analytical expressions of the sensitivities can be obtained by assuming that the analyte molecules on the surface can be modelled as an additional layer of the waveguide, sandwiched between core and cladding materials [74].

Such an approach is very similar to that developed to analytically express slab and rectangular waveguide sensitivities before. The high complexity of this approach was justified by the need to provide a model where effects of temperature or pressure variations could be realistically evaluated. However, is order to study the influence of bound molecules on the surface, such a level of complexity is not entirely required. Specifically, an approximate expression of the effective index in a channel waveguide can be used.

Explicit expression of the effective index for a channel waveguide

We start with a typical model used in guided optics to express the effective index as a function of the refractive indices of the materials. For a channel waveguide with a core, a substrate and a cladding, this model results in the expression:

$$N_{eff} = \Gamma_{core} \cdot N_{core} + \Gamma_{clad} \cdot N_{clad} + \Gamma_{sub} \cdot N_{sub} \tag{5.65}$$

where the Γ coefficients are optical power flow ratios, as defined below.

Ratios Γ of optical power flows

The coefficient $\Gamma_{(R)}$ related to the region (R) is defined as:

$$\Gamma_{(R)} = \frac{1}{P_{Tot}} \cdot \iint_{(R)} p_z(x,y)\, dS = \frac{P_z(R)}{P_{Tot}} \tag{5.66}$$

In this expression, P_{Tot} is the total flow of optical power in the direction of propagation z, and $P_z(R)$ is the same flow through the section defining (R). The scalar field p_z defined in a transverse plane is the time average of the power flow density in the direction of propagation. Therefore, it is expressed from the Poynting vector $\vec{\Pi}$ as:

$$p_z = \left\langle \vec{\Pi} \right\rangle_t \cdot \vec{u_z} = \frac{1}{2} \left(\vec{E} \times \vec{H}^{\star} \right) \cdot \vec{u_z} \tag{5.67}$$

Conservation of the total power flow

Assuming the conservation of the total power flow in the channel waveguide, we have:

$$\Gamma_{core} + \Gamma_{clad} + \Gamma_{sub} = 1 \tag{5.68}$$

Generalized expression of the effective index

From Eq.(5.65) and Eq.(5.66), we can obtain the following expression:

$$N_{eff} = \frac{1}{P_{Tot}} \cdot \iint_{\mathbb{R}^2} n(x,y) \cdot p_z(x,y)\, dS \tag{5.69}$$

where $n(x,y)$ is the distribution of the refractive index in the transverse plane. In this expression, the effective index appears as an average of the distribution of refractive index in the transverse plane, weighted by the power flow density related to the guided mode.

4.4.2 Variations of the effective index induced by surface sensing

According to the generalized expression of the effective index, we can think of two distinct effects occuring when analyte molecules are introduced near the microresonator. A direct effect is the modification of the refractive index distribution. This modification induces a perturbation of the density of optical power flow, which may then be considered as an indirect effect of the presence of analyte.

Modification of the index distribution

During surface sensing, the distribution of refractive index in the transverse plane $n(x, y)$ is modified. We can introduce a distribution of index variation $\delta n(x, y)$ in the transverse plane[22], as:

$$\delta n(x, y) = n(x, y) - n_0(x, y) \tag{5.70}$$

where $n_0(x, y)$ is the distribution of index in absence of analyte.

Perturbation of the power flow density

Since the distribution $p_z(x, y)$ is related to $n(x, y)$ by the dispersion equations, the power flow density in the transverse plane $p_z(x, y)$ is perturbed. We will write this perturbation as:

$$\delta p_z(x, y) = p_z(x, y) - p_{z,0}(x, y) \tag{5.71}$$

where $p_{z,0}(x, y)$ is the distribution of power flow density in absence of analyte.

Resulting effective index variation

The resulting variation of the effective index δN_{eff} can thus be written as the sum of two contributions:

$$\begin{aligned} \delta N_{eff} = \frac{1}{P_{Tot}} \cdot \iint_{\mathbb{R}^2} \delta n(x, y) \cdot p_{z,0}(x, y)\, dS \\ + \frac{1}{P_{Tot}} \cdot \iint_{\mathbb{R}^2} n_0(x, y) \cdot \delta p_z(x, y)\, dS \end{aligned} \tag{5.72}$$

4.5 Application to the optimization of microresonators for surface sensing

From the expression of the effective index variation induced in a surface sensing experiment, the formal expressions of polarization-dependent microresonator sensitivities in surface sensing can be derived. However, we

[22] the transverse plane is the plane perpendicular to the direction of propagation z

will see that depending on the exact application, different expressions must be considered. The application of surface sensing to label-free biosensing is studied specifically, and important conclusions are drawn.

4.5.1 General expressions of the microresonator sensitivities

Simplifying hypothesis

At this stage, we formulate the hypothesis that the second term can be neglected as compared to the first term. In other words, we consider that for small local variations of the refractive index, we can neglect the indirect effect[23] of those variations as compared to their direct effects on the effective index.

Simplified expression for the variation of effective index

In concentration sensing, the perturbation $\delta n(x, y)$ related to the measurand is identically zero everywhere except in the cladding region, therefore, δN_{eff} can be simply expressed as:

$$\delta N_{eff} = \frac{1}{P_{Tot}} \cdot \iint\limits_{cladding} \delta n(x, y) \cdot p_{z,0}(x, y)\, dS \tag{5.73}$$

General, polarization-dependent expressions of microresonator sensitivities

From this expression, we can derive relations for the sensitivity of the microresonator in surface detection, according to the polarization of the guide mode:

$$\begin{cases} S_{res,TE}^{(SD)} = \dfrac{\lambda_{TE}}{N_{eff,TE}} \left(\dfrac{dN_{eff}^{(TE)}}{dC_m^{(X)}} \right)_{(SD)} \\ S_{res,TE}^{(SD)} = \dfrac{\lambda_{TM}}{N_{eff,TM}} \left(\dfrac{dN_{eff}^{(TM)}}{dC_m^{(X)}} \right)_{(SD)} \end{cases} \tag{5.74}$$

[23] the variation of the effective index due to a variation of the distribution p_z is an indirect effect of the local variation of refractive index

Integral forms of the microresonator sensitivities

Using expressions derived in the previous section, we finally obtain:

$$\begin{cases} S_{res,TE}^{(SD)} = \dfrac{\lambda_{TE}}{N_{eff}^{(TE)}\, f'(n_W)} \zeta^{(TE)} \\ S_{res,TM}^{(SD)} = \dfrac{\lambda_{TM}}{N_{eff}^{(TM)}\, f'(n_W)} \zeta^{(TM)} \end{cases} \tag{5.75}$$

where the polarization-dependent ζ parameters are expressed in integral form as:

$$\begin{cases} \zeta^{(TE)} = \dfrac{1}{P_{Tot}} \cdot \displaystyle\iint_{cladding} B(M) \cdot A_X^{(TE)}(M) \cdot p_{z,0}^{(TE)}(M)\, dS \\ \zeta^{(TM)} = \dfrac{1}{P_{Tot}} \cdot \displaystyle\iint_{cladding} B(M) \cdot A_X^{(TM)}(M) \cdot p_{z,0}^{(TM)}(M)\, dS \end{cases} \tag{5.76}$$

4.5.2 Discussion on the evaluation of the sensitivities

The above expressions give the sensitivities of the microresonator to the concentration in analyte in the case of surface sensing. In the evaluation of these sensitivities, the difficulties are related to surface integrals ζ.

Evaluation of the power flow density

For a given mode of the microresonator, $p_{z,0}$ can be easily determined from the calculations of the fields $\vec{E}$ and $\vec{H}$, using Eq.(5.67). This requires the use of a numerical method to solve TE and TM guided modes.

Evaluation of the distributions of molar refractivities

The molar refractivities $A_X^{(TE)}$ and $A_X^{(TM)}$ may be more difficult to evaluate, for several reasons. As discussed before, values of molar refractivities for numerous chemical and biological species can be found in the literature [77]. However, these values are usually determined near 589 nm, and in homogeneous solutions where molecular orientation is random. An issue is then to evaluate molar refractivities for molecular assemblies with specific orientation, and near 1550 nm.

Evaluation of the binding function

The binding function B describes the spatial distribution of analyte molecules in the transverse plane as function of the initial concentration of the solution containing the analyte. More specifically, the binding function describes the equilibrium of the chemical reaction occurring at the surface of the microresonator, responsible for the binding of analyte molecules. In the following, a simplified form of the binding function will be used to provide simplified expressions of the parameters under study.

4.5.3 Discussion on the role of the ζ parameters

Short analysis of microresonator sensitivities

In the microresonator sensitivities expressed in Eq.(5.75), the fractions before $\zeta^{(TE,TM)}$ appear to have limited roles. Indeed, $f'(n_w)$ is given as a known function of the the refractive index of water n_W[24]. As for the effective indices and resonant wavelengths, they are not liable to vary on large scales.

Consequently, optimization of the microresonator sensitivities dominantly relies on the optimization of $\zeta^{(TE)}$ and $\zeta^{(TM)}$.

4.5.4 Optimization of the ζ parameters

In order to optimize these integrals, it appears that the maximum of power flow density must coincide with presence of analyte molecules. This is a fairly simple analysis.

Separation of the cladding region

For further development, we can assume that surface-bound analyte molecules can be found, in the transverse plane, in a limited section (Σ_S) whose extent depends on the typical size of the molecules. We can then define the section (Σ_H) as the complementary section of the cladding, where

[24]The refractive index of water n_W can be replaced, for generality's sake, by a refractive index n_B of the buffer solution which contains the analyte molecules.

analyte molecules are homogeneously distributed. The cladding separation is illustrated in Fig. 5.9.

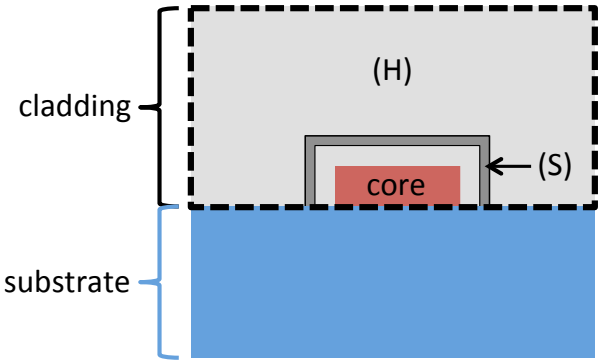

Figure 5.9: Separation of the section of the cladding into two complementary regions (H) and (S). A general case, where analyte molecules are not necessarily in contact with the core, is presented.

With these definitions, the integrals $\zeta^{(TE,TM)}$ can be written as:

$$\zeta^{(TE,TM)} = \zeta_S^{(TE,TM)} + \zeta_H^{(TE,TM)} \tag{5.77}$$

The parameters $\zeta_H^{(TE,TM)}$ and $\zeta_S^{(TE,TM)}$, using the linearity of the surface integral, can be expressed as:

$$\begin{cases} \zeta_H^{(TE,TM)} = \dfrac{1}{P_{Tot}} \cdot \displaystyle\iint_{(\Sigma_H)} \left[B \cdot A_X^{(TE,TM)} \cdot p_{z,0}^{(TE,TM)} \right] (M)\, dS \\ \zeta_S^{(TE,TM)} = \dfrac{1}{P_{Tot}} \cdot \displaystyle\iint_{(\Sigma_S)} \left[B \cdot A_X^{(TE,TM)} \cdot p_{z,0}^{(TE,TM)} \right] (M)\, dS \end{cases} \tag{5.78}$$

Surface and homogeneous parameters ζ

It is important to point out here that ζ_S functions relate to the interaction between the surface and the analyte, while ζ_H functions characterize the homogeneous detection of the analyte molecules that did not bind to the surface. Therefore, the optimization differs depending on the exact application of the sensor.

Optimization for analyte quantification in a simple solution

If the application is to quantify the analyte in a solution containing only analyte and water[25] molecules, then both surface and homogeneous contributions to the sensitivity can be taken into account. Consequently, the $\zeta^{(TE,TM)}$ parameters must be optimized.

Optimization for applications related to label-free biosensing

If the application is related to label-free biosensing, the sensitivity of the detection only relates to specific binding events at the surface of the microresonator, and homogeneous detection of the analyte molecules in the section (Σ_H) can be viewed as a perturbation of the signal. In such applications, $\zeta^{(TE,TM)}$ would be a wrong parameter to optimize.

Signal-to-noise ratio

Generally-speaking, a signal-to-noise ratio compares a signal level to the fluctuations of this signal. In label-free biosensing, the basic detection signal relates to the binding events between analyte molecules and biorecognition molecules[26]. Therefore, the detection of analyte molecules in the bulk of the solution constitutes a perturbation of the detection signal.

We can express an equivalent η of a signal-to-noise ratio for surface detection in label-free sensing:

$$\eta = \frac{\zeta_S}{\zeta_H} \tag{5.79}$$

Discussion

The parameter η is very important. Indeed, if a modification of the waveguide geometry had for effect to increase both parameters ζ_S and ζ_H in the same manner, corresponding to a constant value of η, then the gain in terms of label-free detection would be zero. From this analysis, it is clear

[25] or more generally buffer

[26] biorecognition molecules are previously bound to the microresonator surface during surface functionalization

that for label-free biosensing, the sensitivity of the surface detection by the microresonator is as important as the signal-to-noise ratio η.

In the following, these two polarization-dependent parameters, expressed specifically for label-free biosensing and related applications, will be written as:

$$\begin{cases} S_{res}^{(LFS)} = \dfrac{\lambda}{N_{eff}\, f'(n_W)} \zeta_S \\ \eta_{res}^{(LFS)} = \dfrac{\zeta_S}{\zeta_H} \end{cases} \tag{5.80}$$

4.5.5 Optimization of the sensing properties of a microresonator for label-free biosensing and related applications

General expression of η

The parameter $\eta_{res}^{(LFS)}$ can be expressed, for a given polarization, as:

$$\eta_{res}^{(LFS)} = \frac{\iint\limits_{(\Sigma_S)} \left[B \cdot A_X \cdot p_{z,0}\right](M)\, dS}{\iint\limits_{(\Sigma_H)} \left[B \cdot A_X \cdot p_{z,0}\right](M)\, dS} \tag{5.81}$$

Assumption on the binding function

For a further development of η, we assume that the binding function can be defined as:

$$\begin{cases} B(M) = B_S\,, & M \in (\Sigma_S) \\ B(M) = B_H\,, & M \in (\Sigma_H) \end{cases} \tag{5.82}$$

where B_S and B_H are constants.

Assumptions on the molar refractivities distributions in region (H)

In addition, in the (Σ_H) section, as analyte molecules are homogeneously distributed, we can assume that the molar refractivity A_X is uniformly distributed in (Σ_H). Also A_X can be considered independent from the polarization state since in (Σ_H), the orientation of analyte molecules is

random. Consequently, in this region, $A_X(M)$ can be replaced by a uniform and polarization-independent value A_{X_0}, corresponding to the typical value that can be found in the literature for the molar refractivity of X.

Assumptions on the molar refractivities distributions in region (S)

Similarly, in the (Σ_S) section, from the homogeneity of the distribution B, we can assume that the values of $A_X^{(TE)}$ and $A_X^{(TM)}$ are uniform in this region. However, they cannot be considered as equal in a general case. To overcome this difficulty, we can develop a simplified model for the molar refractivity.

In this model, we assume that A_{X_0} can be related to $A_X^{(TE)}$ and $A_X^{(TM)}$ by the expressions:

$$\begin{cases} A_{X_0} = A_X^{(TE)} + A_X^{(TM)} \\ A_X^{(TE)} = \xi_{TE} \cdot A_{X_0} \\ A_X^{(TM)} = \xi_{TM} \cdot A_{X_0} \end{cases} \tag{5.83}$$

where ξ_{TE} and ξ_{TM} can be viewed as ratios of the molar refractivity that relates to TE and TM, polarization state, respectively. They verify $\xi_{TE} + \xi_{TM} = 1$.

Simplified polarization-dependent expressions of η

Using all the assumptions above, it is possible to write η_{res} as:

$$\eta_{res}^{(LFS)} = \frac{B_S\, A_X}{B_H\, A_{X_0}} \cdot \frac{\iint\limits_{(\Sigma_S)} p_{z,0}(M)\, dS}{\iint\limits_{(\Sigma_H)} p_{z,0}(M)\, dS} \tag{5.84}$$

From this expression, we can rewrite η_{res} as:

$$\eta_{res}^{(SD)} = \eta_B \cdot \eta_{Pol} \cdot \eta_{Pow} \tag{5.85}$$

where:

- $\eta_B = \frac{B_S}{B_H}$ is a characteristic of the surface binding reaction

- $\eta_{Pol} = \frac{A_X}{A_{X_0}} = \xi$ relates to molecular orientation on the surface
- $\eta_{Pow} = \frac{P_z(\Sigma_S)}{P_z(\Sigma_H)}$ is the ratio between the power flows in each section

Final expressions for the microresonator sensitivities in label-free sensing and related applications

Using the same assumptions, we can also derive simplified expressions for the microresonator sensitivities. Overall we have:

$$\begin{cases} S_{res}^{(TE,TM)} = \dfrac{B_S\, A_{X_0}}{P_{Tot}\, f'(n_W)} \cdot \left[\dfrac{\lambda\, \xi\, P_z(\Sigma_S)}{N_{eff}}\right]^{(TE,TM)} \\ \\ \eta_{res}^{(TE,TM)} = \eta_B \cdot \eta_{Pol}^{(TE,TM)} \cdot \eta_{Pow}^{(TE,TM)} \end{cases} \tag{5.86}$$

Discussion

Such simplified expressions are the results of many assumptions. However, they provide several insights on the mechanisms at work in surface sensing, and more specifically for label-free biosensing, using optical microresonators.

A first result is the formalization of an intuitive idea, according to which surface sensing is more sensitive when analyte molecules are interacting with a relatively more important part of the guided power. This is expressed by the ratio between $P_z(\Sigma_S)$, the optical power flow in the region (S) where binding events occur, and the total optical power flow related to the guided mode P_{Tot}.

A second result is the formalization of the polarization-dependence of the microresonator sensitivity. More specifically, χ parameters can be used, in the model, to account for a specific orientation of the molecules bound on the surface. Consequently, this model denotes the importance of a device ability to simultaneously analyse both polarizations, in order to measure conformational changes of bound molecules. Moreover, the model allows a quantification of these effects, related to polarization-dependent properties of the microresonator.

A third result provides a major insight about another intuitive idea, *ie* that a larger evanescent field would provide more sensitive label-free detection. More specifically, this idea would lead to build waveguides maximizing the ratio of optical power flows Γ_{clad}, in a way to maximize $P_z(\Sigma_S)$ as compared to P_{Tot}. In the following, we study this specific effect.

Optimization of η_{Pow} from waveguide design

The aim here is to build a very simple model to verify whether, for surface sensing, it is better to have a maximal amount of the total power in the evanescent field. For this purpose, we consider a slab waveguide where the confinement direction is x. In the transverse plane (x, y), the cladding occupies the semi-infinite space from x = 0 to x = $+\infty$.

We assume that the evolution of the power flow density in the direction of propagation z can be written, in the cladding region, as:

$$p_z(x) = p_z(0) \cdot \exp(-x/L_D)\,,\; x \in [0,\, +\infty] \tag{5.87}$$

In this expression, $p_z(0)$ is the power flow density at the interface, and L_D is the typical decay length of the evanescent field in the cladding. In the following, we also assume that all bound molecules are located in a region (Σ_S) defined as the space between x = x_0 and x = x_1, as illustrated in Fig. 5.10. In this model, the typical extent of the molecule in the confinement direction is $L_M = x_1 - x_0$. The region (Σ_S) is defined as the difference between the cladding region (Σ_{clad}) and (Σ_S).

Since we consider a slab waveguide, the system can be considered as invariant in the y direction. However, for dimensional purposes, we introduce an extent L_∞ of the waveguide in the y direction. Therefore, we can express the optical power flows $P(\Sigma_S)$ and $P(\Sigma_H)$ as:

$$\begin{cases} P(\Sigma_S) = \displaystyle\iint_{(\Sigma_S)} p_z(M)\, dS = L_\infty \int_{x_0}^{x_1} p_z(x)\, dx \\ P(\Sigma_H) = P(\Sigma_{clad}) - P(\Sigma_S) \end{cases} \tag{5.88}$$

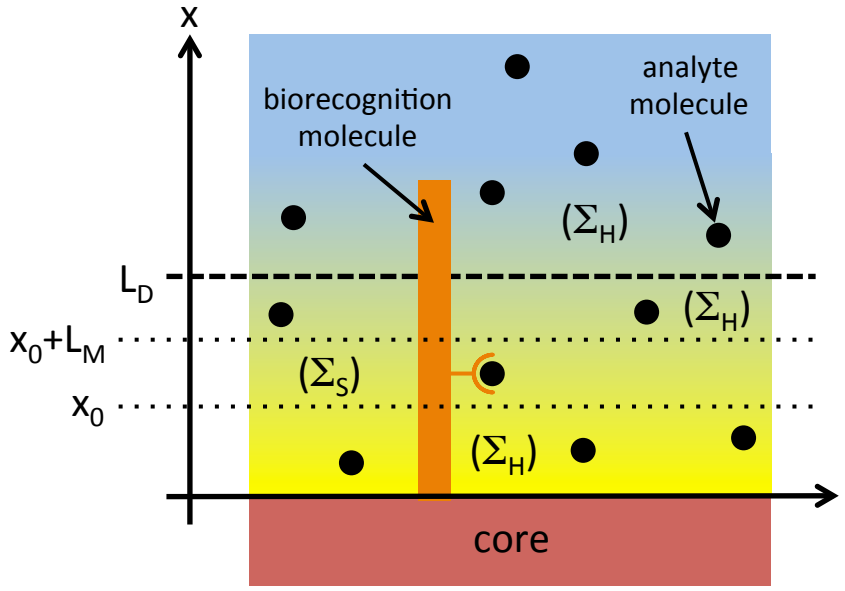

Figure 5.10: Separation of the section of the cladding into two complementary regions (H) and (S). A general case, where analyte molecules are not necessarily in contact with the core, is presented.

After replacing $p_z(x)$ by its expression, and integration on the specified regions, we obtain expressions of the power flows:

$$\begin{cases} P(\Sigma_{clad}) = L_\infty \, L_D \cdot p_z(0) = P_0 \\ P(\Sigma_S) = P_0 \exp(-x_0/L_D) \left[1 - exp(-L_M/L_D)\right] \\ P(\Sigma_H) = P(\Sigma_{clad}) - P(\Sigma_S) \end{cases} \tag{5.89}$$

The ratio η_{Pow} can then be simply expressed as:

$$\eta_{pow} = \frac{P(\Sigma_S)}{P(\Sigma_H)} = \frac{1}{\frac{P(\Sigma_S)}{P(\Sigma_{clad})} - 1} \tag{5.90}$$

From the expressions of the power flows, we can express the ratio η_{Pow} as a function of two normalized parameters: the normalized molecular position $x^\star = x_0/L_D$ and the normalized molecular dimension $L^\star = L_M/L_D$, as:

$$\eta_{pow}(x^\star, L^\star) = \left[\frac{\exp(x^\star)}{1 - \exp(-L^\star)} - 1\right]^{-1} \tag{5.91}$$

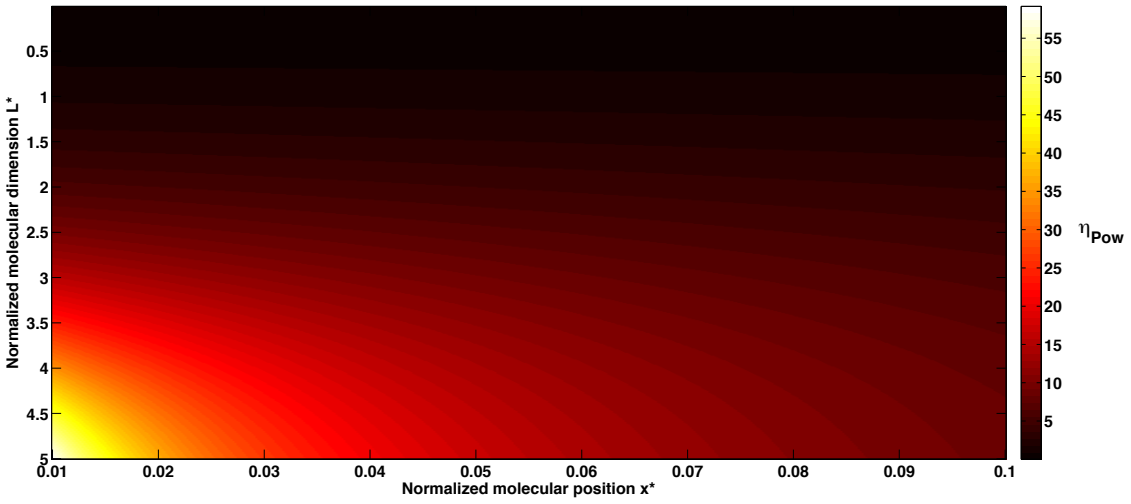

Figure 5.11: Ratio of power flows η_{Pow} as function of the normalized molecular position $x^\star = x_0/L_D$ and the normalized molecular dimension $L^\star = L_M/L_D$

In Fig. 5.11, values of $\eta_{Pow}(x^\star, L^\star)$ for $x^\star \in [0.01, 0.1]$ and $L^\star \in [0.01, 5]$ are plotted. The limited range for $x^\star$ comes from the fact that for all values of $L^\star$, η_{Pow} exponentially tends to zero for larger $x^\star$ values. On the contrary, for a given value of $x^\star$, η_{Pow} exponentially increases for larger values of $L^\star$.

It is important to point out here that, since (Σ_S) and (Σ_H) are complementary surfaces, the ratio η_{Pow} can, in theory, vary between 0 and $+\infty$.

Importance of the distance between core/cladding interface and binding events

The first important observation that can be made from the graph in Fig. 5.11 is the strong decay of η_{Pow}, hence of the signal-to-noise ratio $\eta^{(LFS)}$, when the normalized molecular position $x^\star$ increases. This means that the ability to detect binding events is maximal when they occur at the core/cladding interface. This ability decreases exponentially as binding events occur further and further away from this interface.

From this analysis, we understand that if binding events occur at a significant distance x_0 from the core/cladding interface, which can be the case in label-free biosensing with large biorecognition entities on the surface, the typical extent L_D of the evanescent field in the cladding region must be

designed to be large compared to x_0. However, increasing L_D will directly result in a decrease of the normalized molecular dimension $L^\star$, hence, *in fine* in the decrease of $\eta^{(LFS)}$. The major conclusion here is that, for a given molecule, with a given typical extent L_M, and a given position x_0 of binding events, an optimal value of the typical decay length of the evanescent field exist.

Optimal extent of the evanescent field for label-free biosensing

In order to look for the optimal decay length L_D, we set $u = 1/L_D$. Consequently, for a given value of parameters x_0 and L_M, the power ratio η_{Pow} can be expressed as a function of u:

$$\eta_{pow}(u) = \frac{1 - \exp(-uL_M)}{\exp(ux_0) + \exp(-uL_M) - 1} = \frac{\text{Num}(u)}{\text{Den}(u)} \tag{5.92}$$

The function $\eta_{pow}(u)$ is maximal when its first-order derivative is equal to zero, hence when the following equation is verified:

$$\text{Num}'(u) \cdot \text{Den}(u) = \text{Num}(u) \cdot \text{Den}'(u) \tag{5.93}$$

After expansion of this equation, and removal of the common factor $\exp(ux_0)$, it can be rewritten as:

$$L_M \exp(-uL_M) = x_0 - x_0 \exp(-uL_M) \tag{5.94}$$

By regrouping the terms dependent on u, and applying the logarithm function on either side, we finally obtain:

$$uL_M = \ln\left(1 + \frac{L_M}{x_0}\right) \tag{5.95}$$

From the above equation, describing the value of u that maximizes $\eta_{Pow}(u)$, we derive a very general expression of an optimal decay length $L_D^{(Opt)}$ of the evanescent field for label-free biosensing:

$$L_D^{(Opt)} = \frac{L_M}{\ln\left(1 + L_M/x_0\right)} \tag{5.96}$$

where L_M is the typical dimension of the analyte molecules in the direction of evanescent field decay, and x_0 is the typical distance between the core/cladding interface and the position of the binding site (cf. Fig. 5.10).

Consequently, the highest value of $\eta_{Pow}^{(Opt)}$ for a given label-free biosensing configuration (x_0, L_M) is given by:

$$\eta_{Pow}^{(Opt)} = \eta_{Pow}\left(L_D^{(Opt)}\right) \tag{5.97}$$

In Fig. 5.12 are plotted as functions of the parameters x_0 and L_M (a) the optimal decay length of the evanescent field $L_D^{(Opt)}$ and (b) the optimal value of the power ratio in $\eta_{Pow}^{(Opt)}$ in dB units. The values of the x_0 and L_M parameters vary between 0.01 nm and 200 nm.

In the plot on top of Fig. 5.12, it is clearly visible that higher values of both x_0 and L_M parameters require higher value of typical decay length L_D of the evanescent field. On the opposite, when x_0 tends to zero, which is the case where analyte molecules are directly adsorbed on the surface, then the decay length must be small, all the more so for the detection of small molecules.

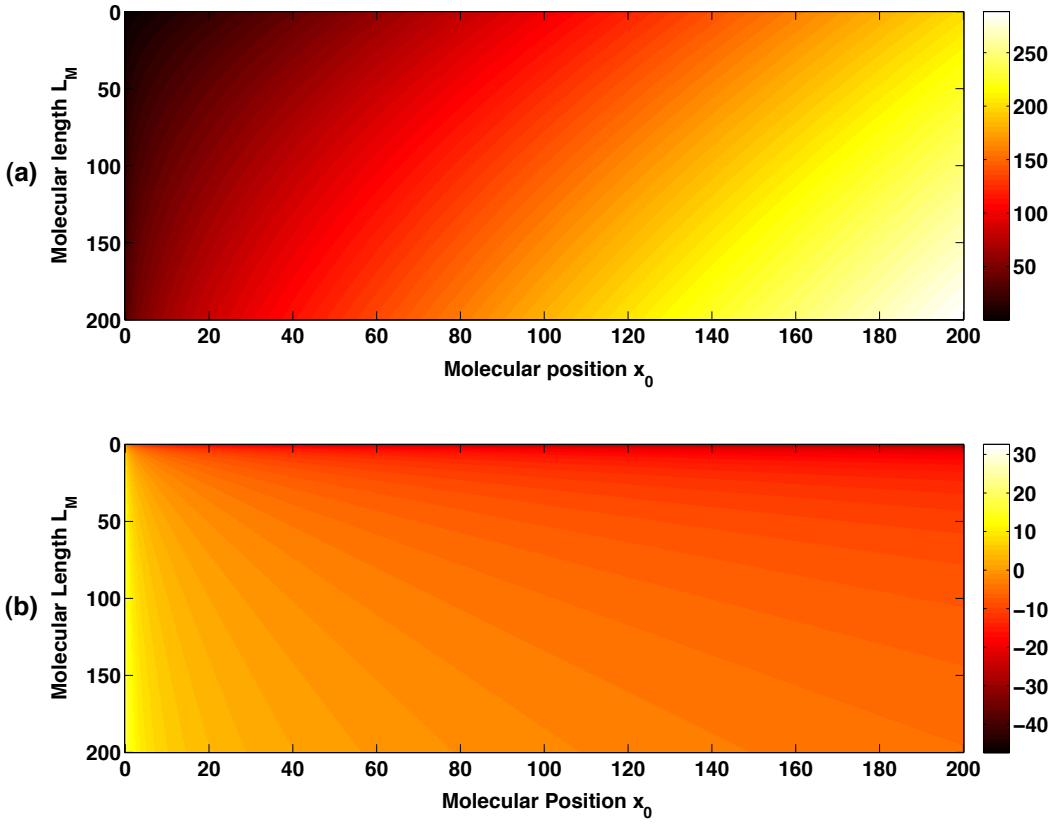

Figure 5.12: As functions of the parameters x_0 and L_M are plotted (a) the optimal decay length of the evanescent field $L_D^{(Opt)}$ and (b) the optimal value of the power ratio $\eta_{Pow}^{(Opt)}$ in dBs. All lengths are in nm.

In the bottom plot of Fig. 5.12, it first appears clearly that the power ratio η_{Pow} can be modulated on several decades. Therefore, this ratio appears as a key parameter for the optimization of optical label-free biosensors. Secondly, it also very clear that the highest signal-to-noise ratios $\eta^{(LFS)}$ will be achieved in situations where the binding occurs as closely to the waveguide interface as possible.

It is important to point out that, in this model, it is assumed that the presence of the biorecognition molecules at the cladding/core interface does not modify significantly the power flow density near the interface. This would the case for limited surface densities of the biorecognition molecules. On the opposite, if the biorecognition molecules form a dense and thick molecular film around the waveguide, it is expected that significant variations of the local power flow density will occur. However, it can be considered, in such a case, that the formed biorecognition film is an extension of the core of the waveguide. Therefore, the typical decay length of the evanescent field can be defined from the cladding/biorecognition film interface. Also, as a consequence, the typical distance x_0 could be equal to zero, since in the case of dense biorecognition films, binding will occur at the top of the biorecognition molecules.

Chapter 6

Instrumentation of evanescent field sensors

Introduction

This is an introduction ...

1 Microfluidics integration

1.1 Introduction

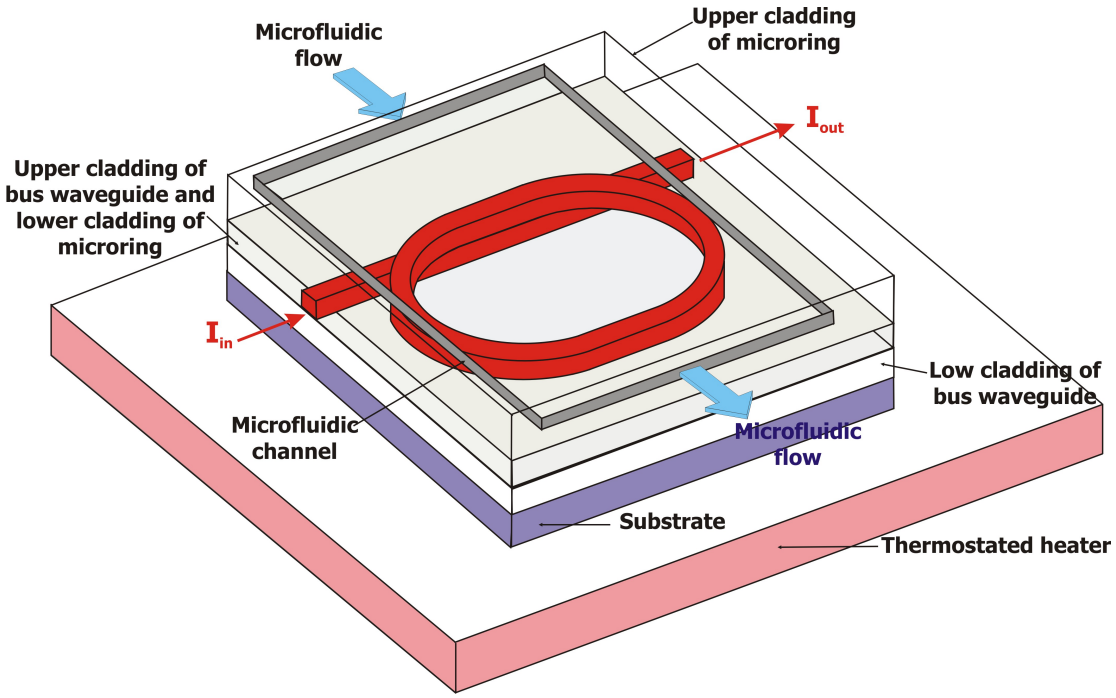

Figure 6.1: Fabrication steps for PDMS microfluidic caps

1.2 Materials for microfluidic circuits

Several materials can be used to build microfluidic caps and tubes, with various properties according to transparency, hardness, resistance to chemical agents. More specifically, for label-free biosensing, some materials are to known to be "biocompatible" while others are not. For instance, many large biomolecules are known to stick to Teflon, making device operation impossible in such cases.

In the scope of this dissertation, PDMS was selected for fabrication of the microfluidic caps, and Teflon was typically used for tubes. Other commonly used materials are also presented.

1.2.1 PDMS

Polydimethylsiloxane (PDMS), or dimethicone, is a mineral-organic polymer (containing carbon and silicon atoms) of the solxane family. It is widely used polymer material for the fabrication of microfluidic chips. For the fabrication of such devices a liquid solution of PDMS mixed with a cross-linking agent is poured into a microstructured mould and heated to catalyse its polymerization. The pattern thus imprinted in the PDMS constitute microfluidics channels once the PDMS cap is fixed to a substrate.

After polymerization, PDMS becomes a hydrophobic elastomer. However, oxydation of the material, using oxygen plasma for instance, produces silanol terminations (SiOH) on its surface, temporarily turning the exposed PDMS surface hydrophilic for short durations.

PDMS is generally considered as a biocompatible material, however with some restrictions [78, 79]. In [80], resistance of PDMS to numerous chemical agents were tested. Overall, PDMS is not sensitive to exposure to most common chemicals, and can thus be used in a wide variety of applications. In addition, PDMS microfluidic channels can be passivated for further resistance to chemicals, if necessary. This can be achieved by coating the channel with Cytop, or other fluoropolymers.

1.2.2 Other materials

Typical materials also used for the fabrication of microfluidic devices are Teflon, PTFE and PEEK. Specifically, PEEK and PTFE are known to show to posses excellent biocompatible properties [81]. However, as rigid materials, their integration on an optical chip can be more difficult than with PDMS microfluidic devices.

1.3 Fabrication of PDMS microfluidic caps

The microfluidic cap is obtained after polymerization of PDMS resin in contact with a mould. The mould, typically made out of SU-8 photoresin, defines the 3D geometry of the microfluidic channel. The basic fabrication steps of the PDMS microrfluidic caps are presented in Fig. 6.2.

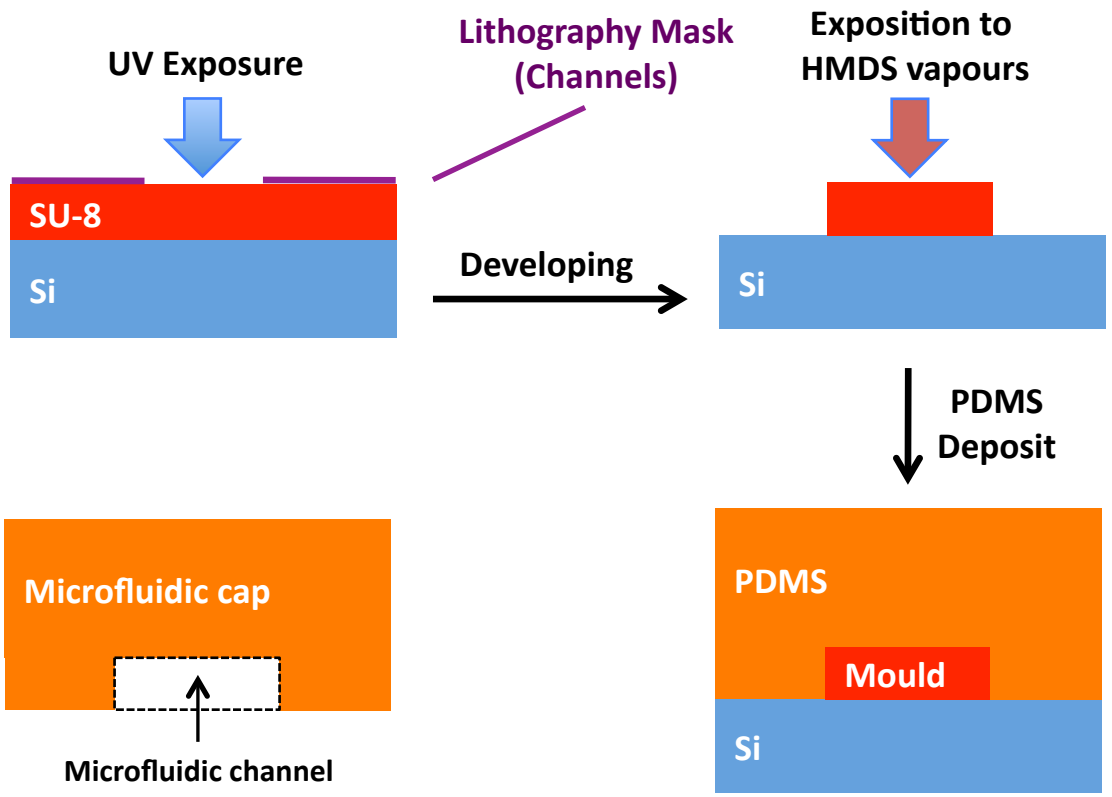

Figure 6.2: Fabrication steps for PDMS microfluidic caps

1.3.1 Fabrication of the SU-8 mould

Fabrication steps

In the fabrication process, the first task is to build the SU-8 mould. Similarly to what was described in Chap.3, a SU-8 thin film is deposited by spin-coating on a silicon substrate[1] with a two-inch diameter. Then, after post-exposure baking (PEB) steps, the resist is exposed to UV, through a photomask, to obtain a pattern directly matching the geometry of the microfluidic channel. After post-exposure-bake, the film is developed, and finally hard-baked.

It has to be pointed out that, since the dimensions of the microfluidic channels are large compared to those of the optical microresonators, the lateral resolution of the UV-lithography is, comparatively, not important.

[1] covered by a native layer of silica, not represented in Fig. 6.2

As a consequence, the lithography mask can be of a much lower resolution that the ones used for the optical devices. Such lithography masks can be simply obtained, for instance, via fine printing[2] on a transparency film.

Once processed, the thickness of the SU-8 film will defined the height H, in the vertical direction, of the microfluidic channel. As outlined before, as the height gets smaller, the pressure build-up due to viscosity forces gets higher, which can result in leakage[3]. For the experiments performed in the scope of this dissertation, the minimal channel height was 20 μm, and the maximal height was 150 μm.

Deposit of high-viscosity resists

In order to achieve such SU-8 film thickness, three commercial SU-8 solutions from Microchem were used: SU8-2025, SU8-2050, SU8-2075 and SU8-2100, with viscosities ranging from to 4,500 cSt to 45,000 cSt[4]. This has to be compared with the viscosity of SU8-2002 solution, used for optical devices, equal to 7.5 cSt. Because of their much higher viscosities, handling of the SU8-solutions for the fabrication of microfluidic moulds is very different from that described in Chap.3.

A first consequence of the high viscosity is the impossibility to filter the resist solutions, or to use syringes to apply the photoresist on the substrate for spin-coating. Because of this, the resist solution must be transferred first to a Becher, from which the resist is poured on the substrate. A useful precaution is to remove all air bubbles that are liable to be trapped in the resist. Typically, this is achieved by letting the solution rest for a while. However, because of the high viscosity, this would take a very long time. It is then preferable to remove air bubbles by placing first the Becher into an ultrasonic bath for 5 minutes, then into a vacuum chamber for 30 minutes.

When the resist is poured on the substrate from the Becher, the high viscosity tends to create a continuous, cylindrical, solution flow between

[2] 1200 dpi, typically

[3] at specific points of the channel, or by complete lost of adhesion of the PDMS to its substrate

[4] viscosity coefficients expressed as kinematic viscosities in centi-Stokes (cSt); $1\text{cSt} = 10^{-2}\,\text{cm}^2/s$

both. The best method found for pouring was to make sure that the flow of resist solution is approximately constant, and arrives on the centre of the substrate, a point from which the liquid slowly moves to wet the outer regions of the wafer.

Another important consequence of the large viscosities is the very high edge beads obtained by spin-coating of the resist. With two-inches wafer, edge beads, due to to border effects, can occur on more than half of the wafer surface, resulting in microfluidic channels with large height variation from input to output. An expensive solution to this problem is to use three-inches wafer instead. A more cost-efficient solution consist in using the spin-coater at maximal rotation speed, around 4000 rpm, in order to minimize the height of the edge bead.

Typical fabrication process

A typical process to achieve a 80 μm-thick SU-8 mould is as follow:

- Approximately 3 mL of SU8-2100 is desposited on a two-inches silicon wafer and spin-coated at 4000 rpm for 60 seconds.
- After spin-coating, the resist is post-baked, for 5 minutes at 65°C then 20 minutes at 95°C, after which it is let to cool down for several minutes.
- For such thickness, the typical exposure energy must be approximately 240 mJ/cm^2. With an MJB3 mask aligner equipped with a lamp achieving an exposure power of 8.5 mW/cm^2, the duration of the exposure must be approximately 30 seconds. For long exposure durations, it is sometimes necessary to perform two of three exposures instead of one, in order to limit heating of the resist during the procedure.
- After exposure, the film is post-baked, typically for 5 minutes at 65°C then 10 minutes at 95°C. It is particularly important to let the film cool down after this post-exposure-bake.
- The film is then developed in a developer bath, typically for 10 minutes. For such long development times, it is necessary to agitate

the developer solution periodically to renew it near the SU-8 patterns. Right after development, the SU-8 patterns are rinsed with isopropanol, and dried with a gentle nitrogen gaz flow.

- As final step, the wafer is put in an oven at 180°C for two hours for hard-baking.

1.3.2 Fabrication of the PDMS cap

First, the PDMS solution is prepared for its future reticulation over the SU-8 mould. Inside a Becher, a 10 mL volume of PDMS solution is mixed with 1 mL of cross-linking solution. While mixing, bubbles are produced in the solution, and have to be removed. This is achieved by placing the bech in an ultrasonic bath for 5 minutes, then in a vacuum chamber for 30 minutes.

Meanwhile, the mould has to be prepared so that after cross-linking, the PDMS may be removed from the mould. Since both PDMS are naturally hydrophobic, the mould is put in contact with hexamethyldisilazane (HMDS) vapours to form an ultra-thin hydrophilic film on the whole surface of the mould.

Once both PDMS solution solution and mould are prepared, the PDMS is poured on the mould in one movement. After which, the whole is put in an oven at 75°C for two hours.

1.4 Chip integration

The chip integration consist in fixing the microfluidic cap on the optical device. This step is particularly important to reduce the possibilities of solution leakage from the microfluidic channel due to excessive pressure build-ups. For the integration of PDMS microfluidic caps with vertically-coupled microring resonators such as described in previous chapters, different technical solutions where tested.

1.4.1 Adhesion by surface activation

A strong adhesion can be obtained between a silica substrate and a PDMS microfluidic cap by oxygen-plasma-assisted surface activation. Before putting

the substrate and microfluidic cap in contact, both of their surfaces are exposed to a low power oxygen plasma for few minutes, which is usually enough to achieve very high adhesion strength.

This technique was tested to integrate PDMS caps with optical devices. In all instances, the adhesion strength obtained between Cytop, as substrate material for the microresonator, and the PDMS was very weak and thus non suitable for operation. This adhesion failure is probably due to the fact that the lower oxygen-plasma is not enough to activate the surface of Cytop. As a consequence, a solution may be to use an equipment such as the RIE apparatus described in Chap.3. However, the activation would be then accompanied with etching of the Cytop layer, which is of course not suitable after the fabrication process is complete.

1.4.2 Adhesion by application of a curable optical adhesive

Optical adhesives are typically used for fixing various optical parts, such as optical lenses, together. These adhesives have the particularity to be highly transparent for visible and infrared radiations. Also, typically, they can be cured from both UV exposure or baking.

Such an optical adhesive, in form of liquid solution, can be applied to the surface of the microfluidic cap that needs to be fixed to the Cytop substrate. Then, when the adhesive is cured, typically in a UV oven, a strong adhesion is obtained between the PDMS cap and the Cytop substrate.

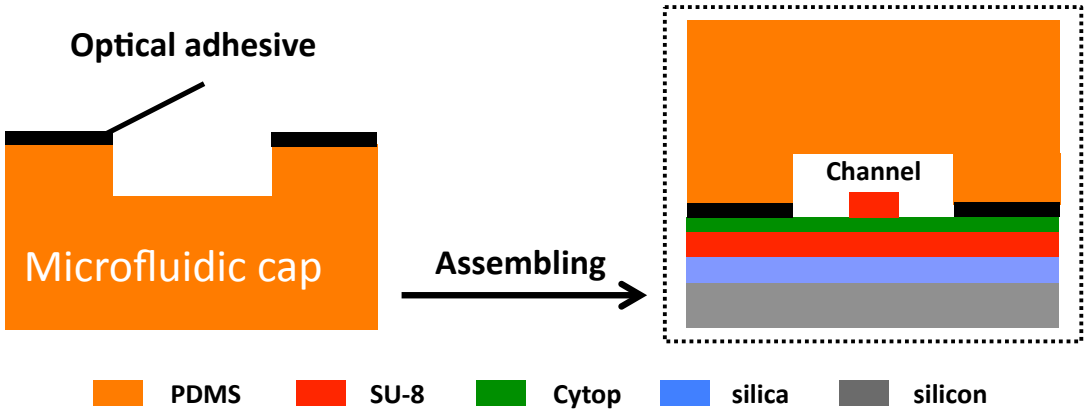

Figure 6.3: Use of an optical adhesive for microfluidic integration.

The application of the adhesive to specific regions of the microfluidic cap can be difficult. Overall, a stamping method provided the best results. First, a thin film of the adhesive is prepared on a substrate, a glass microscope slide for instance. This can be achieved by spin-coating. Then, the microfluidic cap is placed on the adhesive-covered substrate. At this point, the adhesive wets the surface of the PDMS to be fixed to Cytop and, ideally, does not enter the microfluidic channel. After this delicate step, the PDMS cap is recovered, and subsequently positioned on the optical device. Once the channel(s) is (are) properly aligned with optical microresonators, the adhesive can be finally cured. A typical result of such adhesion scheme is presented in Fig. 6.4.

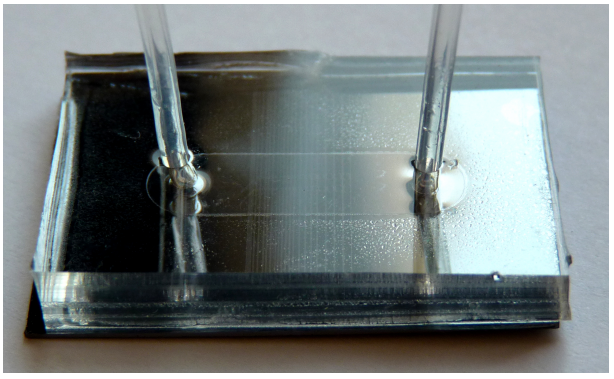

Figure 6.4: Optofluidic cell obtained after microfluidic integration of the optical chip.

The first adhesive used was NOA73 (for Norland Optical Adhesive 73). Once cured, this adhesive achieved high adhesion strength. This was tested by applying high microfluidic flowrates to the microfluidic channel. However, the problem with NOA73 is its high refractive index, similar to that of SU-8. As the Cytop layer above bus SU-8 waveguides is only a few hundreds of nm thick, light propagating in the bus waveguides can easily couple to the adhesive layer.

Because of this leakage of optical power, the overall transmission from laser source to photodetector was greatly diminished. In addition, light, first coupled from the waveguide to the adhesive layer, was subsequently propagating in the PDMS cap, and finally scattered at the output sidewall. This scattering made alignment procedures extremely difficult, and sometimes simply impossible.

A technical solution was found by replacing NOA73 by NOA74. The latter adhesive, with a refractive index of approximately 1.46, was meant to reduce optical leakage from the bus waveguides, and significant improvements where obtained in terms of overall transmission from source to photodetector. However, the main limitation of such adhesive is its low adhesion strength, and an increased difficulty of the stamping procedure due to lower viscosity of the liquid solution. More specifically, while the adhesion strength is sufficient with NOA64 to reproduce optofluidic cells such as presented in Fig. 6.4, attempts to reduce the adhesion surface, mainly to integrate more microfluidic channels on one chip, where unsuccessful. For further integration, short of finding a perfect adhesive, with strong adhesion strength with Cytop, and low refractive index, another technical solution had to be found.

1.4.3 Adhesion by mechanical pressure

A non permanent-adhesion can be achieved between the PDMS cap and the optical chip by applying pressure on top of the PDMS cap. More specifically pressure has to be applied only in regions of the PDMS where there are no microfluidic channels. This can be achieved with a patterned metallic plate maintained in contact against the top of the PDMS cap.

This adhesion technique proved to be very efficient. Indeed, leakage of

liquid from the microfluidic channel thus maintained was never observed.

A second advantage of this technique is related to the fact that the adhesion is not permanent. Hence, according to the requirements of the specific experiments, optical chip or PDMS cap or both can be easily replaced.

1.5 Microfluidic circuit

1.5.1 Introduction

As outlined in Chap.1, evanescent-wave sensors are relative sensors. In other terms, no information can be retrieved if the output of the device, for instance the resonant wavelength of an optical microresonator, is constant. However, information on a measurand can be retrieved by comparing the output induced by a stimulus to a reference situation.

In optofluidic evanescent-wave sensors, the stimulus, whatever its nature, is carried by a liquid solution flown over a sensitive optical element. In the scope of this dissertation, the sensitive element is the microring resonator, and the liquid solution acts as the cladding material of the microring waveguide. In such sensors, information on the analyte solution, carrying the measurand, can only be retrieved if the corresponding output of the sensor is compared to the output induced by a reference solution.

1.5.2 Configuration of the flow for sensing

In homogeneous or surface concentration sensing, the analyte solution is obtained by dissolution or dilution of analyte molecules into a buffer solution, designed to maintain a constant pH. In such cases, using the pure buffer solution as reference solution for the detection is the most convenient.

In Fig. 6.5 is presented a typical arrangement of buffer and analyte solutions, where the latter is sandwiched in between the buffer solution.

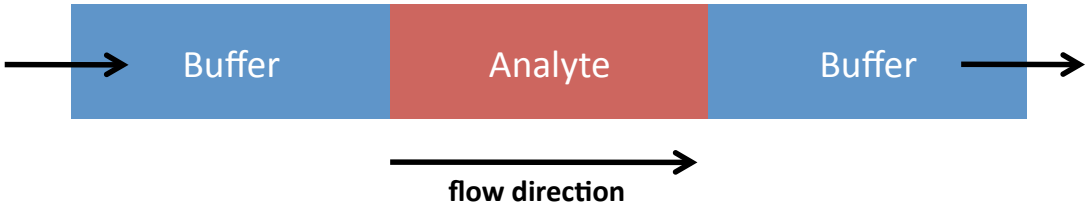

Figure 6.5: Typical configuration of the flow for analyte detection in homogeneous and surface sensing.

1.5.3 Key aspects of the microfluidic circuit

Such configuration of the microfluidic flow is obtained by the combination of various apparatus, forming overall a microfluidic circuit. Herefater are presented the key aspects to take into account for the design of such circuit:

- The volume of the analyte solution, as well as the time it takes for this solution to flow over the microresonator, need to be adaptable to specific experiments.
- When switching the solution from buffer to analyte, and from analyte to buffer, a risk is to introduce air bubbles in the microfluidic circuit. According to Murphy's law, such air bubbles have a strong probability to fix on the surface of the microresonator during sensing experiments, making any analyte detection impossible. Avoiding the formation of air bubbles in the microfluidic circuit, and the ability to flush them out if they occur, is thus a major concern in the design of the circuit.
- Switching the buffer solution should be fast and easy. This implies that the circuit should be designed to minimize the volumes of buffer necessary to perform measurements.
- From the moment where the analyte solution is put in contact with the buffer, the time necessary to bring the analyte to the microresonator should be minimal. Indeed, analyte molecules are free to diffuse to the buffer solution, thus creating variations of the analyte concentrations near the liquid interfaces. This result in an inhomogeneous concentration profile of the solution flown over the microresonator, as pictured

in Fig. 6.6. Effect of the diffusion is typically more important at the back interface. This is simply because the back interface takes more time to reach the resonator than the front interface.

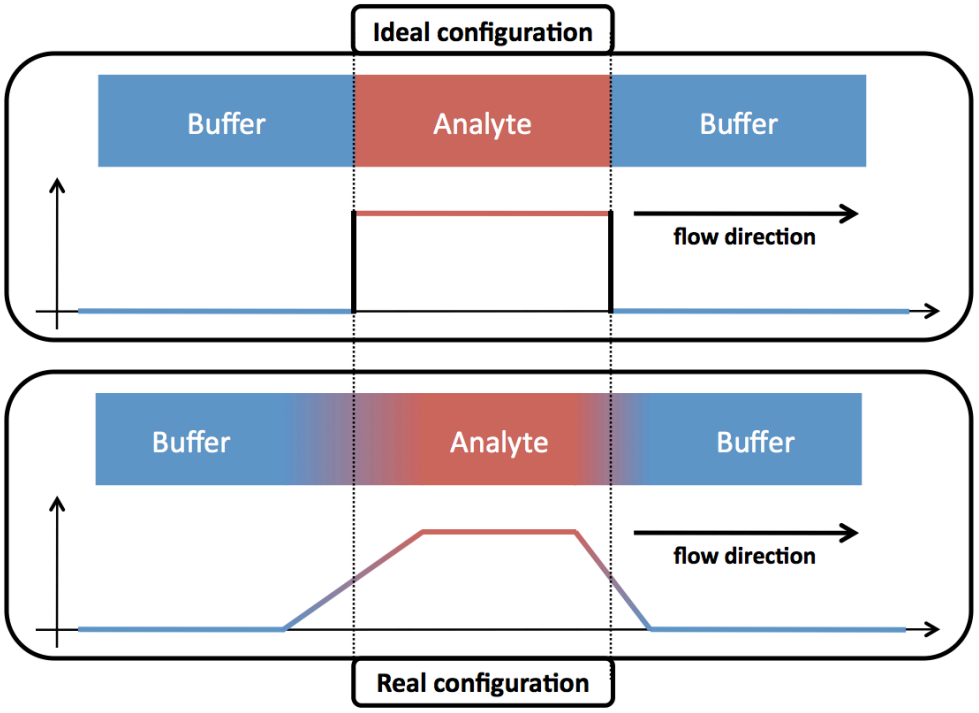

Figure 6.6: Ideal and real flow configurations obtained in optofluidic detection when the analyte reaches the microresonator. Plots correspond to the local values of concentration in analyte molecules.

1.5.4 Diffusion and dead volume/time

Diffusion, resulting in inhomogeneity of the buffer and analyte solutions concentrations, affects the properties of the optofluidic sensor. The volume of liquid corresponding to the typical extent of the diffusion effect is usually referred to as *dead volume* V_{diff}. Indeed, while the volume V_{diff} flows over the microresonator, the analyte concentration is not stationary, and does not correspond to the nominal concentration of the analyte solution. This induces a temporary bias, on the study of surface binding kinetics for instance. The corresponding *dead time* τ_{diff}, during which the detection is biased due to diffusion, can be expressed as:

$$\tau_{\text{diff}} = \frac{V_{\text{diff}}}{v_{\text{flow}}} = \frac{2\Sigma_{\text{chan}} L_{\text{diff}}}{v_{\text{flow}}} \tag{6.1}$$

where v_{flow} is the flowrate and L_{diff} is the typical extent of the diffusion in the direction of the flow. The factor 2 stands for the fact that when analyte molecules diffuse in the buffer solution on a typical length L_{diff}, a region with the same extent, on the other side of the interface, is depleted in analyte molecules (cf. Fig. 6.6).

The typical diffusion length L_{diff} is related to the duration of the contact τ_C by $L_{\text{diff}} = \sqrt{D\tau_C}$ where D is the diffusion coefficient of analyte molecules in the buffer solution. If we defined L_C as the typical channel length, corresponding to τ_C for which buffer and analyte are in contact, L_{diff} can be expressed as:

$$L_{\text{diff}} = \sqrt{\frac{D\Sigma_{\text{chan}}L_C}{v_{\text{flow}}}} \tag{6.2}$$

Consequently, the dead time due to diffusion can be expressed as:

$$\tau_{\text{diff}} = 2\left(\frac{\Sigma_{\text{chan}}}{v_{\text{flow}}}\right)^{3/2} \cdot \sqrt{DL_C} \tag{6.3}$$

In this expression, the two dominant parameters are the section Σ_{chan} and the flowrate v_{flow}. it appears that τ_{diff} can be optimized by minimizing the sections of the channels, and maximizing the flowrate. however, these two parameters, because of the viscosity effects, are not completely independent. A high flowrate applied to a small section of channel will require high pressure applied to the liquid by the pump, and can easily result in leakage. High flowrate also result in a smaller time during which the stationary state can be observed. This expression that reducing the length L_C is effective, despite the fact that τ_{diff} is only proportional to the square root of L_C.

1.5.5 Influence of the microresonator

The diffusion phenomenon is not the only contribution to the dead volume. Indeed, because of the extent of the microresonator L_{res} in the direction of the flow, a stationary detection is only achieved after the liquid interface flows over the whole optical cavity. Accordingly, the corresponding dead time τ_{res} can be expressed as:

$$\tau_{\text{res}} = \frac{\Sigma_{\text{chan}}L_{\text{res}}}{v_{\text{flow}}} \tag{6.4}$$

The dead time τ_{com} combining both effects is simply the sum of both contributions:

$$\begin{cases} \tau_{\text{com}} = \tau_{\text{res}} + \tau_{\text{diff}} \\ \tau_{\text{com}} = \dfrac{\Sigma_{\text{chan}}}{v_{\text{flow}}} \cdot L_{\text{res}} + 2\left(\dfrac{\Sigma_{\text{chan}}}{v_{\text{flow}}}\right)^{3/2} \cdot \sqrt{DL_C} \end{cases} \tag{6.5}$$

1.5.6 Circuit architecture

In order to obtain the flow configuration described earlier, depicted in Fig. 6.5, a key element is the injection valve. A typical injection valve has six connection ports, which can be used as inputs or outputs. Such a valve, as presented in Fig. 6.7, has two positions A and B. By switching the injection from one position to another, both buffer/analyte and analyte/buffer liquid interfaces are obtained. This is described in the diagram in Fig. 6.8.

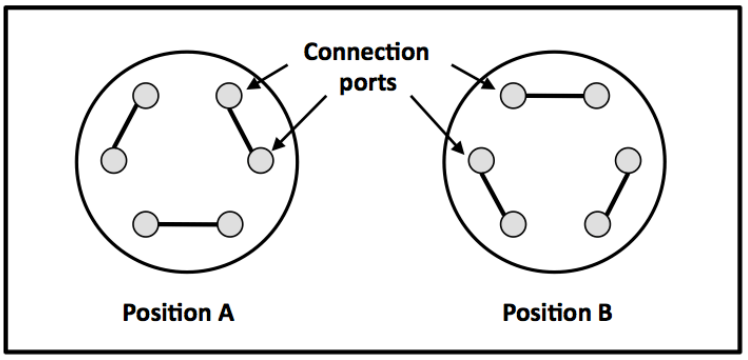

Figure 6.7: Positions of a six-port injection valve.

During a the *loading* phase, a syringe pump (P) continuously pulls the buffer solution from the buffer reservoir (A), via the optofluidic cell. Meanwhile, the analyte solution can be injected from a syringe into a reservoir (R), typically referred as *injection loop*[5].

[5]The analyte reservoir is usually fabricated using a given length of microfluidic tube, the length and the section of the tube defining the total volume of the *loop*.

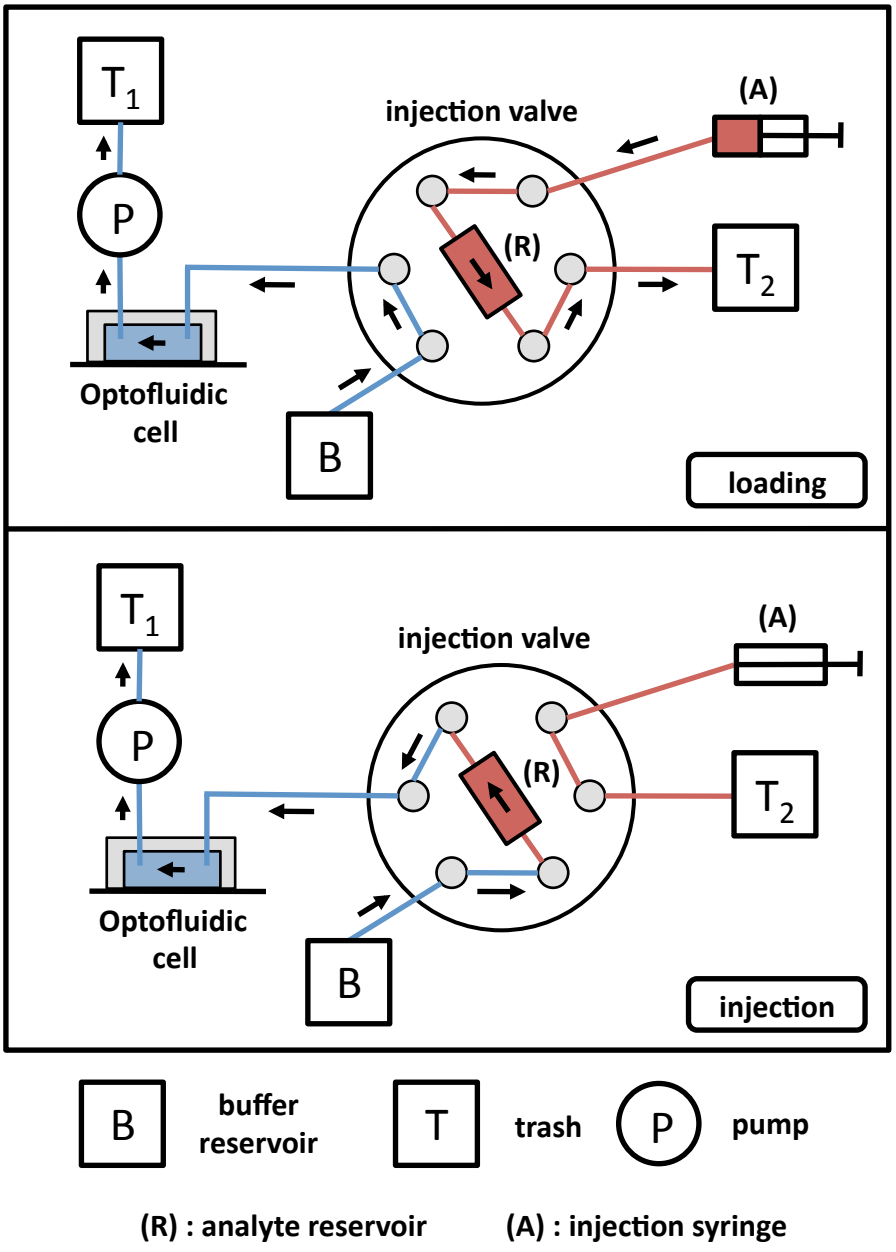

Figure 6.8: Architecture of the microfluidic circuit and flow pattern for both *loading* and *injection* positions of the valve.

Once the injection loop is filled, the excess of analyte solution is directed to a container, commonly referred to as *trash*. the container placed after the pump, where all liquid going through the cell is collected, is also referred to as *trash*.

After the loading phase is complete, the valve is switched to perform the injection of the analyte. In this position of the valve, as described in

Fig. 6.8, by pulling the buffer solution, the pump also pulls the analyte solution from the injection loop, and directs it towards the optofluidic cell. Once the nominal concentration of analyte solution reaches the microring, and enough observation time has elapsed, the valve can be switched back to its initial *loading position*. Also, the operator can wait for the analyte reservoir to be empty before switching the valve. In both cases the result is approximately the same, although switching the valve before the reservoir is empty reduces the typical diffusion length of the second analyte/buffer interface (cf. Fig. 6.6).

2 Optoelectronic instrumentation

2.1 Introduction

As discussed in Chap.1, the instrumentation of the sensor is, regarding the performances of the measuring instrument, as important as the sensor itself. It was also outlined that, depending on the detection scheme, key performances of the sensor could greatly vary. For instance, when comparing the fixed-wavelength method (FWM) to the wavelength-scanning method (WSM), it appeared clearly that FWM optimized the time response of the measuring instrument. Typically, the WSM takes more time to provide measurement values, but offers a much wider measurement span. Regarding the LOD, or resolution, the comparison was difficult. However WSM appeared as more convenient for real-time systematic error correction due to variations of the resonances linewidth. More importantly, for multiplexed detection and/or dual-polarization detection, WSM appeared to be more convenient.

As a matter of fact, since an instrumentation build for WSM can be used, without any modification, for the FWM detection scheme, the design of the instrument was aimed primarily at the application of the WSM detection scheme.

2.2 Optoelectronic architecture

The optoelectronic architecture designed for the instrumentation of the sensor is very similar to that described in Chap.4 for the optical characterization of microring resonators. As can be seen in Fig. 6.9, a slight modifica-

tion of the optical setup was performed in order to measure transmission intensities from both TE and TM polarizations simultaneously. Advantages of such dual-polarization detection scheme will be detailed in Chap.7, focused on results of sensing experiments.

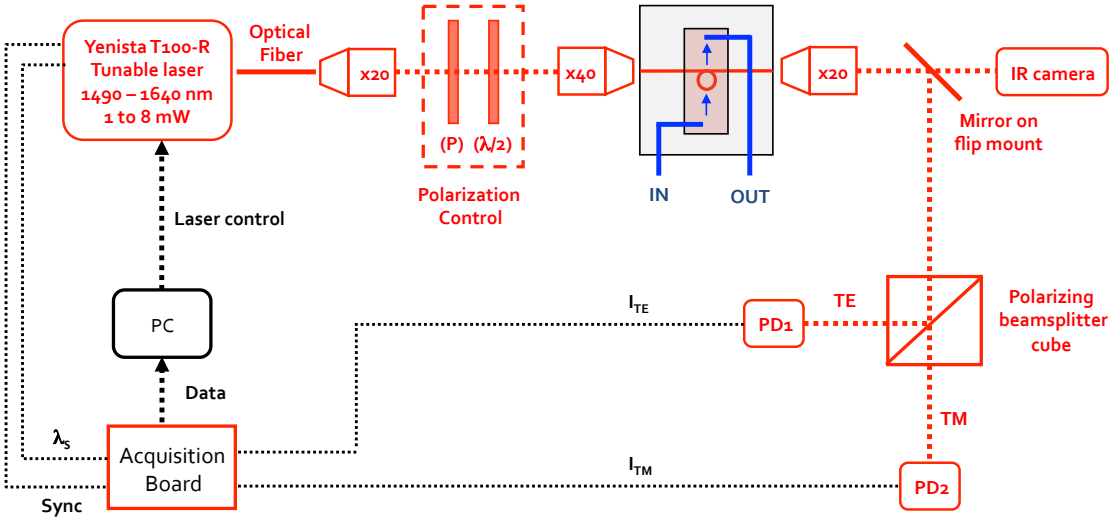

Figure 6.9: Diagram for the optoelectronic instrumentation.

Alignment procedures described in Chap.4 for the optimization of the measurement signal still apply for this modified configuration. However, the introduction of the polarizing beamsplitter cube slightly increases the difficulty of align all optical elements correctly.

It is important to point out here that such instrumentation is only suited for expert operators, since many techniques have to be mastered to achieve and maintain decent conditions for device operations. In order to build a more user-friendly instrument, liable to be used by operators from various backgrounds, an all-fiber configuration would be more suitable.

Whatever the optical setup, the computer program controlling the laser source, the signal acquisition, and delivering pertinent information on the detection to the operator should be the same.

2.3 Control program

The full program, using the NI/LabWindows programming environment for portability and rapidity of execution, was continuously developed during the duration of the PhD, and counts in its final versions several thousand lines of code.

A basic principal applied during the development of the program was to make further modifications and upgrades easy. For this purpose, many functions were written to perform simple tasks, to be used in more complex parent functions. Overall, three groups of basic functions were written:

- Functions to control the various tunable laser sources used in experiments via GPIB link.

- Functions to configure and control the data acquisition board, and also to apply treatments to the acquired data.

- Functions to answer to user related events from the user interface, and to display and record acquired data.

Typical user interface is presented in Fig. 6.10 during an experiment of homogeneous sensing of glucose in aqueous solution. Before the detection, the microresonator is quickly characterized, similarly to what was described in Chap.4. The main purpose of this characterization is to determine, in the whole tuning range of the source, which resonance has the best properties for sensing. This is mainly related to the maximal intensity slope (MIS). From data acquired during characterization, a suitable wavelength range for the two polarization states (TE in red, TM in green) can be selected, corresponding to optimal values of MIS for both. In these ranges, the best resonances for TE and TM modes are selected. For each polarization, a threshold is set, as described in Chap.1, as reference level for measurements of resonant wavelength shifts.

After configuration, programmed is switched to a continuous acquisition mode, where positions of the resonances selected during configuration are continuously evaluated, recorded and plotted.

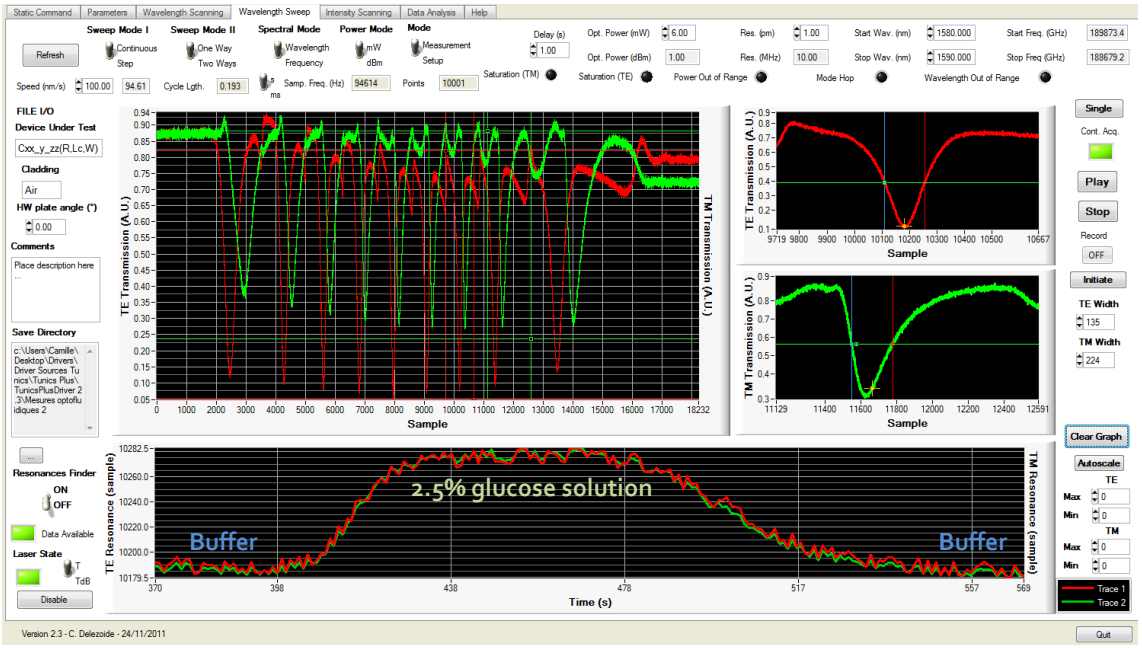

Figure 6.10: Snapshot of the user interface of the control program during an experiment of homogeneous glucose sensing.

3 Temperature control

3.1 Introduction

With large thermo-optic coefficients[6] and, large thermal expansion coefficients[7], polymer materials, and thus polymeric microring resonators, are very sensitive to temperature. In SU-8 microresonators, most of the sensitivity of the effective index to temperature comes from the temperature dependence of bulk SU-8 refractive index.

A direct effect of temperature variations near the microresonator are resonant wavelength shifts unrelated to the measurand (unless the measurand is temperature). Therefore, such variations have to be treated as perturbations. In addition, temperature can potentially modify the microresonator sensitivity to the measurand. Therefore, even the use of a second microresonator as reference cannot strictly cancel perturbation effects of

[6]Thermo-optic coefficients describe the variation of the refractive index of a material according to temperature

[7]Thermal expansion coefficients describe the relative variation of the size of the dimension of a material according to temperature

temperature variations. For all purposes, and efficient strategy to control the temperature during sensing experiments is necessary.

In the development of our prototype of measuring instrument, various strategies have been tested to control thermal effects, specifically to reduce effects of room temperature variations.

3.2 Thermal control from the substrate

The first strategy was already introduced in Chap.4 (§2.1.4), and consist in controlling the average temperature of the microresonator from underneath, by control of the temperature of its silicon substrate.

3.2.1 Description

As presented in Fig. 6.11, sensor and actuators to achieve temperature control are embedded in the mount of the optofluidic cell, where they can react very efficiently to local temperature variations.

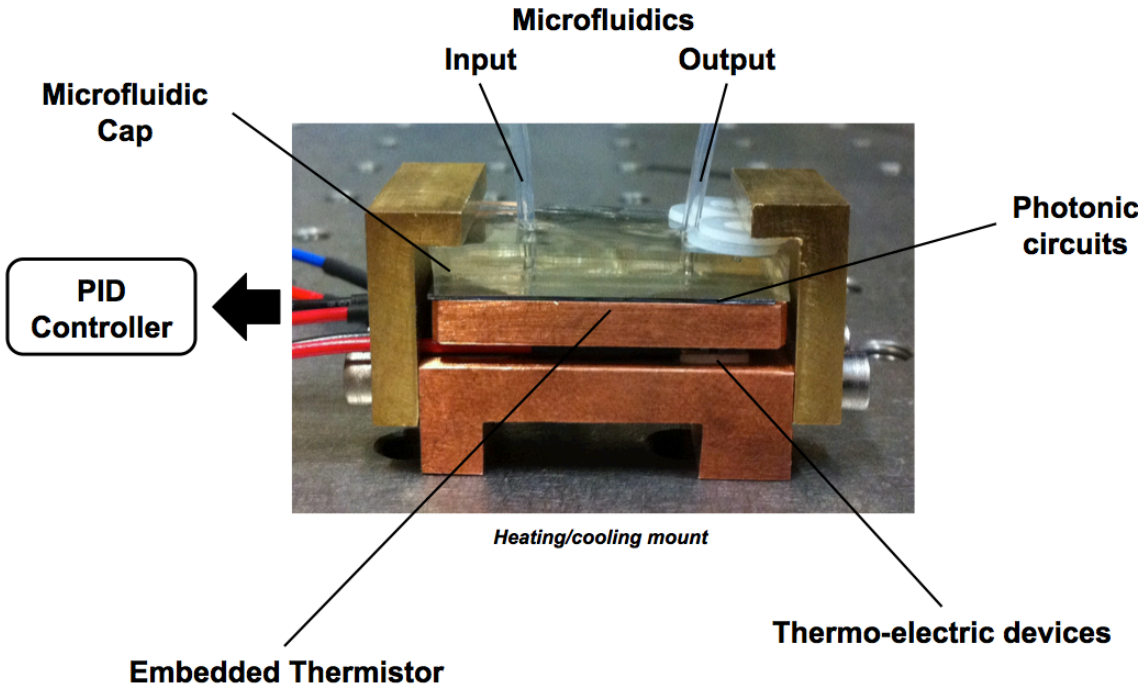

Figure 6.11: Temperature-controlled mount for thermal control of the microresonator.

3.2.2 Thermal equilibrium of the microresonator

Because of heat transfer mechanisms taking place between the microresonator and its environment, the temperature of the microresonator results from a balance between the temperature of the cladding, and that of the substrate.

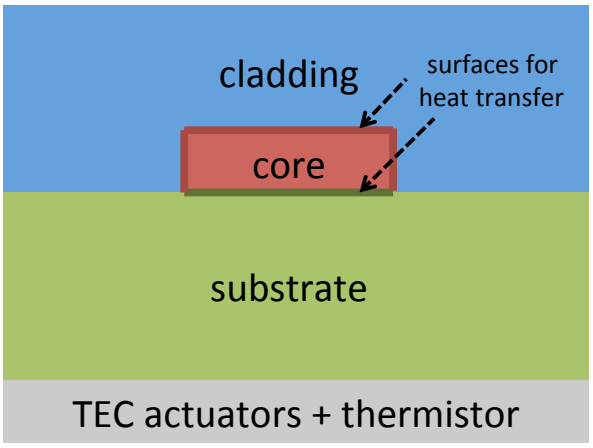

Figure 6.12: Transverse view of the microring waveguide with substrate thermal control. Substrate is composed of Cytop, silica, silicon and copper, from top to bottom. The core material is typically SU-8

Basic model for diffusive heat transfers

This situation can be roughly modelled in a static situation using the thermal effusivity E of a material, defined as:

$$E = \sqrt{k\rho c_p} \tag{6.6}$$

where k is thermal conductivity, ρ is the density and c_p is the specific heat capacity of the material.

For two semi-infinite bodies initially at temperature T_1 and T_2 are brought in perfect thermal contact, the temperature T_m at the contact surface will be expressed as the average temperature weighted by the materials effusivities:

$$T_m = \frac{E_1 T_1 + E_2 T_2}{E_1 + E_2} \tag{6.7}$$

Despite the fact that this model probably cannot quantitatively be applied to micrometric structures such as optical microring resonators, it can

provide some qualitative insight on the strategies to regulate the temperature of the core, which is where most of microresonator sensitivity comes from.

Case of a waveguide with air as cladding

For instance, it is safe to consider that the effusivity of air is much smaller than that of the silicon substrate. Therefore, variations of room temperature, provided that the temperature of the silicon is controlled, will affect the temperature of the waveguide core only slightly.

Case of a waveguide with static aqueous solution as cladding

However, rectangular waveguides, constituting the microresonator, have a more important contact surface with the cladding than with the substrate. Therefore, if cladding and substrate materials have similar effusivities, the average temperature of the rectangular core is liable to depend more on the temperature of the substrate than that of the cladding. If the cladding is liquid water, with much larger effusivisity than air, temperature of the microresonator will be more dependent on room temperature. However, since the water is considered immobile, the control of the temperature of the substrate will result in an progressive homogenisation of the temperatures of all materials. Therefore, provided that time is not an issue, the thermal regulation from the substrate will also be efficient in this configuration, although more time is required to reach an equilibrium.

Case of a waveguide with moving aqueous solution as cladding

The situation is different if the liquid cladding is moving, which is the case in our setup. This motion has two detrimental effects on the ability of the thermal regulation of the substrate to regulate the temperature of the waveguide core. First, the heat transfer between the core and the cladding becomes more efficient, since a convective heat transfer is added to the previously described conductive heat transfer. Secondly, because the fluid in contact with the microresonator is constantly renewed, the temperature of the cladding can never stabilize to that of the substrate, and remains

roughly equal to room temperature. Therefore, in an optofluidic device, temperature control from the substrate is not sufficient to significantly reduce effects of room temperature variations.

3.3 Thermal control of buffer and analyte solutions

As outlined in the paragraphs above, in an optofluidic cell, temperature of the liquid cladding has a dominant role on the temperature of the microresonator waveguide. Therefore, thermal control of buffer and analyte solutions, in addition to the thermal control of the substrate, would provide a reduced sensitivity of the microresonator to room temperature variations.

In order to test this idea, containers of analyte and buffer solution were placed in a thermostated bath. It was quicky observed that such thermal regulation was worst than no regulation at all. Indeed, compared to room temperature variations, that may be of great amplitude over the day, but in the form of a constant drift, small variations of the temperature of the solutions occurred in the form of relatively fast oscillations. Such variations, even of moderate amplitudes in the signal, are much more difficult to correct than slow thermal drifts characteristic of room temperature variations.

This study made it clear that, if regulation of the room temperature itself is considered, such regulation should operate on very large time scales. Such principle was tested, instead of controlling the room temperature, by controlling the temperature in a limited enclosure containing the whole microfluidic circuit, thermally insulated from the rest of the room.

3.4 Thermal control of the microfluidic circuit

In a further development of the measuring instrument, an enclosure was build from thick PMMA walls around the microfluidic circuit to reduce effects of room temperature variations. The heating system, combining a thermal sensor, two resistive heaters and a controller, was designed to maintain the temperature inside the enclosure at temperatures slightly above maximal room temperature. In such a configuration, the temperature variation inside the enclosure is monotonous, and typically limited in amplitude to 0.1°C per hour. In addition, fast perturbations of the temperature

inside the enclosure, with moderate amplitudes, are averaged by the cooling/heating action of the temperature-controlled mount.

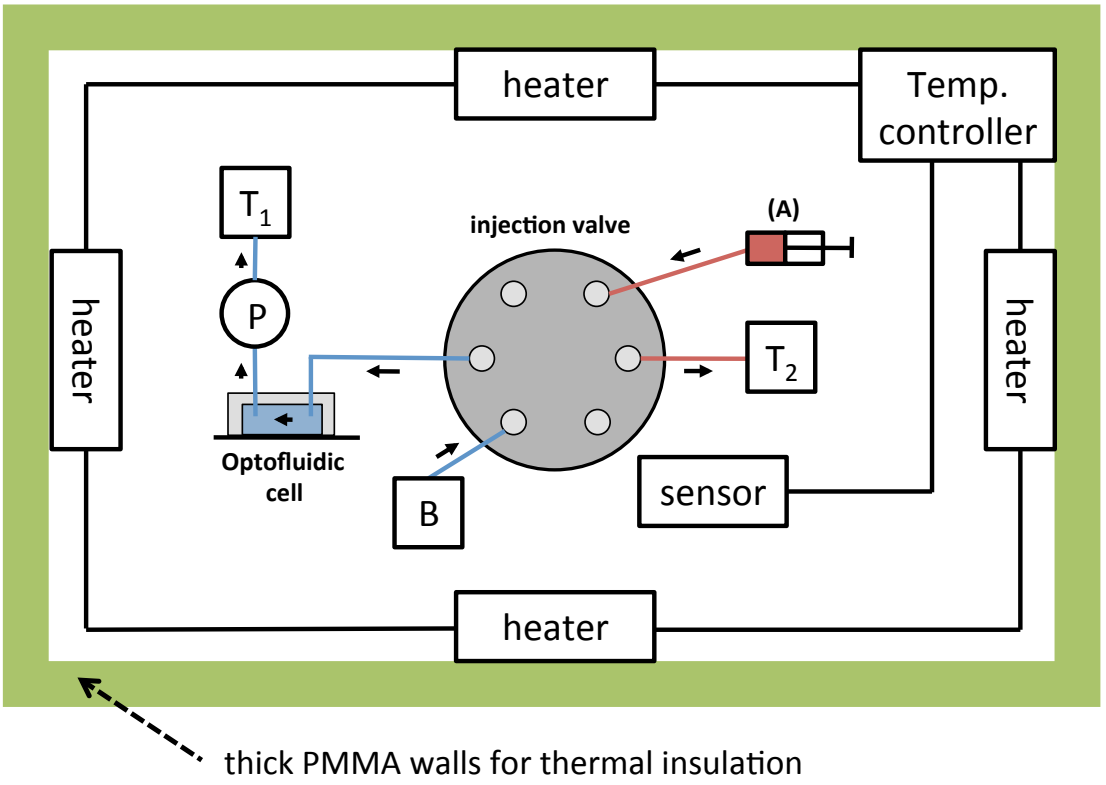

Figure 6.13: Schematic view of the microfluidic circuit with unilateral temperature control

Conclusion

This is a conclusion

Chapter 7

Sensing experiments

Introduction

In this chapter, we present and discuss results from homogeneous and sensing experiments.

1 Homogeneous sensing experiments

1.1 Refractive index of glucose as function of the concentration

In this section, the aim is to determine the refractive index of an aqueous solution of glucose as function of the glucose concentration, for a wavelength centered on 1550 nm.

The main issue lies in the fact that values for glucose of the polarizability α, or the molar refractivity A, are not available in the literature, to the best of our knowledge. However, such properties can be deduced around the sodium D-line, at 589 nm, from tabulated values of the refractive indices of an aqueous solution of glucose as function of the concentration.

Values of refractive index at 589 nm

In Tab. 7.1 are gathered some selected measurement results of refractive indices for D-glucose solutions at 589 nm and 20°C. It is important to point out that from this tabulated data, it is visible that the glucose concentration in mol/L is not strictly proportional to the glucose mass percentage in solution.

(D-) Glucose mass (%)	**Concentration (mol/L)**	**Index @ 589 nm (RIU)**
0	0	1.3330
0.5	0.028	1.3337
1	0.056	1.3344
2	0.112	1.3358
3	0.168	1.3373
4	0.225	1.3387
5	0.282	1.3402
6	0.340	1.3417
7	0.398	1.3432
8	0.457	1.3447
9	0.516	1.3462
10	0.576	1.3477
20	1.199	1.3635
30	1.873	1.3805
40	2.603	1.3986
50	3.396	1.4181
60	4.261	1.4394

Table 7.1: Tabulated values of refractive index for an aqueous solution of D-glucose as function of the relative mass and the molar concentration.

Using the tabulated data presented in Tab. 7.1, the refractive index of glucose solution is plotted in Fig. 7.1 as function of the molar concentration, also as function of the mass (%).

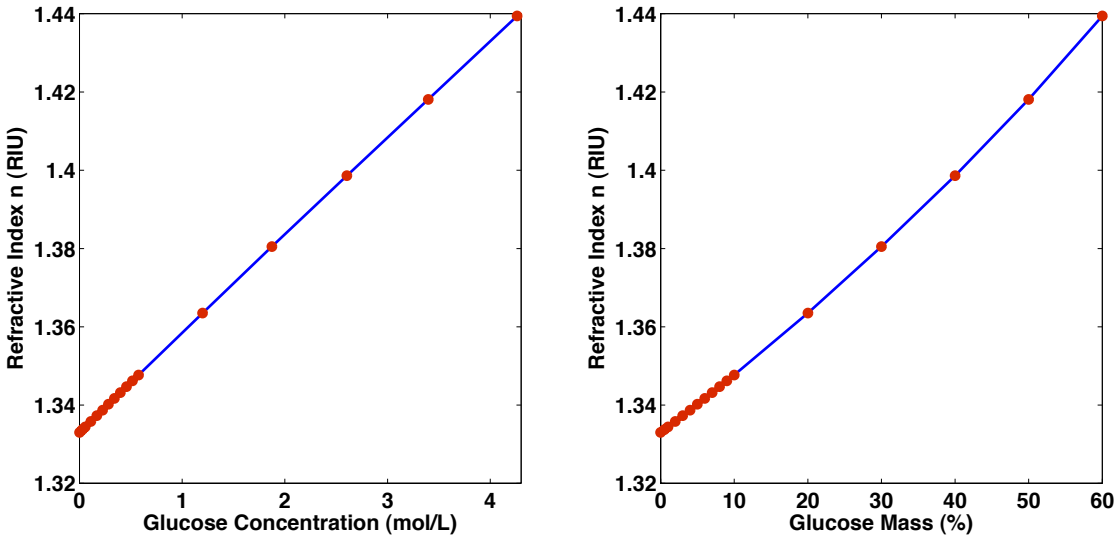

Figure 7.1: Refractive index of an aqueous solution of glucose as function of the glucose concentration (mol/L) and the relative glucose mass (%)

A direct comparison of both curves shows that a better linear behaviour is obtained by describing the refractive index as a function of the concentration, in mol/L.

Linearisation of the refractive index and sensitivity to glucose at 589 nm

In the following, since optofluidic sensors are first and foremost designed to measure low variations of RI, we focus on a limited range of glucose mass in solution, from 0 to 5 %, corresponding to concentrations from 0 to 282 mmol/L. In this range, a linear fit of the curve plotted in Fig. 7.1 gives the following expression for the refractive index $n(C)$:

$$n(C) = 1.3330 + 0.025535 \cdot C \tag{7.1}$$

The residual error of the linear fit is inferior to 5.10^{-5} RIU, which is the uncertainty on the index due to the limited resolution of the tabulated values. Therefore, it is not necessary to consider second-order corrections.

From this linear fit, the sensitivity of the refractive index to the glucose concentration can be evaluated. At 589 nm and 20°C, this sensitivity is:

$$S_{\text{Glu}}(589\,\text{nm}) = \left[2.55 \cdot 10^{-2} \pm 6 \cdot 10^{-4}\right] \text{ RIU}/(\text{mol}/L) \tag{7.2}$$

Sensitivity to glucose at 1550 nm

In Chap.5, a model based on Lorentz-lorenz formula was used to determine the sensitivity S_{Glu} of the homogeneous RI of an aqueous solution to a concentration $C[X]$ of analyte. According to this model, the sensitivity S_{Glu} can be written here as:

$$S_{\text{Glu}} = \frac{A_{\text{Glu}}}{f'(N_0)} \tag{7.3}$$

where A_{Glu} is the molar refractivity of glucose, and N_0 is the RI of pure water. The function f' is defined by:

$$f'(x) = \frac{6x}{(x^2+2)^2} \tag{7.4}$$

According to this model, the sensitivity $S_{\text{Glu}}(\lambda_1)$ at wavelength ${}_{\text{Glu}}\lambda_1$ can be expressed as:

$$S_{\text{Glu}}(\lambda_1) = \frac{A_{\text{Glu}}(\lambda_1)}{A_{\text{Glu}}(\lambda_2)} \cdot \frac{f'\left[N_0(\lambda_2)\right]}{f'\left[N_0(\lambda_1)\right]} \cdot S_{\text{Glu}}(\lambda_2) \tag{7.5}$$

In the literature [82], value of the RI of pure water for all wavelengths is only provided at 25°C. At this temperature, the RI at 589 nm is evaluated at 1.3324, and the RI at 1550 nm is evaluated at 1.3180. Therefore, we obtain:

$$\frac{f'\left[N_0(589)\right]}{f'\left[N_0(1550)\right]} \approx 0.991 \tag{7.6}$$

If we assume that the ratio $A_{\text{Glu}}(1550)/A_{\text{Glu}}(589)$ is in the same order of magnitude, then the correction applicable due to the change of wavelength is inferior to the uncertainty due to the limited resolution of the tabulated data. With this consideration we can consider than at 1550 nm and 20°C, the sensitivity can be evaluated as:

$$S_{\text{Glu}}(1550\,\text{nm}) = \left[2.53 \cdot 10^{-2} \pm 6 \cdot 10^{-4}\right]\ \text{RIU}/(\text{mol}/L) \tag{7.7}$$

We can also assume that the variation of this sensitivity with temperature is within the expressed uncertainty at typical room temperatures.

Using the ratio between concentration and mass percentage of glucose applying to small quantities (cf. Tab. 7.1), the sensitivity of the RI to relative glucose mass in solution $S^{(m)}_{\text{Glu}}$ can be evaluated at 20°C as:

$$S^{(m)}_{\text{Glu}}(1550\,\text{nm}) = \left[1.42 \cdot 10^{-3} \pm 3 \cdot 10^{-5}\right]\ \text{RIU}/(\%) \tag{7.8}$$

Sensitivity to sucrose at 1550 nm

With the same protocol, the sensitivity S_{Suc} of the RI to sucrose ($C_{12}H_{22}0_{11}$) can be compared to the sensitivity S_{Glu} to glucose ($C_6H_{12}0_6$). The molar sensitivity to sucrose, under identical conditions, is evaluated as:

$$S_{\text{Suc}}(1550\,\text{nm}) = \left[4.8 \cdot 10^{-2} \pm 1 \cdot 10^{-3}\right]\ \text{RIU}/(\text{mol}/L) \tag{7.9}$$

As for the sucrose mass sensitivity, it is evaluated as:

$$S^{(m)}_{\text{Suc}}(1550\,\text{nm}) = \left[1.44 \cdot 10^{-3} \pm 3 \cdot 10^{-5}\right]\ \text{RIU}/(\%) \tag{7.10}$$

We show here that some molecules, even though they result in different molar sensitivities, correspond to similar mass sensitivities. This is verified for molecules with similar structures in terms of chemical bonds, such as glucose and sucrose, as illustrated in Fig. 7.2.

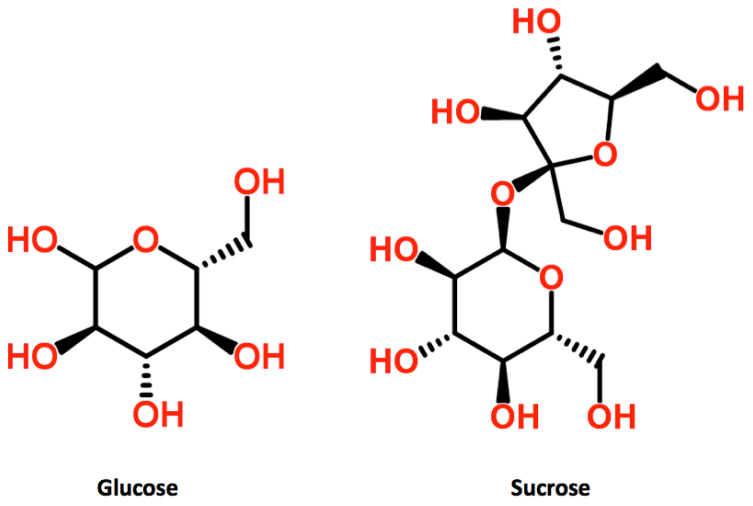

Figure 7.2: Chemical structures of glucose and sucrose molecules.

1.2 Evolution of the resonance linewidth in homogeneous sensing

In a first experiment, effects of the modification of the RI of the cladding on the resonances of a microring resonator is measured. The microresonator under study has a geometry similar to the microresonator characterized in Chap.4., with a slight difference in gap separation (approximately 100 nm).

1.2.1 Description of the experiment

For each measurement, the solution is directly deposited on the optical chip, in order to cover a large area centered on the microresonator. The temperature of the substrate is controlled, as described in Chap.6, at a constant level near initial room temperature. As a consequence, the drop of solution is rapidly brought to substrate temperature after deposition.

Solutions with relative sucrose masses of 0[1], 5, 10, 15, 20, 30, 40 and 50 % were used. Between two measurements, the surface of the microresonator is thoroughly rinsed with DI water. The transmitted intensity of the

[1] 18 MΩ DI water

microresonator as function of the wavelength is, for each concentration, measured with a step-by-step method with a 5 pm resolution.

1.2.2 Recorded intensity transmittances

The evolution of a selected resonance as function of the sucrose relative mass, acting as cladding of the microring resonator, is presented in Fig. 7.3. A first observation is in the evolution of the resonance linewidth for sucrose masses up to 15 %. It is noticeable that despite the relatively large variation in refractive index (cf. Tab. 7.2, the shape of the resonance does not undergo large modifications. This result is to compare with similar experiments performed with laterally-coupled microring resonators [19]. In such experiments, variations of few percents (in mass) of the analyte concentration strongly modifies the resonance linewidth. This demonstrate the increased linearity of the microresonator response, and the increased measurement span provided by a vertical coupling configuration.

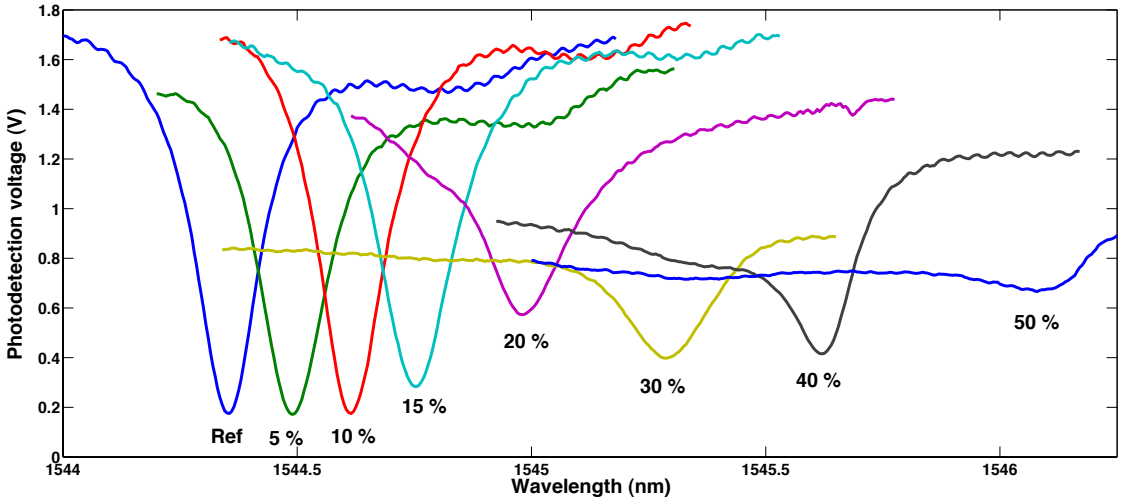

Figure 7.3: Evolution of the resonance shape and position as function of the relative sucrose mass in solution.

1.2.3 Evolution of microresonator characteristics

Effect of higher-order propagation modes

For relative sucrose masses over 15 %, the resonance is less and less visible, for several reasons. First, the modifications of the cladding RI in-

crease the optical losses inside the microresonator. This is due to a lesser confinement of the propagation mode in the core of the waveguide. In addition, absorption of light around 1550 nm by glucose molecules may also explain greater optical losses (cf. Chap.2).

Greater optical losses directly result in a modification of the balance between attenuation and coupling coefficients a and τ (cf. Chap.2), modifying all characteristics of the resonance: contrast C, MIS and FWHM, as it is summed up in Tab. 7.2.

Sucrose mass (%)	**0**	**5**	**10**	**15**	**20**	**30**	**40**	**50**
Index (RIU)	1.319	1.326	1.333	1.341	1.349	1.367	1.386	1.406
Contrast (%)	81.3	80.2	81.8	71.5	43.1	38.2	45.6	14.7
MIS (V/nm)	13.22	10.22	13.18	10.28	4.58	3.46	8.06	3.44
FWHM (pm)	165	180	170	195	200	225	NA	NA
Shift (pm)	0	135	260	400	625	930	1265	1730

Table 7.2: Evolution of resonance characteristics as function of the sucrose concentration

Effect of higher-order propagation modes

A second effect is due to the presence of a higher-order propagation mode in the microresonator. A resonance peak related to this mode is first visible for sucrose masses from 0 to 15 %, in each case as a small modulation of the transmittance on the left side of the main resonance[2]. For these lower sucrose masses, effect of this modulation on the linewidth of the main peak are not significant. However, it is particularly visible for resonances at 20, 30 and 40% that the higher-order resonance modifies the linewidth of the main resonance. Specifically, at 30 %, both resonances are approximately aligned, resulting in an apparent variation of the linewidth of the main resonance peak.

Transfer function of the microresonator

Despite all variations of the resonance shape mentioned above, and the poor sensing conditions, the application of the wavelength-scanning method (cf. Chap.1) for tracking the spectral position of the resonance

[2]related to the fundamental mode

provides a relatively good measurement of the response of the resonator. As illustrated in Fig. 7.4, this response can be linearised piece-by-piece. The non-linearity observed does not simple come from the non-linearity of the microresonator response, but also from the non-linear behaviour of the RI as function of the relative mass, as can be seen in Fig. 7.1.

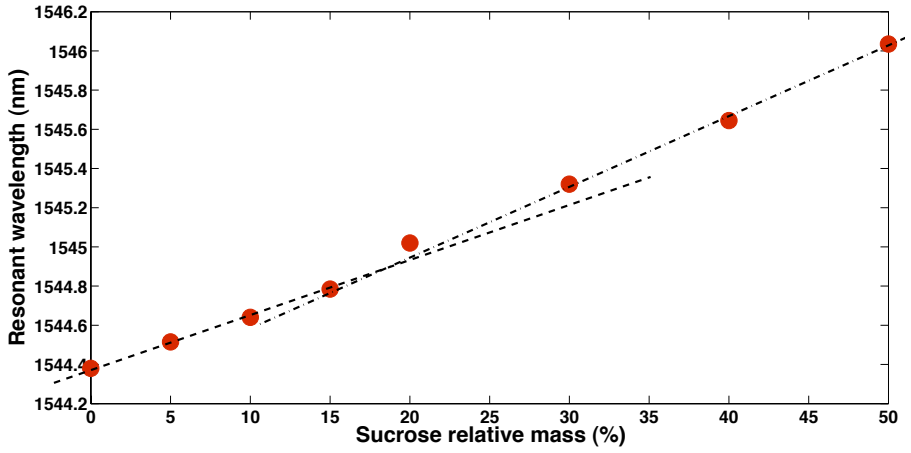

Figure 7.4: Transfer function of the microresonator: resonance spectral position (as wavelength) as function of the relative sucrose mass.

Microresonator sensitivity to sucrose

In this experiment, the microresonator sensitivity to the relative mass of sucrose in aqueous is roughly evaluated as:

$$S_{res}^{(m)}(\text{Suc}) = [27 \pm 1] \text{ pm}/(\%) \tag{7.11}$$

As for the microresonator sensitivity to the RI of the cladding material, it is evaluated here as:

$$S_{res}^{(m)}(N_{clad}) = [19.3 \pm 0.7] \text{ nm/RIU} \tag{7.12}$$

Discussion

These sensitivities of the microresonator under study, relevant for homogeneous sensing, are low compared to the state-of-the-art. This is due to the fact that the device was primarily fabricated to optimize sensitivity in surface detection, and not homogeneous detection. However, larger sensitivities can be obtained by fabricating microresonator waveguides with

lower cross sections, as described in Chap.5.

With a very small sensitivity to homogeneous variations of the cladding RI, and a very good linearity of the microresonator's response for small analyte concentrations, this experiment shows that the designed microresonator is well-suited for label-free biosensing.

1.3 Optofluidic detection of glucose in aqueous solution

1.3.1 Objectives

In the experiments described in this section, the performances of the whole instrument is tested by studying its response to the injection of a reference analyte solution, an aqueous solution of glucose, with relative masses in solution typically ranging from 1 to 10%. The primary objective of such a study is to examine the various biases that can occur during a label-free biosensing experiment. The absolute resolution in terms of measurements of wavelength shifts can also be accurately derived from such experiments.

1.3.2 Description of the experimental protocol

Microfluidic circuit

In these experiments of optofluidic detection of glucose in aqueous solution, the microfluidic circuit as presented in Chap.6 is used. The flowrate of the microfluidic circuit is typically a few mL/h. The "buffer" solution is the same DI water used to prepare the aqueous solutions of glucose. For reproducibility of the measurements, solutions are carefully prepared with high-precision micro-pipettes.

Microresonators

Typical transmissions for the TE and TM polarizations of microresonators under test in this section are presented in Fig. 7.5. The modulation of the envelope, as modelled in Chap.2 and characterized in Chap.4, is induced by the presence - for both polarizations - of one or several higher-order propagation modes in the structure. This is typical of microresonator waveguides with large cross-sections.

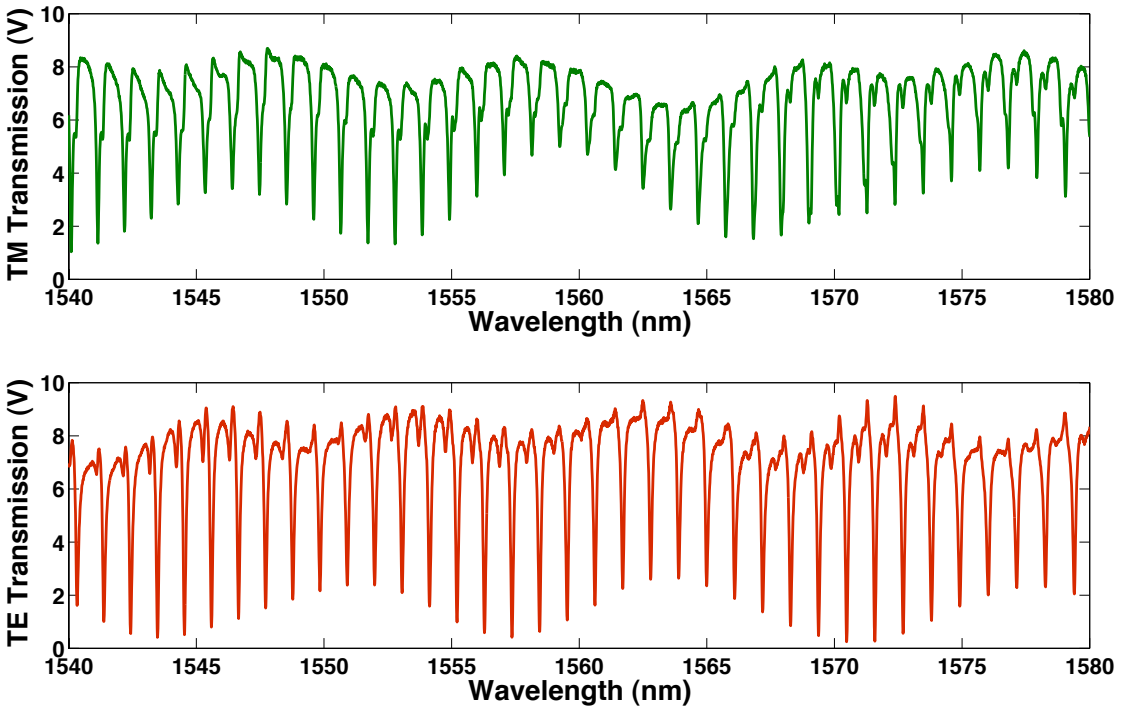

Figure 7.5: Experimental transmissions for TE and TM polarizations of a typical microresonator.

In the TE and TM intensity transmittances presented in Fig. 7.5, higher-order modes are visible, in the form of additional sets of resonance peaks (cf. Fig. 7.6).

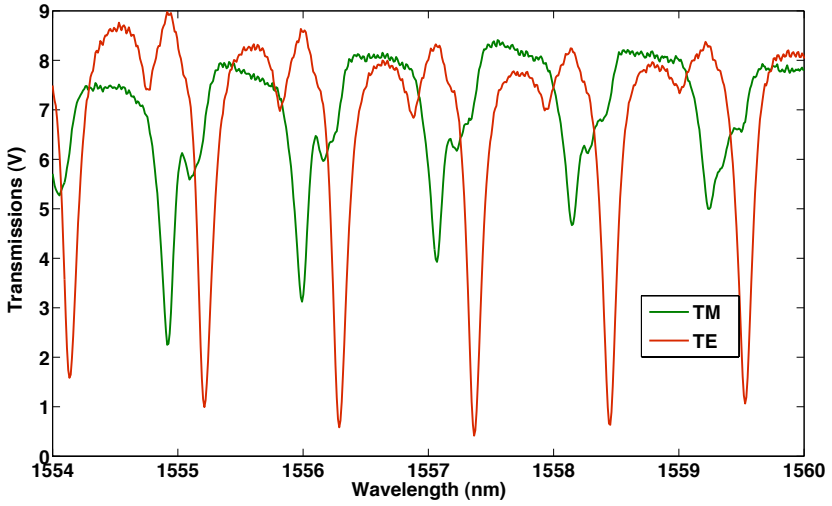

Figure 7.6: Presence of higher-order modes in the TE and TM intensity transmittances.

Despite important envelope modulations, and the presence of additional sets of resonances due to higher-order propagation modes, the spectral positions of the resonances from the fundamental TE and TM modes can be accurately tracked using the wavelength-scanning method, and the various schemes presented in Chap.1.

The following results show, provided a robust method to measure the resonant wavelengths is used, that it is not necessary for the waveguide to be single-mode. Indeed, higher-order modes are much more attenuated in the microring than fundamental modes. As a result, a higher-order resonance has a much lower contrast than a fundamental resonance. Therefore, the influence of higher-order propagation modes on the measured intensity transmittance is minimal.

1.3.3 Repeatability of the optofluidic detection

The ability to detect, with accuracy and repeatability, large shifts of the resonance wavelength is demonstrated in Fig. 7.7. Resonance shifts up to 350 pm obtained with a 10 % glucose solution are measured with a resolution on the wavelength shift of approximately 0.5 pm.

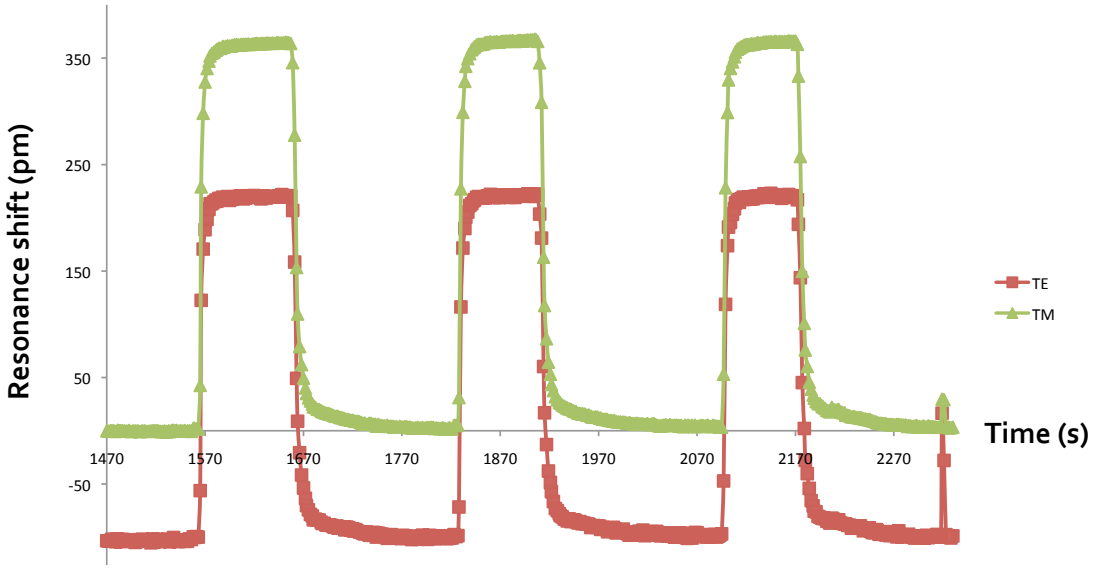

Figure 7.7: Repeatability of the detection of glucose solution with relative mass of 10% for TE and TM polarizations.

1.3.4 Transfer function of the microresonator in optofluidic detection

Performing repeated measurements, similar to what is presented in Fig. 7.7, linearity of the response of the microresonator for both polarizations was evaluated using aqueous solutions of 0, 0.5, 2.5, 5 and 10% in glucose. Each point of the transfer function in Fig. 7.8 is obtained by averaging the stationary shift measured for five repeated cycles of glucose solution injection.

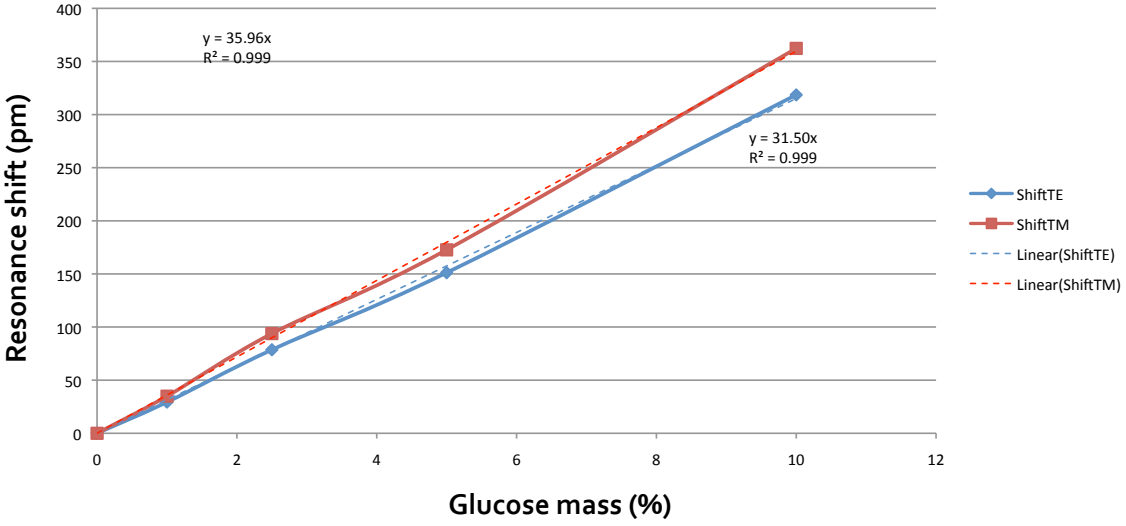

Figure 7.8: Transfer function of the microring resonator, measured for glucose masses of 0, 0.5, 2.5, 5 and 10% and both polarizations.

From these plots, it is clear that the sensitivity to the cladding RI in homogeneous sensing is polarization-dependent. The microresonator sensitivity to glucose mass is equal to 31.5 pm/%(Glu) for TE polarization, and to 36 pm/%(Glu) for TM polarization. These mass sensitivities are similar to that measured with sucrose in the previous section.

It is important to point out here that these measurements, with non-optimal results in terms of linearity and repeatability, were obtained with thermal control of the substrate only (cf. Chap.6). In the following, we show how this limited thermal control makes the instrument sensitive to room temperature variations. Then, we show how the thermal control of the microfluidic circuit is efficient to reduce these effects, up to the point

where they can be easily corrected.

1.3.5 Biased optofluidic detection due to room temperature variations

As explained in Chap.6, due to the solution flow, the temperature of the microresonator is dominantly influenced by the temperature of the solution[3]. In this configuration, the thermal control of the substrate is not sufficient to correct effects due to room temperature variations.

Protocol

In order to characterize the effect of room temperature variations on the detection, a large analyte reservoir (injection loop) was filled with aqueous solution of glucose at 1%. A flowrate of 1 mL/h was selected to maximize the duration of the detection, which is approximately 300 seconds (cf. Fig. 7.9).

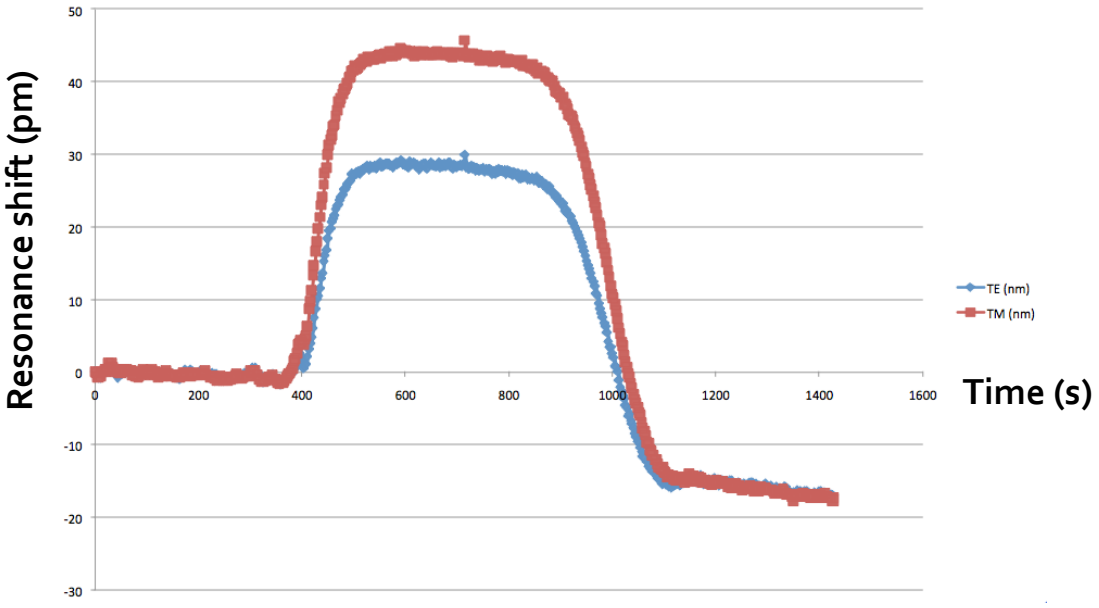

Figure 7.9: Biased response due to variation of the temperature of the buffer solution during the experiment.

[3]The microfluidic circuit being in thermal equilibrium with the room atmosphere, the temperature of the solution is equal to the room temperature.

Analysis of the optofluidic response

In the first phase of the detection, roughly between t_0=0s and t_1=400s, DI water is flown over the microring resonator. During this phase, constant negative drifts of the TE and TM resonances are measured, with a total amplitude of approximately 1 pm from t_0 to t_1. In addition, oscillations of the signals with typical amplitude of 1 pm are observed. The constant negative drifts are a direct effect of an increasing temperature of the solution. However, oscillations of the signals are induced by the reaction of the substrate thermal control to these environmental variations.

From t_1=400s to t_2=500s, effect of the diffusion of glucose molecules from the analyte solution to the DI water buffer is observed.

From t_2=500s to t_3=800s, it can be assumed that the concentration of the solution detected by the microring is stationary. Similarly to the first phase, constant negative drifts of the signals are observed. These drifts are slightly faster (*ie* with higher rates) than those observed during the first phase. This might be due to an increase of the thermal diffusion coefficient of the cladding, from DI water to glucose solution.

From t_3=800s to t_4=1100s, effect of the diffusion of glucose molecules is once again observed, with a longer extent (cf. Chap. 6).

From t_4=1100s to t_5=1400s, the solution flowing over the microresonator is pure DI water. From this last phase, two observation are made. First, the difference of signal levels between first and last phases, approximately 15 pm, cannot be entirely explained by the thermal drifts. On the other hand, the thermal drift is much more important in the last phase than during the first phase.

The latter observation can only be explained by an important variation of the temperature of the solution between t_0 and t_4. Indeed, before t_0 the thermal control of the substrate was set to match the temperature of the solution, resulting in a very slow thermal drift. With a significant increase of the temperature of the solution, the heat transfer between the solution and the microring waveguide is more efficient. As a consequence, the thermal

control is less efficient to regulate the temperature of the microresonator, which results in a faster drift.

The large variation of reference level between t_0 and t_4 can also be explained by an inhomogeneous room temperature. As a result, a significant difference in temperature can be induced between the analyte solution (in the analyte reservoir) and the reference solution (in the buffer reservoir).

Conclusion

With this experiment, we have demonstrated that the main limitation to measurement accuracy in this optofluidic instrument comes from the difficulty to handle room temperature variations. This difficulty is partly due to a very important thermal sensitivity of microring resonator build from polymer materials.

On the other hand, with variations of room temperature of several degrees Celsius over few hours, experimental conditions where far from optimal. Under such environmental conditions, building a measuring instrument liable to perform high-resolution optofluidic detection was a major challenge.

The best technical solution found was by thermal insulation of the whole microfluidic circuit from room atmosphere. Results obtained with this strategy are presented in the following.

1.3.6 Optofluidic detection with temperature-controlled microfluidic circuit

The scheme for thermal control of the microfluidic circuit is detailed in Chap.6. Similarly to the experiment presented in the previous section, handling of room temperature variations is demonstrated by performing measurements over very long durations.

In the following are presented results of optofluidic detection of aqueous solution of glucose at 1, 2.5 and 5%.

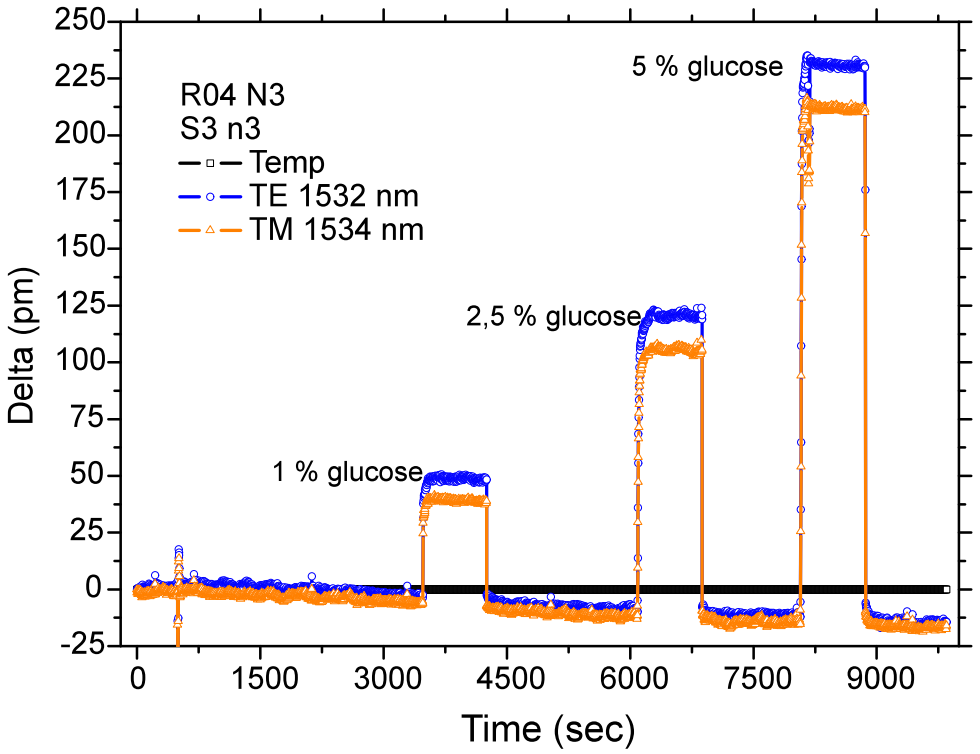

Figure 7.10: Measurements over a long period of time and for various glucose concentrations. Thermal controls of the substrate and the microfluidic circuit are active.

A typical result obtained with this additional control is presented in Fig. 7.10. The total duration of the experiment is approximately 2 hours and 30 minutes. Over this period, tracked TE and TM resonances shifted of approximately 20 pm because of thermal drift. In comparison to the results presented in the last section (cf. Fig. 7.9), it can be observed that the thermal drifts of TE and TM responses are constant over time. In addition, the drift measured when the reference solution is flowing on the microresonator is identical to that measured when a glucose solution is flowing. This major improvement can be explained by the fact that, with the thermal insulation of the microfluidic circuit, the temperature variation between the analyte solution and the reference solution is minimal.

Because the thermal drift is constant over time and identical for both analyte and reference solutions, it can be easily corrected by applying a

linear correction of the TE and TM signals, as presented in Fig. 7.11.

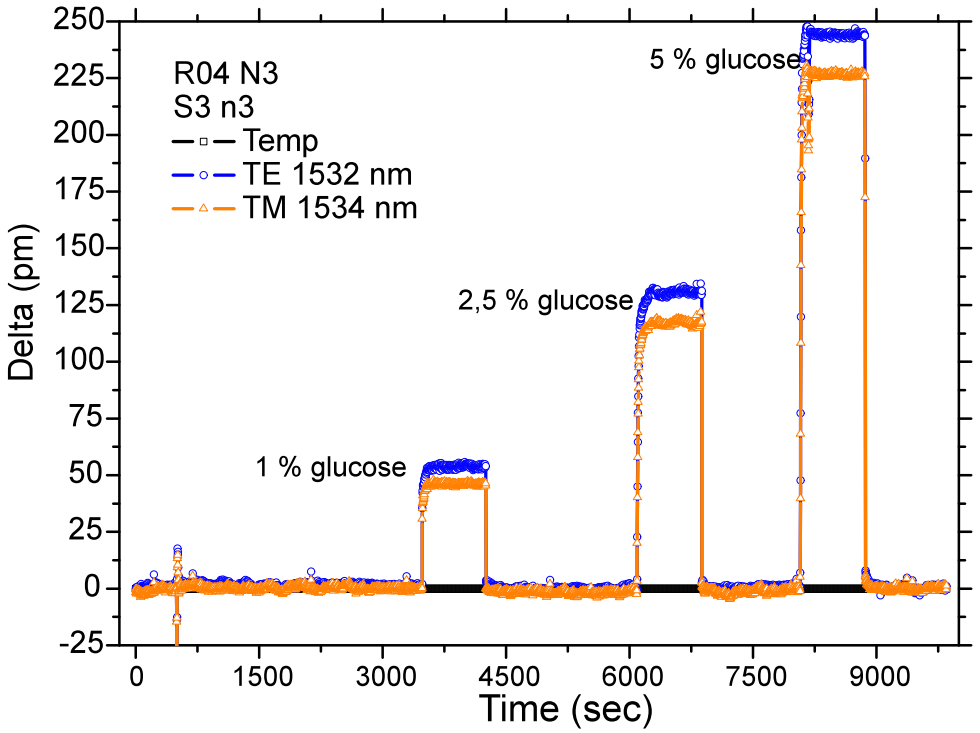

Figure 7.11: Measurements over a long period of time and for various glucose concentrations. As compared to Fig. 7.10, the thermal drift is corrected.

This experiment demonstrate the efficiency of the technical solution applied to reduce effects of room temperature variations on the microresonator response.

2 Surface sensing experiments

2.1 Static detection of TAMRA-cadaverine

The aim of the experiments presented below was to test the ability to detect low concentrations of a biological molecule on the SU-8 surface of a microring resonator. This implied to prepare the optical devices so that such molecules could covalently bind to their surface. It also implied the ability

to quantify the surface concentration of molecules on the surface.

This work was done in collaboration with Marion Salsac, Claude Nogues, Hervé Leh and Malcolm Buckle from Laboratoire de Biologie et de Pharmacologie Appliquée (LBPA) at ENS Cachan, and was published in [18].

2.1.1 Description

Surface binding detection experiments were carried out using solutions with various concentrations of Tetramethylrhodamine-5-carboxamide (5-TAMRA) cadaverine. As pictured in Fig. 7.12, a cadaverine molecule is formed by a carbon chain with two amino groups, one on each end. In a 5-TAMRA cadaverine molecule, one of the amino group is attached to a Rhodamyne-based fluorescent molecule, the other amino group remaining available for surface binding.

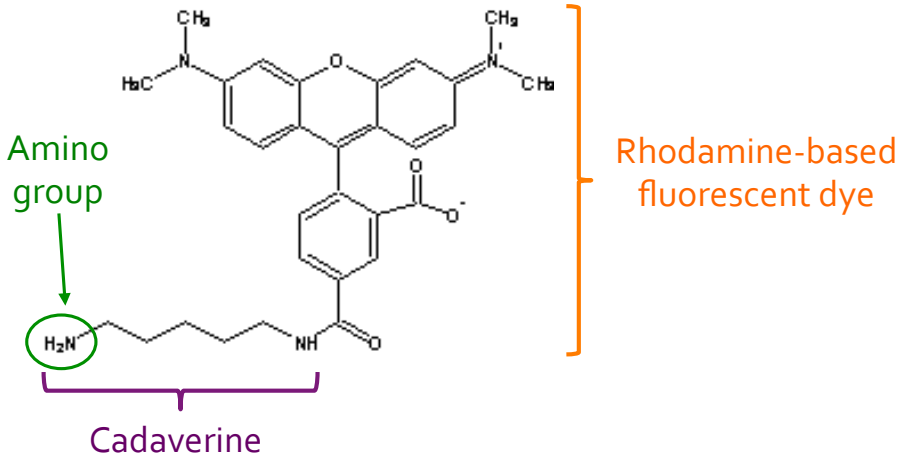

Figure 7.12: 5-TAMRA cadaverine molecule.

For our experimental purposes, using the 5-TAMRA cadaverine (5-TC) molecule had two main advantages. First, numerous biological molecules own a amino group, similarly to the cadaverine molecule. Therefore, successful binding of TAMRA cadaverine on the surface would demonstrate the ability of the functionalized microresonator to detect several biological entities. On the other hand, the fluorescent molecule attached to the cadaverine molecule allows, via fluorescence analysis, a rough quantification of the surface concentration of binded molecules on the SU-8 surface.

2.1.2 Functionalization of SU-8

In early experiments, attempts were made to bind 5-TC molecules on SU-8 surfaces prepared under the same exact conditions as presented in Chap.3, for the fabrication of SU-8 microresonators. It was observed that, directly after hard-bake, the SU-8 surface did not react with 5-TC molecules in solution. This was later explained by analysis of processed SU-8 films with FTIR spectroscopy, showing the absence of functional groups on the SU-8 surface after the hard-bake step.

From these observations, the hard-bake step, responsible for the further cross-linking of the epoxy groups constituting the SU-8 film, and inherently the resistance of the SU-8 film, was also responsible for the non-reactivity of the SU-8 surface. Consequently, an additional treatment had to be found to activate the SU-8 so that molecules may bind to its surface.

Activation by oxygen plasma

In microfabrication, as presented in Chap.3, an exposition of the polymer to oxygen plasma is liable to activate its surface, *ie* to improve the adhesion of a second film to its surface. Such treatments were attempted to free reactive groups on the SU-8 surfaces after-bake. It was observed that exposure to oxygen plasma turned the initial hydrophobic SU-8 surface into an hydrophilic surface. However, significant modifications of the reactivity of the surface was obtained at the cost of an etch of the SU-8 surface, making this process not suitable to preserve the integrity of the optical device.

Activation by UV/ozone treatment

A solution to prepare the SU-8 surface while preserving the integrity of the optical device was found using an UV/ozone cleaner. A UV/ozone cleaner is typically used in microfabrication to remove organic impurities from film surfaces. Mechanisms at work in such apparatus is described in [83]. Numerous experiments have been performed at LBPA to characterize and optimize the state of the surface. The principal results related to the preparation of SU-8 surface for binding 5-TC molecules are presented in

the following.

In a first experiment, effect of the duration of the UV/ozone treatment on the state of the SU-8 surface was measured using FTIR microscopy. Measurement results are presented in Fig. 7.13.

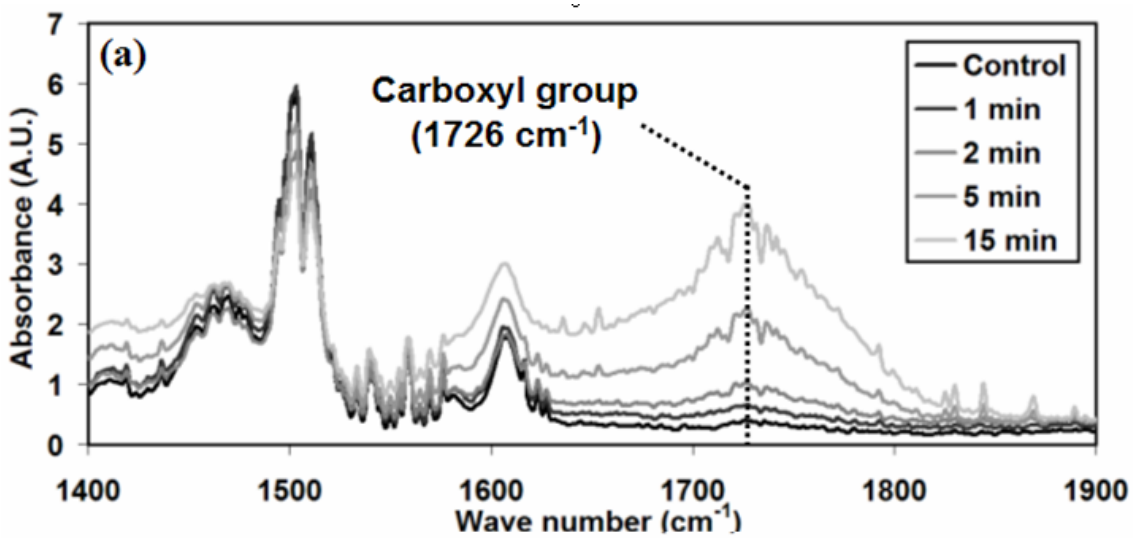

Figure 7.13: Effect of the UV/ozone treatment on SU-8 measured by FTIR spectrometry.

From these measurements, the quantity of carboxyl groups (peak at 1726 cm^{-1}) appears to increase with the duration of the treatment, illustrating the higher capacity of the treated surface to bind 5-TAMRA cadaverine molecules through peptide bonds. However, a study of the fluorescence signal produced by spots of 5-TAMRA cadaverine grafted on treated surfaces of SU-8 demonstrated that a one-minute exposure to UV/ozone was optimal to obtain maximal reactivity, as longer treatments created more carboxyl groups in the bulk of the material but not on its surface.

2.1.3 Quantification of surface concentrations from fluorescence analysis

The aim of the second experiment was to relate a measured fluorescence signal to a quantity of 5-TAMRA cadaverine, in moles. This was achieved by depositing drops of 5-TC solution in various concentrations on treated SU-8 surfaces. Once the drops of solution are dried, it is assumed that the quantity of molecules on the surface is equal to the concentration of

the solution multiplied by the volume of the drop. Measurements were reproduced several times to characterize the uncertainty of such calibration. results are displayed in Fig. 7.16.

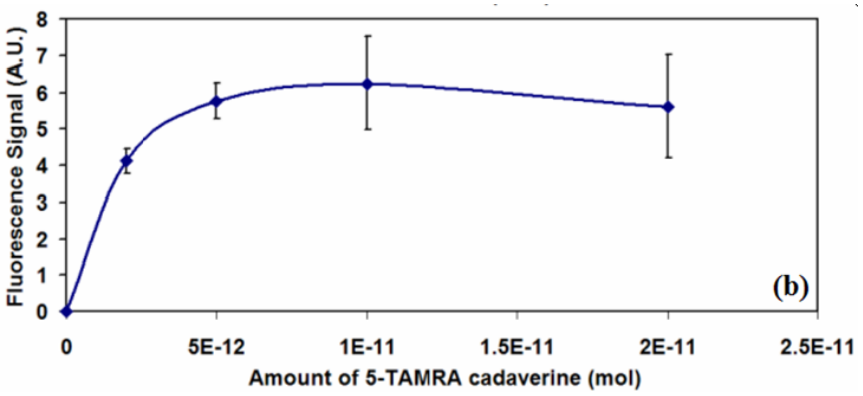

Figure 7.14: Calibration curve for quantification: fluorescence signal as function of 5-TAMRA cadaverine quantity in moles.

For quantities of 5-TC molecules over $5{\cdot}10^{-12}$ mol, the fluorescence signal is saturated, probably due to the quenching of the fluorescence when molecules accumulate on the surface on several layers. However, for lower quantities of 2 pmol and under, the fluorescence signal appears proportional to the quantity of molecules. This can be interpreted by the fact that for low quantities, the SU-8 surface is not saturated, and 5-TC molecules are more liable to form a single molecular layer.

In a subsequent experiment, fluorescent spots of 5-TC were obtained by first depositing drops of solution of known concentrations on a treated SU-8 surface. After a 10-minute incubation period, the surface was thoroughly rinsed with DI-water to remove molecules that were not adsorbed. Then, fluorescence signal of each spot is measured, and associated surface concentrations of 5-TC molecules grafted on the SU-8 surface are deduced, from the quantity provided by the calibration curve (cf. Fig. 7.16), and from the measurement of the fluorescent spot surfaces.

2.1.4 Microresonator response to grafted 5-TC molecules

The effect of the surface densities of immobilized 5-TAMRA cadaverine on the spectral response of the resonators was studied under the same conditions used for the optical characterization described in Chap.5. During

the experiment, each drop of 5-TC solution was deposited on the treated SU-8 surface of a microring resonator, so that it covers its entire surface. After a 10-minute incubation period, the surface was thoroughly rinsed with DI water. Then, a large amount of DI water was deposited on the surface of the device, to act as cladding material.

Such a procedure, referred to later as binding cycle, was repeated with 5-TC solutions with molar concentrations of 0 (reference), 0.1, 0.2, 0.4 and 1 μM[4].

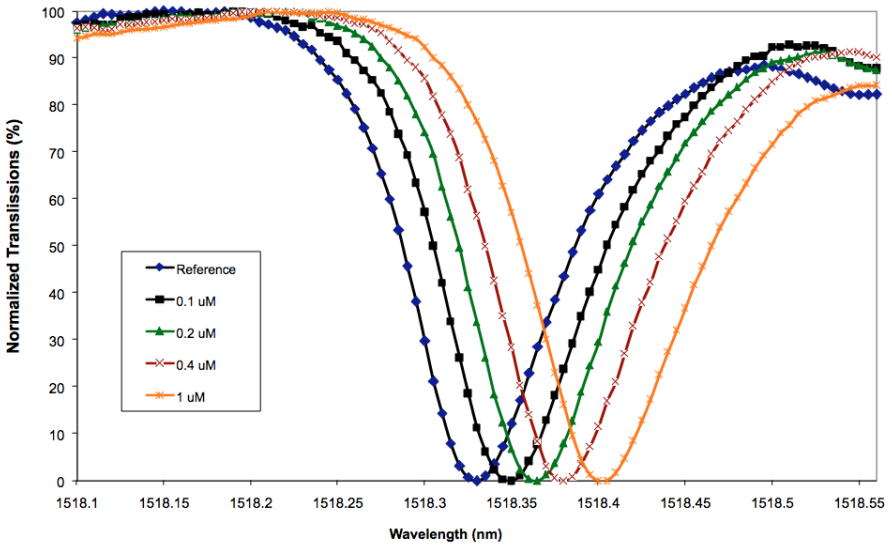

Figure 7.15: Intensity transmittances corresponding to a selected resonance measured after each 5-TC binding cycle.

In Fig. 7.15 are presented the measured intensity transmittances corresponding to a resonance peak of the microring resonator. Transmittances were measured after each procedure. After DI water deposit, a delay of 5 minutes was applied in order to let the temperature of the liquid stabilize to the controlled temperature of the substrate (cf. Chap.6).

In order to relate measured shifts of the resonance peaks to a variation of the surface concentration of 5-TC molecules, the same protocol was used to graft increasing amounts of molecules on a SU-8 thin film prepared in the exact same conditions as the SU-8 microresonator used for the experiment. After each cycle, fluorescence signal was measured in order to evaluate the

[4] 1 μM = 10^{-6} mol/L

surface concentration obtained after each binding cycle. The uncertainty on the surface concentration was estimated at 30% of the central value.

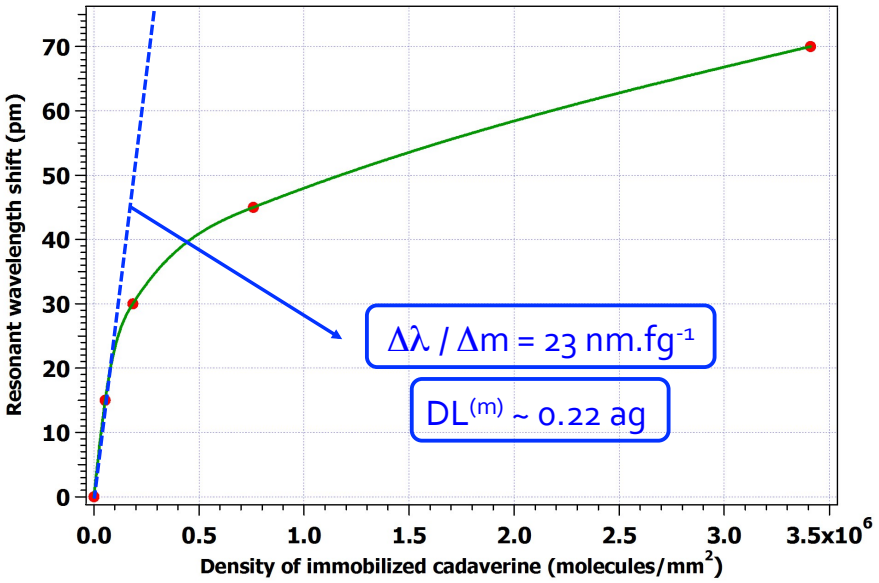

Figure 7.16: Resonant wavelength shift as a function of the surface density of grafted 5-TC molecules in molecules per mm^2.

From measurements of the microresonator response and the evaluation of surface concentrations, a 15 pm shift is attributed to a density of 53,900 molecules/mm^2 on the sensing surface Σ_{tot} of the resonator. With Σ_{tot} = 0.0143 mm^2 and a molar mass M = 517 g/mol for the 5-TAMRA cadaverine, we can estimate the microresonator sensitivity S_{5-TC} obtained at the lower concentrations to S_{5-TC} = 23 nm/fg. Considering the wavelength-stability of the laser source and the noise level, the resolution in wavelength shift $R[\delta\lambda]$ achieved for these measurements was evaluated at 5 pm. Accordingly, the limit of detection (LOD) (cf. Chap.1) for this experiment was evaluated at approximately 0.22 ag which corresponds to 250 molecules grafted on the surface of the microring resonator.

With this experiment, the very high sensitivity that can be achieved in surface detection with polymer microring resonators is demonstrated. More recent results, this time on the label-free detection of molecules via antigen-antibody biological interaction are still being processed and will be presented as soon as available.

2.2 Optofluidic detection of adsorption/desorption kinetics of TAMRA on anti-TAMRA

to be completed ... Hereafter are presented the more important results. In the following, TAMRA refers to the 5-TC molecule, and anti-TAMRA refers to the antibody of the 5-TC.

2.2.1 Injection of anti-TAMRA in buffer A

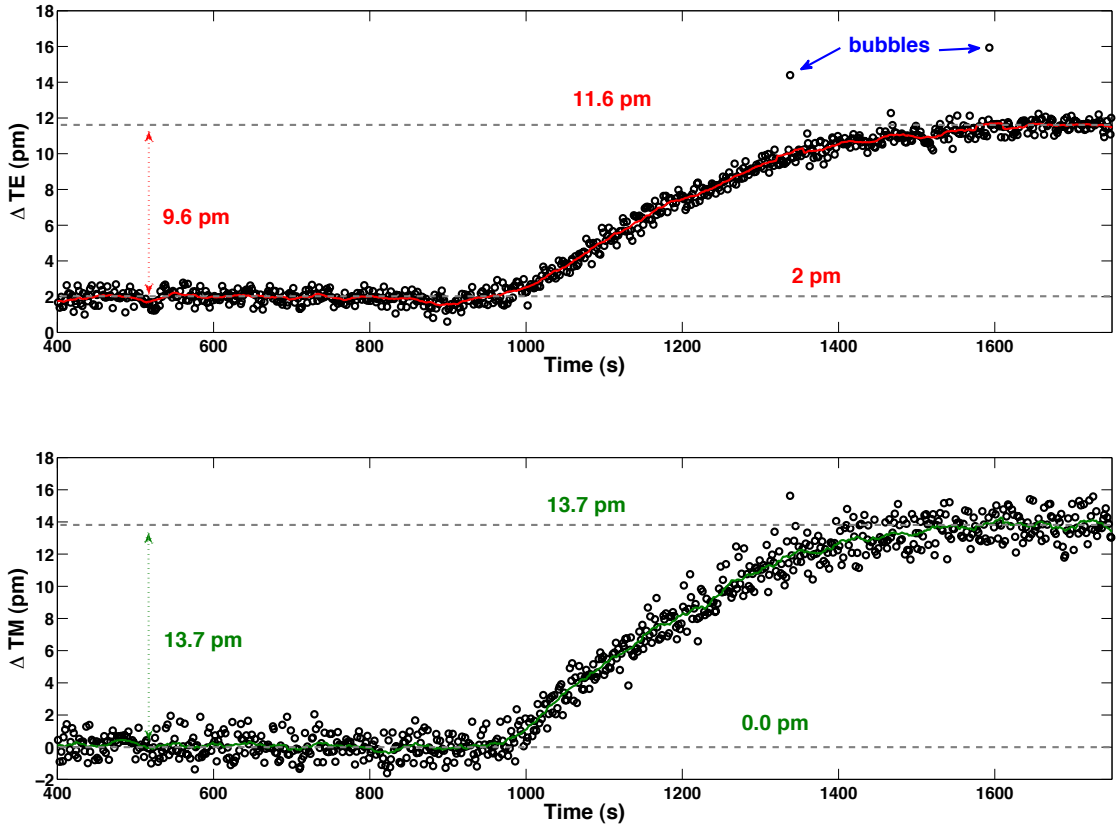

Figure 7.17: TE and TM responses of the microring resonator to the adsorption of anti-TAMRA molecules on its surface. The concentration of anti-TAMRA in the injected solution is 0.1 μM. Thermal drifts of TE and TM responses are corrected from simultaneous measurements of the substrate temperature.

2.2.2 Transition from buffer A to buffer B

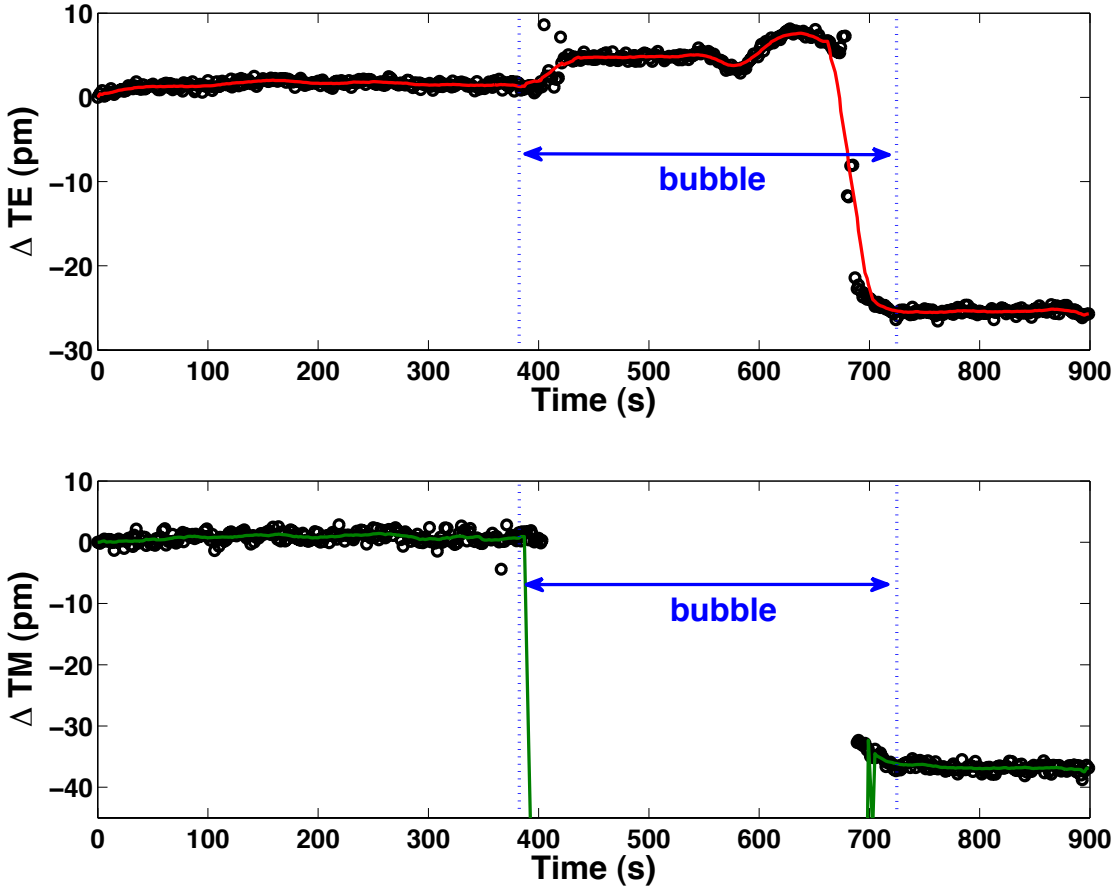

Figure 7.18: TE and TM responses of the microring resonator to the modification of the buffer during the experiment. Heratic responses is measured right after the buffer switch, due to the arrival and stabilization of a large air bubble over the microresonator under study. Thermal drifts of TE and TM responses are corrected from simultaneous measurements of the substrate temperature.

2.2.3 Adsorption/desorption kinetics of TAMRA on anti-TAMRA

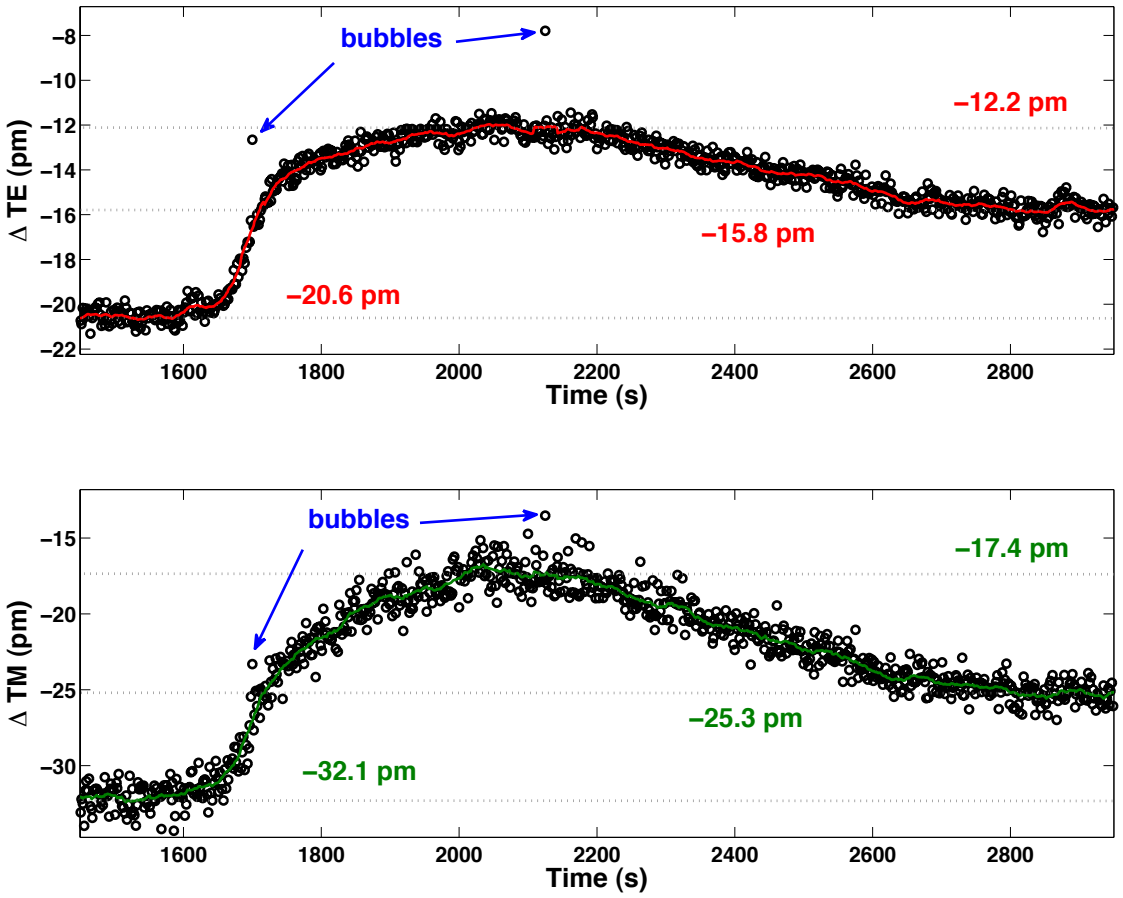

Figure 7.19: TE and TM responses of the microring resonator to the adsorption/desorption of TAMRA molecules with anti-TAMRA molecules grafted on the surface. The concentration of TAMRA in the injected solution is 10 μM. Thermal drifts of TE and TM responses are corrected from simultaneous measurements of the substrate temperature.

Conclusion

1 General thoughts

The work described in this dissertation is incorporated within the framework of a long-term, multidisciplinary research project between several laboratories, with widely diversified scientific backgrounds. This diversity was undoubtedly a formidable source of progress but required, on numerous occasions, tremendous efforts to achieve mutual understanding. In retrospect, the fruit of such efforts was, in my view, a much deeper understanding of the implications of research in the modern world, where borders between scientific disciplines are less and less relevant.

The wide variety of subjects tackled in this dissertation is a direct result of such research environment. From the initial project to build a label-free biosensing instrument based on polymer microresonators, numerous issues had to be addressed in order to obtain an apparatus which is not simply of interest to physicists. On the contrary, the primary objective of the research presented in this dissertation was to develop an instrument for biologists and biochemists. This objective stimulated a necessary reflection on fundamental processes involved in optical biosensors, and more specifically in microresonator-based sensors. I hope that these reflections will be found useful for the further development of such systems.

Besides theoretical aspects, numerous technical issues had to be addressed in order to present a prototype of instrument able to detect dynamic surface interactions in microfluidic regime, with a very high resolution. In this dissertation, most of these difficulties are overlooked, only to give more room to the most efficient solutions found. It should be clear to the reader that the time required for the resolution of technical problems accounted for an overwhelming part of the work performed within the scope

of this dissertation. In that respect, such difficulties might have been the source of intense frustration. However, most technical issues were in the end overcame, and the skills developed to do so will remain.

2 Developed skills

2.1 Theoretical skills

The study of electromagnetic theory was fundamental to understand many phenomena involved in the measuring instrument developed. Guided optics was of course a major center of interest, in order to build analytical models for the microring resonators, and their sensitivities to various physico-chemical quantities. For the further study of these sensitivities, elements of the theory of light-matter interactions were also useful. In that respect, classical tools were chosen for their simplicity, but semiclassical or quantum-electrodynamical approaches would be necessary for further understanding of, for instance, the optical detection of single binding events.

Developing the opto-thermo-fluidic instrumentation to measure the response of the transducer[5] required the use of basic elements from various disciplines related to physics: optical systems, laser physics, fluid dynamics, heat transfers and mechanics. Such theoretical tools were also necessary to understand key aspects of procedures related to microfabrication, and how they can be optimized. In addition, some fundamentals of chemistry were necessary to understand such procedures, and also in the design and preparation of homogeneous and surface sensing experiments.

In the scope of the dissertation, surface biochemistry was also studied, in order to understand key aspects of surface preparation, functionalization, and interaction with an analyte.

2.2 Experimental skills

A major component of the experimental skills developed in the scope of this dissertation has been in the initiation to microfabrication techniques, for the fabrication of optical microresonators and the microfluidic cap.

[5] the microring resonator

Techniques such as thin-film deposition by spin-coating, mask alignment, UV-lithography, Reactive Ion Etching (RIE), and wafer slicing were repeatedly used, and progressively mastered.

Regarding the experimental setup, skills to place and align various optical elements were developed, in order to optimize the detection signal, or simply to obtain a measurable signal in particularly difficult conditions. Additionally:

- handling of microfluidics instrumentation
- handling of thermal regulation systems
- handling of data acquisition systems

2.3 Computer skills

Development of the program to control most aspects of the instrument, and the user interface in C/C++. Work to optimize the portability, rapidity and the updates of the program.

3 Main achievements

3.1 Analytical models for microring resonators

- review of phenomena susceptible to occur in microring resonator
- addition to classical black-box model for modeling multi-modal behavior
- addition to classical black-box model for modeling dispersion

3.2 Numerical simulation of microring resonators

- Requirements and limitations in the use the 3D-FDTD method to model polymer microring resonator
- Discussion on hybrid analytical-numerical approaches

3.3 Fabrication of polymeric, vertically-coupled microring resonators

A time and cost-efficient fabrication method was developed to fabricate vertically-coupled polymer microracetrack resonators. Optical performances obtained, with Q factors above 35 000 with water as cladding, exceeded the previous state-of-the-art, and have not been matched yet.

3.4 Understanding of key parameters for the LOD

In the literature, the Q factor of a microresonator is often believed to be the ultimate parameter to consider to optimize the limit of detection in microresonator-based sensing. It was demonstrated that the maximal intensity slope (MIS) was more relevant to describe the performances of the optical transducers. In addition, it was pointed out that the only role of the Q factor, or the MIS, was to reduce the uncertainty on the measurements due to optical intensity fluctuations. Since such fluctuations are only one of the many sources of measurement uncertainties, it was clearly established that the role of such parameters in the optimization of the LOD may be irrelevant, in the case where the combined uncertainty is limited by the instrumentation.

3.5 Optimization of waveguide for homogeneous and surface sensing

- Models for the optimization of slab and rectangular waveguide for homogeneous sensing
- Models to reduce the waveguide sensitivities to external perturbations
- Models to optimize waveguides, or plasmons, for surface sensing
- Specific case of label-free biosensing, with derivation of an optimal evanescent field decay length

3.6 Demonstration of highly-sensitive surface sensing

Demonstration of the sensitive response of the SU-8 microresonator to TAMRA-cadaverine bound on its surface. The limit of detection in a static configuration (not specific) was evaluated at 250 molecules, from fluorescence analysis.

3.7 Demonstration of optofluidic sensing

Numerous experiments of optofluidic detection were performed, with resolutions in the measurements of resonant wavelength down to 0.3 pm in real-time, and below with data averaging. Wide measurement span obtained thanks to the vertical configuration was demonstrated using sucrose and glucose solutions in homogeneous detection.

3.8 Demonstration of optofluidic label-free sensing

In late experiments, binding kinetics of TAMRA-cadaverine on its antibody where observed. Although the surface binding achieved is, unexpectedly, believed to be poorly efficient, the high-resolution achieved, down to 0.1 pm and under, allows for a direct comparison of results with that obtained with commercially available techniques such as SPR.

Bibliography

[1] S. O'Malley, "Recent advances in label-free biosensors applications in protein biosynthesis and hts screening," in *Protein Biosynthesis* (T. E. Esterhouse and L. B. Petrinos, eds.), Nova Science Publishers, Inc., 2008.

[2] M. A. Cooper, "Optical biosensors in drug discovery," *Nature Reviews Drug Discovery*, vol. 1, pp. 515–528, July 2002.

[3] P. Arora, A. Sindhu, N. Dilbaghi, A. Chaudhury, P. Arora, A. Sindhu, N. Dilbaghi, and A. Chaudhury, "Biosensors as innovative tools for the detection of food borne pathogens," *Biosensors and Bioelectronics*, 2011.

[4] X. Fan, I. M. White, S. I. Shopova, H. Zhu, J. D. Suter, and Y. Sun, "Sensitive optical biosensors for unlabeled targets: A review," *analytica chimica acta*, vol. 620, no. 1, pp. 8–26, 2008.

[5] J. Arlett, E. Myers, and M. Roukes, "Comparative advantages of mechanical biosensors," *Nature Nanotechnology*, vol. 6, pp. 203–215, Mar. 2011.

[6] J. Fraden, *Handbook of modern sensors: Physics, Designs, and Applications*. Springer, third edition ed., 2003.

[7] J. S. Wilson, ed., *Sensor Technology Handbook*. Elsevier, 2005.

[8] R. M. White, "A sensor classification scheme," *IEEE Transactions on ultrasonics, ferroelectrics, and frequency control*, vol. 34, no. 2, pp. 124–126, 1987.

[9] B. N. Taylor, *Guidelines for Evaluating and Expressing the Uncertainty of NIST Measurement Results (rev*. DIANE Publishing, 2009.

[10] K. Okamoto, *Fundamentals of optical waveguides*. Academic Press, 2005.

[11] A. B. Sanghvi, K. P. H. Miller, A. M. Belcher, and C. E. Schmidt, "Biomaterials functionalization using a novel peptide that selectively binds to a conducting polymer," *Nature Materials*, vol. 4, pp. 496–502, May 2005.

[12] A. Maxwell, S.-W. Huang, T. Ling, J.-S. Kim, S. Ashkenazi, and L. Jay Guo, "Polymer microring resonators for high-frequency ultrasound detection and imaging," *IEEE Journal of Selected Topics in Quantum Electronics*, vol. 14, no. 1, pp. 191–197, 2008.

[13] A. Wanekaya, W. Chen, N. Myung, and A. Mulchandani, "Nanowire-based electrochemical biosensors," *Electroanalysis*, vol. 18, no. 6, pp. 533–550, 2006.

[14] J. Homola, S. S. Yee, and G. Gauglitz, "Surface plasmon resonance sensors: review," *Sensors and Actuators B: Chemical*, vol. 54, no. 1-2, pp. 3–15, 1999.

[15] X. D. Hoa, A. G. Kirk, and M. Tabrizian, "Towards integrated and sensitive surface plasmon resonance biosensors: a review of recent progress," *Biosensors and Bioelectronics*, vol. 23, no. 2, pp. 151–160, 2007.

[16] Y. Chen and H. Ming, "Review of surface plasmon resonance and localized surface plasmon resonance sensor," *Photonic Sensors*, vol. 2, pp. 37–49, Jan. 2012.

[17] R. Bruck, E. Melnik, P. Muellner, R. Hainberger, and M. Lammerhofer, "Integrated polymer-based mach-zehnder interferometer label-free streptavidin biosensor compatible with injection molding," *Biosensors and Bioelectronics*, vol. 26, pp. 3832–3837, May 2011.

[18] C. Delezoide, M. Salsac, J. Lautru, H. Leh, C. Nogues, J. Zyss, M. Buckle, I. Ledoux-Rak, and C. Nguyen, "Vertically coupled polymer microracetrack resonators for label-free biochemical sensors," *Photonics Technology Letters, IEEE*, vol. 24, no. 4, pp. 270–272, 2012.

[19] C.-Y. Chao, *Polymeric microring resonators and its application as a biosensor*. PhD thesis, University of Michigan, 2005.

[20] T. Barwicz, M. A. Popovic, P. T. Rakich, M. R. Watts, H. A. Haus, E. P. Ippen, and H. I. Smith, "Microring-resonator-based add-drop filters in SiN: fabrication and analysis," *Opt. Express*, vol. 12, no. 7, pp. 1437–1442, 2004.

[21] S. Choi, K. Djordjev, Z. Peng, Q. Yang, S. Choi, and P. Dapkus, "Laterally coupled buried heterostructure high-q ring resonators," *IEEE Photonics Technology Letters*, vol. 16, pp. 2266–2268, Oct. 2004.

[22] G. H. Vander Rhodes, B. B. Goldberg, M. S. Unlu, S. T. Chu, and B. E. Little, "Internal spatial modes in glass microring resonators," *IEEE Journal of Selected Topics in Quantum Electronics*, vol. 6, no. 1, pp. 46–53, 2000.

[23] M. S. Luchansky, A. L. Washburn, T. A. Martin, M. Iqbal, L. C. Gunn, and R. C. Bailey, "Characterization of the evanescent field profile and bound mass sensitivity of a label-free silicon photonic microring resonator biosensing platform," *Biosensors and Bioelectronics*, vol. 26, no. 4, pp. 1283–1291, 2010.

[24] C.-Y. Chao, W. Fung, and L. Guo, "Polymer microring resonators for biochemical sensing applications," *IEEE Journal of Selected Topics in Quantum Electronics*, vol. 12, pp. 134–142, Jan. 2006.

[25] H. Ma, A. K. Y. Jen, and L. R. Dalton, "Polymer-based optical waveguides: materials, processing, and devices," *Advanced Materials*, vol. 14, no. 19, pp. 1339–1365, 2002.

[26] J. M. Liu, *Photonic devices*. Cambridge University Press Cambridge, 2005.

[27] E. Hecht, *Optics*. Addison-Wesley, 2002.

[28] G. W. Scherer, "Stress-induced index profile distortion in optical waveguides," *Appl. Opt.*, vol. 19, pp. 2000–2006, Jun 1980.

[29] M. Campoy-Quiles, P. Etchegoin, and D. Bradley, "On the optical anisotropy of conjugated polymer thin films," *Physical Review B*, vol. 72, July 2005.

[30] C. Pitois, A. Hult, and D. Wiesmann, "Absorption and scattering in low-loss polymer optical waveguides," *JOSA B*, vol. 18, no. 7, pp. 908–912, 2001.

[31] M. L. Gorodetsky, A. A. Savchenkov, and V. S. Il'chenko, "Ultimate q of optical microsphere resonators," *Optics Letters*, vol. 21, no. 7, pp. 453–455, 1996.

[32] P. J. Foster, J. K. Doylend, P. Mascher, A. P. Knights, and P. G. Coleman, "Optical attenuation in defect-engineered silicon rib waveguides," *Journal of Applied Physics*, vol. 99, no. 7, pp. 073–101, 2006.

[33] S. Michel, J. Zyss, I. Ledoux-Rak, and C. T. Nguyen, "High-performance electro-optic modulators realized with a commercial side-chain DR1-PMMA electro-optic copolymer," in *Proc. SPIE*, vol. 7599, p. 759901, 2010.

[34] V. S. Il'chenko and M. L. Gorodetskii, "Thermal nonlinear effects in optical whispering gallery microresonators," *Laser Physics*, vol. 2, no. 6, pp. 1004–1009, 1992.

[35] H. Rokhsari, S. M. Spillane, and K. J. Vahala, "Loss characterization in microcavities using the thermal bistability effect," *Applied physics letters*, vol. 85, no. 15, pp. 3029–3031, 2004.

[36] A. M. Armani, R. P. Kulkarni, S. E. Fraser, R. C. Flagan, and K. J. Vahala, "Label-free, single-molecule detection with optical microcavities," *Science*, vol. 317, pp. 783–787, Aug. 2007.

[37] A. Zhang, K. T. Chan, M. S. Demokan, V. W. C. Chan, P. C. H. Chan, and A. H. P. Chan, "Annealing effects on the loss and birefringence of silicon oxynitride rectangular optical waveguides," *Applied Physics Letters*, vol. 87, no. 10, pp. 101–105, 2005.

[38] B. M. A. Rahman, D. M. H. Leung, S. S. A. Obayya, and K. T. V. Grattan, "Bending loss, transition loss, mode coupling, and polarization coupling in bent waveguides," in *Proc. SPIE*, p. 699600, Apr. 2008.

[39] C. Brooks, P. E. Jessop, H. Deng, D. O. Yevick, and G. Tarr, "Passive silicon-on-insulator polarization-rotating waveguides," *Optical Engineering*, vol. 45, no. 4, pp. 044603–044603–5, 2006.

[40] E. A. J. Marcatili, "Bends in optical dielectric guides," *Bell System Technical Journal*, pp. 2103–2132, Sept. 1969.

[41] D. Marcuse, "Bending losses of the asymmetric slab waveguide," *Bell System Technical Journal*, vol. 50, pp. 2551–2563, Oct. 1971.

[42] M. Miyagi and S. Nishida, "Bending losses of dielectric rectangular waveguides for integrated optics," *JOSA*, vol. 68, no. 3, pp. 316–319, 1978.

[43] Y. Takuma, M. Miyagi, and S. Kawakami, "Bent asymmetric dielectric slab waveguides: a detailed analysis," *Applied Optics*, vol. 20, no. 13, pp. 2291–2298, 1981.

[44] R. Baets and P. E. Lagasse, "Loss calculation and design of arbitrarily curved integrated-optic waveguides," *JOSA*, vol. 73, no. 2, pp. 177–182, 1983.

[45] R. T. Deck, M. Mirkov, and B. G. Bagley, "Determination of bending losses in rectangular waveguides," *Journal of lightwave technology*, vol. 16, no. 9, p. 1703, 1998.

[46] A. Melloni, F. Carniel, R. Costa, and M. Martinelli, "Determination of bend mode characteristics in dielectric waveguides," *Journal of Lightwave Technology*, vol. 19, no. 4, p. 571, 2001.

[47] L. J. Guo, A. Maxwell, C.-Y. Chao, T. Ling, J.-S. Kim, S.-W. Huang, and S. Ashkenazi, "Polymer microring resonators and their sensor applications," vol. 6896, p. 689612, SPIE, 2008.

[48] G. Ghosh, *Handbook of Thermo-Optic Coefficients of Optical Materials With Applications*. Handbook of Optical Constants of Solids, Academic Press, 1998.

[49] L. F. Stokes, M. Chodorow, and H. J. Shaw, "All-single-mode fiber resonator," *Opt. Lett.*, vol. 7, pp. 288–290, Jun 1982.

[50] B. E. Little, J. P. Laine, and S. T. Chu, "Surface-roughness-induced contradirectional coupling in ring and disk resonators," *Optics letters*, vol. 22, no. 1, pp. 4–6, 1997.

[51] T. Tamir and E. Garmire, *Integrated optics*. Topics in applied physics, Springer-Verlag, 1979.

[52] C.-Y. Chao and L. Guo, "Reduction of surface scattering loss in polymer microrings using thermal-reflow technique," *IEEE Photonics Technology Letters*, vol. 16, pp. 1498–1500, June 2004.

[53] L. Caruso and I. Montrosset, "Analysis of a racetrack microring resonator with MMI coupler," *Journal of Lightwave Technology*, vol. 21, pp. 206–289, Jan. 2003.

[54] Q. Xu, D. Fattal, and R. G. Beausoleil, "Silicon microring resonators with 1.5-μm radius," *Opt. Express*, vol. 16, pp. 4309–4315, Mar 2008.

[55] A. Delage, D.-X. Xu, R. W. McKinnon, E. Post, P. Waldron, J. Lapointe, C. Storey, A. Densmore, S. Janz, B. Lamontagne, P. Cheben, and J. H. Schmid, "Wavelength-dependent model of a ring resonator sensor excited by a directional coupler," *Journal of Lightwave Technology*, vol. 27, pp. 1172–1180, May 2009.

[56] A. Taflove and S. Hagness, *Computational Electrodynamics: The Finite-Difference Time-Domain Method*. Artech House Antennas and Propagation Library, Artech House, 2000.

[57] R. Stoffer, K. R. Hiremath, and M. Hammer, "Comparison of coupled mode theory and FDTD simulations of coupling between bent and straight optical waveguides," in *AIP Conference Proceedings: Microresonators as building blocks for VLSI photonics (2004)*, vol. 709, pp. 366–377, 2004.

[58] K. R. Hiremath, M. Hammer, R. Stoffer, L. Prkna, and J. Ctyrok, "Analytic approach to dielectric optical bent slab waveguides," *Optical and Quantum Electronics*, vol. 37, no. 1, pp. 37–61, 2005.

[59] M. Heiblum and J. Harris, "Analysis of curved optical waveguides by conformal transformation," *Quantum Electronics, IEEE Journal of*, vol. 11, no. 2, pp. 75–83, 1975.

[60] D. B. Hall, P. Underhill, and J. M. Torkelson, "Spin coating of thin and ultrathin polymer films," *Polymer Engineering & Science*, vol. 38, no. 12, pp. 2039–2045, 1998.

[61] D. E. Bornside, C. W. Macosko, and L. E. Scriven, "Spin coating: One-dimensional model," *Journal of Applied Physics*, vol. 66, no. 11, pp. 5185–5193, 1989.

[62] B. D. Washo, "Spin coating: One-dimensional model," *IBM Journal of Research and Development*, vol. 21, no. 2, pp. 190–198, 1977.

[63] R. Feng and R. J. Farris, "Influence of processing conditions on the thermal and mechanical properties of SU8 negative photoresist coatings," *Journal of Micromechanics and Microengineering*, vol. 13, p. 80, 2003.

[64] S. Keller, G. Blagoi, M. Lillemose, D. Haefliger, and A. Boisen, "Processing of thin su-8 films," *Journal of Micromechanics and Microengineering*, vol. 18, no. 12, p. 125020, 2008.

[65] J. Zhang, K. L. Tan, G. D. Hong, L. J. Yang, and H. Q. Gong, "Polymerization optimization of su-8 photoresist and its applications in microfluidic systems and mems," *Journal of Micromechanics and Microengineering*, vol. 11, no. 1, p. 20, 2001.

[66] H. Abe, M. Yoneda, and N. Fujiwara, "Developments of plasma etching technology for fabricating semiconductor devices," *Japanese Journal of Applied Physics*, vol. 47, no. 3, pp. 1435–1455, 2008.

[67] C. Y. Poon and B. Bhushan, "Comparison of surface roughness measurements by stylus profiler, AFM and non-contact optical profiler," *Wear*, vol. 190, no. 1, pp. 76–88, 1995. <ce:title>Macro and Micro-Tribology and Mechanics of Magnetic Storage Systems</ce:title>.

[68] G. Lifante, *Integrated photonics: fundamentals*. J. Wiley, 2003.

[69] E. A. J. Marcatili, "Dielectric rectangular waveguide and directional coupler for integrated optics," *Bell System Technical Journal*, pp. 2071–2102, Sept. 1969.

[70] G. B. Hocker and W. K. Burns, "Mode dispersion in diffused channel waveguides by the effective index method," *Appl. Opt.*, vol. 16, pp. 113–118, Jan 1977.

[71] A. Kumar and D. Gupta, "Vector modes of rectangular-core dielectric waveguides: An improved perturbation approach," *Optics communications*, vol. 274, no. 2, p. 327,Äì332, 2007.

[72] J. E. Goell, "A circular-harmonic computer analysis of rectangular dielectric waveguides," *Bell System Technical Journal*, pp. 2133–2160, Sept. 1969.

[73] R. Scarmozzino, A. Gopinath, R. Pregla, and S. Helfert, "Numerical techniques for modeling guided-wave photonic devices," *Selected Topics in Quantum Electronics, IEEE Journal of*, vol. 6, pp. 150–162, Jan. 2000.

[74] O. Parriaux and G. J. Veldhuis, "Normalized analysis for the sensitivity optimization of integrated optical evanescent-wave sensors," *Lightwave Technology, Journal of*, vol. 16, no. 4, p. 573,Äì582, 1998.

[75] R. Feynman, *The Feynman Lectures on Physics: Volume 2*, vol. 2 of *The Feynman Lectures on Physics*. Boston: Addison-Wesley, 1963.

[76] F. Vollmer and S. Arnold, "Whispering-gallery-mode biosensing: label-free detection down to single molecules," *Nat Methods*, vol. 5, pp. 591–596, July 2008.

[77] R. Todeschini, V. Consonni, R. Mannhold, H. Kubinyi, and H. Timmerman, *Handbook of Molecular Descriptors*. Methods and Principles in Medicinal Chemistry, Wiley, 2008.

[78] M. Bélanger and Y. Marois, "Hemocompatibility, biocompatibility, inflammatory and in vivo studies of primary reference materials low-density polyethylene and polydimethylsiloxane: A review," *Journal of Biomedical Materials Research*, vol. 58, no. 5, pp. 467–477, 2001.

[79] S. L. Peterson, A. McDonald, P. L. Gourley, and D. Y. Sasaki, "Poly(dimethylsiloxane) thin films as biocompatible coatings for microfluidic devices: Cell culture and flow studies with glial cells," *Journal of Biomedical Materials Research Part A*, vol. 72A, no. 1, pp. 10–18, 2005.

[80] A. Mata, A. Fleischman, and S. Roy, "Characterization of polydimethylsiloxane (pdms) properties for biomedical micro/nanosystems," *Biomedical Microdevices*, vol. 7, pp. 281–293, 2005.

[81] W. Sawyer, K. D. Freudenberg, P. Bhimaraj, and L. S. Schadler, "A study on the friction and wear behavior of ptfe filled with alumina nanoparticles," *Wear*, vol. 254, no. 56, pp. 573 – 580, 2003.

[82] G. M. Hale and M. R. Querry, "Optical constants of water in the 200 nm to 200 um wavelength region," *Appl. Opt.*, vol. 12, pp. 555–563, Mar 1973.

[83] J. R. Vig, "UV/ozone cleaning of surfaces," *J. Vac. Sci. Technol. A*, vol. 3, no. 3, pp. 1027–1034, 1985.